MEMRISTIVE DEVICES FOR NEUROMORPHIC COMPUTING APPLICATIONS

A Dissertation
Presented to
The Academic Faculty

by

Joshua C. Shank

In Partial Fulfillment
of the Requirements for the Degree
Doctor of Philosophy in the
School of Electrical and Computer Engineering

Georgia Institute of Technology
August 2016

MEMRISTIVE DEVICES FOR NEUROMORPHIC COMPUTING APPLICATIONS

Approved by:

Dr. W. Alan Doolittle, Advisor
School of Electrical and Computer Engineering
Georgia Institute of Technology

Dr. Muhannad Bakir
School of Electrical and Computer Engineering
Georgia Institute of Technology

Dr. A. Bruno Frazier
School of Electrical and Computer Engineering
Georgia Institute of Technology

Dr. Faisal Alamgir
School of Materials Science and Engineering
Georgia Institute of Technology

Dr. William Hunt
School of Electrical and Computer Engineering
Georgia Institute of Technology

Date Approved: July 29, 2016

To my parents, siblings, and friends for all the great discussions we've had.

ACKNOWLEDGEMENTS

I wish to thank my parents for teaching and supporting me throughout these many years. I would also like to thank my professors and particularly my advisor Dr. Alan Doolittle for many helpful conversations and brainstorming sessions that led to this work. This work would not have been possible without the other members of the Advanced Semiconductor Technology Facility, specifically Jordan Greenlee, Brooks Tellekamp, Brendan Gunning, Chloe Fabien, Joseph Merola, and Evan Clinton.

The staff of the Institute for Electronics and Nanotechnology also deserves special thanks. In particular I would like to thank those members of the staff that helped me build the Denton Discovery 2 Sputtering System including: Gary Spinner, Jason Herrington, John Pham, Vinh Nguyen, Thomas Johnson-Averett, Dean Sutter, and Scott Fowler.

TABLE OF CONTENTS

LIST OF FIGURES

SUMMARY

The performance of digital computers has begun to saturate due to material, size, and power limitations. In addition to solving these dilemmas, new computing paradigms are being investigated. This thesis explores neuromorphic computing as a possible new computational paradigm, specifically an all hardware approach based on biological neural processing. Chapter 1 introduces neuromorphic computing, neurobiology, memristive devices for neuromorphic computing, and the memristive material lithium niobite ($LiNbO_2$).

Chapters 2 discusses the synthesis of lithium niobite by room temperature sputtering as well as some basic physical, optical, chemical, and electrical properties. Chapters 3 and 4 explore more complex properties of lithium niobite including the effects of high energy radiation on lithium niobite devices and the effects of light interacting with the mobile ions in lithium niobite.

Chapters 5 – 7 discuss three devices useful for mimicking sub-structures within a biological neuron. These devices are two-terminal lithium niobite memristors, lithium niobite based batteries, and a new memdiode based on Nb_2O_5. Chapter 8 returns to the synthesis of lithium niobite, but in the form of bulk wafers, and discusses their potential application toward replicating the "sea of ions" surrounding biological neurons.

Chapters 9 and 10 conclude this thesis by discussing device models for lithium niobite memristors and their application in several neuromorphic circuits to add biologically realistic behavior without increasing the complexity of the circuit.

CHAPTER 1

INTRODUCTION

1.1 Historical and Fundamental Limitations in CMOS Computing

Semiconductor electronics revolutionized the computing industry by providing inexpensive, reliable, and scalable components for both the memory and arithmetic processing functions of a computer. Since their initial introduction, the periodic reduction in transistor size, termed Moore's Law [1], has yielded computer processors with more transistors, increased speed, and increased functionality. Since the first commercial integrated circuit was introduced in 1964 [2], this microelectronic scaling has enabled a wide range of new technologies in diverse markets such as communications, entertainment, security, energy, transportation, and healthcare [3, 4].

While the exponential growth of microelectronic circuit densities has driven decades of economic growth, industry [4] and academic [5] studies predict the end of Moore's Law scaling within the next 10 – 20 years due to leakage currents encountered in nanoscale devices [4-7]. As early as 2006, leakage currents were reported to consume 20 – 30% of a CMOS processor's power [5]. The thermal limitations imposed by these leakage currents have led to saturation in the power, operational frequency, and performance of CMOS processors as shown in Figure 1-1 [8]. While the performance limitations imposed by leakage currents have largely been mitigated by multi-core processors [9], direct drain-to-source tunneling is predicted to end microelectronic scaling [6, 7]. The ITRS 2013 roadmap predicts that transistor gate lengths will approach 5 nm by 2030 [4]. Calculated tunneling current densities for such small devices indicate

that tunneling current will be 60 – 90 % of the transistor's total current in both the on and off states [6] limiting their ability to act as switches.

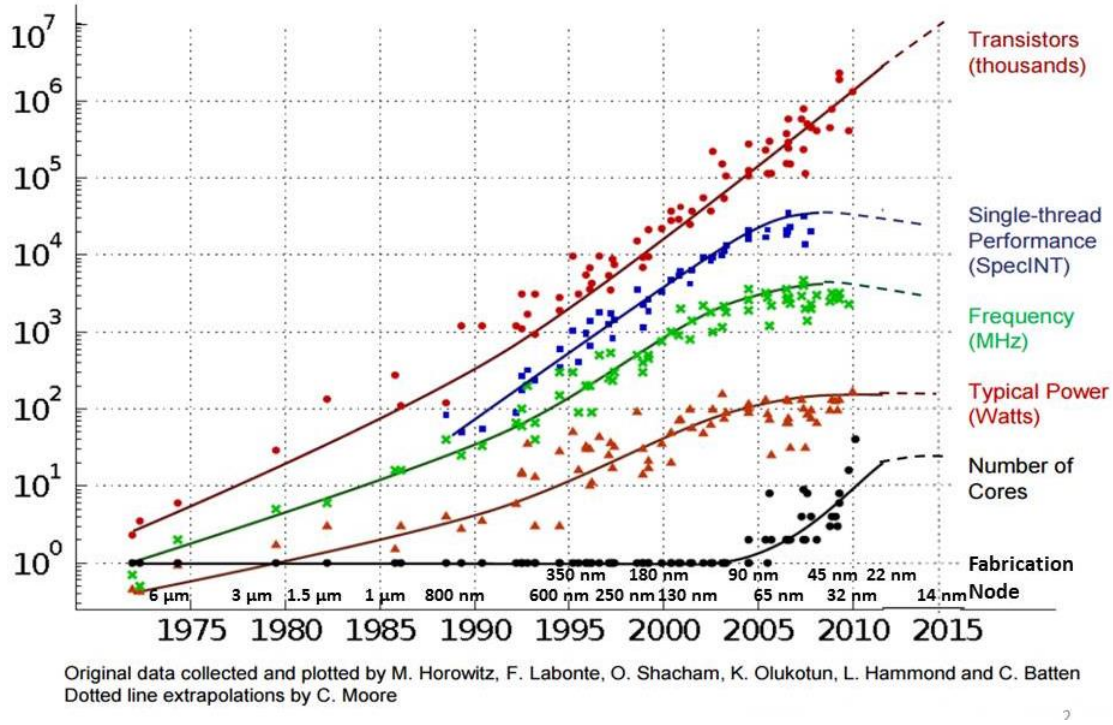

Figure 1-1: CMOS processor trends showing saturation in processor performance despite the increasing number of transistors. [8]

With the impending end of Moore's Law scaling, new approaches are being considered to improve computer performance [4]. The performance of general purpose computing can still be improved through non-scaling means including: high mobility channel materials, low interface trap density gate dielectrics, 3-D integration, power management, and heat removal [4]. However, emerging application specific technologies are also being developed to improve performance of specific tasks with 100 fold increases in processing speed [5]. These emerging technologies provide new and diverse computing paradigms such as GPU computing [10], quantum computing [11], optical

computing [12], or neuromorphic computing [13] that may be applied alone or in conjunction with general purpose CMOS processors.

1.2 Neuromorphic Computing

Neuromorphic computing uses microelectronic circuitry to mimic the biological computation performed in the human brain [13]. While CMOS computers excel at tasks such as basic arithmetic, the human brain performs poorly at these tasks. In contrast, CMOS computers must use computationally expensive algorithms for tasks such as pattern recognition, system control, and processing noisy data. The human brain excels at these tasks enabling us to recognize objects even at a variety of angles, walk as an unstable inverted pendulum, correlate sights, sounds, and smells, and pick out a person from a crowded room by any of these senses. Additionally, the human brain performs all of these tasks with a power consumption of about 20 watts [14].

While digital and biological computation speeds cannot be directly compared due to their different computation paradigms, a rough comparison can be made by analyzing the scale of each technology. The Intel microprocessor (Broadwell-U), released in 2015, has a reported computational speed of about $8x10^{11}$ operations per second in a 28W chip using on-board GPU computing [15]. In comparison, the human brain contains 10^{12} neurons each containing 10^4 synapses performing complex operations at speeds between 0.1 – 100 Hz [14]. This yields computational speeds between 10^{15} – 10^{18} operations per second, 3 – 6 orders of magnitude faster than a modern processor with similar power consumption. Thus, if neuromorphic computation can emulate the biological brain it will

provide a computational paradigm that compliments the strengths and weaknesses of a CMOS computer while consuming less power and accelerating the computational speed.

1.2.1 Introduction to Neurobiology

In order to replicate the benefits of biological computation, it is necessary to understand at least the basics of its operation. The brain operates by the generation, propagation, scaling, and integration of voltage spikes termed action potentials [16]. Each of these operations is an analog process with variations in the spike rate, spike amplitude, and spike shape. There are multiple theories for how information is encoded in these variables and experimental evidence that multiple methods may be simultaneously applied in the brain [17]. Likewise, memory is also an active area of neurobiology research and may be stored in multiple ways. However, unlike Von Neumann computing, at least one form of memory in the brain is stored within the synaptic connections that also process data [16].

An individual neuron is the basic complete computational unit for processing action potentials. However, a neuron can be divided into physical structures that perform different computational tasks. These structures include: the synapses, the dendritic tree, the soma (cell body), the axon hillock, and the axon as shown in Figure 1-2. Each of these biological structures can be compared to a corresponding electronic analogue. This thesis examines the fabrication, function, and properties of several materials and devices that mimic these biological structures.

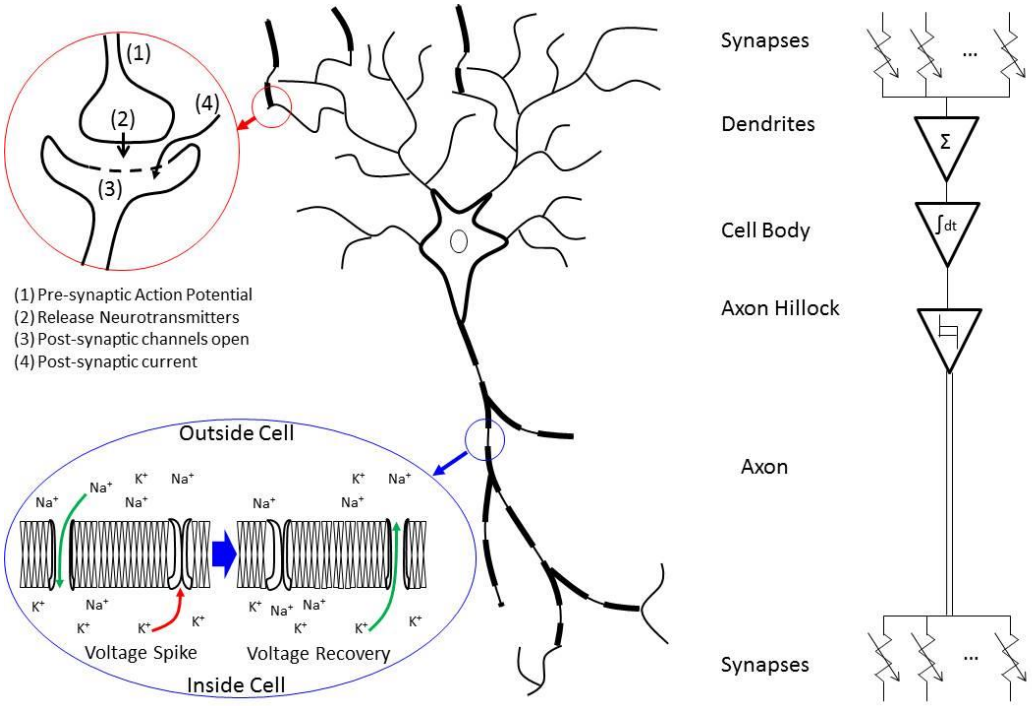

Figure 1-2: Schematic of a neuron with diagrams of synaptic function and action potential generation. A neuron consists of multiple structures that each performs a unique computational task as shown on the functional diagram to the right. Any particular neuron may have all or some of these structures. The diagram of synaptic function (Top Left) describes a typical chemically gated synapse. The diagram of action potential generation (Bottom Left) depicts the voltage gated ion channels in a neuron during an action potential. When the Na^+ channels are open but the K^+ channels are still closed the voltage increases (Left of sub-diagram). When the Na^+ channels close and the K^+ channels open, the voltage recovers (Right of sub-diagram) [16].

A typical neuron has between 10^3 – 10^4 synapses that connect it to other neurons [14]. As shown in Figure 1-2, when an action potential arrives at the synapse from the pre-synaptic neuron, the synapse allows an ionic current to flow into the post-synaptic neuron from the intracellular fluid. The magnitude of this current is determined by the synaptic conductance, which is at least one form of memory within the neuron [16]. Thus the synapse acts as a chemically gated transistor with memory. Synapses are often implemented in neuromorphic circuitry as digital connections or as transistor circuits that store the synaptic conductance as voltages on capacitors or floating gates [18]. These implementations suffer from analog/digital conversion, voltage decay, and high device

mismatch [18]. More recently, synapses have been implemented using two-terminal memristive devices [19]. These devices naturally implement long-term memory, but do not possess gain as observed in biological synapses [20]. Application of lithium niobite memristors for short-term memory has previously been examined [21] and application for long term memory will be examined in Chapter 2.

The dendritic tree transports the synaptic ion current toward the soma (cell body). In its simplest form, the dendritic tree is a transmission line and can be described by passive cable equations with ionic resistors and capacitors. However, the structure of the dendritic tree strongly impacts this function controlling the distance and direction of current propagation. In addition, research indicates that some dendritic trees also provide active amplification and filtering as well as controlling communication between synapses [22]. The biological ion channels that enable amplification have previously been implemented in neuromorphic circuitry using electroformed Mott memristors [23]. Chapter 7 will discuss a new "memdiode" that is simpler to fabricate and exhibits similar capacitance, rectification, and hysteresis. These properties may be useful for both signal propagation and amplification. While not explicitly addressed in this thesis, Appendix B provides a brief discussion, in the context of future work, of how the dendritic tree structure affects spike propagation and synaptic learning.

The soma or cell body primarily serves the non-computational functions of the neuron, such as storing genetic material, which need not be replicated in a neuromorphic circuit. However, the cell membrane surrounding the soma does provide charge storage that integrates the input current from the dendritic tree. The voltage across this membrane, which is typically 5 nm thick [14], is given by Equation 1.1 [16].

$$V_m = \frac{RT}{F} \ln\left(\frac{p_K[K^+]_o + p_{Na}[Na^+]_o + \cdots}{p_K[K^+]_i + p_{Na}[Na^+]_i + \cdots}\right) \quad \text{Equation 1.1}$$

Where R is the universal gas constant, T is temperature, F is Faraday's constant, p_x is the relative permittivity of ion species X and $[X^+]_{o(i)}$ is the concentration of ion species X outside (o) or inside (i) the cell. The soma can thus be considered as a capacitor or battery storing charge to form a voltage. Application of a lithium niobite battery as an ionic integrator similar to the cell membrane will be discussed in Chapter 6.

The axon hillock resides at one side of the soma and is responsible for initiating action potentials [16]. When the cell potential exceeds a threshold value, positive feedback opens large numbers of voltage gated sodium channels causing the cell voltage to increase further. After a short delay, the voltage gated sodium channels close and voltage gated potassium channels open causing the cell voltage to decrease. Eventually the voltage gated potassium channels close and the neuron returns to its resting voltage [16]. The threshold voltage and timing of this process are functions of the neuron's recent history acting as another form of memory [24]. The axon hillock is thus a threshold detector with short-term memory. While the axon hillock is not explicitly addressed in this PhD thesis, the ion dynamics are similar to those in the dendritic tree and axon. Therefore, the memdiode discussed in Chapter 7 may be applicable.

The axon forms the final component of a neuron and is responsible for propagating the action potential to other neurons. Propagation occurs by passive conduction between active nodes that amplify the action potential using voltage gated ion channels similar to the axon hillock described above and shown in Figure 1-2. The axon can be described mathematically by the Hodgkin-Huxley model shown in Figure 1-3 [25]. Later work demonstrated that the dynamic conductances described in the Hodgkin-

Huxley model could be implemented by memristive systems [26]. A recent circuit using Mott Memristors replicated the functionality of an axon [23]. As previously noted, a new memdiode will be discussed in Chapter 7 that is simpler to fabricate and may be useful for both the signal propagation and amplification functions of an axon. It should be noted that since the original publication of the Hodgkin-Huxley model new discoveries have added complexity to the model of an axon. These additions are discussed in Appendix B.

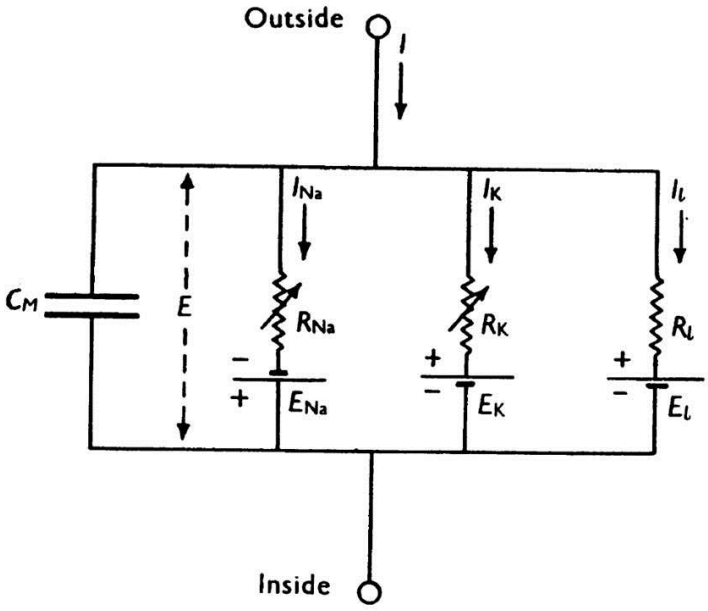

Figure 1-3: The original Hodgkin-Huxley model describing the ion kinetics of a biological axon [25].

While the basic neuron structures all serve specific functions, it is incorrect to assume that a complete neural processor can be built from a single neuron combining these structures. As described in an annual review of neuroscience: "Out of the 10^{12} neurons in the human nervous system, there are ~10,000 distinct morphological classes" [22]. Each of these neuron classes serves a specific function enabled by its morphological properties. A review of these morphological effects is discussed in Appendix B.

1.2.2 Previous Work in Neuromorphic Computing

The term ‘Neuromorphic’ was first introduced to academic literature by Carver Mead in 1990 to describe “systems based on the organizing principles used by the nervous system” [13]. While this description is quite broad, later definitions draw fine lines between neuromorphic, bio-inspired, and biomimetic systems [27]. For the purpose of this work, we will ignore any such distinctions as the circuit complexity and level of biological mimicry develops through the history of neuromorphic research.

Early work mimicking biological functionality using analog VLSI technology focused on sensory perception, specifically vision [28, 29] and hearing [30, 31]. These systems successfully replicated many important functionalities of sensory perception by analyzing the associated biological structures and capturing the gross behavior of each structure in an analog circuit. For example, by analyzing the retina, Mahowald and Mead [28] produced a circuit mimicking the retinal photoreceptors, horizontal cells, and bipolar cells [28]. Mimicking these cells reproduced functionality including the logarithmic light sensitivity of a photoreceptor that provides us with sensitivity to many orders of magnitude of light intensity and the local spatial and temporal weighting of the horizontal cell layer that allows us to see high contrast images [28]. Likewise, early audio sensory perception focused on reproducing the spatial filtering of frequencies within the cochlea while maintaining enough temporal resolution to recognize patterns such as speech or musical rhythm [30]. However, these early efforts largely ignored the mechanisms behind the biological functions and the manner in which biology encodes information, namely in action potentials.

Despite the cellular level of functional detail these early systems reproduced, they emphasized the importance of subcellular adaptation mechanisms. For example, in

biological retinal neurons, differences in photoreceptor sensitivity and synaptic strength are compensated by feedback adaptation mechanisms that are still an active area of research [32, 33]. Likewise, early retinal circuits suffered from fabrication variations and sensitivity to transistor offset voltages [13]. Adaptation was accomplished by a UV stimulated shunt conductance on a floating gate transistor [13]. While this is clearly not the adaptation mechanism used in biological neurons, the circuit designers noted: "Once we understand the principles of adaptation, we can incorporate them into our silicon retina" [13]. This co-development of neuromorphic systems alongside active research on neurobiological systems leads to mixtures of bio-mimicry with functional VLSI design.

The introduction of action potentials to neuromorphic circuits was first reported in 1991 as the level of bio-mimicry increased from the cellular level to the sub-cellular level [34]. The kinetics of sodium and potassium ion channels responsible for action potential generation were reproduced using differential pair CMOS transistor circuits [34]. While this circuit successfully demonstrated action potentials similar to a pyramidal neuron, the primary neuron in the neocortex, this function only covers the soma and axon hillock functionalities of a biological neuron.

This early neuron circuit operated at biological frequencies [34] (0.1 – 100 Hz) [14]. While an electronic artificial neuron could certainly operate orders of magnitude faster than the ionic biological neuron, it is important to match the neural circuit's speed to the system it senses or controls. Finally, the early artificial neuron consumed only 60 µW of power [34]. While this is 4 orders of magnitude less power than an operational amplifier built with the same technology, it is still at least 6 orders of magnitude more power than a biological neuron [34]. Future work reduced this power consumption to 300

nW in 2003 [35] and 7.5 nW in 2009 [36], still more power consumption than the 20 pW for a biological neuron.

The early neuromorphic systems laid the foundations for the emerging field of neuromorphic computing, but left many research avenues open including: power efficiency [19, 35-39], information coding [18, 38, 40, 41], memory mechanisms [19, 40, 42, 43], volatile adaptation [38, 44], circuit density [19, 37], and neural connections [18, 19, 45]. The guideline for approaching all of these topics was laid out by Carver Mead when he defined the field: "the real trick is to invent a representation that takes advantage of the inherent capabilities of the medium…using the nervous system as a guide, we will attempt to find a natural way to integrate them into an overall system-design strategy" [13].

1.3 Memristors

Neuromorphic computing research predominately focused on silicon analog VLSI technology from the early 80's through 2008 because that was the dominant medium available. However, in 2008 with the realization of physical memristive devices [46], a new medium with biologically relevant capabilities became available.

Memristors, first theorized by Leon Chua in 1971 [47], are the fourth fundamental passive two terminal device complementing resistors, capacitors, and inductors. These passive circuit elements are described by relationships between voltage (V), current (I), charge (Q), and flux-linkage (ϕ) according to Equations 1.2a-f.

Fundamental Definition	$dQ = I * dt$	Equation 1.2a
Fundamental Definition	$d\phi = V * dt$	Equation 1.2b

Resistor	$dV = R * dI$	Equation 1.2c
Capacitor	$dQ = C * dV$	Equation 1.2d
Inductor	$d\phi = L * dI$	Equation 1.2e
Memristor	$d\phi = M * dQ$	Equation 1.2f

The absence of this last equation was conspicuous at the time and Chua argued that it should exist based on completeness [47]. Theoretical analysis of the memristor equation revealed that such a device should act like a variable resistor with memory of its input. Thus the name memristor (memory – resistor) was chosen [47].

In 1976, Chua introduced a broader class of devices termed memristive systems [26]. These systems include the original memristor definition, but can describe additional effects such as multiple input forces, multiple output variables, and multiple internal mechanisms capable of modifying the memristance (M) [26]. This broader definition has been important for describing and modeling physical memristors because the more restrictive 1971 definition does not allow for effects such as threshold voltages [46, 48-51], volatile relaxation [52], thermal [23], optical [53], or magnetic inputs [54-56], or multi-port devices [57, 58]. All of these effects have been observed in physical devices and no known device fits the more restrictive 1971 definition. Similar to the debate between neuromorphic vs. biomimetic systems, there has been considerable debate as to what constitutes a "true" memristor [59, 60]. We will once again ignore this distinction and accept any device matching the 1976 definition as a memristor.

While resistive switching memories have been researched since at least the early 1960's [61], in 2008 HP Labs first linked resistive switching memories to the memristor formalism [46]. Since that announcement, memristive behavior has been discovered in a

wide range of devices. These devices can broadly be divided into categories based on their internal memristance mechanism. Such categories include: filamentary memristors [46, 48-51, 62], mobile ion wavefront memristors [21, 63, 64], oxidation/reduction memristors [57, 58], spintronic memristors [54-56], ferroelectric memristors [65], and Mott metal-insulator switches [23]. A discussion of these memristor classes is provided in Appendix C. The majority of memristor research has focused on memristors based on ion motion including the filamentary and mobile ion wavefront memristors.

Both filamentary and mobile ion wavefront memristors operate due to the movement of mobile atoms that modify the local electronic conductivity. In filamentary memristors, localized breakdown of a thin insulating material causes the movement and removal of atoms forming a thin filament connecting two metal electrodes [66]. This electroforming process often removes atoms violently from the film causing damage to the contacts [66, 67]. Once electroformed, filamentary memristors are switched by electrically driving atoms to create or destroy a high conductance region along the filament [46, 67]. This switching process requires electric fields above 10^6 V/cm [68], produces power densities on the order of 10^{12} W/cm^3 [62], and reaches temperatures of 800 K [69]. While filamentary memristors are most commonly used as digital devices [70], within neuromorphic computing filamentary memristors have primarily been used to replicate biological synapses [19, 71]. By carefully controlling the magnitude and timing of the applied voltage/current, filamentary memristors can be made to have analog resistance values [72]. However, one estimate stated that a neuromorphic chip with 10^6 neurons/cm^2 each connected with 10^4 synapses made from state-of-the-art filamentary

memristors operating at biological frequencies (10 Hz) would have to dissipate 2 kW of power [19], which is 2 orders of magnitude more power than the entire brain uses.

In contrast to filamentary memristors, mobile ion wavefront memristors do not form a localized filament and do not require electroforming. One example of this type of memristor is the co-sputtered Ag/Si memristor [63]. The ion profile for this memristor is created during the sputter deposition process as silver dopant atoms are introduced part of the way through the deposition [63]. Mobile ion wavefront memristors have an analog resistance range making them useful for analog neuromorphic computing, but do not have as wide a dynamic range (R_{ON} / R_{OFF}) as filamentary memristors.

The memristors analyzed herein are mobile ion wavefront memristors made from lithium niobite ($LiNbO_2$). This material displays memristive behavior due to the motion of highly mobile lithium ions that act as dopants [21, 73, 74]. One rather unique aspect of lithium niobite compared to other memristive materials is the volatile nature of its memristive behavior due to the low activation energy for lithium motion [75, 76].

1.4 Lithium Niobite ($LiNbO_2$)

Lithium niobite ($LiNbO_2$) is a minimally studied sub-oxide of the common optical [77, 78] and acoustic [78] wave guiding material lithium niobate ($LiNbO_3$). Lithium niobite is structurally related to several lithium ion battery cathode materials including $LiCoO_2$. These materials possess a layered structure in which planes of lithium ions separate sheets of metal oxide as shown in Figure 1-4.

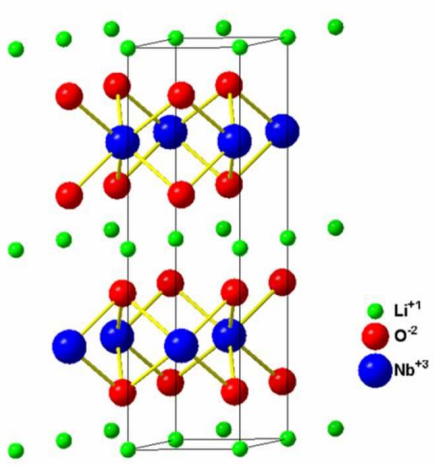

Figure 1-4: Ball and stick structural model of lithium niobite ($LiNbO_2$). Planes of loosely bound lithium sit between sheets of niobium oxide.

The primary structural difference between lithium niobite and other battery cathode materials is a 180^o twist in the crystal structure. This results in the niobium atoms occupying trigonal-prismatic sites in $LiNbO_2$ (space group $P6_3/mmc$) [79] rather than octahedral sites in $LiCoO_2$ (space group $R\bar{3}m$) [80]. The consequence of this structural change is a three band electronic structure, shown in Figure 1-5, with significant metal-metal bonding and high electronic conductivity [81, 82]. The tunable electrical and optical properties that make lithium niobite useful for neuromorphic computing result from changes to this band structure as lithium is moved within the crystal or removed (delithiation) from the crystal.

1.4.1 Theoretical Band Structure

The three band structure in lithium niobite occurs due to crystal field splitting in the trigonal-prismatic coordination [82, 83] resulting in a completely filled lower valence band, a completely filled upper valence band, and an empty conduction band. Partial density of states calculations indicate that these bands are composed almost exclusively

of niobium and oxygen orbitals while lithium has a localized orbital [81, 82, 84]. The lithium atoms are almost completely ionized [76, 82, 84] donating an electron to fill the upper valence band. As lithium atoms are removed from lithium niobite, forming Li_xNbO_2 with $x < 1$, electrons are removed from the upper valence band forming a degenerately doped p-type material [82]. Removal of all of the lithium would theoretically result in a half filled upper valence band [85], although such extreme delithiation has never been demonstrated.

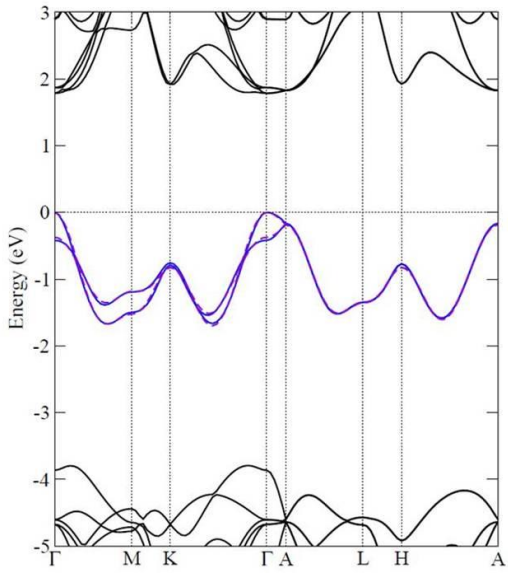

Figure 1-5: Theoretical three band structure for lithium niobite as calculated by Ylvisaker et al. [82] The bottom band is full occupied and is not electrically or optically active. The middle band (valence band) is the primary electronic band as Li_xNbO_2 ($x < 1$) is degenerately doped p-type. The top band (conduction band) is empty.

1.4.2 Functional Properties

Memristive behavior occurs in lithium niobite [21, 74] due to lithium ion motion modifying the local occupancy of states [73, 86]. While models of lithium niobite memristors produce orders of magnitude changes in memristance [87], only smaller percentage changes have been experimentally observed [21]. This discrepancy is perhaps

because the most dramatic changes in memristance occur when the lithium concentration is near the ideal stoichiometry [87], a condition that is difficult to experimentally achieve [88] as shown in Figure 1-6. The lithium ions in lithium niobite are loosely bound to the crystal and can be removed chemically forming Li_xNbO_2 with lower memristive potential [88]. For example, deionized water used for cleaning a sample surface can remove up to 11% of the lithium from lithium niobite [88]. A list of reported chemical delithation values is given in Table 1 [88]. While the ease of lithium removal is a fabrication challenge for lithium niobite based devices, the motion of lithium ions necessary for memristive behavior is also enabled by the loose lithium binding and a low (~300 meV) activation energy barrier for motion [75, 76]. This low activation energy also enables room temperature diffusion and volatile behavior [75, 76].

Table 1: Chemical delithiation potentials of various solutions as reported by Moshopoulou [88].

Chemical Solution	Percent Lithium Removed
85% H_3PO_4	6
H_2O	11
HBr	12
60% HNO_3	16
95% H_2SO_4	27
3% HCl	28
37% HCl	31

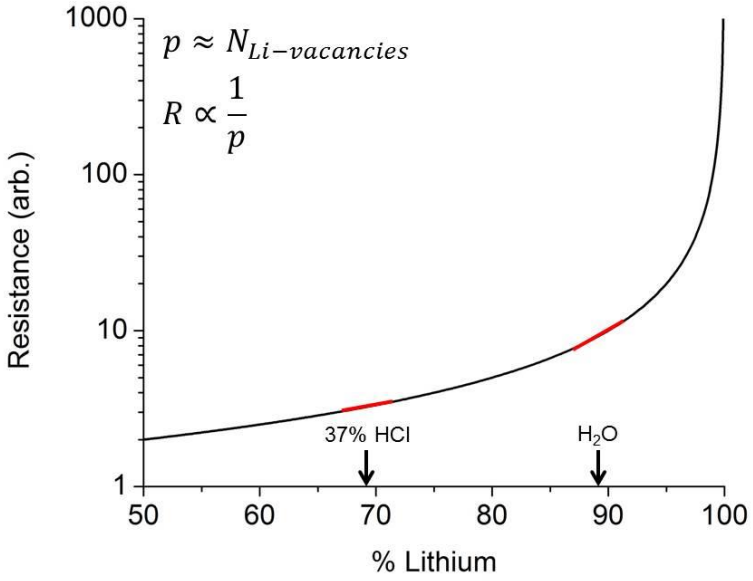

Figure 1-6: Theoretical calculation for the resistance of lithium niobite vs. the percentage of lithium within the crystal. The maximum resistance change occurs for lithium concentrations near the stoichiometric concentration, although experimentally this is difficult to achieve due to the ease of chemical lithium removal.

Early work on lithium niobite primarily focused on fundamental material properties [75, 76, 79, 82, 84, 86, 88-92] and applications as a superconductor [75, 85, 88, 93] and battery cathode [90, 94]. Through this early research it was discovered that most physical and electrical properties of lithium niobite are dependent on the lithium content including: the crystalline lattice parameters [90], the superconductivity transition temperature [85], the battery open-circuit voltage [90, 94], and the resistivity [90].

CHAPTER 2

SPUTTER DEPOSITION OF LITHIUM NIOBITE

2.1 History of Lithium Niobite Fabrication

Synthesis of lithium niobite has previously been demonstrated by reaction of powdered precursors [79, 85, 90], liquid phase electrolysis [88, 92, 95], and by molecular beam epitaxy [21, 64]. Early work with reacted powders likely contained unreacted precursors [79] or other impurities [82] leading to experimental discrepancies such as both metallic [88] and semiconducting [90] temperature dependent resistivity and varying magnetic properties including diamagnetic [75], paramagnetic [85, 90], and antiferromagnetic [79] behavior. The reactions [91] necessary to form powdered lithium niobite occur at temperatures between 700 – 900 ^{o}C [79] and do not produce material suitable for microelectronics.

Synthesis of lithium niobite by liquid phase electrolysis produces bulk crystals with millimeter to centimeter dimensions [88, 92, 95]. This process involves electrodeposition from a molten lithium borate solution at temperatures between 800 – 900 ^{o}C [92, 95]. This method produces high quality single crystals [95] useful for exploring the material properties of lithium niobite, but the molten lithium borate solution readily dissolves oxides and is incompatible with many other microelectronic materials [96].

The final method for synthesis of lithium niobite is by metal-halide molecular beam epitaxy (MBE) [21, 64]. This method substitutes evaporation of niobium by electron beam evaporation, which is incompatible with an oxygen environment, with a

$NbCl_5$ source [64]. The $NbCl_5$ is chemically cracked on the wafer surface by excess lithium forming metallic niobium and the high vapor pressure material LiCl, which desorbs. Lithium niobite is formed by a careful balance of lithium flux, $NbCl_5$ flux, and oxygen flux from a remote plasma source [64]. This halide-MBE process is also capable of producing Nb, NbO, $LiNbO_3$, and Li_3NbO_4 [64]. However, while the MBE method for lithium niobite synthesis produces high quality thin films suitable for microelectronics, the 950 ^oC environment, excess lithium flux, and chlorine environment may produce technical constraints for incorporation with other microelectronic materials.

2.2 Building a Sputtering System

Previous methods of lithium niobite synthesis have supplied the refractory metal niobium through high temperatures and reactive chemistries because metallic niobium is difficult to evaporate (vapor pressure = 4.86×10^{-22} Torr at 900^oC) [64] and difficult to dissolve [97]. In contrast, sputter deposition can easily provide a flux of niobium atoms because sputtering operates on the transfer of kinetic energy [98] rather than equilibrium vapor pressure (as in evaporation) or chemical solvency (as in electrodeposition).

In order to explore sputter deposition of lithium niobite, a research-grade sputtering system was needed that could achieve: high substrate temperatures, co-deposition from multiple targets, multiple gas flows for reactive sputtering, and an electrically isolated platen for *in situ* plasma cleaning in order to explore the effects of all of these variables on the synthesis of lithium niobite. The sputtering system constructed

for this purpose is the Denton Discovery 2 sputtering system located in the IEN Marcus inorganic cleanroom as shown in Figure 2-1.

Figure 2-1: The Denton Discovery 2 sputtering system located in the Marcus Inorganic Cleanroom.

2.2.1 Initial System Setup

In collaboration with the Institute for Electronics and Nanotechnology (IEN) staff, a used Denton Discovery 18 sputtering system was purchased and modified to meet the requirements of this research. In order to make the system operational, a vacuum pumping system had to be built, the control system had to be replaced, and heat reflectors had to be added for high temperature operation.

The Denton Discovery 2 originally had only 2 confocal sputtering cathodes. These cathodes have directly cooled targets that are 3.625 inches in diameter. The directly cooled targets are metal bonded directly to the copper cooling block that has chilled water flowing through it. The combination of efficient heat transfer in the directly cooled design along with the large area targets allows these cathodes to operate at high

power. However, replacing the directly cooled targets requires disassembling the entire cathode, which takes multiple hours to complete. The cathode disassembly procedure can be found in Appendix A. A third cathode was added to the system in order to provide a cathode with easily exchangeable targets. It is a 3 inch diameter indirectly cooled cathode with a magnetron magnet configured to handle magnetic target materials. The indirectly cooled design clamps the target onto the cooling block making the target less efficiently cooled, but changing targets can be done in minutes rather than hours. The magnet configured for magnetic materials is stronger than a typical magnetron magnet and allows the system to deposit nickel as a lithium blocking electrode [99] and to explore the deposition of lithium cobalt oxide which is structurally similar to lithium niobite, but is more resistive (0.52 – 3.4 TΩ-cm) [100] and exhibits variable magnetism [101].

2.2.2 Vacuum Systems

The Denton Discovery 2 did not have a vacuum pumping system when purchased. A 6 inch diameter BOC Edwards EXT250M turbomolecular pump (nominal 240 L/s N_2) backed by a QDP40 oil-free rough pump was added to the system. The rough pump also has a direct connection to the main process chamber in order to pump down the system from atmospheric pressure. Due to the system geometry, the turbo pump has a poor conduction path to the main process chamber limiting the pump-down speed. A pump-purge procedure was attempted to accelerate the pump down process. This procedure utilized the direct rough pump to chamber connection to pump down the chamber to 10 Torr and then the dry nitrogen purge line to purge the chamber to 300 Torr. It was expected that this procedure would remove adsorbed water vapor and CO_2 accelerating the pump down time to high vacuum. As shown in Figure 2-2, while the pump-purge

procedure did slightly accelerate the pump down time once the procedure was complete, the added time to complete the pump-purge procedure eliminated any advantage and slowed down the total pump down time.

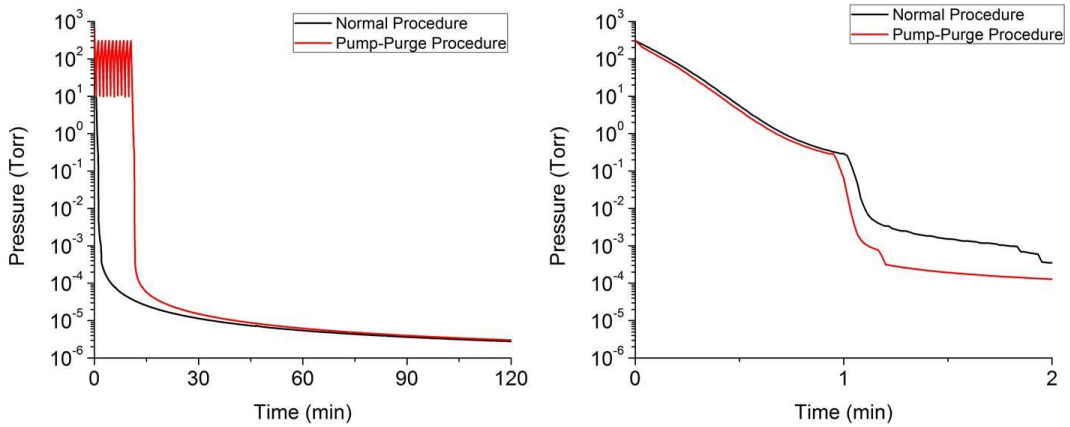

Figure 2-2: Comparison of the normal pump-down procedure and the pump-purge procedure. (Right) Once the pump-purge process was completed the chamber pumped down faster than the normal pump down process for the same pressure range. (Left) However, including the time required to complete the pump-purge cycles, the pump-purge procedure was slower than the normal pump down procedure.

Because the pump-purge procedure was unable to accelerate the pump down time, a cryo pump was added directly to the side of the main process chamber. The combination of a faster pumping speed (nominal 1500 L/s air, 4000L/s water vapor) and a direct connection conduction path reduced the pump down time from multiple hours to approximately 20 minutes. While adding the cryo pump accelerated the pump down time, it cannot be used to control pressure during a deposition and must be carefully monitored during high temperature processes as will be discussed in Section 2.2.6.

During a sputter deposition process, the pressure is controlled by fixing a set mass flow of process gas (Ar, O_2, or N_2) and then controlling the pumping speed using a throttle valve in front of the turbo pump. This procedure produces more reproducible films than a mass flow controlled system particularly during reactive sputtering [102].

Details about the relationship between mass flow, chamber pressure, and throttle valve position can be found in Appendix A.

2.2.3 Deposition Uniformity

The Denton Discovery 2 has a 6 inch diameter platen located at the confocal point of the three sputtering targets. In order to test the deposition uniformity over this area, a deposition was performed from the smallest (3 inch diameter) target onto a 6 inch diameter wafer with a grid of shadowed regions. The deposition thickness was measured by stylus profilometer after the deposition was complete and found to have a mean thickness of 592.2 nm with a standard deviation of 10.7 nm across the wafer. The thickness uniformity is thus better than a 2% error of the total thickness. No pattern was found in the film thickness across the wafer. Uniform deposition over a 6 inch diameter wafer is a significant improvement over previous lithium niobite deposition systems (MBE and electrodeposition) which have both been limited to approximately 1 cm^2 samples.

2.2.4 Reactive Deposition

In order to sputter deposit ceramic films, it is often desirable to introduce reactive gas species into the sputtering plasma. For example, the deposition of Nb_2O_5 can be accomplished by sputtering a metallic niobium target in an oxygen environment. While this procedure allows for fast deposition, controllable film properties, and cheaper equipment (DC vs RF power source and metallic vs pressed ceramic targets), the physics of reactive sputter deposition are nontrivial [103] and must be characterized on each sputtering system.

Figure 2-3 shows typical reactivity curves for the effect of oxygen on a niobium target in the Denton Discovery 2. As the oxygen flow is increased the niobium target voltage is initially stable until a threshold is reach. Above this threshold, the target voltage increases rapidly until re-stabilizing at a new value. When decreasing the oxygen flow, the threshold from high voltage to low voltage occurs at a lower oxygen flow than the initial threshold producing hysteresis. These transitions occur due to the competition of oxygen reacting with the target surface changing the target impedance and the sputtering process removing the reacted layer. At low oxygen flows, the reacted material can be removed faster than it accumulates leaving the target surface clean. At high oxygen flows, the reacted oxide accumulates on the target changing the surface composition. The target voltages and operational regimes are functions of both target power and operating pressure as shown in Figure 2-3.

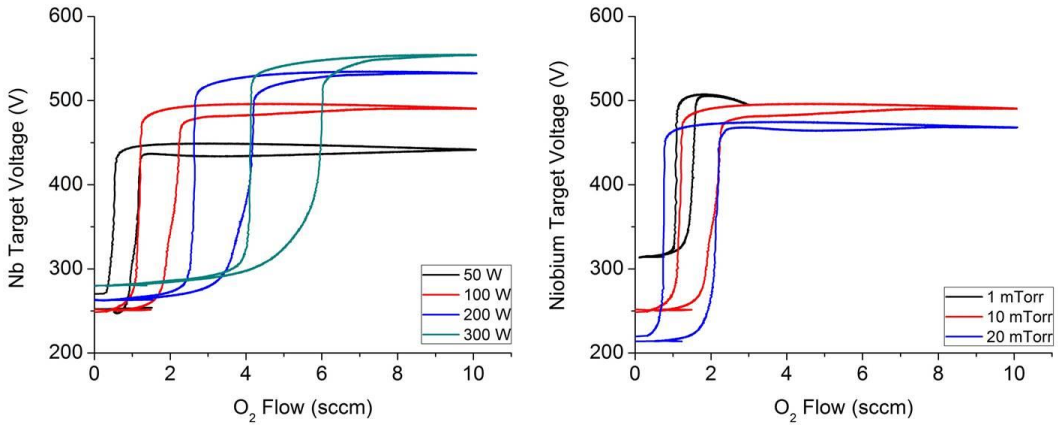

Figure 2-3: Reactivity curves for a niobium target exposed to an oxygen plasma in the Denton Discovery 2. The voltage levels, threshold flows, and target hysteresis are functions of both target power and chamber pressure.

2.2.5 Co-deposition from Multiple Targets

When depositing metal alloys or ceramics with more than two elements, such as lithium niobite ($LiNbO_2$), it is often advantageous to separate the atomic constituents into multiple targets and co-deposit [102]. The Denton Discovery 2 was built such that each target has its own power source that can be individually controlled in the control software. An example of co-deposition is shown in Figure 2-4 in which both a lithium oxide target (left) and niobium target (right) are simultaneously energized to produce lithium niobite.

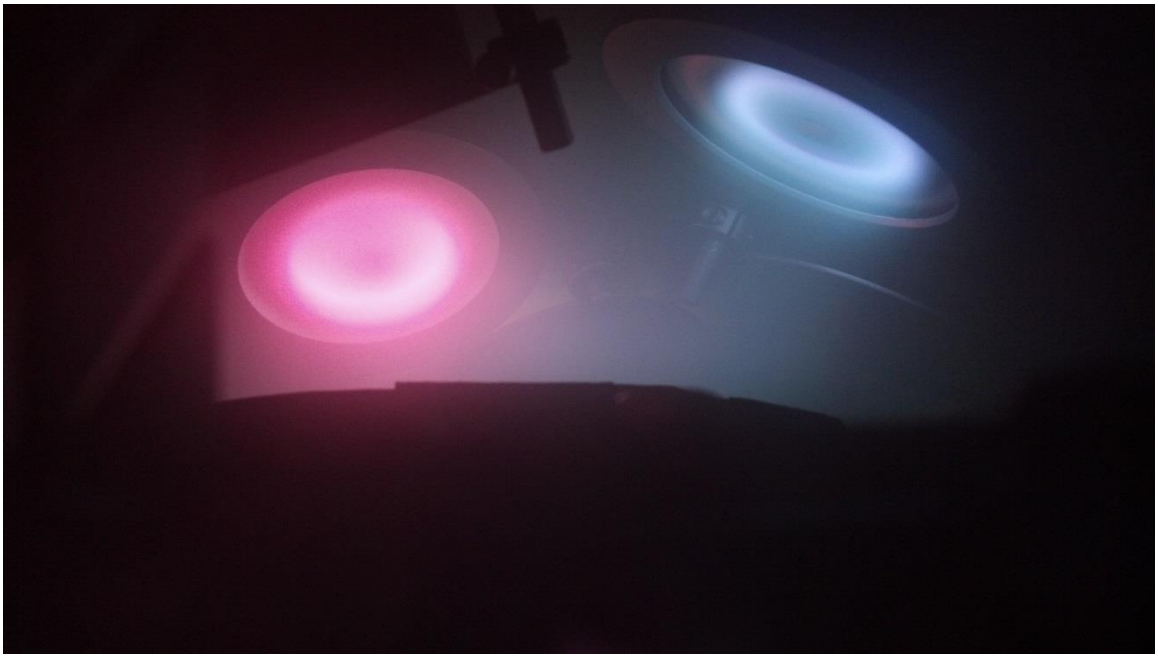

Figure 2-4: Sputtering plasmas from co-depositing lithium niobite from a lithium oxide (Li_2O) target (left) and a niobium target (right). The difference in plasma color is due to oxygen from the lithium oxide target becoming ionized and emitting a pink glow.

In addition to co-depositing from multiple targets, the Denton Discovery 2 can also energize the wafer platen in order to clean a wafer before deposition or etch back the film during deposition. Exposing films to ion bombardment during growth has been shown to change film morphology, density, and stress [104]. Because there is no magnetic confinement on the platen, a plasma lit on the platen exists both above the

platen affecting the wafers as well as below the platen as shown in Figure 2-5. Due to this unconfined plasma, special precautions must be taken when using the platen plasma during high temperature depositions as discussed in Appendix A.

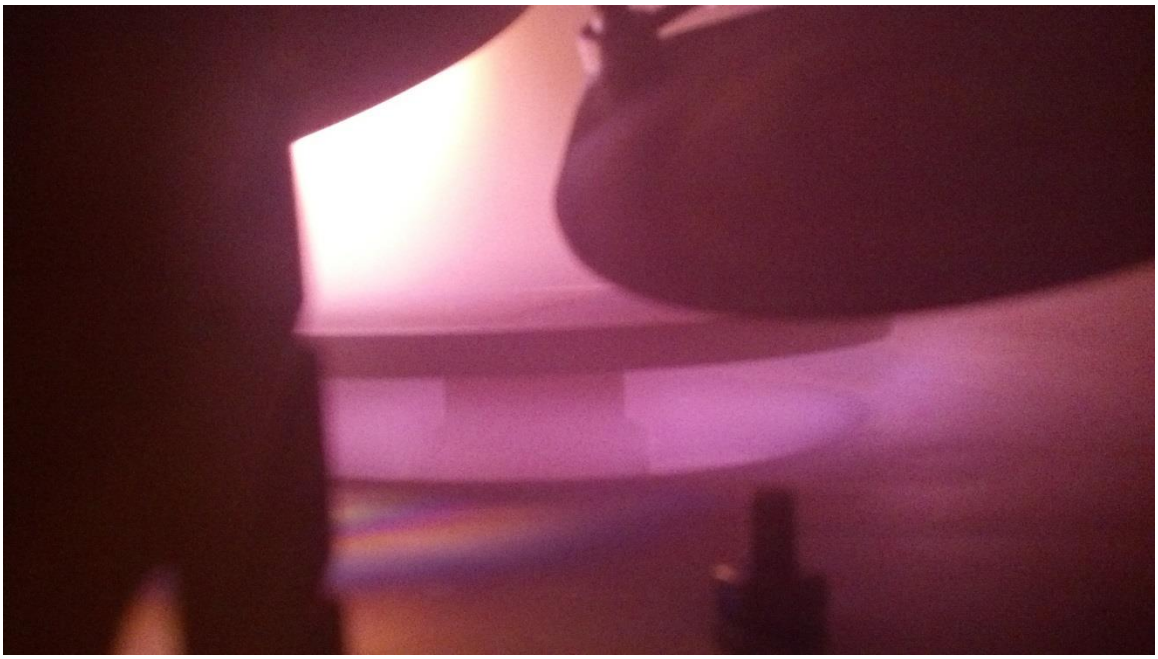

Figure 2-5: A plasma lit on the platen during a deposition. This plasma bombards the wafer surface with ions changing many properties of the depositing film.

2.2.6 High Substrate Temperatures

Growth of high quality crystalline films usually requires elevated substrate temperatures. For example lithium niobate ($LiNbO_3$) can be grown by molecular beam epitaxy [105, 106] or metal-organic chemical vapor deposition [107], but only at temperatures between 700 – 950 ^{o}C. The Denton Discovery 2 had to be heavily modified in order to reach these temperatures. 7200 W of quartz infra-red tube heaters were added behind the platen. Polished heat reflectors were added under the platen in order to hold the infra-red lamps and direct their radiation onto the back-side of the platen. The heaters

were then enclosed in a four layer heat shield in order to contain the heat within a small area behind the platen. Without this heat shield the o-rings on the chamber exceeded 200 ^{o}C and began to melt. Finally, active cooling had to be added to the chamber wall in order to remove heat that leaked out from between the heat shield and the platen. Another heat shield enclosing the sides of the platen was added to help contain the heat behind the platen. As shown in Figure 2-6, after these modifications the platen could be heated to a glow. The maximum measured platen temperature is above 850 ^{o}C, although this was measured with only 4800 W of heater installed.

Figure 2-6: The platen glowing during a high temperature process.

Due to the incomplete containment of infra-red radiation during a high temperature process, it is often necessary to close off the cryo pump during these processes. Enough radiation escapes to heat the cryo pump arrays releasing trapped gases. For platen temperatures above 600 ^{o}C, the cryo pump begins to increase the system pressure if left open.

2.3 Sputter Deposition of Lithium Niobite

Sputter deposition of lithium niobite has never previously been reported. Therefore, initial attempts at sputter deposition of lithium niobite followed the methods used for the related compounds $LiNbO_3$ [108-110] and $LiCoO_2$ [111-113] by depositing at high substrate temperatures from a single pressed powder sputtering target with mean composition Li – Nb – 2O. This method initially produced weakly crystalline c-oriented lithium niobite as shown in Figure 2-7.

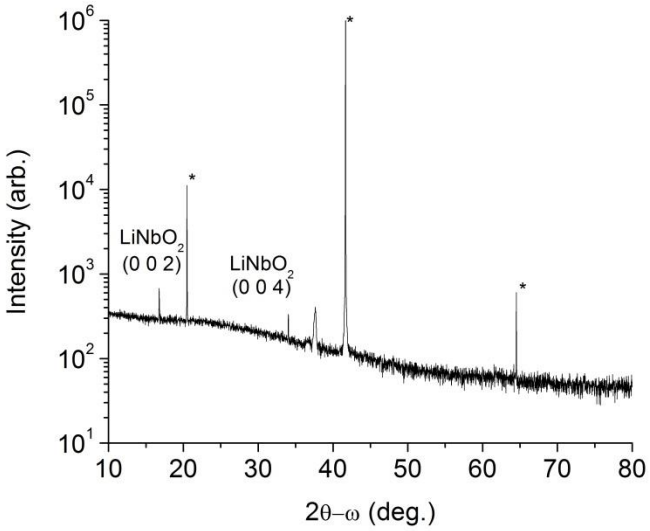

Figure 2-7: X-ray diffractogram of a film RF sputter deposited from a single pressed powder target with mean composition Li-Nb-2O. The film was deposited at 100W power, 10 mTorr argon pressure, and 800 °C substrate temperature. Weak x-ray diffraction peaks are visible for the (0 0 2) and (0 0 4) orientations. Peaks labeled with a * are from the sapphire substrate. The peak at 37.6° is from the XRD stage.

While depositing lithium niobite, it is desirable to avoid high substrate temperatures in order to limit lithium diffusion into other microelectronic materials. Lowering the substrate temperature from 800°C to 500°C also produced lithium niobite,

as shown in Figure 2-8, but in the (1 0 1) orientation rather than the c-orientation observed at the higher substrate temperature.

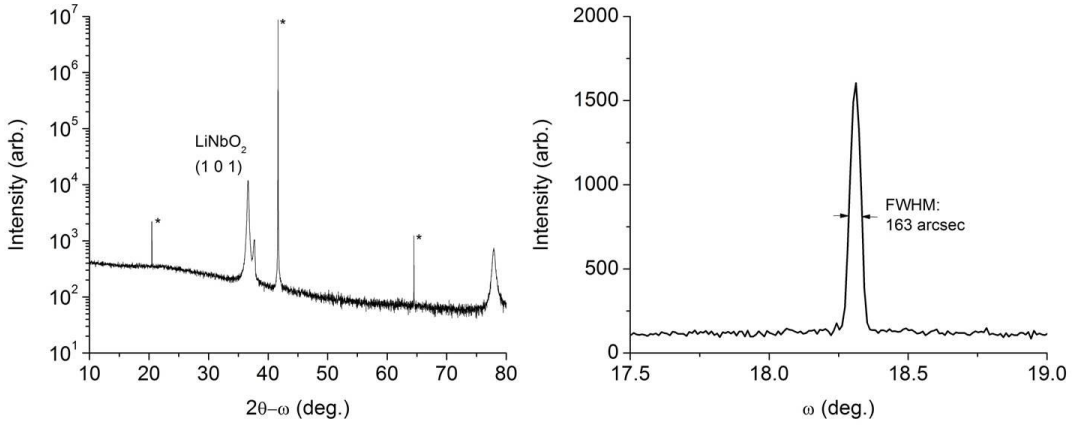

Figure 2-8: X-ray diffractogram (left) of a film RF sputter deposited from a single Li-Nb-2O target at a substrate temperature of 500°C. The resulting material is (1 0 1) oriented lithium niobite with an XRD peak located at 36.6°. The symmetric rocking curve width (right) is 163 arcsec indicating highly oriented material with little tilt. Peaks labeled with a * are from the sapphire substrate. The peak at 37.6° is from the XRD stage.

Identifying (1 0 1) oriented lithium niobite by XRD alone is difficult due to the close proximity of peaks from other Li-Nb-O compounds and the wide range of lithium niobite XRD peak locations due to changes in lithium content. It was previously shown that changing the lithium content of Li_xNbO_2 ($0.5 < x < 1$) also changes the lattice spacing of the lithium niobite crystal [90]. Calculating the spacing between (1 0 1) planes in lithium niobite for the previously reported range of a-spacing (2.900 – 2.925 Å) and c-spacing (10.46 – 10.465 Å) lattice parameters yields XRD 2θ-ω peak locations between 36.476° – 36.773° neglecting any additional shifts due to film strain. In addition, many other Li-Nb-O compounds have XRD 2θ-ω peaks near this range of angles including: Nb_{FCC} (1 1 1) at 36.77°, NbO (1 1 1) at 36.95°, $LiNb_3O_8$ (6 0 0) at 36.99°, and Li_3NbO_4 (2 2 2) at 36.99°. In order to confirm the deposited material was (1 0 1) oriented lithium

niobite, rather than a strained film with different composition, an asymmetric XRD peak was found for the (1 0 0) planes of lithium niobite as shown in Figure 2-9.

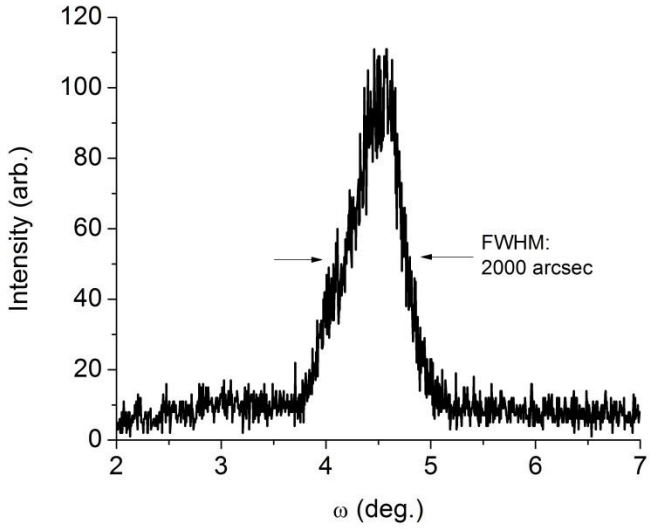

Figure 2-9: Asymmetric (1 0 0) rocking curve of the (1 0 1) oriented lithium niobite film deposited from a single Li-Nb-2O target at a substrate temperature of 500°C. The existence of this peak confirms the film as lithium niobite rather than an alternative Li-Nb-O phase.

While initial results depositing lithium niobite from a single Li-Nb-2O target were promising, successive depositions were inconsistent with peaks from additional phases present in the x-ray diffractograms. Shown in Figure 2-10 is an x-ray diffractogram from a film deposited under identical conditions to the film from Figure 2-8. In addition to the (1 0 1) lithium niobite peak there is a (0 0 6) lithium niobate peak. This film was deposited immediately after cleaning the Li-Nb-2O target indicating that target aging was required to produce the previous lithium niobite films. Attempts to compensate for the target aging by adding reactive oxygen to the plasma or co-sputtering with a metallic niobium target were unsuccessful in producing a repeatable deposition condition.

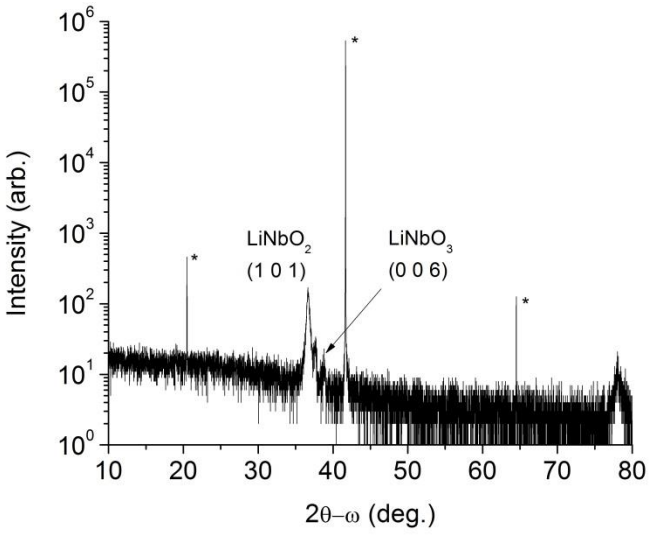

Figure 2-10: X-ray diffractogram of a film RF sputter deposited from a single Li-Nb-2O target at a substrate temperature of 500°C. A peak from $LiNbO_3$ is present in addition to the desired $LiNbO_2$ peak. Peaks labeled with a * are from the sapphire substrate.

Aging of compound ceramic targets is a well-established phenomenon in which the history of the target usage affects the surface composition of the target and the resulting film depositions [113]. One major cause of target aging is preferential sputtering in which some elements are removed from the target surface faster than other elements. Preferential sputtering can be caused by either differences in surface binding energy or by differences in elemental mass [114]. It is therefore not surprising that a sputtering target containing lithium (mass: 6.94 amu), oxygen (mass: 15.99 amu), and niobium (mass: 92.91 amu) suffers from preferential sputtering.

In order to reduce the effects of preferential sputtering, depositions were performed by co-depositing from a lithium oxide (Li_2O) target and a niobium target separating the light and heavy elements. As shown in Figure 2-11, crystalline (1 0 1) oriented lithium niobite was obtained for a niobium target power of 50 W and a lithium

oxide target power of 200 W or 300 W. These depositions were performed at room temperature with 10 mTorr of argon process gas.

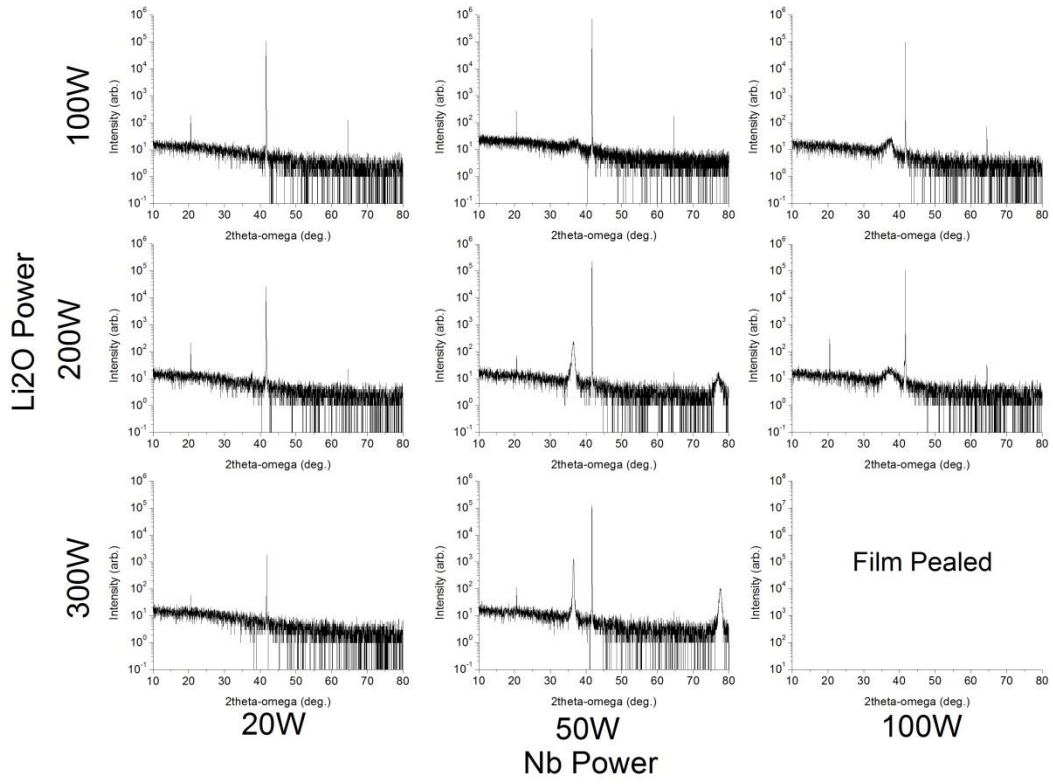

Figure 2-11: Grid of x-ray diffractograms produced by the initial search for sputter deposited lithium niobite by co-depositing from a lithium oxide and a niobium target. Crystalline lithium niobite was found for depositions at 50W of niobium power and 200W or 300W of lithium oxide power.

It was found that by lowering the deposition pressure to 1 mTorr, the film crystallinity as measured by XRD peak intensity increased dramatically as shown in Figure 2-12. This deposition condition became the "standard" lithium niobite condition used for lithium niobite based devices.

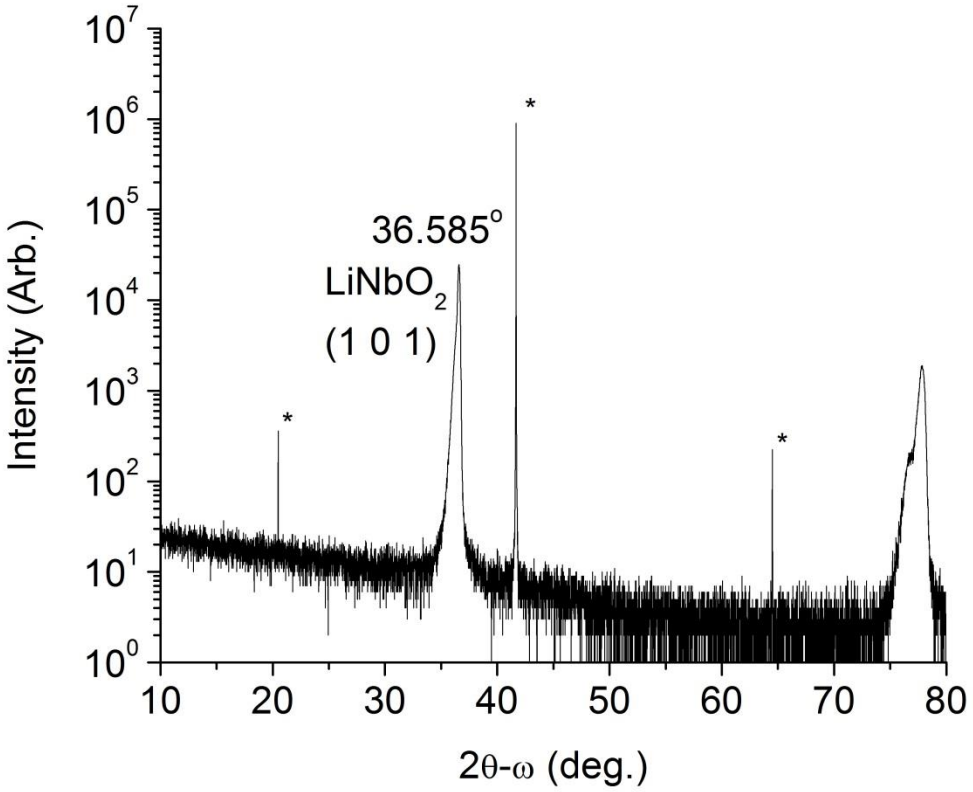

Figure 2-12: x-ray diffractogram of the "standard" sputter deposited lithium niobite. This film was deposited at room temperature with 1 mTorr process gas pressure.

2.4 Characterization of Sputter Deposited Lithium Niobite

The sputter deposited lithium niobite standard condition was analyzed in order to understand its structural, chemical, electrical, and optical properties. The initial structural feature that is apparent upon examining the XRD is a low angle shoulder in the lithium niobite peak. This feature is clearly visible in the (2 0 2) peak of Figure 2-12 or in the zoomed in (1 0 1) peak shown in Figure 2-13.

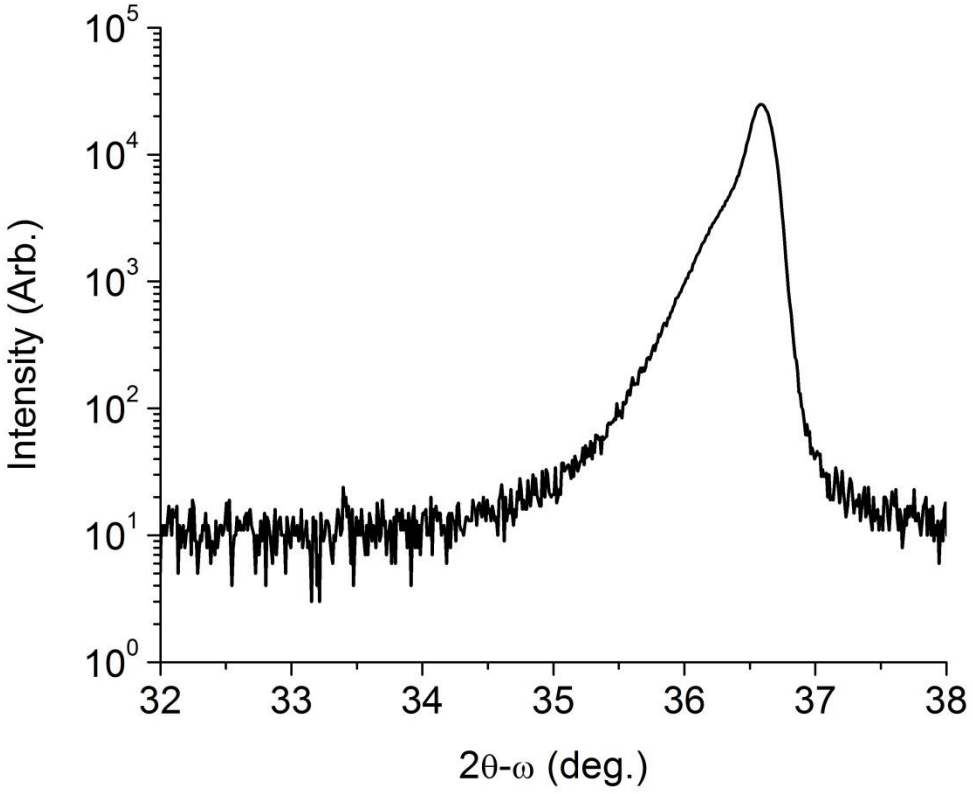

Figure 2-13: (1 0 1) x-ray diffractogram peak from the standard lithium niobite deposition condition showing a main peak and a low angle shoulder.

Scanning around the (1 0 1) peak in reciprocal space yields Figure 2-14 where the 2 theta – omega axis measures the spacing between crystalline planes and the omega offset axis measures the tilt in the crystalline planes away from the substrate (i.e. zero omega offset is aligned to the underlying sapphire substrate). XRD features can spread in 2 theta – omega due to either gradients in strain or due to Scherrer broadening [115, 116] caused by small crystal sizes as described by Equation 2.1 where τ is the average particle size, K is a shape constant close to unity, λ is the x-ray wavelength, β is the line broadening in radians, and θ is the diffraction angle.

$$\tau = \frac{K\lambda}{\beta \cos(\theta)} \qquad \text{Equation 2.1}$$

From Figure 2-14, two features are apparent. The main peak is a feature broad in omega offset yet fairly narrow in 2 theta – omega. The low angle shoulder is very narrow in omega offset and broad in 2 theta – omega. The breadth of the main peak in omega offset suggests a feature with a high spread of tilt away from the sapphire substrate. Likewise, the narrowness of the shoulder in omega offset indicates a feature well aligned to the sapphire substrate with little tilt. However, the breadth of the shoulder in 2 theta – omega suggests a feature with either a strain gradient or small dimensions.

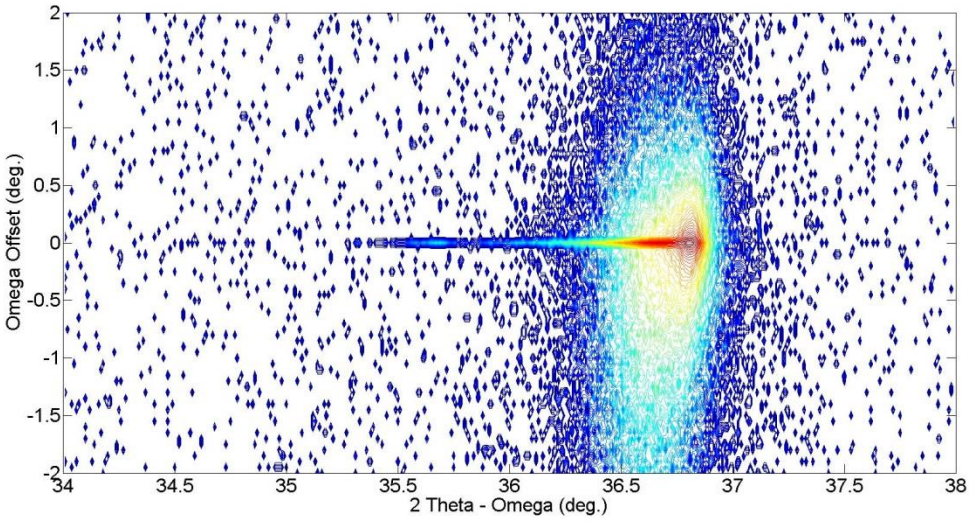

Figure 2-14: XRD reciprocal space map of the (1 0 1) lithium niobite peak showing two distinct features. The main peak is broad in omega offset while the low angle shoulder is broad in 2 theta – omega.

Examining the cross sectional scanning electron microscopy (SEM) image shown in Figure 2-15, two structural features are also apparent. Close to the sapphire substrate are small particles that transition into small columnar grains further into the film. However, around 250 nm into the film tapered crystallites form and begin propagating taking up more of the film's volume. While correlating cross sectional SEM features with

XRD features is difficult, the two features observed in the SEM qualitatively match the two features described by the XRD reciprocal space map.

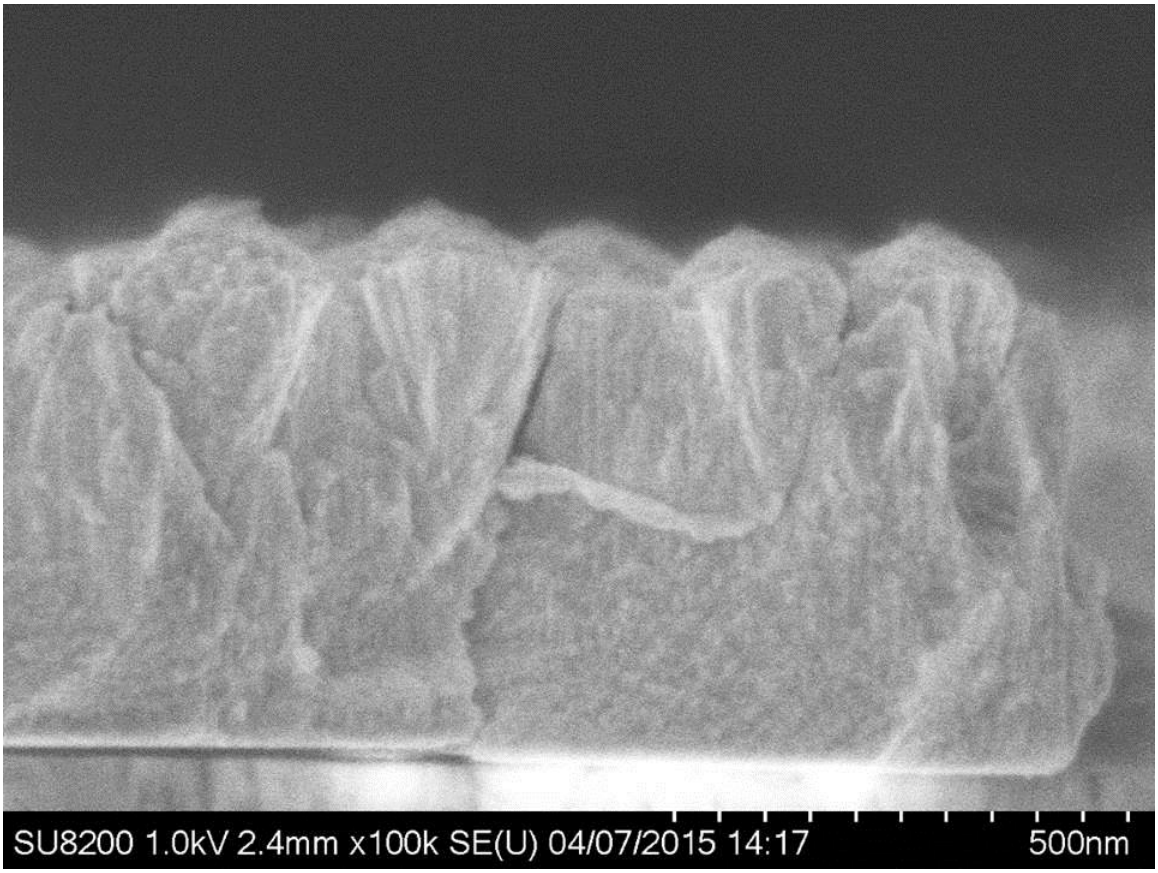

Figure 2-15: cross sectional SEM of the standard lithium niobite sputtering condition showing a two layer structure with small particles near the substrate and tapered crystallites nucleating approximately 250 nm into the film.

The small particles that transition into small columnar grains may correspond to the low angle shoulder observed in the XRD. The columnar grains appear well aligned to the sapphire substrate with little tilt between grains. Applying the Scherrer Equation (Equation 2.1) to the low angle XRD shoulder predicts a particle size of 9.1 – 19.6 nm. The columnar grains seen in the cross sectional SEM are approximately 14.6 ± 2.0 nm across.

Likewise, the tapered crystallites observed in the cross sectional SEM may correspond to the main XRD peak. The tapered crystallites exhibit a wide degree of tilt away from the sapphire substrate, although it is impossible to determine how the crystalline planes are affected by this structural SEM feature.

As expected from the cross sectional SEM, atomic force microscopy (AFM) reveals a rough surface with 14.8 nm rms roughness. As shown in Figure 2-16, the rough surface is caused by features that are approximately 200 nm across. The features observed in the AFM are the same size as the tapered crystallites observed in the cross sectional SEM.

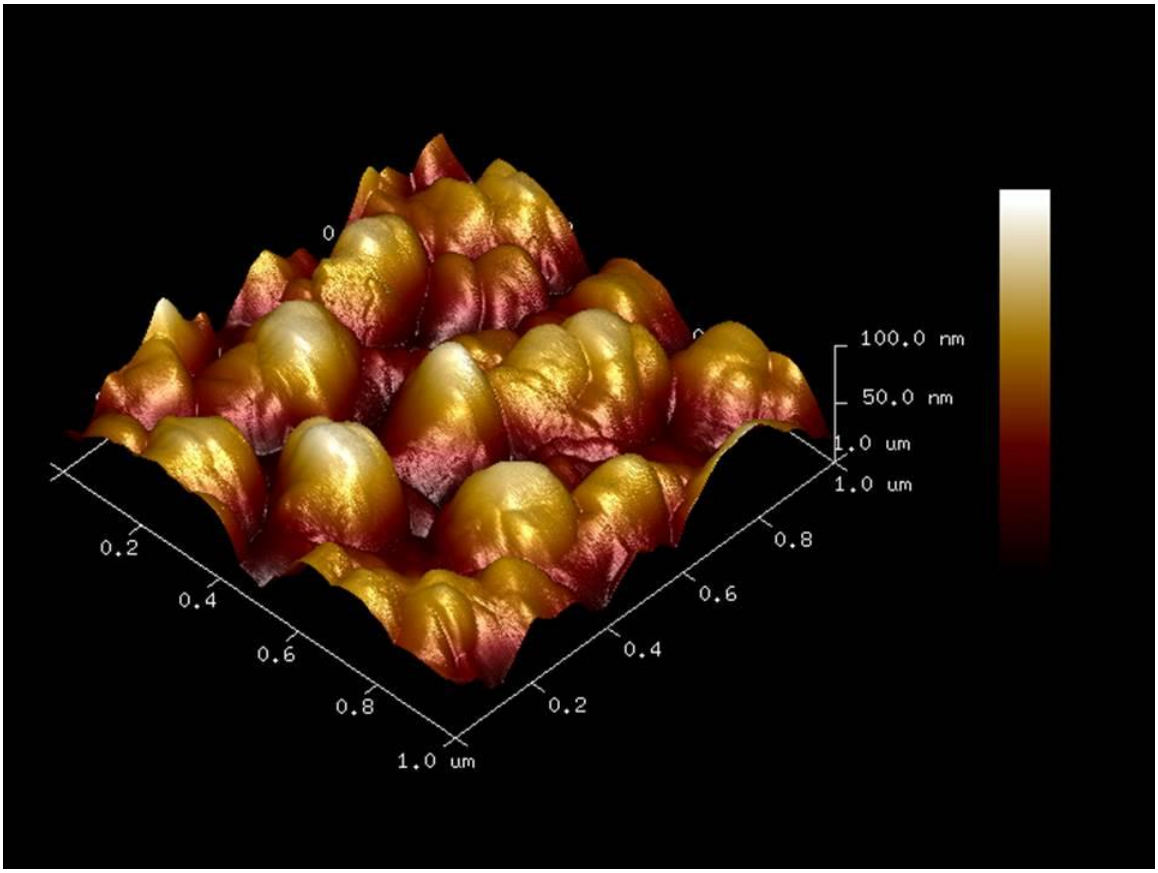

Figure 2-16: AFM surface showing a rough surface with approximately 200 nm diameter features protruding from the film.

Looking at the film surface, shown in Figure 2-17, with an optical microscope or large area AFM, a pattern of lines is observed. The cause of this self-organized pattern is unknown, although similar features have been observed when films are exposed to ions at an oblique angle [117, 118] such as may be the case in confocal sputtering. An alternative explanation for the self-organized pattern is directionally dependent adatom surface mobility promoting surface transport and nucleation along specific crystalline axis. However, the three-fold symmetry of the underlying sapphire substrate is not observed.

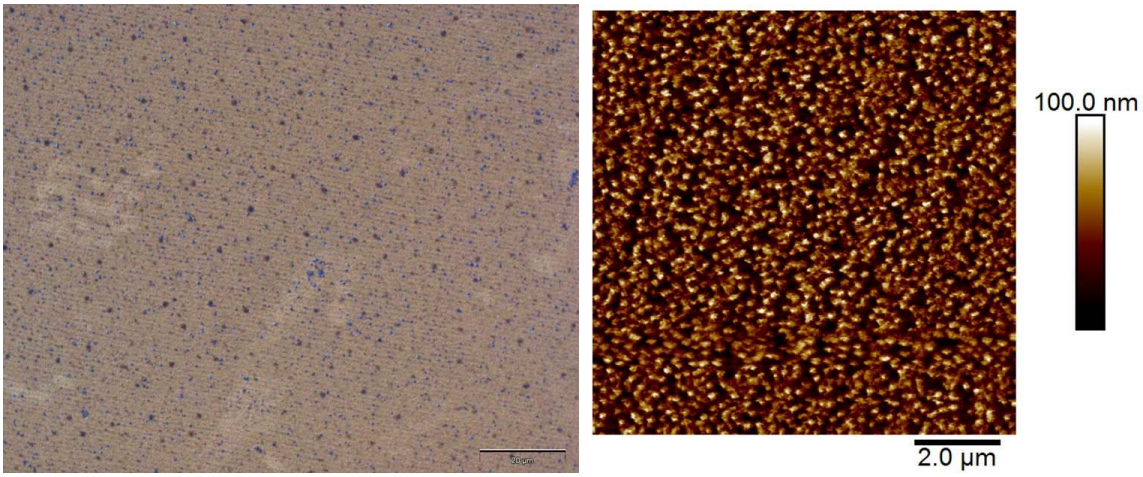

Figure 2-17: (Left) optical microscope image and (Right) large area AFM image showing a stripe feature on the surface of the sputter deposited lithium niobite.

In addition to structural characterization, the lithium niobite standard deposition condition was chemically analyzed using x-ray photoelectron spectroscopy (XPS). The XPS spectra for the standard deposition condition are shown in Figure 2-18 including spectra from both the film's surface and after milling into the bulk of the film. The surface spectra can be fit using only the Nb^{3+} and Nb^{5+} oxidation states. The ratio of the areas of these two peaks weighted by the oxidation state yields a mean oxidation state of 4.25. In contrast, the existence of a surface oxide and preferential sputtering during the XPS depth profile causes a lower mean oxidation state of 2.92 after milling into the film.

Preferential sputtering during the depth profile removes more oxygen than niobium and causes a mixture of many oxidation states [119]. While this ambiguity in absolute oxidation state determination prevents quantization of the exact oxidation state, comparisons from one sample to another allow relative changes in oxidation state to be determined.

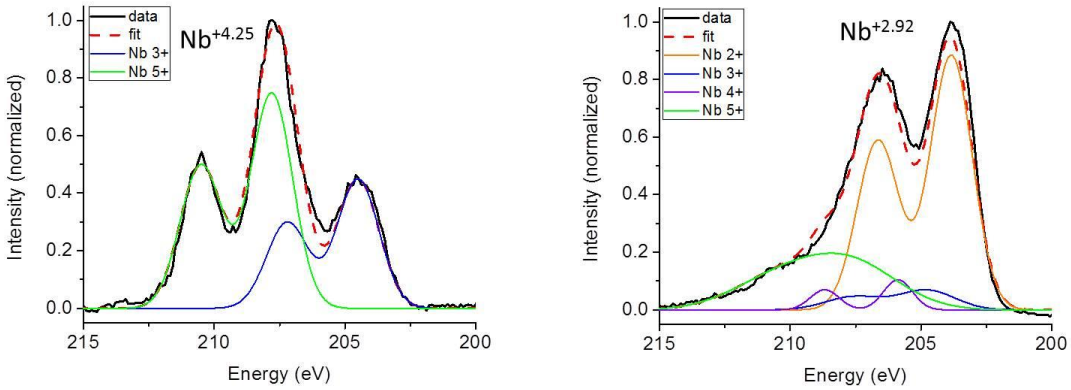

Figure 2-18: XPS niobium spectra of the sputter deposited lithium niobite on the (Left) surface and (Right) after ion milling into the bulk of the film. These plots indicate that the surface contains a fully oxidized Nb^{5+} state while the film bulk is close to the ideal Nb^{3+} state.

In order to compare the sputter deposited film to a known lithium niobite standard, XPS of bulk lithium niobite, grown by liquid phase electro-epitaxy [95], was performed. As shown in Figure 2-19, the niobium XPS spectrum for the sputter deposited film is nearly identical to the XPS spectrum for the bulk grown material indicating that the sputtered material has a chemical environment around the niobium atoms that is similar to the previously characterized [95] bulk grown material.

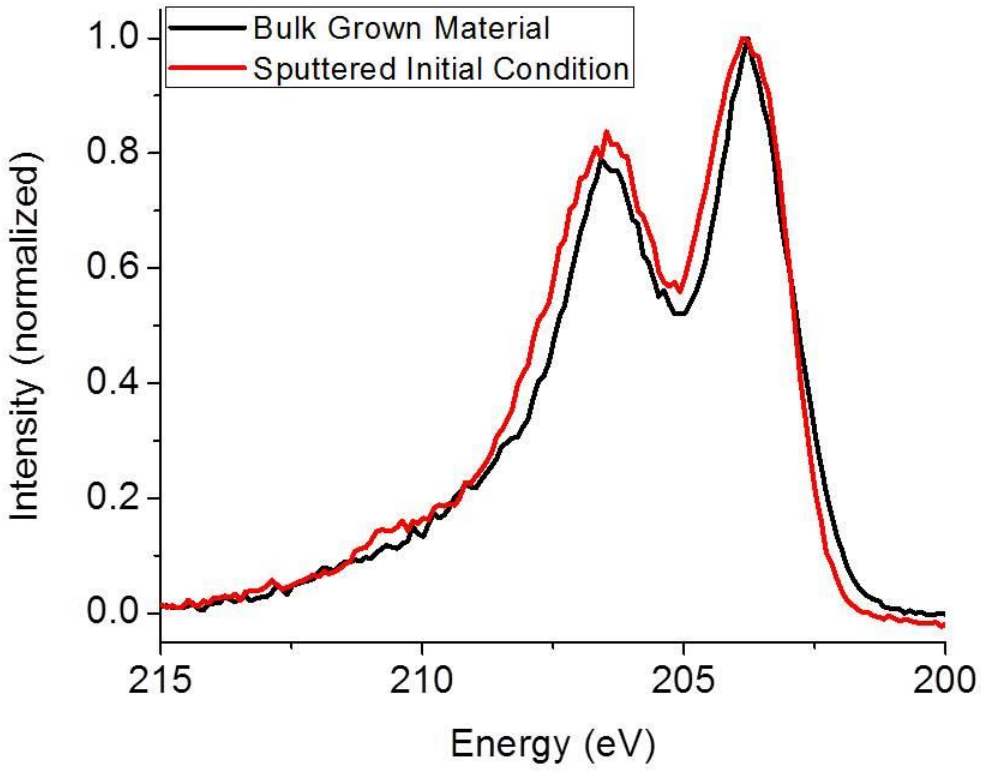

Figure 2-19: XPS niobium spectra for sputter deposited and bulk grown lithium niobite showing nearly identical spectra indicating similar chemical bonding around the niobium in these two materials.

The electrical [90] and optical [53] properties of lithium niobite are known to depend on the amount of lithium in the material. However, it may be noted that no linear combination of Li_2O and Nb can form $LiNbO_2$. In order to obtain the ideal 2:1 oxygen to niobium ratio, excess lithium must a) not incorporate into the deposited film or b) evolve out of the film after it has been deposited. The sputter deposited lithium niobite reacts with air upon removal from the sputtering chamber to form an insulating film on top of the deposited film, as shown in Figure 2-20. The surface layer that forms is water soluble and upon dissolution from a 2 inch diameter wafer turns 100 mL of deionized water basic with a pH of 10 – 11, likely due to the formation of LiOH.

Figure 2-20: Images of sputter deposited lithium niobite (Left) before and (Right) after treatment with deionized water. The films as deposited react with the air forming an insulating surface film that is water soluble.

Examining the XPS spectra for lithium, niobium, and oxygen, shown in Figure 2-21, the reacted surface layer is composed of lithium and oxygen with no niobium present. After milling into the deposited film, niobium and oxygen are both present. Lithium may also be present after milling, but the lithium 1s spectrum overlaps the niobium 4s spectrum making its quantization indeterminate. It can also be noted from the XPS spectra in Figure 2-21 that the oxygen binding energy shifts from the surface region to the bulk of the film, which indicates that the oxygen is bound differently on the surface and after milling. This suggests two distinctly different films as shown in the cross sectional SEM in Figure 2-22.

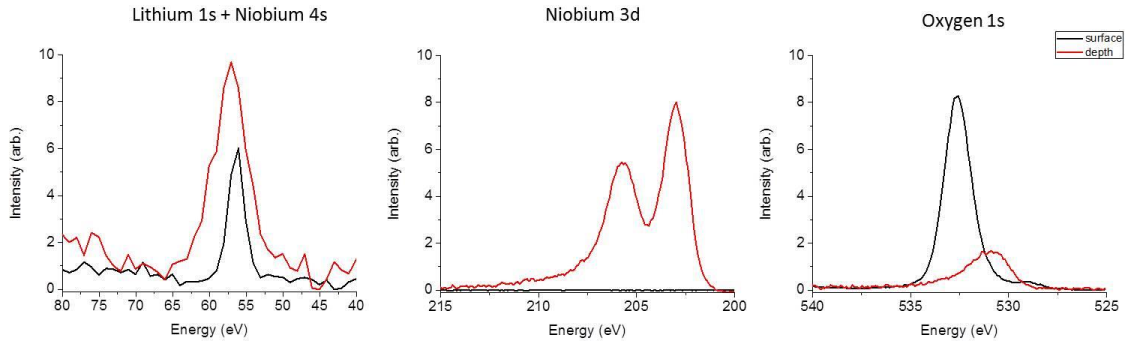

Figure 2-21: XPS spectra of the reacted surface film and the sputtered lithium niobite. The surface is composed solely of lithium and oxygen while the main film contains niobium and oxygen and possibly lithium. The lithium 1s signal from the film bulk is washed out by the niobium 4s signal making positive identification difficult.

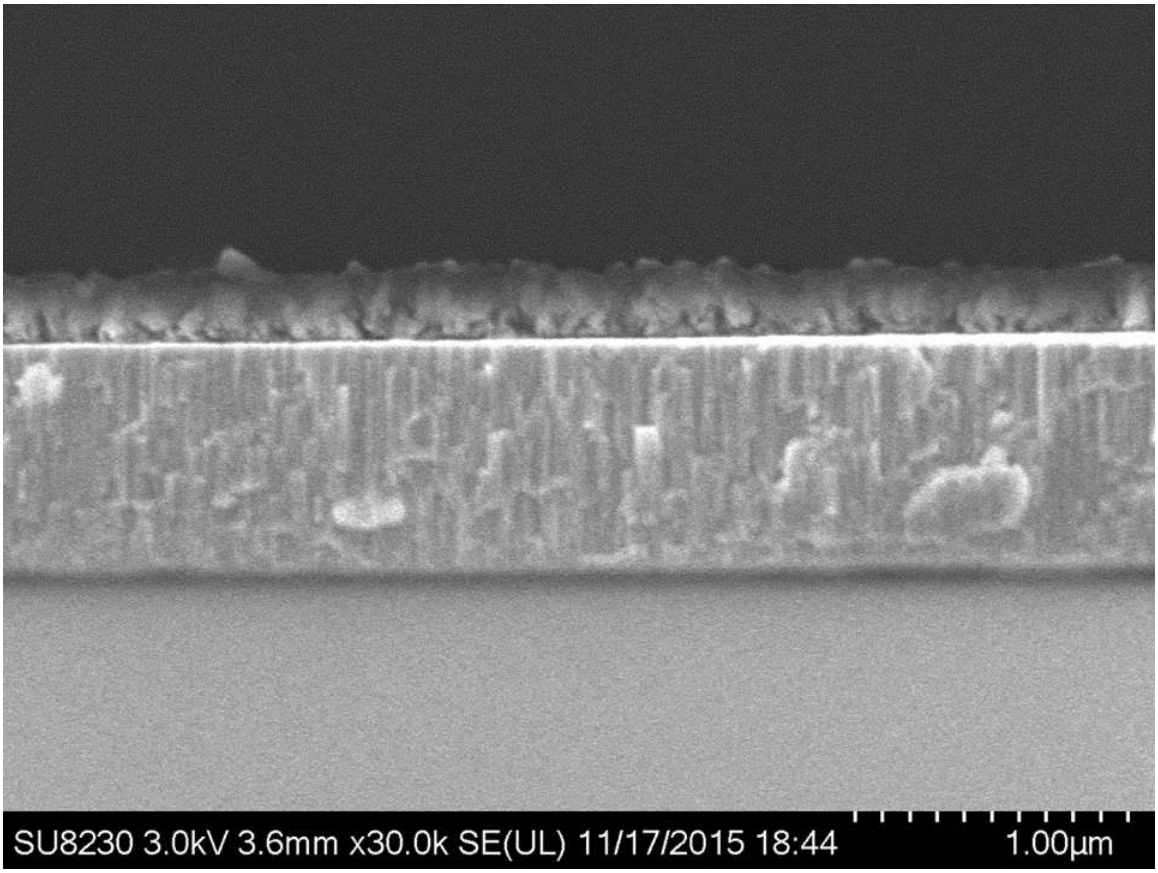

Figure 2-22: Cross sectional SEM of a sputter deposited film showing the reacted surface layer on top of the main sputtered film.

After reacting the sputtered material with deionized water to remove the lithium oxide layer, the film visually appears as a dark material as shown in Figure 2-20. Lithium niobite has been reported to appear as: wine-red [79], bluish-black [79], garnet red [79], reddish brown [90, 120], black [90, 120], burgundy-red [75, 85, 86], grey [85], dark cherry [93], dark gray [86, 93], bourdeaux red [91], blue black shiny [91], brownish [76], burgundy [76], red [88, 92], black with a metallic shine [92], and gray-black [88]. The general trend throughout all of these reported colors is that lithium niobite with a near stoichiometric amount of lithium appears red corresponding to the 2 eV band gap while lithium niobite with a significant amount of lithium removed from the crystal appears dark and acts as a metal with the fermi level inside the valence band. The dark color of the sputtered material therefore suggests that the sputtered film is lithium deficient after reacting with the deionized water. As was discussed in Section 1.4.2, deionized water is known to remove approximately 11% of the lithium from lithium niobite [88].

While detecting lithium by XPS is difficult due to the overlapping Li 1s and Nb 4s signals, Secondary Ion Mass Spectroscopy (SIMS) can detect lithium. Unfortunately, SIMS cannot quantitatively identify the amount of lithium without a known standard, which does not exist for lithium niobite. However, relative comparisons can be made between samples as shown in Figure 2-23 which shows depth profiles for both a sputtered film and a bulk piece of lithium niobite grown by liquid phase electro-epitaxy. From the SIMS specta, the Li/Nb signal ratio in the sputtered film is 6.24 ± 0.15 while the Li/Nb signal ratio in the bulk lithium niobite is 8.65 ± 0.19. Therefore the sputter deposited lithium niobite is lithium deficient compared to the bulk grown material.

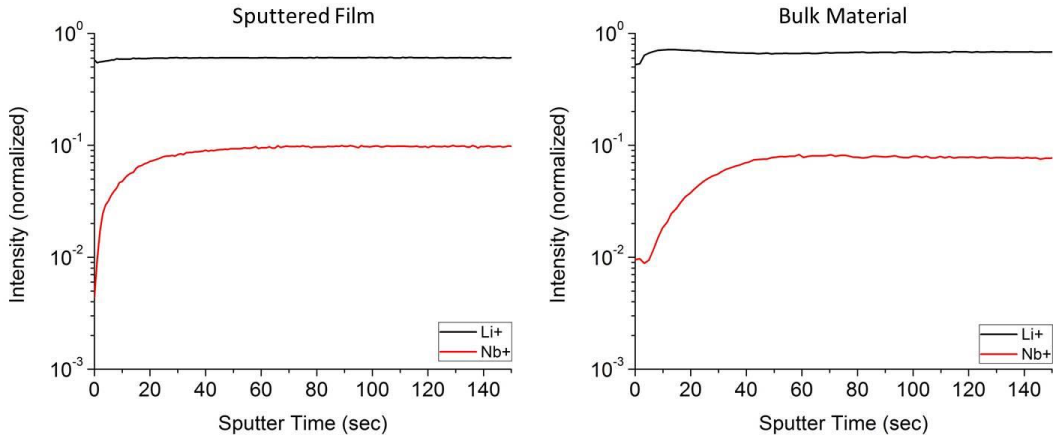

Figure 2-23: SIMS depth profiles of (Left) sputter deposited lithium niobite and (Right) bulk grown lithium niobite. The lithium to niobium ratio is lower in the sputter deposited film likely due to reaction with deionized water removing lithium from the film.

Lithium niobite has a reported band gap of approximately 2.0 eV [64, 75]. In order to determine the band gap of the standard lithium niobite deposition condition, a deposition was performed on double side polished sapphire. The double side polished wafer reduces optical scattering in transmission mode optical absorption spectroscopy. In order to determine the band gap from optical absorption spectroscopy, the Tauc method must be employed [121]. The Tauc method requires that the type of optical transition (i.e. allowed-direct, allowed-indirect, forbidden-direct, or forbidden-indirect) must be known before the method can be used. In lithium niobite, the Fermi-level is inside the valence band emptying electrons away from the gamma point. Therefore, optical absorption transitions occur at k-vectors away from the gamma point causing lithium niobite to have a forbidden-direct transition. A more in depth discussion of optical transitions in lithium niobite is provided in Chapter 4.

The Tauc plot for sputter deposited lithium niobite is shown in Figure 2-24. The band gap can be found by extrapolating the linear transition region to the x-axis yielding a band gap of 2.07 eV.

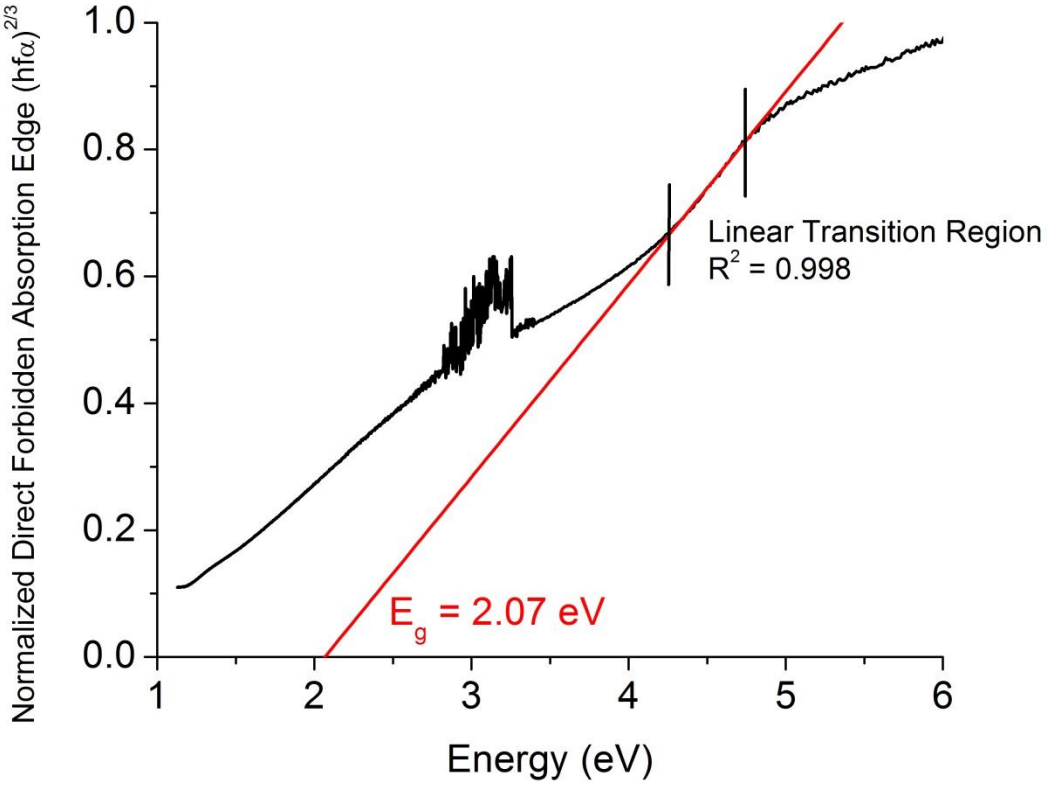

Figure 2-24: Tauc plot of sputter deposited lithium niobite showing a 2.07 eV band gap. The Tuac coefficient for a Direct Forbidden transition was used because the band structure for lithium niobite causes direct optical transitions away from the gamma point.

Having characterized the structural, chemical, and optical properties of sputter deposited lithium niobite, the purpose of exploring this material was to obtain electrically active memristors for neuromorphic computing applications. Contacts were evaporated onto a lithium niobite film in a ring-dot pattern [74]. Titanium/gold contacts were used in order to have a lithium blocking titanium layer [99] and a soft gold layer for probing. The effects of lithium blocking and lithium absorbing contacts will be discussed in Chapter 5.

As shown in Figure 2-25, the fabricated device exhibited the pinched hysteresis loop characteristic of a memristor. In addition to the memristive hysteresis loop, each successive scan caused the device to become more resistive resulting in a clockwise rotation in the current-voltage curve. This rotation is characteristic of a volatile memristor in which a feedback mechanism (such as lithium ion diffusion) can reset the device. Further modelling of this effect is discussed in Chapter 9. The neuromorphic application of a volatile memristor with feedback may be found in replicating biological volatile adaptation mechanisms. Specific volatile biological behaviors will be further discussed in Chapter 10 along with how to reproduce them using volatile memristors.

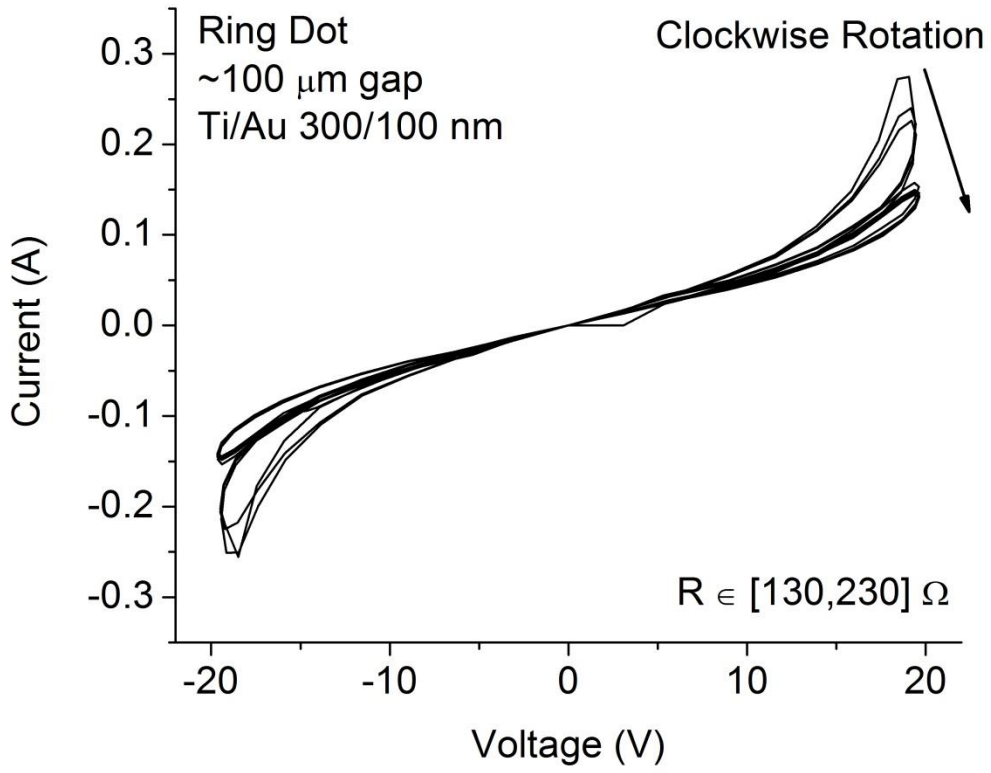

Figure 2-25: current-voltage sweeps of a sputtered lithium niobite device showing memristive hysteresis.

2.5 Processing Parameters

In order to investigate the effects of various deposition parameters on the physical and chemical properties of the deposited film, niobium target power, lithium oxide target power, operating pressure, and substrate temperature were varied around the standard deposition condition.

Each film was structurally characterized by measuring the film thickness by stylus profilometer and the film crystallinity by XRD. An XRD crystallinity metric for each film was determined from the XRD peak height scaled by the sapphire substrate peak height and the film thickness.

Chemical characterization of each film was performed by analyzing XPS measurements. The oxygen to niobium ratio was determined by dividing the total area under the O 1s peak by the area under the Nb 3d peak. Each area was scaled by known relative sensitivity factors for these peaks, which are 2.4 for niobium and 0.66 for oxygen [122]. In addition, the mean niobium oxidation state was calculated, according to Equation 2.2, from fitting the niobium XPS spectra.

$$Mean\ Oxidation = \frac{\sum_{n=0}^{n=5} n * PeakArea(n)}{\sum_{n=0}^{n=5} PeakArea(n)} \qquad \text{Equation 2.2}$$

where n is the integer oxidation states of niobium (0 – 5) used to fit the measured XPS spectrum. These integer oxidation states exhibit doublets in XPS with known binding energies that shift to higher energy as niobium becomes oxidized [123]. All oxygen to niobium ratios and niobium oxidation states reported are measured from XPS spectra

after argon milling into the film. This procedure avoids sample to sample variations in surface oxide formation, but results in lower reported oxygen to niobium ratios than the actual film composition due to preferential sputtering removing more oxygen than niobium [119]. For example, XPS analysis of bulk grown lithium niobite yielded an oxygen to niobium ratio of 1.81, lower than the ideal value of 2.

2.5.1 Niobium Target Power

The niobium target power was varied between 30 W and 150 W. Over this range, the thickness of the deposited material increases nearly linearly at a rate of 5.6 nm/W as the niobium target power is increased, as shown in Figure 2-26. In addition, the crystallinity of the film, measured by normalized XRD intensity, increases rapidly for low niobium target powers and decreases slowly for higher niobium power, which may occur due to chemical changes in the film's deposited with more niobium. Chemically, as shown in Figure 2-26, the niobium oxidation state decreases as the niobium target power increases. This is consistent with adding more niobium to the film and making the film more metal rich. The oxygen to niobium ratio also decreases as the niobium target power increases, although the film deposited with 40 W niobium power is an outlier from this trend. These chemical trends indicate a narrow niobium power range of 40 – 50 W wherein the desired Nb^{3+} oxidation state and 2:1 O:Nb ratio of lithium niobite are obtained. This region also corresponds with the best XRD figures of merit as shown in Figure 2-26.

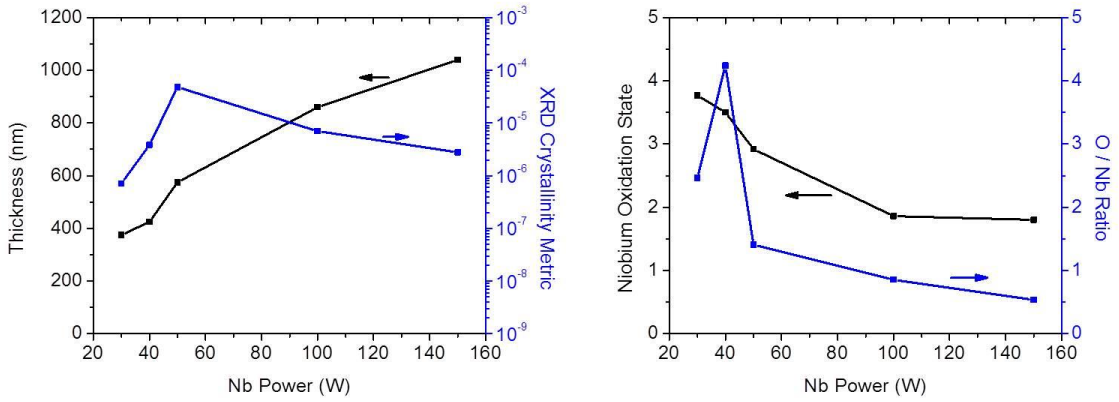

Figure 2-26: (Left) structural XRD and (Right) chemical XPS trends for changing niobium target power.

2.5.2 Lithium Oxide Target Power

The lithium oxide (Li_2O) target power was varied between 100 W and 300 W. Over this range, the thickness of the deposited material increases as the Li_2O target power is increased in a nearly linear manner at a rate of 1.55 nm/W, as shown in Figure 2-27. Unlike the range of niobium target powers investigated, the film crystallinity decreases throughout the entire range of Li2O target power. Not surprisingly, increasing the Li_2O target power increases the oxidation state in the deposited film. This is consistent with adding more oxygen to the film. However, the measured oxygen to niobium ratio does not track with the niobium oxidation state and is mostly unchanged by changing the Li_2O target power.

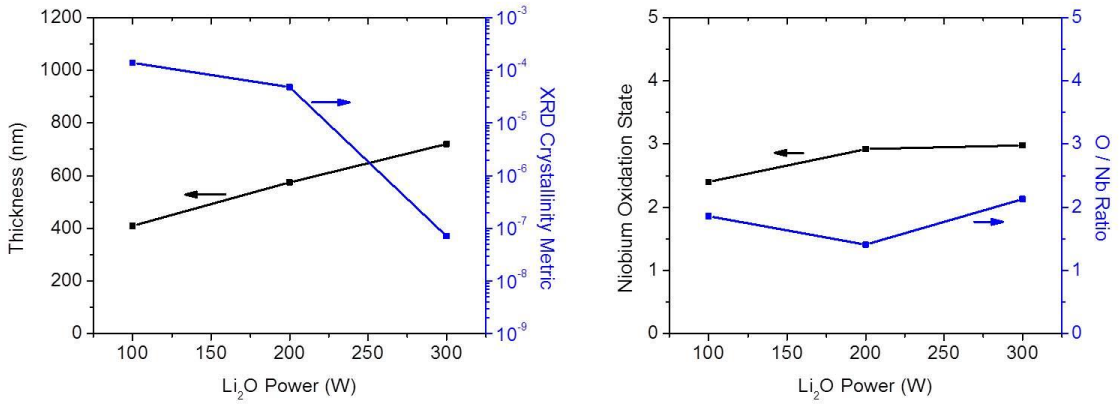

Figure 2-27: (Left) structural XRD and (Right) chemical XPS trends for changing lithium oxide target power.

2.5.3 Pressure

The operating pressure was varied between 1 mTorr and 30 mTorr. Over this pressure range the mean free path of an atom should vary between 20 cm and 0.7 cm respectively according to the kinetic model for gas collisions shown in Equation 2.3.

$$\Gamma = \frac{k_B T}{\pi d^2 P} \qquad \text{Equation 2.3}$$

where Γ is the mean free path, k_B is Boltzmann's constant, T is temperature, d is the diameter of an atom (Argon assumed), and P is pressure. The range of mean free paths investigated extends both longer and shorter than the 10 cm target to substrate distance spanning cases from molecular to viscous flow, which result in dramatically different energetic species impinging on the substrates.

Increasing the pressure between 1 – 10 mTorr had little impact on the thickness of the deposited film, although the film crystallinity decreased over this range, as shown in Figure 2-28. The decrease in film crystallinity may be due to increased scattering as the

mean free path becomes shorter than the target to substrate distance. In sputter deposition, unscattered atoms carry a large amount of kinetic energy, typically 4 – 40 eV [98], which can provide the energy necessary for crystallization. The films deposited at pressures between 1 – 10 mTorr show only small increases to the niobium oxidation state and oxygen to niobium ratio. This small increase may be due to increased scattering of the larger niobium atoms compared to the smaller oxygen atoms.

The film deposited at 30 mTorr is approximately 1/3 the thickness of the films deposited at lower pressures and exhibits an oxygen to niobium ratio approximately 2.5 times higher than the films deposited at lower pressure despite a relatively unchanging niobium oxidation state. Since the oxygen to niobium ratio increased without increasing the niobium oxidation state, excess lithium must be incorporated into the film and while we cannot measure Li-O bonding with XPS, such bonding must exist. The film deposited at 30 mTorr also exhibits a higher crystallinity than the low pressure trend would predict which may be due to the change in chemical composition.

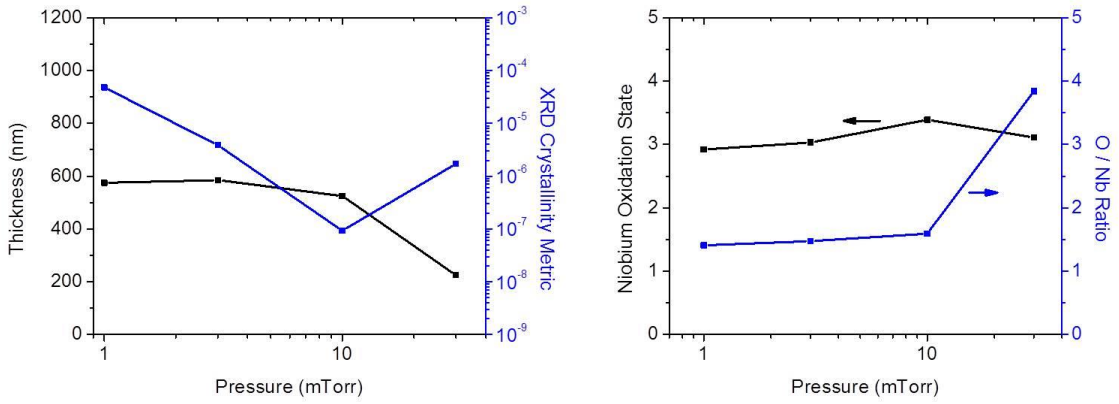

Figure 2-28: (Left) structural XRD and (Right) chemical XPS trends for changing deposition chamber pressure.

2.5.4 Substrate Temperature

The substrate temperature was varied between room temperature and 800 ^{o}C. Unintentional heating of the substrate at room temperature was controlled by water cooling the platen. The measured temperature did not exceed 40 ^{o}C for the unintentionally heated films. As shown in Figure 2-29, increasing the substrate temperature to 500 ^{o}C had little effect on the film thickness, crystallinity, niobium oxidation state, or oxygen to niobium ratio. However, increasing the substrate temperature to 800 ^{o}C caused a decrease in the film thickness and crystallinity. The film deposited at 800 ^{o}C also exhibited a higher niobium oxidation state and higher oxygen to niobium ratio. In addition to the quantitative chemical measurements, the film deposited at 800 ^{o}C was transparent as opposed to the opaque films deposited at lower temperatures. The XRD peak for the 800 ^{o}C sample was also located at a slightly higher angle (2θ-ω = 36.87^{o}) than all other films investigated (2θ-ω = 36.39^{o} – 36.76^{o}). Of the known Li-Nb-O compounds with XRD peaks near 2θ-ω = 36^{o} – 37^{o}, Li_3NbO_4 and $LiNb_3O_8$ are the only transparent compounds, with a band gap of approximately 4 eV [124, 125], having a higher ideal niobium oxidation state of Nb^{5+}, and a higher angle XRD 2θ-ω peak than all other compounds in this range. Thus, the 800 ^{o}C sample is likely dominated by Li_3NbO_4 or $LiNb_3O_8$.

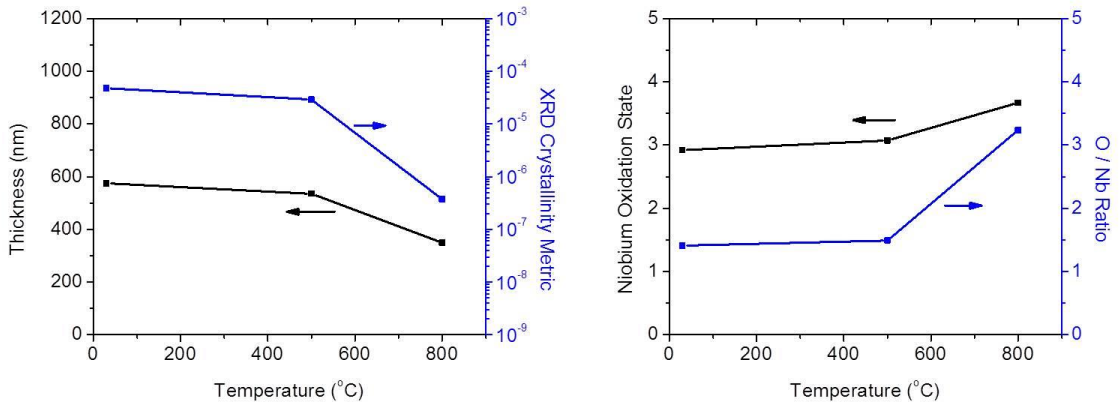

Figure 2-29: (Left) structural XRD and (Right) chemical XPS trends for changing substrate temperature.

In addition to the structural and chemical changes observed in the film deposited at 800 ^{o}C, the XRD reveals a weak low angle peak (18.6^{o}) as shown in Figure 2-30. This peak is associated with α-$LiAlO_2$. Conversion of sapphire into an interfacial layer of α-$LiAlO_2$ [126, 127] and γ-$LiAlO_2$ [128] by lithium and lithium oxide at high temperatures has been previously shown and is energetically favorable as indicated by the negative calculated change in the Gibbs free energy.

$$Li_2O + Al_2O_3 \rightarrow 2LiAlO_2$$

$$\Delta G = -29.34\ kcal\ @\ 800^oC$$

$$\Delta G = -25.87\ kcal\ @\ 0^oC$$

Examining the cross sectional SEM for this film, shown in Figure 2-30, reveals an interfacial layer between the sapphire substrate and the main film likely due to the conversion of sapphire into $LiAlO_2$.

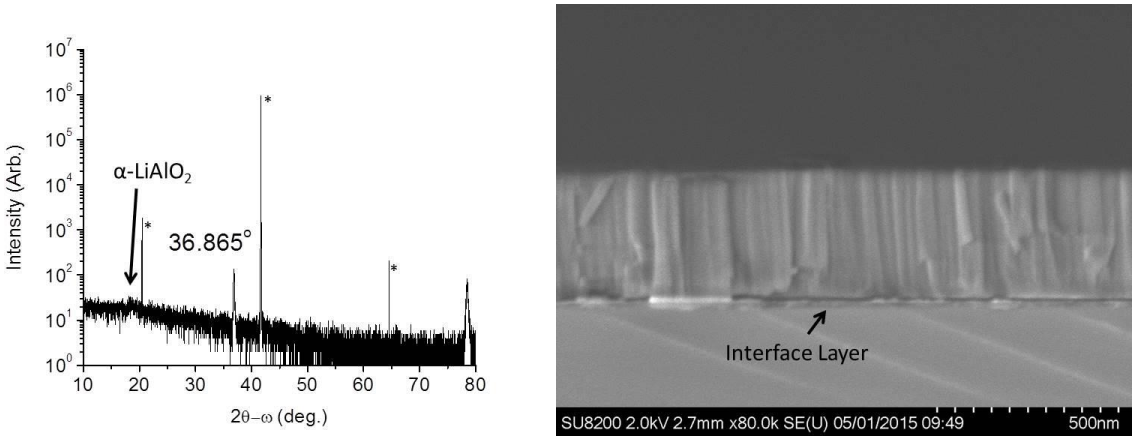

Figure 2-30: (Left) x-ray diffractogram and (Right) cross sectional SEM of a film deposited at 800 oC showing the presence of lithium aluminate and an interface layer between the sapphire substrate and main film. It is proposed that excess lithium from the sputtering process can diffuse into and react with the sapphire substrate at this temperature.

2.5.5 Platen Plasma

The final sputter deposition parameter that can be controlled in the Denton Discovery 2 is the platen plasma power. The platen was attached to an RF source and depositions were performed for 30 minutes at 0 W, 20 W, and 50 W of platen power. As shown in Figure 2-31, the resulting XRD peaks for these films vary dramatically with platen plasma power. The 0 W standard condition exhibits a 2θ-ω XRD peak at 36.6^{o} cooresponding to lithium niobite as previously observed. However, the films deposited with a non-zero platen plasma power have lower angle peaks that do not correspond to lithium niobite. Therefore, while it is sometimes suggested that ion bombardment from a platen plasma can have beneficial effects [104], a platen plasma does not aid in the sputter deposition of lithium niobite.

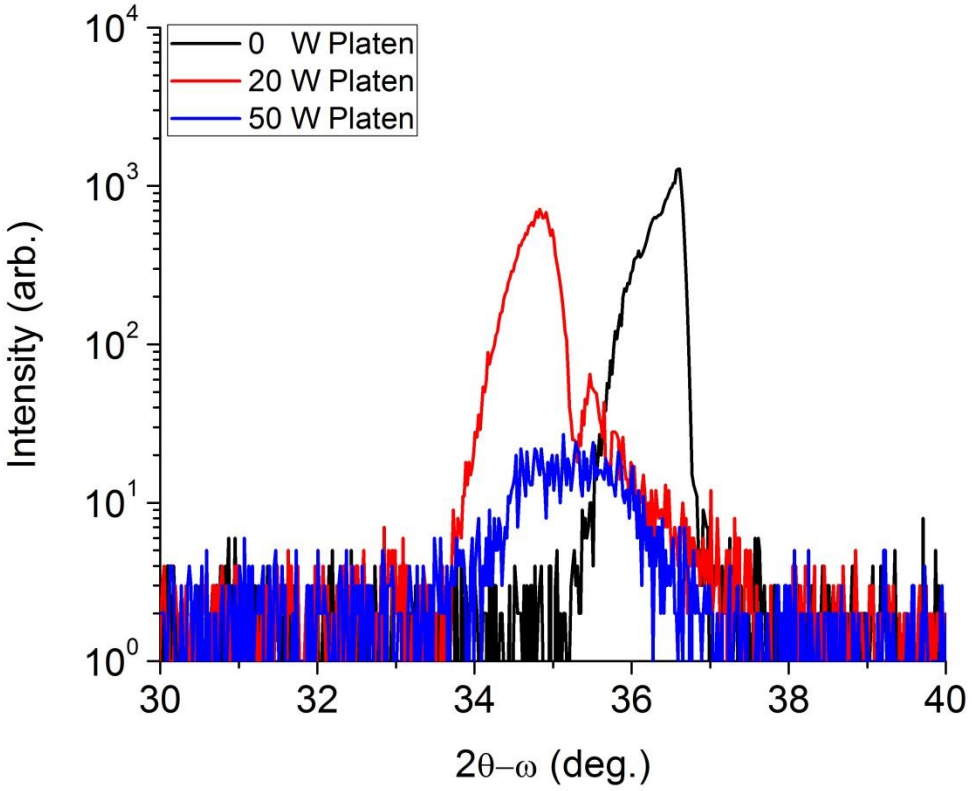

Figure 2-31: X-ray diffractograms of films deposited with varying platen plasma powers. *In-situ* plasma etching during deposition appears detrimental to obtaining crystalline lithium niobite.

2.5.6 Deposition Time

One of the structural features observed in the standard deposition condition was a two layer structure with small particles near the sapphire substrate and the formation of tapered crystallites approximately 250 nm into the film. As discussed in Section 2.4, correlation of these features observed in SEM with the XRD data suggested that the low angle shoulder observed in XRD corresponded to the small particles while the main peak corresponded to the tapered crystallites. The standard deposition condition was repeated for a variety of deposition times in order to see how the XRD shoulder and main peak evolve.

As shown in Figure 2-32, a short 10 minute deposition produces a very weak and broad peak in the XRD. A longer 30 minute deposition produces an XRD peak that is predominately composed of the low angle shoulder with little to none of the primary 36.6° lithium niobite XRD peak present. Lastly, the standard deposition condition deposited for 60 minutes produces a combination of the primary lithium niobite peak and the low angle shoulder as previously observed. This progression from a broad hump to only the shoulder feature to a combination of the shoulder and main peak suggests that as the deposited film grows thicker, crystalline material accumulates first in structures that produce the low angle XRD shoulder and then in structures that produce the primary lithium niobite XRD peak. These two structures are likely the small particles and tapered crystallites previously discussed.

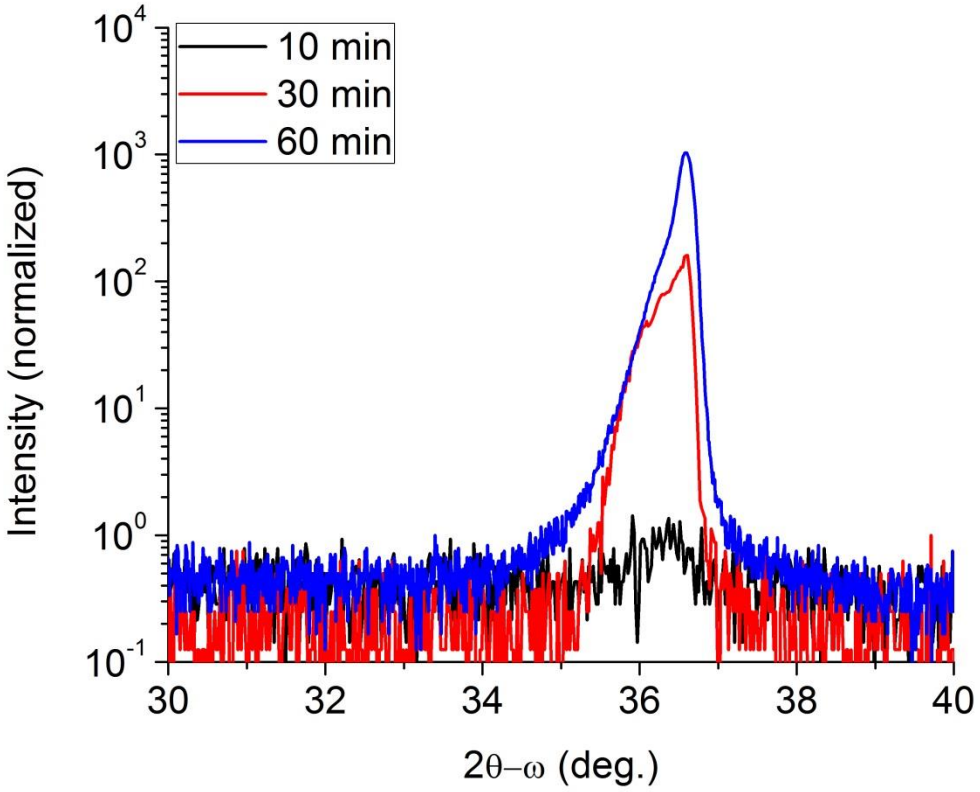

Figure 2-32: x-ray diffractograms of sputter deposited lithium niobite films showing a progression from little crystalline material to forming the low angle shoulder XRD feature to a combined low angle shoulder and main lithium niobite XRD peak.

2.5.7 Substrates

Lithium niobite was sputter deposited onto a variety of substrates. Two features of interest in performing this deposition were a) how does the substrate lattice spacing affect the lithium niobite deposition and b) on what substrates is the sputter deposited lithium niobite stable? The first question concerns epitaxial alignment between the underlying substrate and the lithium niobite film. Such an epitaxial relation would be unusual for room temperature sputtered material. In addition, while (1 0 1) oriented lithium niobite has short range trigonal (3.07 Å spacing) and hexagonal (3.05 Å spacing) features, as

shown in Figure 2-33, no long range hexagonal pattern exists to form a traditional epitaxial relationship.

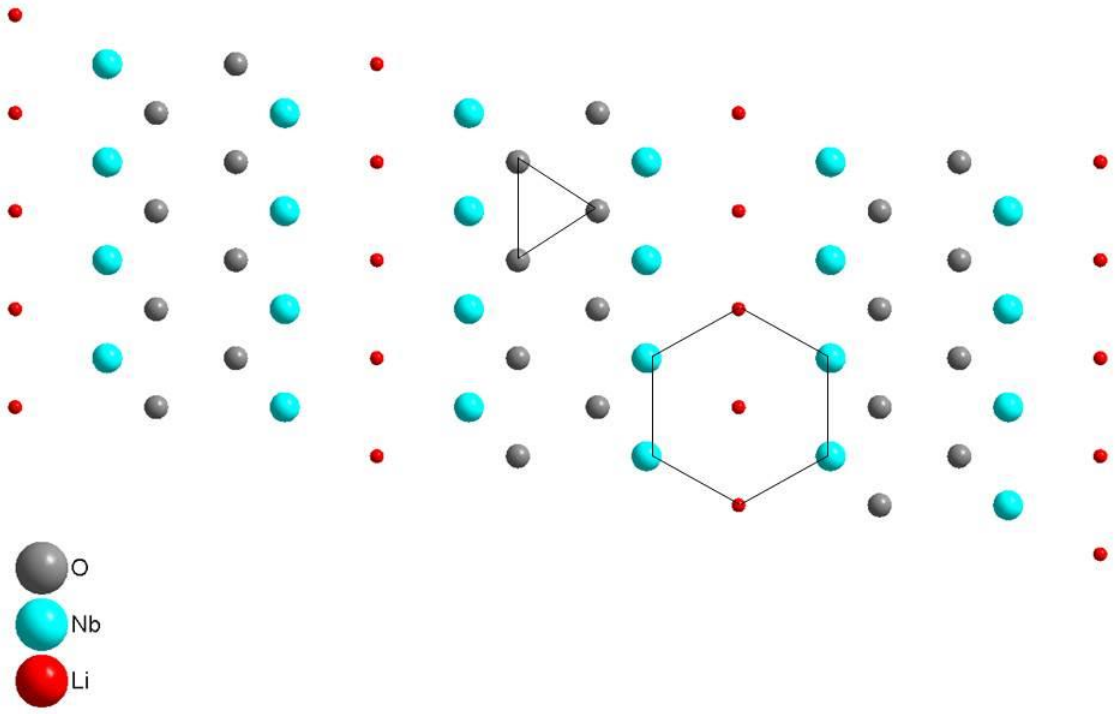

Figure 2-33: (1 0 1) lithium niobite crystal plane showing both hexagonal and trigonal features but no long range repeating hexagonal or trigonal pattern to form an epitaxial relation.

The second question concerning film stability originates from the mobile nature of lithium atoms. Many materials are capable of absorbing lithium as an interstitial atom. While this feature is useful for creating lithium ion battery anodes/cathodes, the volumetric expansion of the substrate is often catastrophic [129-133]. Depositions were performed on SiC, n-type GaN, semi-insulating GaN:Fe, AlN, $LiTaO_3$, (1 1 1) oriented silicon, (1 0 0) oriented silicon, ZnO, epitaxial aluminum on silicon, and sputter deposited Nb on sapphire.

As shown in Figure 2-34, sputter deposition of lithium niobite onto SiC produced the same (1 0 1) lithium niobite peak in XRD and no features were visible when viewed with an optical microscope. Therefore deposition onto SiC appears stable as was previously reported for growth by molecular beam epitaxy [64].

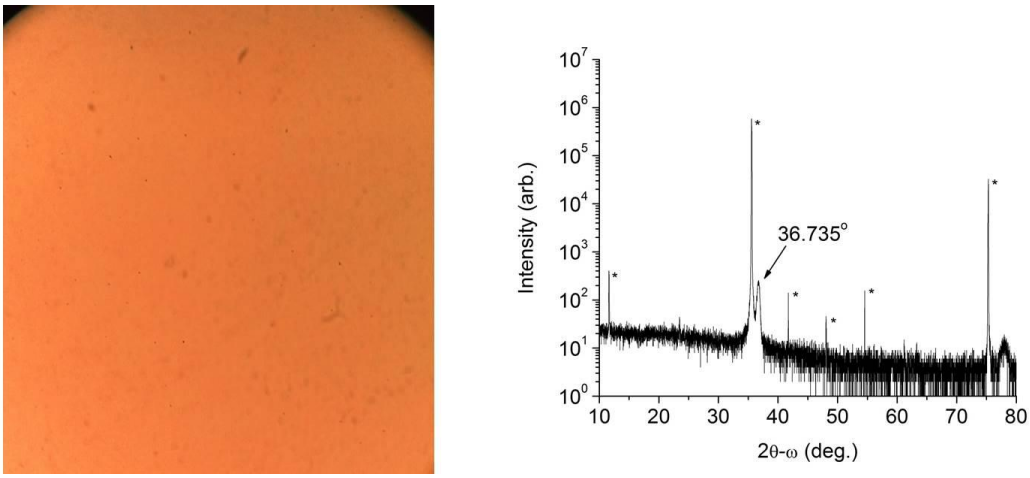

Figure 2-34: (Left) optical image and (Right) x-ray diffractogram of sputter deposited lithium niobite on SiC. The SiC substrate XRD peaks are indicated with *.

As shown in Figure 2-35, sputter deposition of lithium niobite onto n-type GaN produced the same (1 0 1) lithium niobite peak in XRD. It should be noted that an XRD peak at 17.08^{o} is also present that could correspond to the (0 0 2) orientation of lithium niobite. However, this peak location also corresponds to a forbidden peak of GaN making positive identification difficult. Small grains are visible when the film is viewed under an optical microscope and small pits are present. It is assumed that these pits are caused by the underlying GaN template.

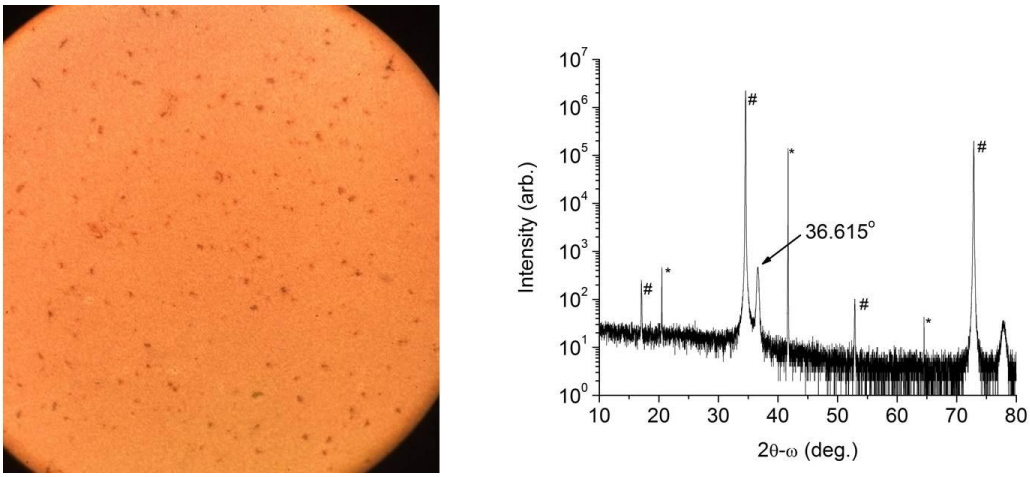

Figure 2-35: (Left) optical image and (Right) x-ray diffractogram of sputter deposited lithium niobite on an n-type GaN template. The sapphire substrate XRD peaks are indicated with * while the GaN template peaks are indicated with #.

As shown in Figure 2-36, sputter deposition of lithium niobite onto iron doped semi-insulating GaN:Fe produced the same (1 0 1) lithium niobite peak in XRD and that no features were visible when viewed with an optical microscope.

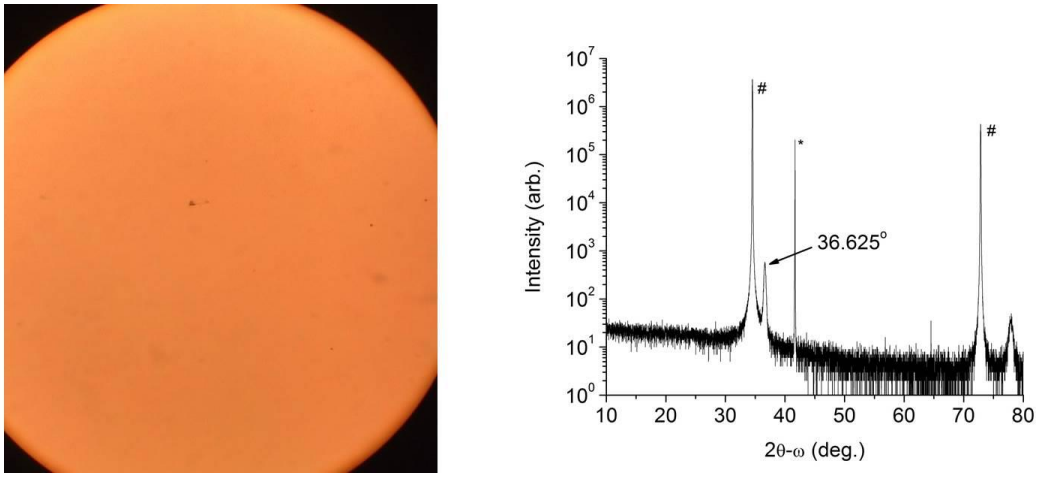

Figure 2-36: (Left) optical image and (Right) x-ray diffractogram of sputter deposited lithium niobite on a semi-insulating GaN template. The sapphire substrate XRD peaks are indicated with * while the GaN template peaks are indicated with #.

As shown in Figure 2-37, sputter deposition of lithium niobite onto AlN produced the same (1 0 1) lithium niobite peak in XRD and that no features were visible when viewed with an optical microscope.

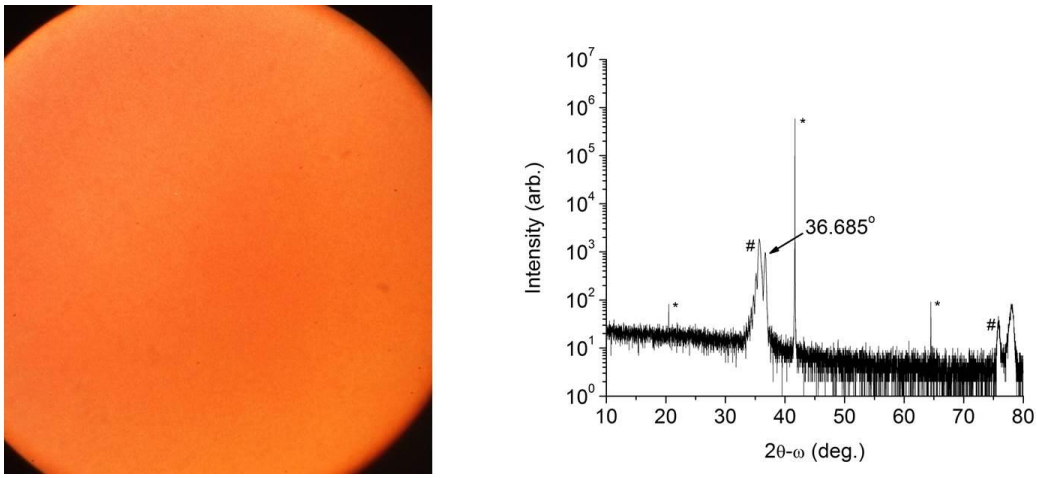

Figure 2-37: (Left) optical image and (Right) x-ray diffractogram of sputter deposited lithium niobite on an AlN template. The sapphire substrate XRD peaks are indicated with * while the AlN template peaks are indicated with #.

As shown in Figure 2-38, sputter deposition of lithium niobite onto $LiTaO_3$ produced the same (1 0 1) lithium niobite peak in XRD. Cracking is visible in the film when viewed with an optical microscope likely due to the pyroelectric nature of $LiTaO_3$ [134].

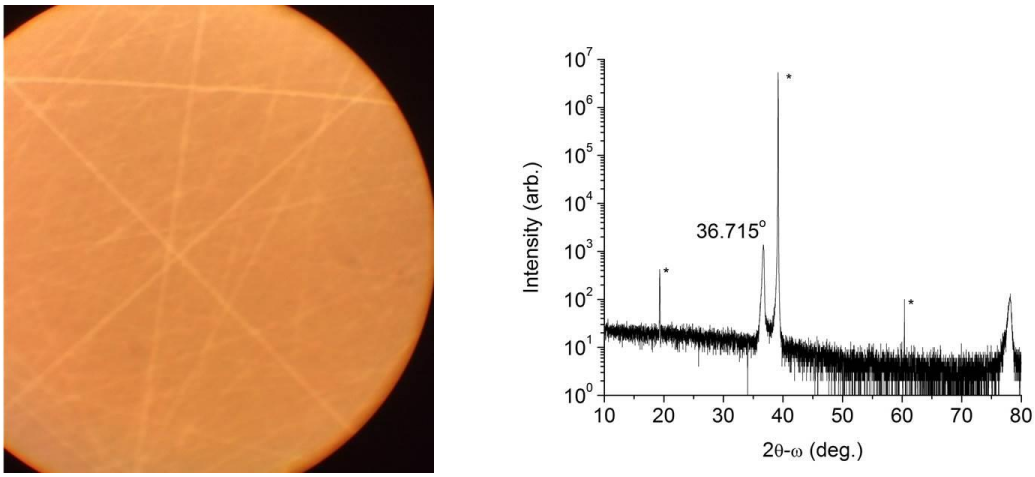

Figure 2-38: (Left) optical image and (Right) x-ray diffractogram of sputter deposited lithium niobite on $LiTaO_3$. The $LiTaO_3$ substrate XRD peaks are indicated with *. Film cracking is visible under optical magnification likely due to the pyroelectric nature of $LiTaO_3$.

Depositions of lithium niobite onto substrates that can absorb large quantities of lithium are expected to be unstable due to volumetric expansion of the substrate. Depositions onto silicon, epitaxial aluminum, and ZnO were all unstable with the films pealing as shown in Figure 2-39. For the silicon substrates, substrate orientation and surface preparation did not affect the film stability.

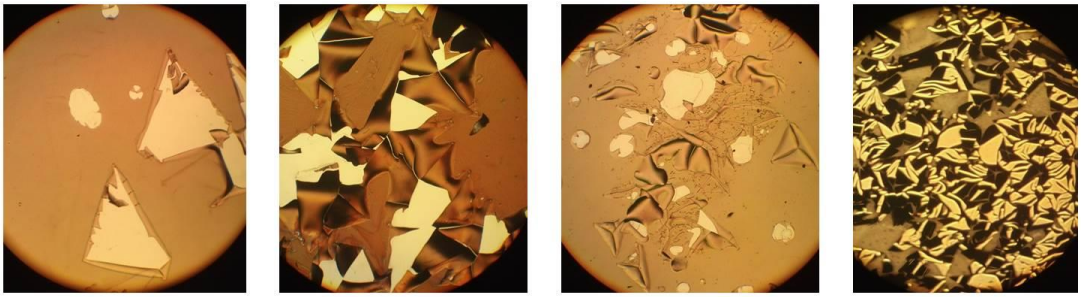

Figure 2-39: Depositions performed on (1 1 1) oriented silicon, (1 1 1) oriented silicon cleaned with HF, (1 0 0) oriented silicon, and ZnO from left to right. All of these depositions produced unstable films that pealed likely due to lithium absorption into the substrate causing volumetric expansion of the substrate.

While deposition of lithium niobite onto smooth epitaxial aluminum produced an unstable film that pealed, one deposition on epitaxial aluminum remained stable. Examining the microstructure of this successful aluminum film, as shown in Figure 2-40, the aluminum film that produced a stable lithium niobite deposition grew in a columnar morphology with voids between the columns. The only difference between the films that produced unstable versus stable lithium niobite was the time spent in the vacuum transfer system (~miniminal versus 12 hours) suggesting the influence of oxidation in the formation of the nanostructured Al. Using nanostructures to absorb the volumetric expansion of lithium intercalated materials has been explored for creating stable lithium ion battery anodes [131-133] and also led to a stable lithium niobite film.

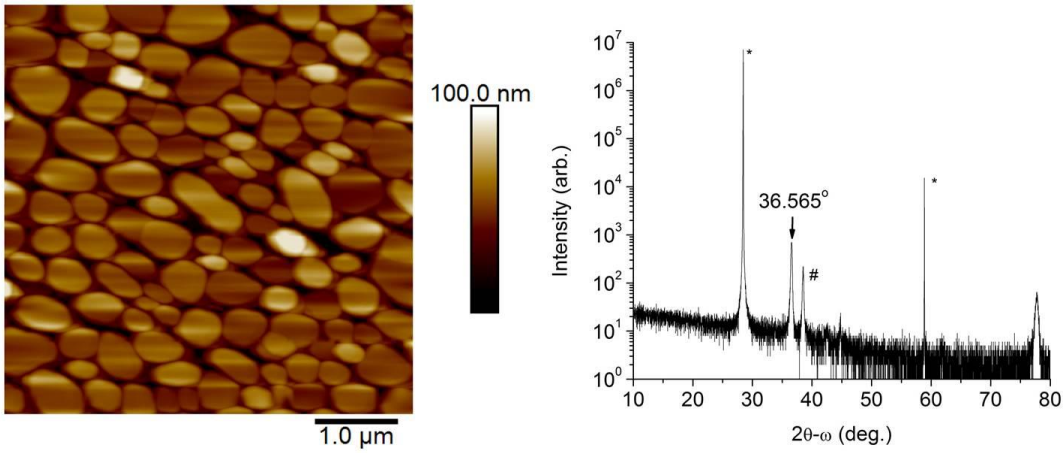

Figure 2-40: (Left) AFM image of epitaxial aluminum on silicon and (Right) x-ray diffractogram of sputter deposited lithium niobite on this substrate. The silicon substrate XRD peaks are indicated with * while the aluminum peaks are indicated with #.

The final substrate explored was an *in-situ* sputter deposition of niobium onto a sapphire substrate followed by the standard lithium niobite deposition. As shown in Figure 2-41, the sputter deposited niobium has an XRD peak at 38.355° aligning with (1 1 0) body-centered cubic niobium. The lithium niobite deposition then produces the same

(1 0 1) XRD peak previously observed. The ability to deposit lithium niobite onto a metallic surface without breaking vacuum may be useful for creating vertical devices based on lithium niobite.

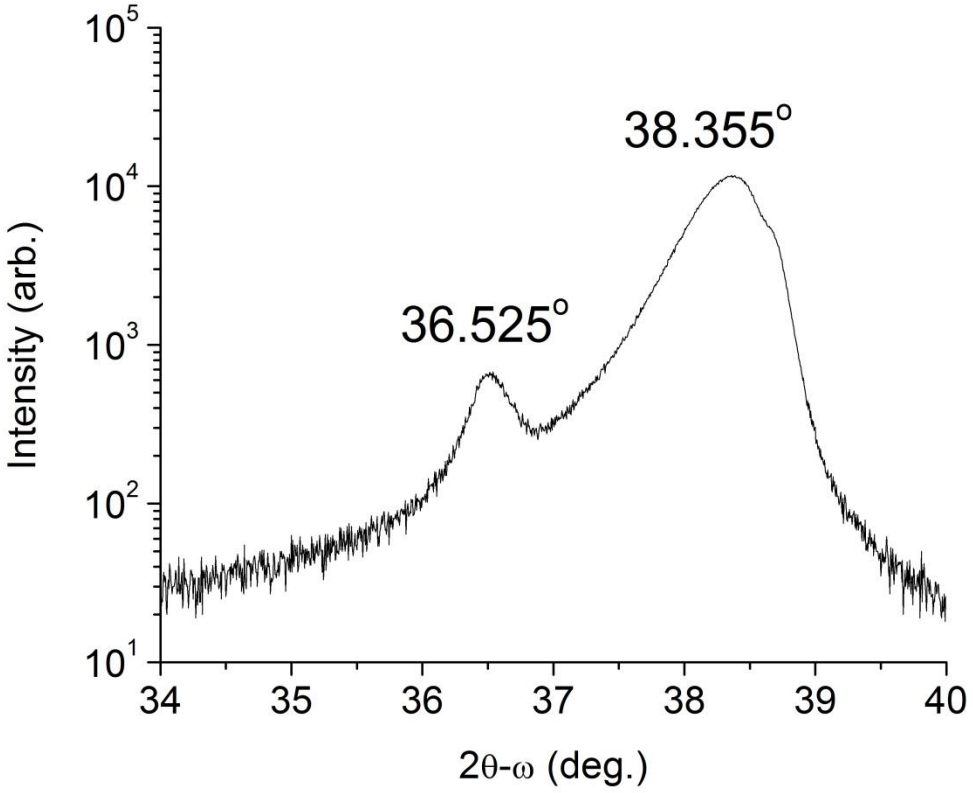

Figure 2-41: x-ray diffractogram of sputter deposited lithium niobite on sputter deposited niobium.

In addition to examining the structural stability of lithium niobite films deposited on varying substrates, the crystallographic relationship between the deposited films and the substrates was examined. As shown in Figure 2-42, for substrates with lattice spacing less than the lattice spacing of lithium niobite the XRD peak location for the sputter deposited lithium niobite decreases with decreasing substrate lattice constant. This is consistent with the film under compressive strain increasing the out-of-plane crystal lattice thus decreasing the location of the XRD peak angle.

However, for substrates with lattice spacing greater than the lattice spacing of lithium niobite the XRD peak location decreases with increasing substrate lattice constant, as shown in Figure 2-42. This trend is opposite the expected trend indicating that some process other than strain to the underlying substrate is responsible for the crystal lattice parameters.

One potential non-strain mechanism for changing the crystal lattice parameters is the absorption of lithium into the underlying substrate. Examining the four materials in Figure 2-42 with lattice spacings larger than lithium niobite, each substrate has progressively smaller atomic densities (SiC = 0.097 atoms/A^3, AlN = 0.096 atoms/A^3, GaN = 0.088 atoms/A^3, Nb = 0.055 atoms/A^3) creating more open space in the crystal lattice and the potential to absorb increasing amounts of lithium from the thin film lithium niobite. If lithium is absorbed from the thin film into the underlying substrate, the lattice parameters of the lithium niobite will change as shown in Figure 2-42.

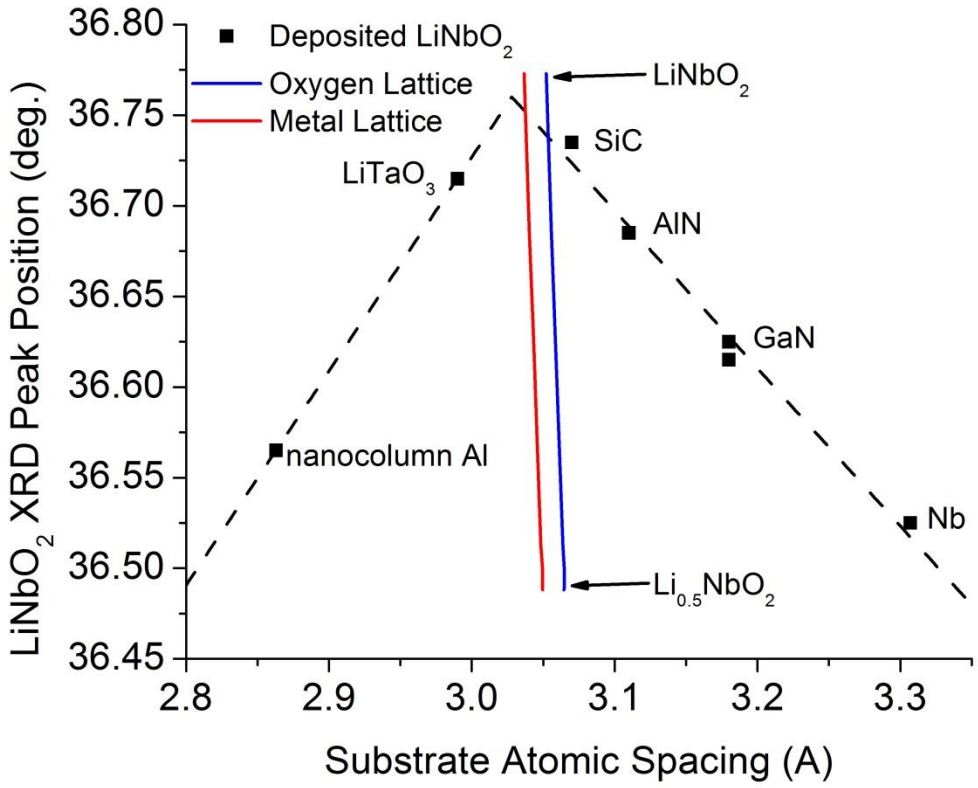

Figure 2-42: Effect of the substrate on the lattice parameters of sputter deposited lithium niobite.

2.5.8 *ex-situ* Annealing

While the substrate affected the lithium niobite film's structural stability during deposition, it is also desirable to know how *ex-situ* environmental effects affect the structural and chemical stability of the lithium niobite films. The thermal stability of the deposited lithium niobite was investigated by *ex-situ* annealing. A set of lithium niobite films was deposited at room temperature and then individual samples were annealed for one hour under vacuum at temperatures ranging from 400 – 700 ^{o}C.

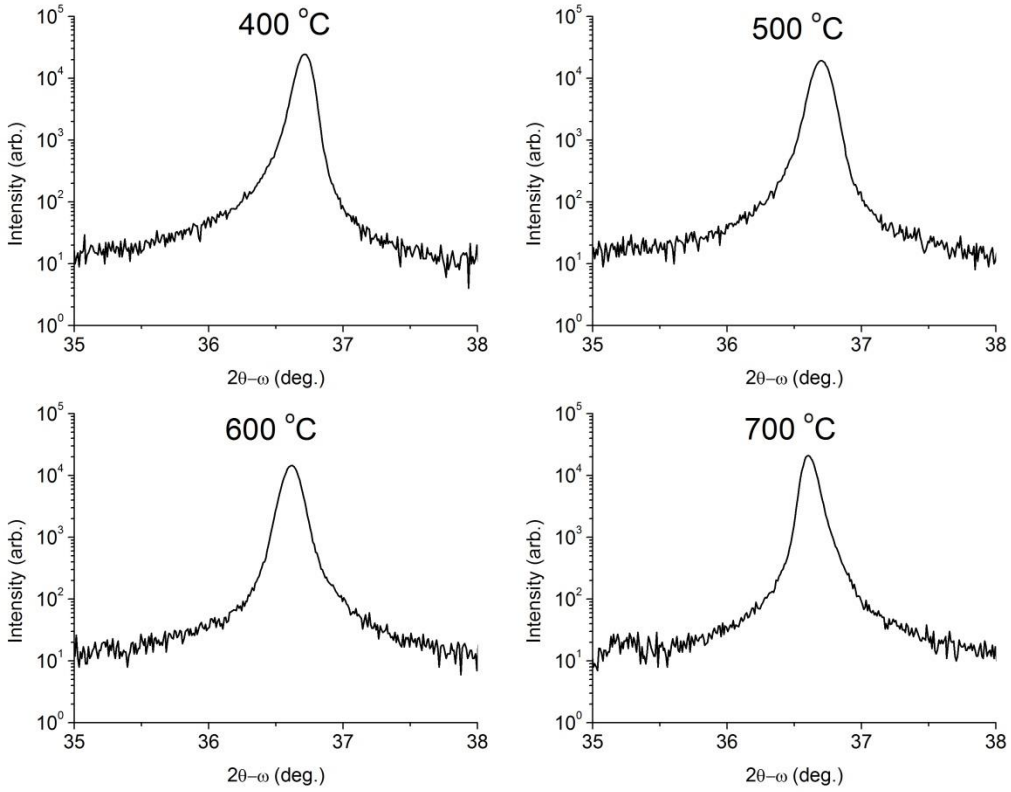

Figure 2-43: x-ray diffractograms of sputter deposited lithium niobite annealed under vacuum at a variety of temperatures from 400 – 700 °C.

As shown in Figure 2-43, there is very little qualitative change in the (1 0 1) lithium niobite XRD peak as a function of annealing temperature. The only notable change is a slight shift in the XRD peak to lower 2θ-ω angle as the annealing temperature is increased. As shown in Figure 2-44, the peak shifts as a nearly linear function of annealing temperature at a rate of 1.57 ± 0.06 arcsec/°C. This peak shift to lower angle corresponds to a larger spacing between the (1 0 1) crystalline planes. It has previously been shown that the crystalline lattice spacing of lithium niobite increases as lithium is removed from the crystal [90]. Loss of lithium from the crystal lattice when annealed under vacuum has been shown for lithium niobate [135]. Because lithium is more loosely

bound in lithium niobite than in lithium niobate, it is therefore likely that vacuum annealing causes a loss of lithium from lithium niobite and an associated shift in the XRD peak location. Thus, it may be possible in the future to introduce an in-situ anneal so as to achieve stoichiometric lithium niobite instead of the supersatureated lithium niobite produced herein.

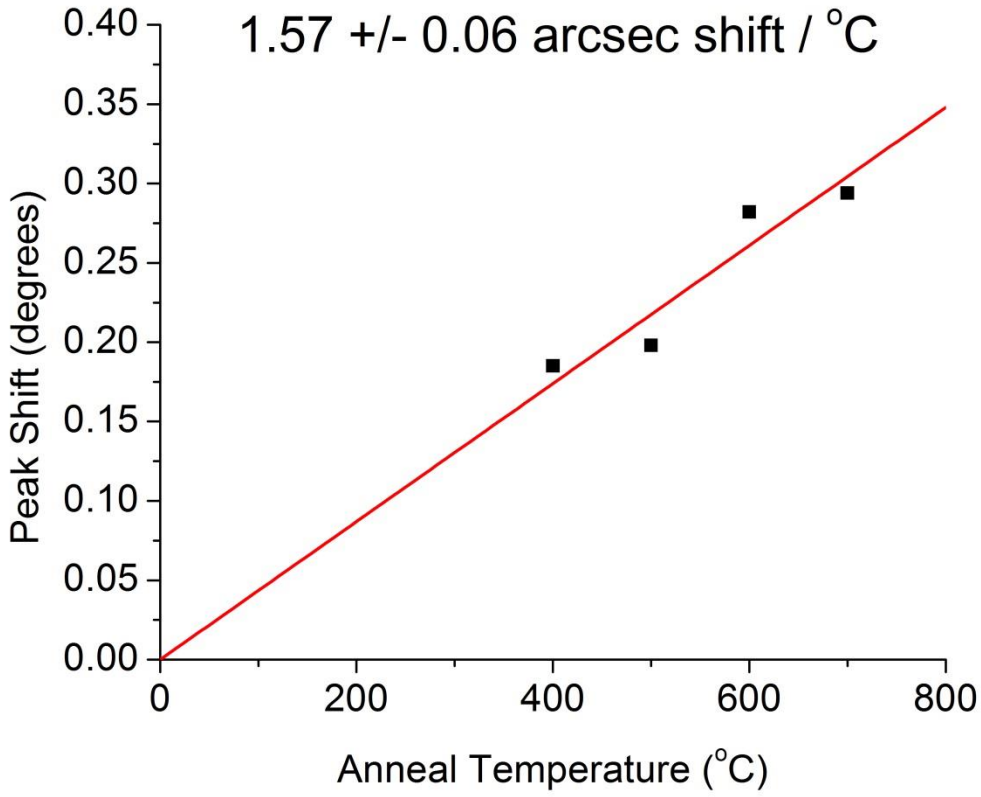

Figure 2-44: Trend of XRD peak shift when sputter deposited lithium niobite is annealed for 1 hour under vacuum.

Examining the broader range XRD scan for the 700 °C anneal, shown in Figure 2-45, additional peaks are visible. These peaks correspond to multiple orientations of NbO_2 suggesting that some of the lithium niobite ($LiNbO_2$) has decomposed into NbO_2 by removing lithium from the material.

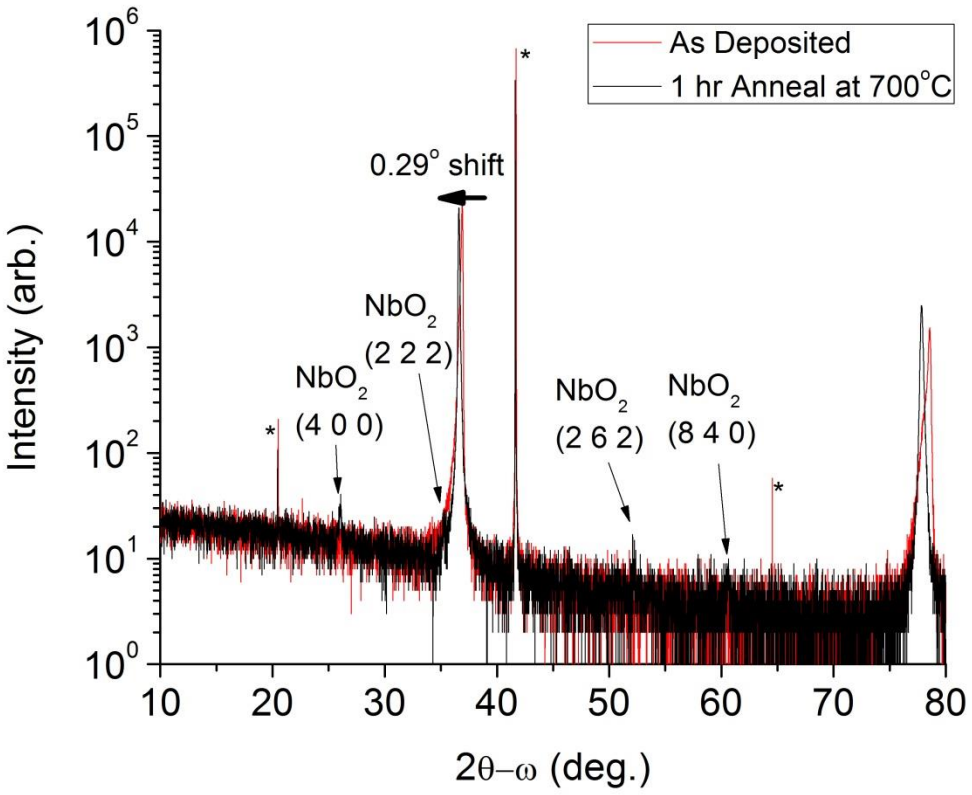

Figure 2-45: X-ray diffractograms of lithium niobite as-deposited and after annealing under vacuum at 700 °C. The annealing treatment caused a shift in the main XRD peak to lower angle consistent with removing lithium from the crystal. NbO_2 XRD peaks also appeared after annealing suggesting that some of the $LiNbO_2$ lost all of its lithium.

Sputter deposited lithium niobite therefore appears sensitive to elevated temperatures under vacuum as lithium can be removed from the film. This effect can eventually lead to the film decomposing into NbO_2.

2.6 Alternate Deposition Condition

While the standard lithium niobite deposition condition is well understood and produces functional memristive devices, the two layer structure with tapered crystallites and the reactivity with air are not ideal attributes. As previously noted in Section 2.4, the reactivity with air is likely due to excess lithium in the film. This excess lithium results from trying to form $LiNbO_2$ from a linear combination of Li_2O and Nb. In order to address the problem of excess lithium, a new deposition condition was found by lowering the power to the lithium oxide target, raising the power to the niobium target and introducing oxygen as a reactive gas to the sputtering plasma. Details on this deposition condition can be found in Appendix A.

As shown in Figure 2-46, the new deposition condition also produces single orientation (1 0 1) lithium niobite. Examining the (2 0 2) XRD peak it is also apparent that the new deposition condition produces a single XRD peak with no shoulder. The lack of two XRD features suggests that the new deposition condition may also consist of a single layer structure rather than the two layer structure observed from the standard deposition condition.

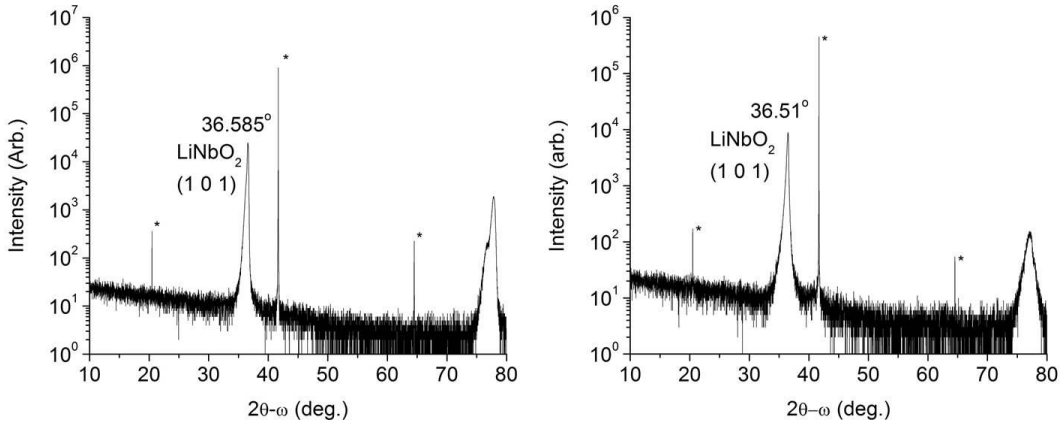

Figure 2-46: X-ray diffractograms of (Left) the standard lithium niobite deposition condition and (Right) a new deposition condition that adds reactive oxygen to the plasma. By adding oxygen to the

plasma both the air reactivity due to excess lithium and the two layer structure appear to have been solved.

The cross sectional SEM image shown in Figure 2-47 confirms that the new deposition condition produces a single structural layer without tapered crystallites. In addition, the XRD rocking curve of the new deposition condition, shown in Figure 2-47, has a full width at half maximum of 164 arcsec indicating a low degree of tilt between crystalline planes. The penalty for this improved XRD figure of merit is a highly columnar structure which may be suitable for some applications and not for others.

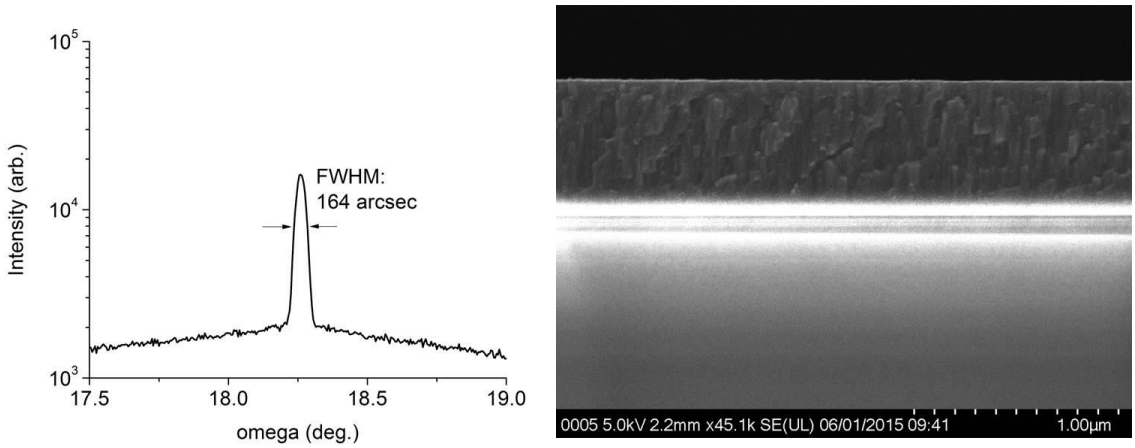

Figure 2-47: (Left) XRD rocking curve of the new deposition condition showing well oriented crystalline material and (Right) cross sectional SEM of the new deposition condition showing a single structural layer to the film.

CHAPTER 3

RADIATION TOLERANCE OF LITHIUM NIOBITE

As the amount of information gathered in space increases through the use of satellites, telescopes, and space stations, a complementary increase occurs in the amount of information transmitted back to Earth. In order to reduce the bandwidth requirements for satellites, more processing will have to be performed in space. Neuromorphic computers are a good candidate for this type of processing, being particularly useful for pattern recognition. By replicating the functionality of the brain, these computers also replicate the brain's ability to recognize patterns and exclude extraneous data while minimizing power consumption [34]. In order for any neuromorphic architecture to provide reliable computation in space, the material and devices must be radiation tolerant and their radiation response must be known.

To explore the application of lithium niobite ($LiNbO_2$) memristors in space based circuitry, devices were exposed to 1.8 MeV proton radiation. In addition to observing the direct effects of proton radiation on the memristors, room-temperature self-healing mechanisms were observed due to highly mobile lithium ions. Two-terminal memristive devices were tested on both thin film and thick bulk material, and the effects of proton damage on the small signal impedance was analyzed.

Density of states and wave-function calculations performed on lithium niobite predict electrical conduction predominantly in the niobium oxide layers with significant contributions from metal-metal bonding [82]. NMR relaxation studies indicate that the lithium ions have an activation energy on the order of 100 meV and an average residence time on the order of 100 μs before hopping to a neighboring site in the lithium plane,

making Li highly mobile and $LiNbO_2$ memristors rapidly programmable [75, 76]. While lithium niobite is a 2 eV semiconductor, it has an intrinsic Fermi level near the valence band edge and exhibits semi-metallic conduction [90]. Lithium is often deintercalated to form sub-stoichiometric Li_xNbO_2, where the lithium vacancies act as acceptors, lowering the Fermi level inside the valence band [82]. When an electric field is applied, these lithium vacancies freely drift across the material changing the doping profile of the device [73]. These unique physical and electronic properties of lithium niobite affect the radiation damage and recovery mechanisms.

3.1 Experimental Setup

The devices used in this study were annular ring-dot structures, as shown in Figure 3-1. These devices were packaged into custom high frequency packages with gold wire bonds and SMA connectors. The added resistance from packaging was less than 2 ohms, which has been subtracted out of the measurement using an in situ calibration standard with known open, short, and load impedances [136, 137].

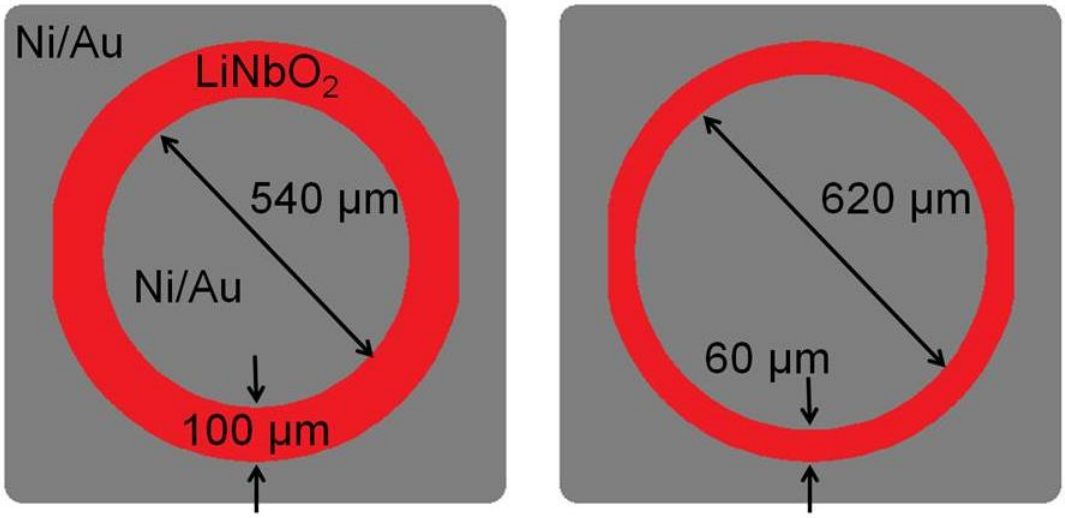

Figure 3-1: Schematic of the ring-dot devices fabricated for the radiation study.

Two terminal lithium niobite memristors were irradiated with 1.8 MeV protons to seven fluences between 10^{12} and 10^{14} cm^{-2} using the Pelletron particle accelerator at Vanderbilt University. During irradiation and annealing the devices were ungrounded and unbiased. At each fluence, a series of electrochemical impedance spectroscopy (EIS) measurements were taken to characterize the low frequency resistance and the lithium ion mobility. The EIS measurements record the small signal impedance of the device as a function of frequency from 40 Hz to 100 MHz. These data can be used to separate the electronic and ionic contributions to the device impedance because the ions can respond to the signal at low frequencies, contributing to the impedance, but cannot respond to the signal at higher frequencies at which only electronic conduction occurs [138]. A typical spectrum for a lithium niobite memristor is shown in Figure 3-2.

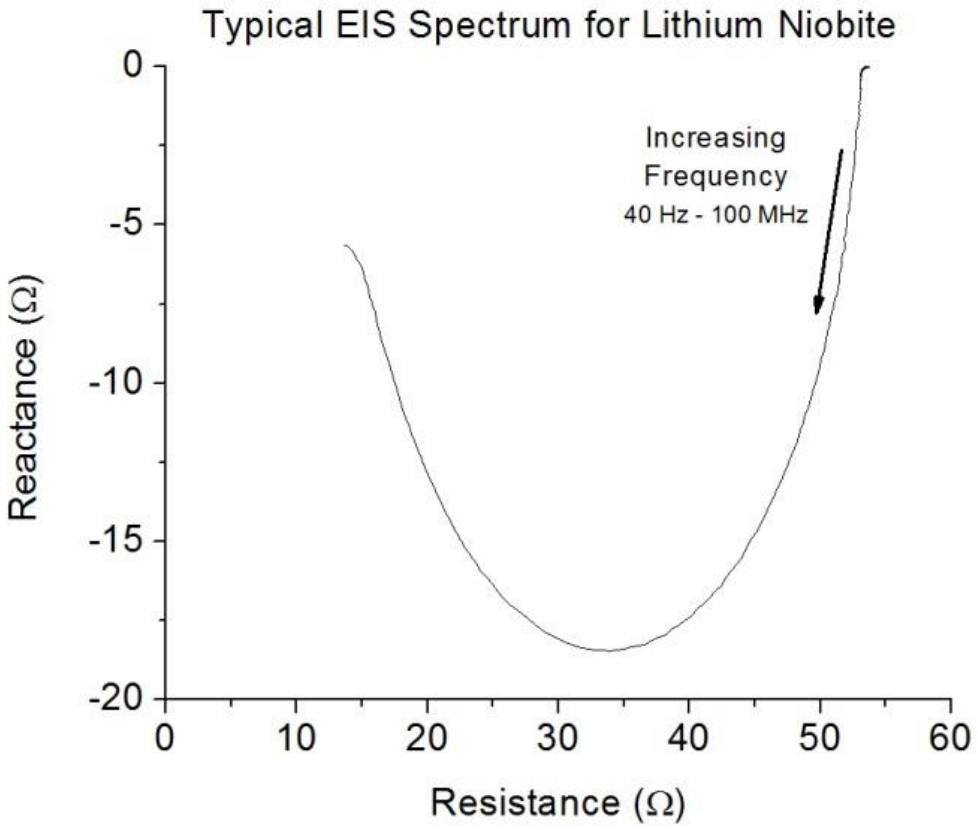

Figure 3-2: Typical electrochemical impedance spectra for a lithium niobite device.

At low frequencies the mobile lithium ions are able to track with the applied voltage creating polarization dipoles that reduce the internal electric field. The resultant reduction in current corresponds to an increased resistance. As the frequency increases, lithium ions are no longer able to track the applied voltage. This causes a phase shift between the applied signal and the polarization of the slowly moving ions resulting in a capacitive reactance and a decrease in the resistance as the polarization no longer fully opposes the applied field. At high frequencies the lithium ions can no longer respond to the applied voltage, and the reactance and the polarization contribution to the resistance each approach zero.

Because of the expectation for rapid annealing due to highly mobile lithium ions, EIS measurements were performed in situ in order to examine the effects of short-term annealing immediately after radiation exposure. Due to the decreased RF impedance from longer cables and feedthrough connectors needed to reach into the beamline vacuum chamber, EIS was limited to frequencies less than 5 MHz.

TRIM Monte Carlo simulations of the described experiment, shown in Figure 3-3, predict a maximum damage range of 40 μm for 1.8 MeV protons in $LiNbO_2$ and a maximum range of approximately 42 μm. Since the proton range is large and could result in implantation of hydrogen, both thin film material (0.2 μm) and bulk material (~110 μm) were used in order to compare displacement damage in the thin film sample with the additional implantation of hydrogen possible in the bulk sample. Such hydrogen implantation could result in the passivation of electrically active defects or act as a compensating donor due to the chemical similarity of hydrogen and lithium. The 110 μm thick bulk material was grown by liquid phase electro-epitaxy [95] and subsequently polished. The 200 nm thin film material was sputter deposited onto a sapphire substrate. Two devices of each type were tested for this experiment.

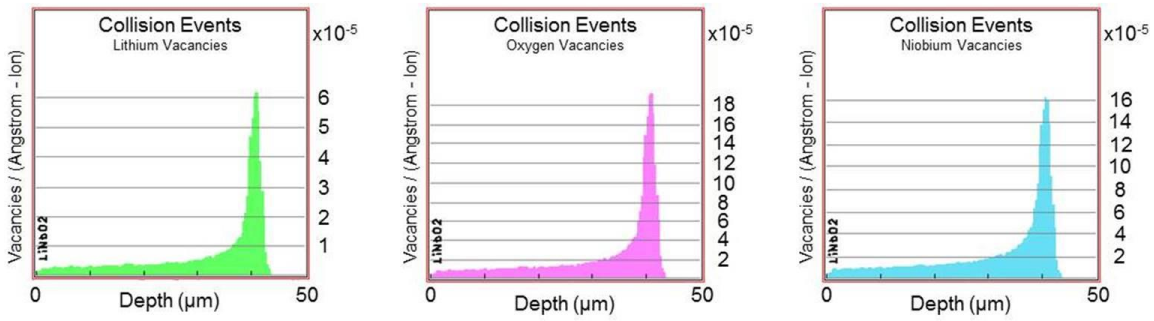

Figure 3-3: TRIM proton radiation simulations showing the expected number of lithium, oxygen, and niobium vacancies formed as a function of depth when lithium niobite is exposed to 1.8 MeV proton radiation.

3.2 Results

3.2.1 Initial Radiation Damage

The average resistance between 100 Hz and 1000 Hz was measured by EIS as an indication of the combined electronic-ionic resistance, as shown in Figure 3-4. This frequency range covers the frequencies most common in biological neurons and thus is the resistance most relevant to a neuromorphic circuit.

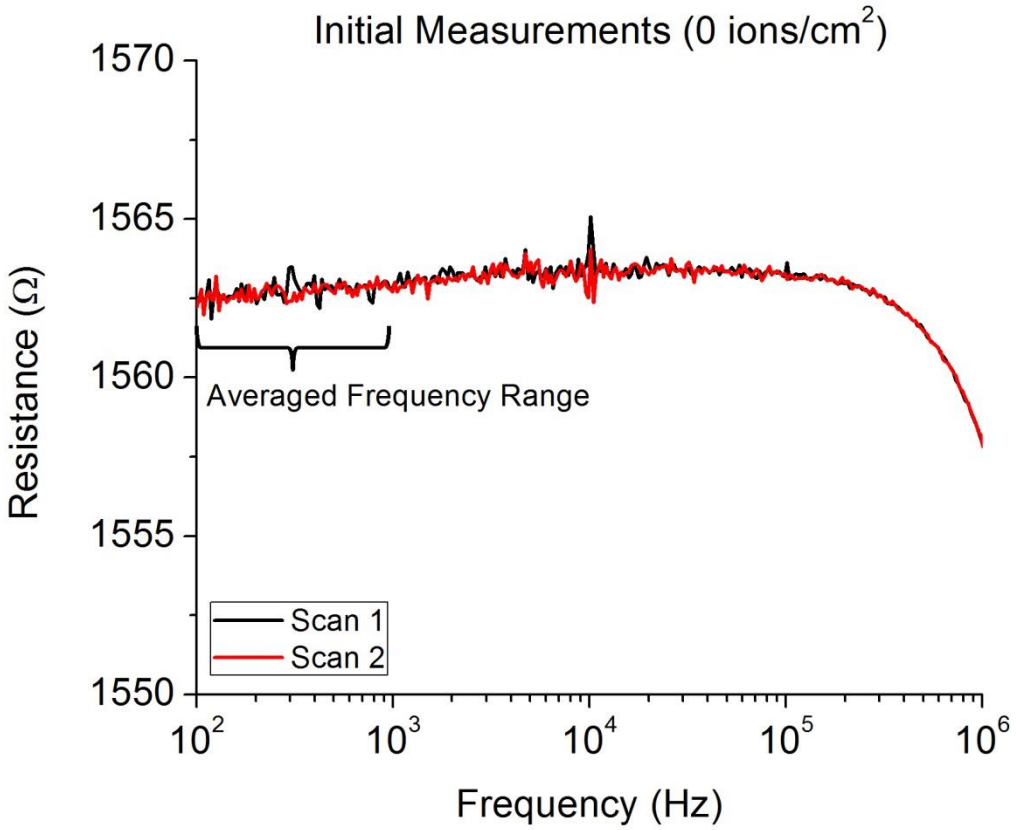

Figure 3-4: Device resistance as a function of frequency for a typical lithium niobite memristor. The measurements are repeatable across multiple scans. The range of data that is averaged for the radiation study is indicated. This low frequency range is the measured range most relevant to neuromorphic computing.

As the total proton fluence increased, the initial low frequency resistance decreased, as shown in Figure 3-5 for the thin film device.

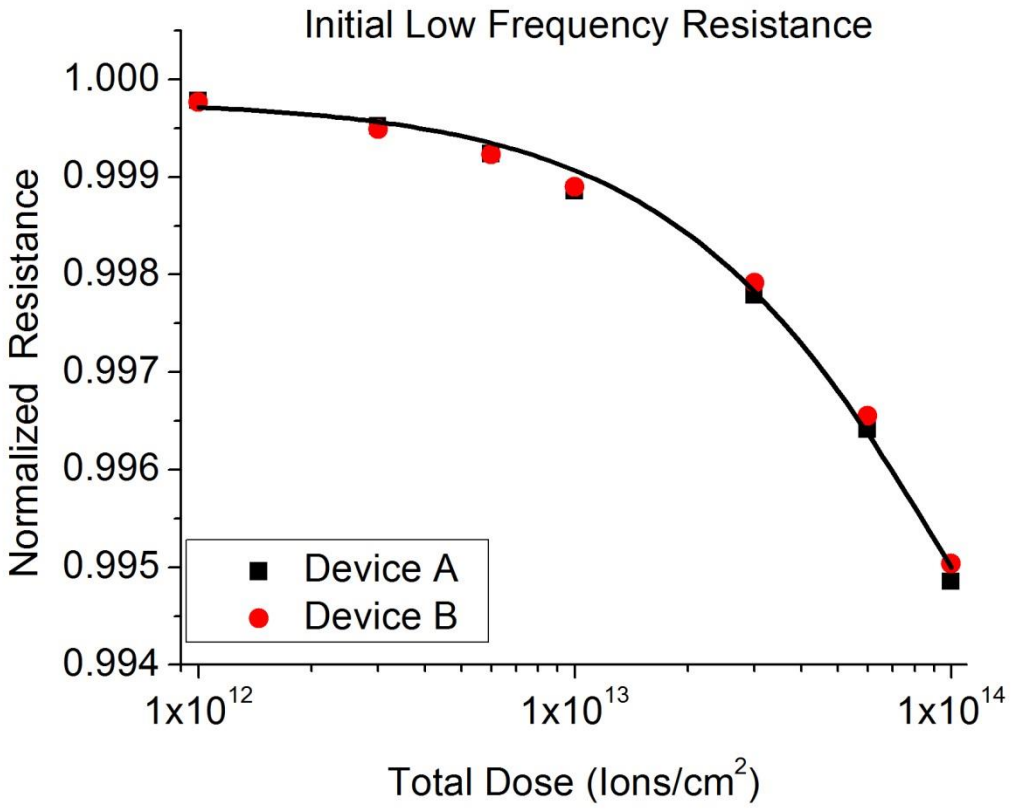

Figure 3-5: Trends in initial device resistance as a function of total proton dose. The resistance of each device is normalized to its pre-radiation resistance.

These data follow the exponential trend, given in Equation 3.1 for the thin film samples, which fits the data with a coefficient of determination, $R^2 = 0.994$.

$$R_{Normalized} = 0.00758\, e^{-\frac{Dose}{1.00*10^{14}}} + 0.992 \qquad \text{Equation 3.1}$$

This trend indicates that approximately 63% of the maximum possible damage had occurred at a fluence of $1.0\text{x}10^{14} \pm 1.8\text{x}10^{13}$ cm^{-2} and that 1.8 MeV proton irradiation can change the initial low frequency resistance by a maximum of 0.76 ± 0.087%. While this exponential trend fits well over the range of fluences tested, other damage mechanisms may dominate at higher fluences causing the trend to deviate from actual device performance.

The bulk sample followed a similar trend with a 1/e point at $1.3x10^{14}$ cm^{-2} and a maximum resistance change of 0.28%. The lower percent change in the bulk sample is consistent with only a portion of the material being affected.

The bulk device was modeled as two parallel resistors, shown in Figure 3-6, where radiation damage affects the top resistor R_1 while leaving the underlying material beyond the 42 µm range (R_2) unchanged, consistent with TRIM calculations in Figure 3-3.

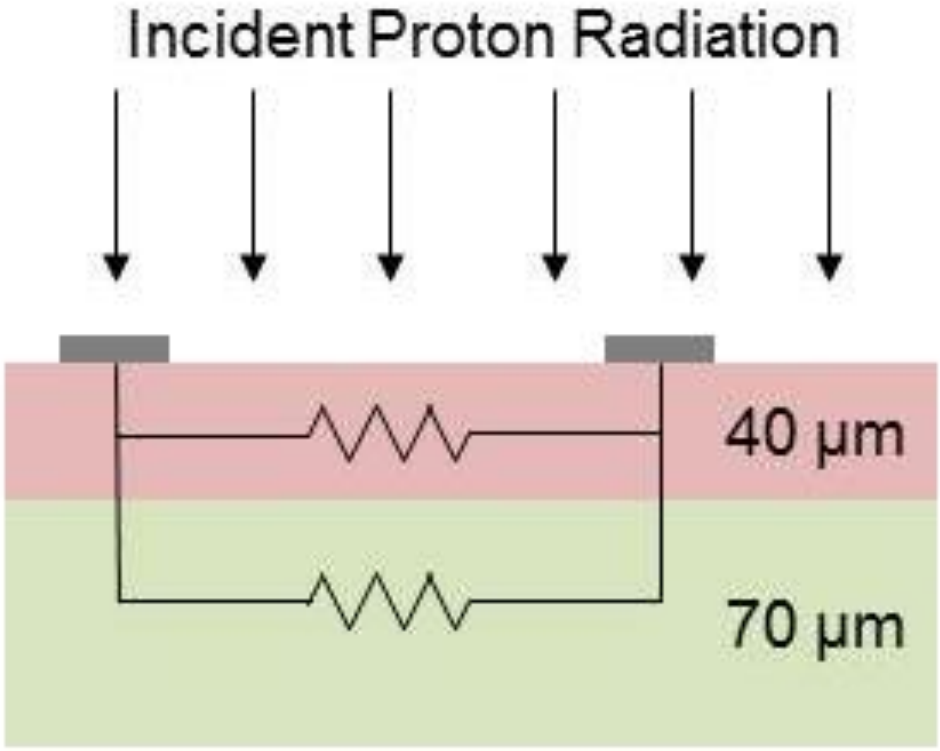

Figure 3-6: Two layer resistance model showing radiation induced changes to the top 40 microns of bulk material predicted from the TRIM calculations and a 70 micron thick layer that remains unchanged.

To eliminate the possible effects of proton implantation on the resistivity changes in the memristors, the resulting damage in the thin and thick samples were compared. The

bulk device two resistor model is evaluated both using the expected thicknesses from the TRIM simulation and the radiation induced changes using the percent change observed in the thin film device. If these two resistance ratios are identical then the proton implantation has minimal effect. The TRIM Monte Carlo simulation predicts a 42 μm range of radiation damage with a peak in damage near 40 μm. Using a thickness for R_1 of 41 ± 1 μm and a total thickness of 110 ± 5 μm, the ratio between R_1 and R_2 can be evaluated as shown in Equation 3.2.

$$\frac{R_1}{R_2} \equiv \frac{\frac{\rho * l}{w * h_1}}{\frac{\rho * l}{w * h_2}} = \frac{h_2}{h_1} = \frac{69 \pm 5}{41 \pm 1} = 1.68 \pm 0.13 \qquad \text{Equation 3.2}$$

where ρ, l, and w are the resistivity, length, and width of the device, respectively. Given that these quantities will not change between the two layers for the un-irradiated material, the resistance ratio then reduces to a ratio of the thicknesses h_1 and h_2, which is 1.68 ± 0.13.

Evaluating the two resistor model as a function of radiation damage, Equation 3.3 and Equation 3.4 are produced, where Equation 3.3 describes the total device resistance of two parallel resistors and Equation 3.4 describes the total device resistance after radiation assuming that the top material R_1 is changed by the same percentage as the thin film sample, which should be absent of significant proton implantation.

$$R_{total}^{initial} = [(R_1)^{-1} + (R_2)^{-1}]^{-1} \qquad \text{Equation 3.3}$$

$$R_{total}^{post-radiation} = \left[\left(R_1 * \left(1 - \%change_{thinfilm}\right)\right)^{-1} + (R_2)^{-1}\right]^{-1} \qquad \text{Equation 3.4}$$

Evaluating Equation 3.3 and 3.4 with the measured initial and post-radiation resistances gives $R_1 = 11.8 \pm 0.26\ \Omega$ and $R_2 = 7.38 \pm 0.26\ \Omega$ and a resistance ratio of $R_1/R_2 = 1.60 \pm 0.066$. This value is well within the range modelled in Equation 3.2 suggesting that the effects of irradiation are the same on the bulk and thin film devices and that hydrogen implantation does not significantly affect the device performance.

3.2.2 Short Term Annealing

To examine the short term annealing at each fluence, several post-irradiation measurements were made from 3 minutes to 15 minutes. For all fluences greater than 10^{13} cm^{-2}, the resistance recovered indicating short-term annealing as shown in Figure 3-7 for the maximum fluence tested, 10^{14} cm^{-2}.

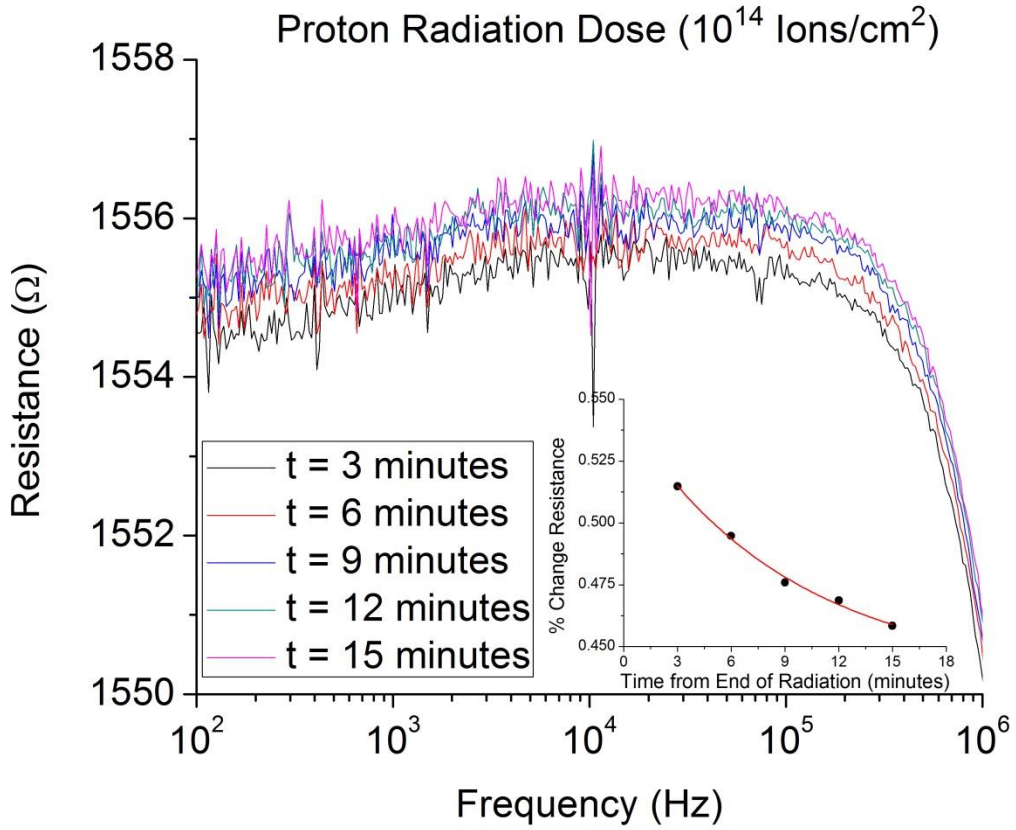

Figure 3-7: Resistance as a function of frequency for a lithium niobite memristor radiated with 10^{14} ions/cm^2 protons. Successive measurements show the device resistance increasing back toward the pre-radiation value indicating room-temperature annealing and self-healing of radiation damage.

The time-dependent resistance recovery followed an exponential trend with a time constant of 9.15 minutes, as shown in Equation 3.5, for the same 10^{14} cm^{-2} proton irradiation case.

$$R(t) = 1.66\, e^{-\frac{time}{9.15}} + 6.85 \qquad \text{Equation 3.5}$$

For fluences less than 10^{13} cm^{-2} no statistically valid self-healing was observed. The standard deviation for measured resistances between 100 Hz and 1000 Hz during a single scan varied from 0.25 ohms to 0.3 ohms (0.02% error). Since the maximum change

in the average low frequency resistance across the five successive EIS measurements was less than the standard deviation for a single measurement, no statistically valid self-healing occurs at these low fluences.

3.3 Discussion

3.3.1 Damage Mechanisms

Radiation damage can generally be divided into four mechanisms: (a) Impurity production through nuclear interactions, (b) Charge trapping through direct ionization or through charge implantation, (c) Local heating, and (d) Displacement damage.

(a) Impurity production through nuclear reactions is not expected to contribute to the radiation damage observed in this study. While ^{7}Li has a relatively unstable nucleus and a cross section of 60 mb for 1.8 MeV protons [139], given the maximum penetration depth of 40 μm and a total proton fluence of $1x10^{14}$ cm^{-2}, the maximum density of dopants that could be created is on the order of 10^{16} cm^{-3} assuming every proton created a dopant. While this assumption is extremely unlikely, it still results in a change several orders of magnitude lower than the expected density of acceptors (10^{21} cm^{-3}) due to lithium vacancies and would leave the doping profile relatively unchanged.

(b) Ionization and charge trapping are not expected to contribute to the radiation damage in lithium niobite due to the material's semi-metallic nature, which will quickly neutralize any created charge. In addition, due to the high density of acceptors in lithium niobite, the density of charge created by ionizing radiation is expected to be orders of magnitude smaller than the free carrier density. For this reason, charge trapping is also not expected to affect thin film devices grown on an insulating substrate because any

charge redistribution within the lithium niobite will be much smaller than the free charge carrier density.

(c) While any heat generated from the proton beam could enhance the diffusion of displacement damage, local heating from the proton radiation is not expected to contribute to the radiation damage effects due to the low power of the proton beam – approximately 4 mW/cm^2. Thermal simulations of lithium niobite under measurement conditions predict temperature changes less than 1 ^oC.

(d) Displacement damage is expected to be the primary damage mechanism for proton irradiation through the creation of vacancies and interstitial atoms. The devices tested in this study were sub-stoichiometric in lithium based on the initial resistance of the tested devices. Because sub-stoichiometric lithium niobite already contains large numbers of lithium vacancies, it is expected that additional lithium vacancies will not significantly contribute to the effects of proton irradiation. Effects due to displacement damage will likely result from lithium interstitials in the niobium oxide layers or niobium and oxygen vacancies and interstitials. TRIM Monte Carlo simulations, shown in Figure 4, predict approximately 3 times the density of niobium and oxygen vacancies compared to lithium vacancies.

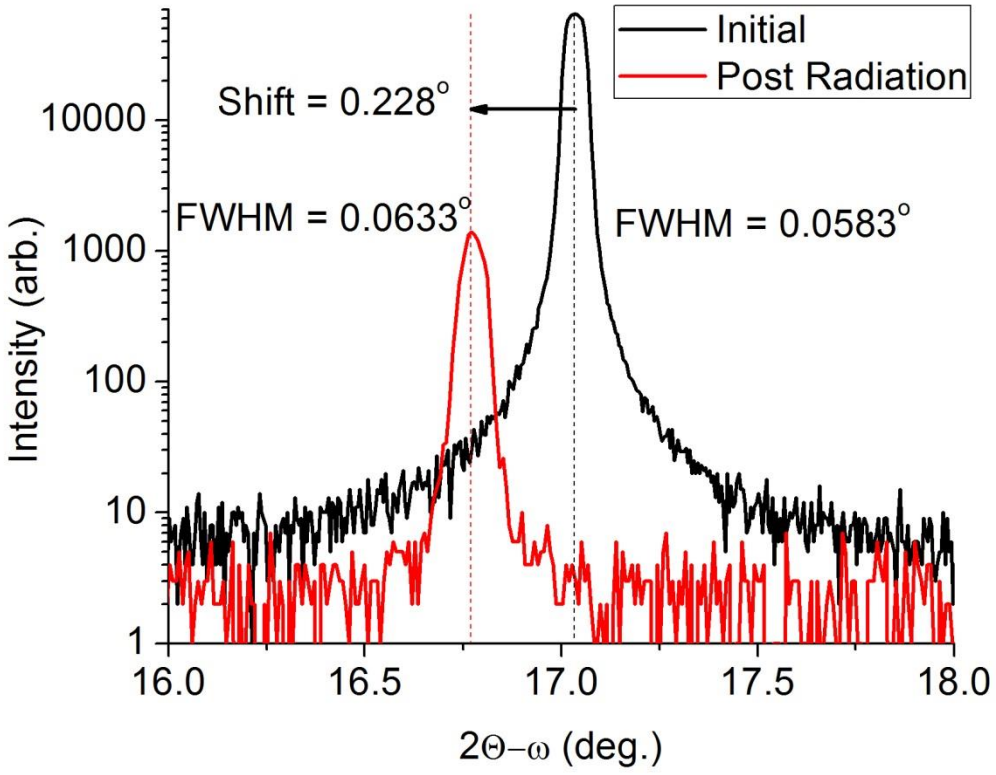

Figure 3-8: x-ray diffractograms of lithium niobite before and after proton radiation. A shift in XRD peak position indicates an increase in the lattice spacing while an increase in the 2θ-ω peak width indicates a decrease in the lattice spacing consistency.

Using x-ray diffraction, shown in Figure 3-8, a previous radiation study of lithium niobite demonstrated an increase in the crystal's c-spacing, a decrease in the c-spacing consistency, and a decrease in the grain orientation consistency [137]. This result is consistent with interstitial atoms displaced to random locations in the crystal lattice.

The reduced impedance observed upon exposure to large fluences of proton radiation is consistent with lithium ions becoming trapped within radiation induced vacancies. The low frequency impedance is largely controlled by the ability of lithium ions to freely move, creating an internal polarization field that opposes the applied

voltage. By trapping the lithium ions within radiation induced defects, the induced polarization decreases resulting in a smaller impedance.

3.3.2 Self-Healing / Short-term Annealing

The expected proton damage mechanism in lithium niobite is from the creation of vacancies, interstitial atoms and Frenkel pairs through displacement damage. Therefore any short-term annealing will be caused by the diffusion and recombination of these defects. Work with silicon has shown an enhancement to short-term annealing when there are excess free charge carriers from either carrier injection or radiation induced generation [140]. While no injection annealing is expected from the low voltage EIS measurements, rapid short-term annealing is expected in lithium niobite due to the high concentrations of mobile lithium ions and the semi-metallic nature of lithium niobite.

Due to the observation of a single time constant in the short-term annealing data and the wide range of atomic masses in lithium niobite, it is likely that diffusion from only one type of atom is responsible for the majority of the room temperature annealing. As lithium is extremely mobile at room temperature with a 100 μs residence time [75] and the proposed damage mechanism does not involve direct lithium displacement, it is unlikely that lithium is directly responsible for the short term annealing. Of the two remaining atoms, oxygen and niobium, the lower mass of oxygen makes it favorable for short-term annealing. The diffusion of either of these atoms back to their original site, freeing the trapped lithium, would result in more lithium-induced polarization and an increase in the low frequency impedance as observed.

3.4 Summary of Lithium Niobite Radiation Tolerance

Lithium niobite ($LiNbO_2$) exhibits small changes in resistance when exposed to 1.8 MeV proton irradiation up to fluences of 10^{14} ions/cm^{-2}. At the maximum fluence tested, 10^{14} ions/cm^{-2}, the device resistance changed by 0.48%. An exponential fit to the resistance change indicates a saturation in the damage effects occurs at 0.75% change in the resistance. Both thin and thick film memristors were examined and found to behave similarly. Even though proton irradiation was shown to produce significant lattice damage as determined from x-ray diffraction measurements, the effect of this damage on the resistance changes was small. This resistance change due to radiation damage is attributed to displacement damage primarily at niobium and oxygen lattice sites trapping lithium ions that significantly contribute to the low frequency impedance. Short-term annealing is observed after radiation exposure with an annealing time constant of 9.15 minutes. This short-term annealing is attributed to the diffusion of the displaced niobium and oxygen back to their original sites freeing the trapped lithium ions. The observation of only one time constant in the short-term annealing data makes it likely that only one atomic species is free to move at room temperature.

Due to the small effect that proton irradiation had on the lithium niobite device performance and the fact that radiation damage in space for these devices would predominantly occur due to protons [141], it is expected that lithium niobite is a suitable material for neuromorphic computing in space applications.

CHAPTER 4

OPTICALLY MEDIATED BAND-STRUCTURE MODIFICATIONS IN LITHIUM NIOBITE

Multi-functional materials that couple mechanical, electrical, optical, and magnetic properties are important for future system designs. Lithium niobite ($LiNbO_2$), a multi-functional sub-oxide of lithium niobate ($LiNbO_3$), has been researched in a wide variety of fields including superconductor physics [85], battery materials [90], and memristive devices [21] because of its unusual band structure and the resulting electronic properties [82]. $LiNbO_2$ is a 2 eV band-gap semiconductor that is degenerately hole doped by lithium vacancies forming Li_xNbO_2. Previous research has shown: a density of states similar to high temperature cuprate superconductors [82, 84], a low temperature superconducting transition [85], both semiconducting [90] and metallic [88] temperature dependent resistivity, highly mobile lithium ions [75, 76], and memristive behavior [21, 74].

X-ray diffraction data identifies lithium niobite as a layered material with niobium oxide layers separated by sheets of loosely bound lithium ions as shown in Figure 4-1. Niobium atoms with a nominal valence of 3+ occupy trigonal-prismatic sites between oxygen atoms [79]. As lithium is removed from the material, niobium and oxygen within a layer move closer together while the separation between the niobium oxide layers increases. This leaves the c-parameter relatively independent of lithium content, but the a-parameter increases as lithium is removed from the crystal [90]. In this way, the band structure is modified by the removal of Li and the subsequent structural changes. However, the removal of lithum has been shown to also change the occupation of the

bands and thus, two mechanisms for band structure modification are possible by removal of Li enhancing its multi-functional utility [73]. Previous work reported more than a two order of magnitude change in resistivity due to changes in lithium content [90]. Additionally, changes in the magnetic moment have been reported [90], but there is some disagreement about the magnetic nature of lithium niobite in the literature [82, 89].

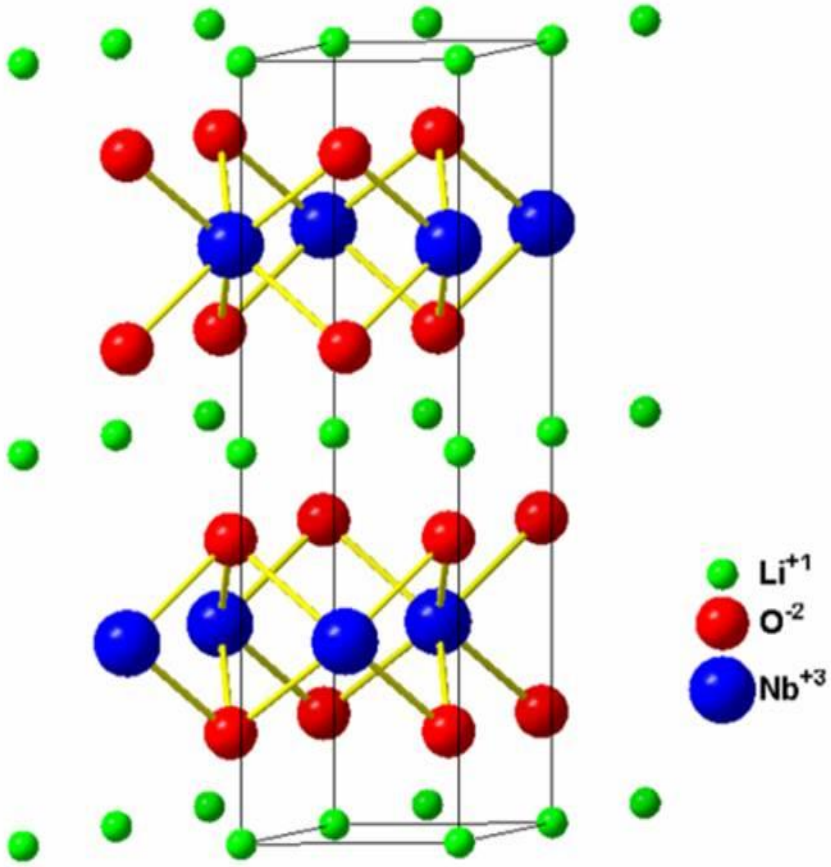

Figure 4-1: Physical structure of lithium niobite with layers of trigonal-prismatic niobium oxide separated by sheets of mobile lithium ions.

4.1 Theoretical Band Structure of Lithium Niobite

Band structure calculations predict that electron states nearest the Fermi energy are comprised primarily of niobium 4d and oxygen 2p electron states. Due to crystal field-splitting in the trigonal-prismatic system, the hybridized Nb 4d – O 2p states should form three bands, (d_{xy}, d_x^2- $_y^2$), (d_z^2), and (d_{xz}, d_{yz}). However, there exist alternative views [82, 84, 89] of the explicit makeup of each of these three bands. Regardless of the source of each band, unanimity exists that the lowest band is a deep "valence" band irrelevant to the present photoluminescence because it remains occupied due to insufficient photon energy for promotion from this band. The Fermi energy is predicted to be between the top two bands forming a semiconductor band gap. In the rigid-band picture, as lithium is removed from the crystal the Fermi energy drops into the valence band forming a p-type degenerately doped semiconductor. Band structure calculations also show that the conduction band around the gamma point is flat suggesting very heavy conduction electrons [82, 84]. While it is not expected that these states would be thermally occupied, the flat conduction band should be revealed in optical measurements.

Band structure calculations were previously made for varying niobium to oxygen distances in order to simulate varying concentrations of lithium. This is a reasonable approximation because the bands of interest are almost entirely made from niobium and oxygen orbitals. These calculations predict that as lithium is removed from the crystal and the niobium to oxygen distance decreases, the crystal should transition from a direct to an indirect band structure [82]. Until now, there has been no experimental evidence in support of this band structure modification via intercalation/deintercalation.

4.2 Experimental Setup

Photoluminescence spectroscopy was performed on lithium niobite to confirm the predicted band structure features including a flat conduction band, a partially empty, degenerately doped, valence band caused by the removal of lithium, and a transition from a direct band-gap semiconductor to an indirect band-gap semiconductor.

Single crystals of lithium niobite were grown by liquid phase electro-epitaxy following the previously published method [95]. Free standing crystals were removed from the molten solution and mechanically polished with grit ranging from 9 μm to 60 nm. The resultant crystals were approximately 100 μm thick.

Photoluminescence was stimulated using a 325nm HeCd laser with output power of 18mW which was filtered, collimated, and focused onto the sample to an estimated 100-300 μm diameter spot size. The resultant photoluminescence was filtered with a 331 nm long-pass filter to remove the reflected laser light and prevent the formation of harmonics within the SPEX 1403 2 meter monochromator. The photoluminescence spectrum was measured using a Products for Research Inc. GaAs:Cs-0 11 stage PMT detector mounted on the spectrometer. The measurements were limited by the PMT spectral response and the laser line filter to a range from 350nm (3.54 eV) to 800nm (1.55 eV).

Samples were mounted to a Janis open cycle cryogenic stage using carbon tape. The tape was shown to have no photoluminescence at room temperature and negligible intensity luminescence at cryogenic temperatures. Temperature dependent measurements were taken from 78 K to 300 K. The sample was not exposed to the laser during transitions between temperatures.

Modification of the lithium content in lithium niobite was performed by deintercalation of lithium in either 37% HCl or 20% HCl diluted in deionized water following the methods previously published [88]. Previous work indicates that this method of deintercalation should not remove more than 30% of the lithium from the crystal [88]. Since the same sample was used for various deintercalation levels, experimental measurement of the lithium content after each deintercalation was not possible as lithium content is typically observed by destructive measurements such as ICP-AES or TOF-SIMS using standards for quantification that do not exist. Non-destructive surface measurements capable of detecting lithium, such as XPS, do not reveal any information about the bulk of the crystal and are complicated by an overlapping niobium signal.

4.3 Photoluminescence Spectroscopy

4.3.1 Room Temperature Photoluminescence

Room temperature photoluminescence of as-grown lithium niobite, shown in Figure 4-2, shows a single band of transitions around the expected band-gap of 2 eV indicating band-to-band transitions. While room temperature photoluminescence has been observed in several complex oxide materials such as perovskites [142], it is unusual to see photoluminescence in battery cathode materials which by design have large numbers of vacancy defects and highly mobile ions. The existence of strong room temperature photoluminescence in $LiNbO_2$ may be due to the unique heavy mass electron's inability to move to and interact with these defects.

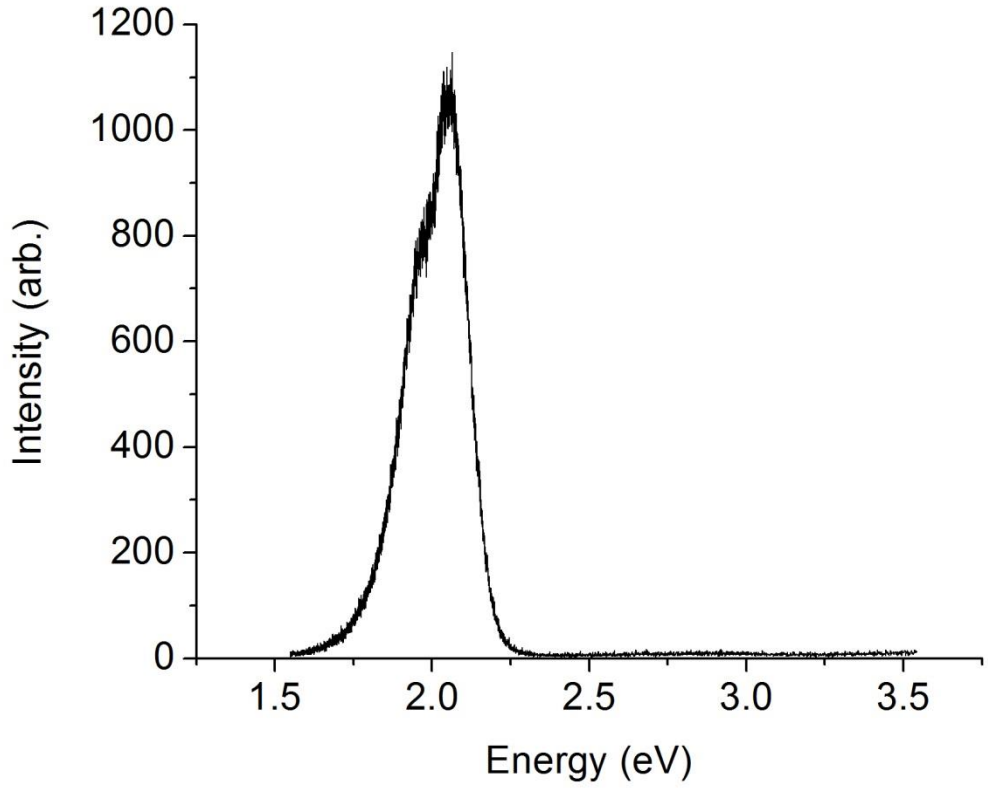

Figure 4-2: Room temperature photoluminescence of as grown lithium niobite showing a single band-to-band transition around 2eV.

Looking only over the energy range of this band, shown in Figure 4-3, this band of transitions can be fit with three Gaussian curves centered at 1.92 eV (Peak A), 1.95 eV (Peak B), and 2.06 eV (Peak C). The full width at half of the maximum intensity for this band of transitions is 218 meV, which is almost 8.5 times the expected thermal width for a band-to-band transition. This increased line width is consistent with near band gap transitions in other degenerately doped semiconductors [143] and with other fast ion conductor materials [144].

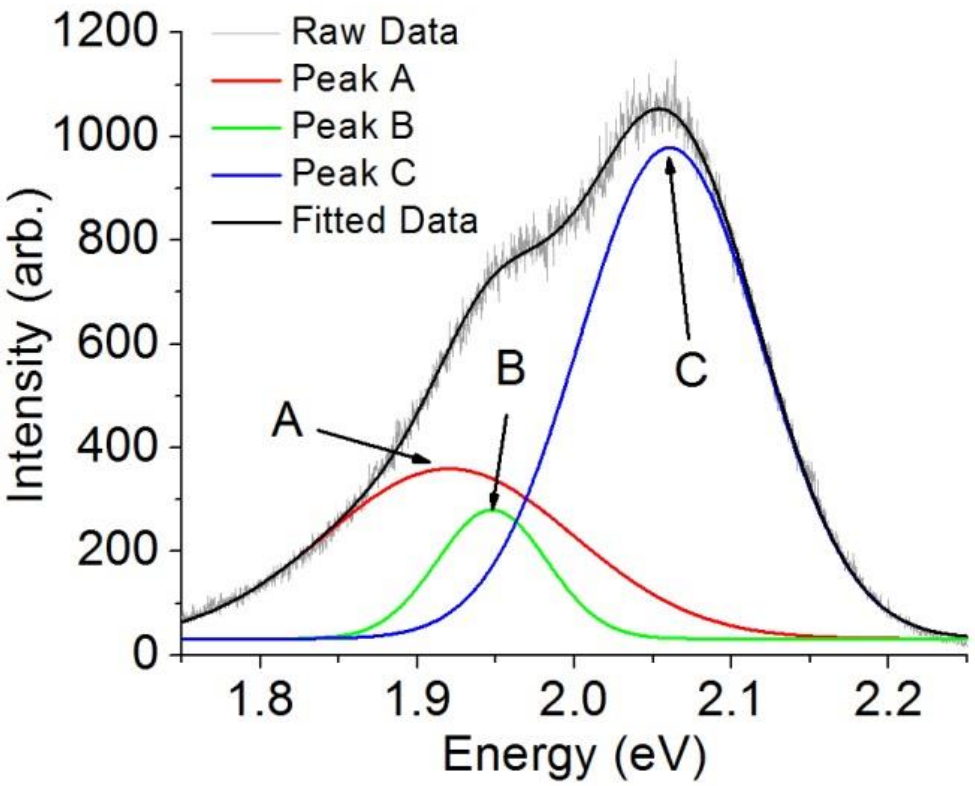

Figure 4-3: Room temperature photoluminescence of as grown lithium niobite fit to three Gaussian peaks showing a broad range of transitions consistent with a range of transitions from a flat conduction band to a partially empty valence band.

Examining the three fitted peaks in Figure 4-3 and the expected band structure in Figure 4-4, it is possible to assign transitions to the three fitted peaks. Peak A is a broad peak centered at the lowest energy, and is consistent with transitions from the bottom of the flat conduction band down to the partially empty valence band. Peak B is slightly higher in energy than peak A, but is narrower and has less intensity. Peak B is consistent with a transition from thermally excited electrons in the second nearly degenerate conduction sub-band down to the partially empty valence band. Peak C is consistent with transitions near the A point k-vector with a slightly wider energy gap and a predicted

higher density of valence states [82] resulting in a more intense emission. These three transitions are shown in Figure 4-4 as bands of transitions on the expected band structure.

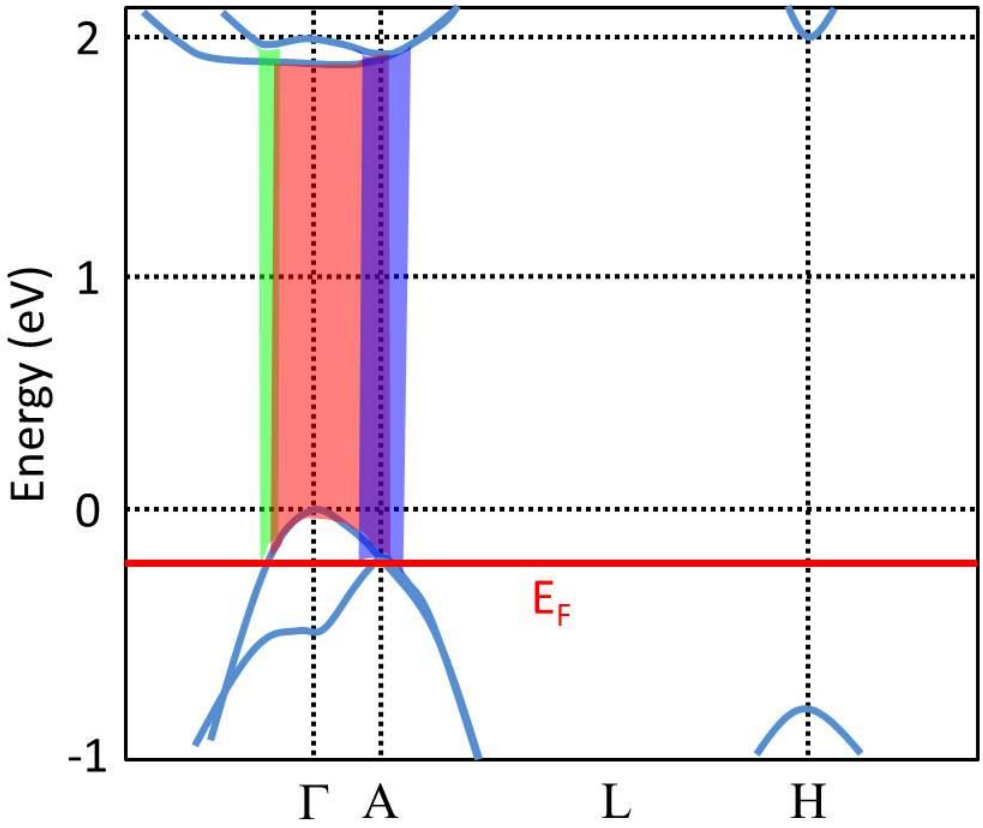

Figure 4-4: Relevant portions of the calculated band structures of lithium niobite reproduced from data in *Ylvisaker et al.*[4] The direct band structure of stoichiometric lithium niobite is shown with the three observed photoluminescence transitions from a flat conduction band to a degenerate valence band.

4.3.2 Temperature Dependent Photoluminescence

Temperature dependent photoluminescence spectroscopy was performed at temperatures ranging from 78 K to 300 K. As shown in Figure 4-5, the PL intensity increases significantly at lower temperatures consistent with a reduction in non-radiative recombination due to phonon scattering. In addition to temperature dependent changes in intensity, the primary peak energy and the distribution of emitted light also change with temperature.

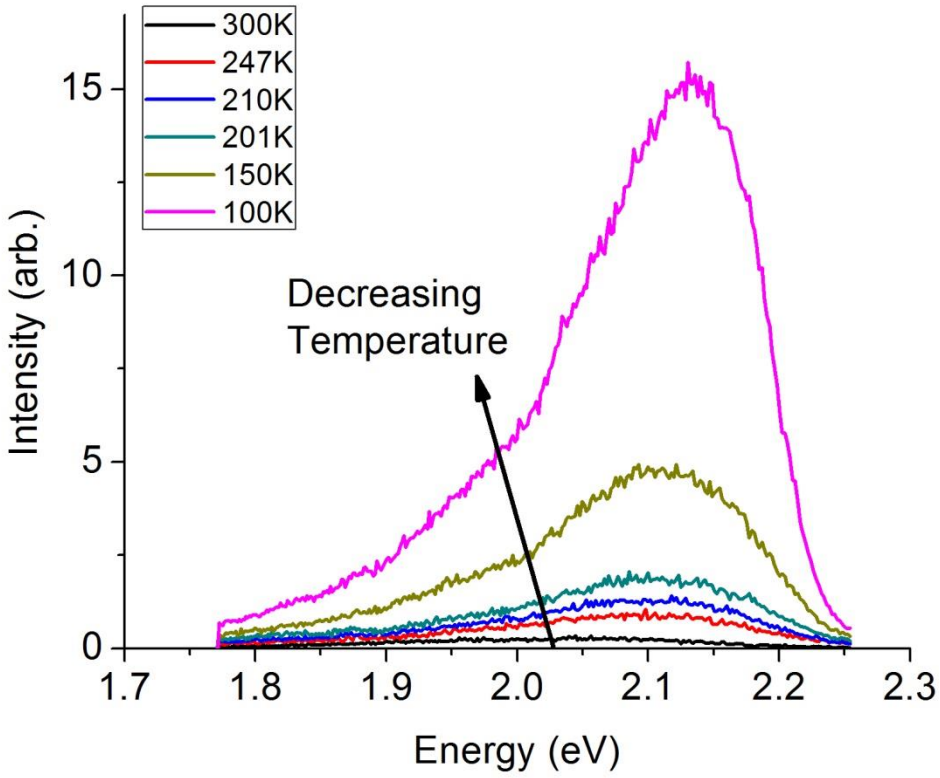

Figure 4-5: Temperature dependent photoluminescence of as grown lithium niobite showing the expected increase in intensity as temperature decreases.

Comparing the spectra at 78 K and 300 K, shown in Figure 4-6 with normalized intensity, the peak intensity shifts 108 meV to a higher energy at lower temperatures and the low energy shoulder is suppressed. The peak shifting to higher energy is consistent with a decrease in the lattice parameters at lower temperature causing a widening of the band gap. The low energy shoulder in the room temperature spectrum, fitted to peak B in Figure 4-3, is attributed to transitions from thermally excited electrons in the nearly degenerate sub-conduction band. The suppression of these transitions at low temperature supports this conclusion.

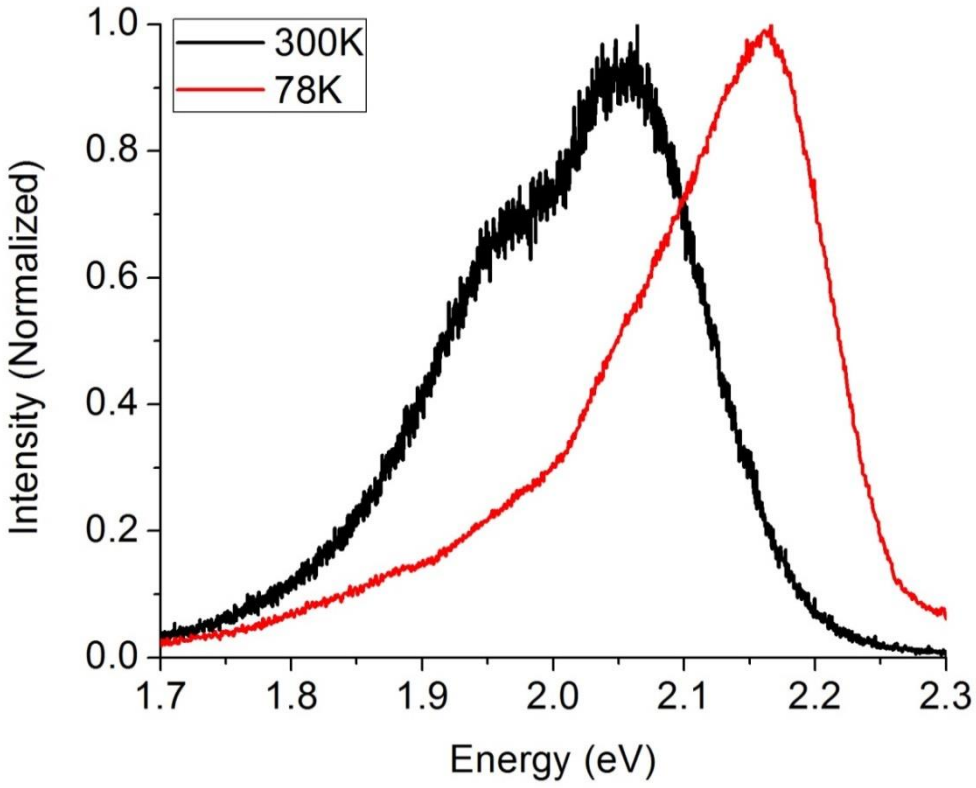

Figure 4-6: A comparison of the room temperature and cryogenic photoluminescence spectra for lithium niobite showing a shift in the luminescence intensity and a suppression of the low energy shoulder at low temperature.

Temperature dependent photoluminescence of band to band transitions can be fit to the temperature dependent band gap Equation 4.1 to find the band gap at 0 Kelvin $E_g(0)$, the crossover temperature β, and the linear temperature coefficient α [145].

$$E_g(T) = E_g(0) - \frac{\alpha T^2}{T+\beta} \qquad \text{Equation 4.1}$$

This equation has two regimes split around the crossover temperature β. At low temperature (T << β) the temperature dependence follows a quadratic form while at high temperature (T >> β) it follows a linear form.

For a non-degenerately doped semiconductor, the photoluminescence peak position could be fit to Equation 4.1. However, because the Fermi energy is inside the

valence band in this degenerately doped material, the transitions extend to states well past the valence band edge as shown in Figure 4-4. Due to this degeneracy, it is incorrect to use the energy at peak intensity from the photoluminescence spectra as the band gap energy. Instead, a lower energy should be chosen for fits to the temperature dependent band gap equation, shown in Equation 4.1. Two separate fits were made using the temperature dependent photoluminescence data at 10% and 50% the maximum intensity corresponding to the calculated [82] (1.9 eV) and experimentally observed [64] (2.0 eV) band gap. As will be shown, the results of the two fits show negligible differences in the α/β ratio indicating the band gap shifts are independent of the changes in shape of the photoluminescence spectra with temperature.

Fitting the measured data for lithium niobite to Equation 4.1 predicts a crossover temperature much larger than the measured temperature range ($\beta >> 300K$) suggesting that the data is best fit by the quadratic region of Equation 4.1. Simplifying Equation 4.1 to the quadratic form, shown in Equation 4.2, the data can be fit with a coefficient of determination $R^2 > 0.95$.

$$E_g(T) = E_g(0) - \frac{\alpha}{\beta}T^2 \qquad \text{Equation 4.2}$$

The zero kelvin band gap $E_g(0)$ for the 50% maximum intensity fit is determined to be 2.04 eV accurately matching data from absorption measurements previously published [64]. $E_g(0)$ for the 10% maximum intensity fit is 1.91 eV matching the calculated band gap [82]. The ratios α/β are respectively 1.63×10^{-6} and 1.32×10^{-6} for these two fits, consistent with other semiconductor materials such as 7.4×10^{-7} for silicon and 2.7×10^{-6} for GaAs [145].

The width of the photoluminescence spectra decreases as the temperature decreases at a rate of $4.1x10^{-4}$ eV/K. This is much larger than the Boltzmann constant ($8.6x10^{-5}$ eV/K) providing further evidence that the width of the photoluminescence spectra is not limited by thermal broadening.

4.3.3 Stoichiometric Dependence on Photoluminesence

As shown in Figure 4-7, lithium niobite samples with sub-stoichiometric lithium content, Li_xNbO_2, exhibited a 52 meV shift in the photoluminescence spectrum as well as additional higher energy transitions around 2.67 eV. The shift in the primary peak to higher energy is consistent with the addition of lithium vacancy dopants (acceptors) that lower the Fermi energy further into the valence band. Examining the calculated band structure, shown in Figure 4-4, the appearance of a higher energy transition is consistent with transitions to the local valence band maxima around the K and H k-vectors. According to the calculated band structure for various mole fractions of lithium, lowering the Fermi level to the local maxima at the K and H k-vectors requires the removal of approximately 20% of the lithium from the crystal4 which is easily attainable using HCl [88].

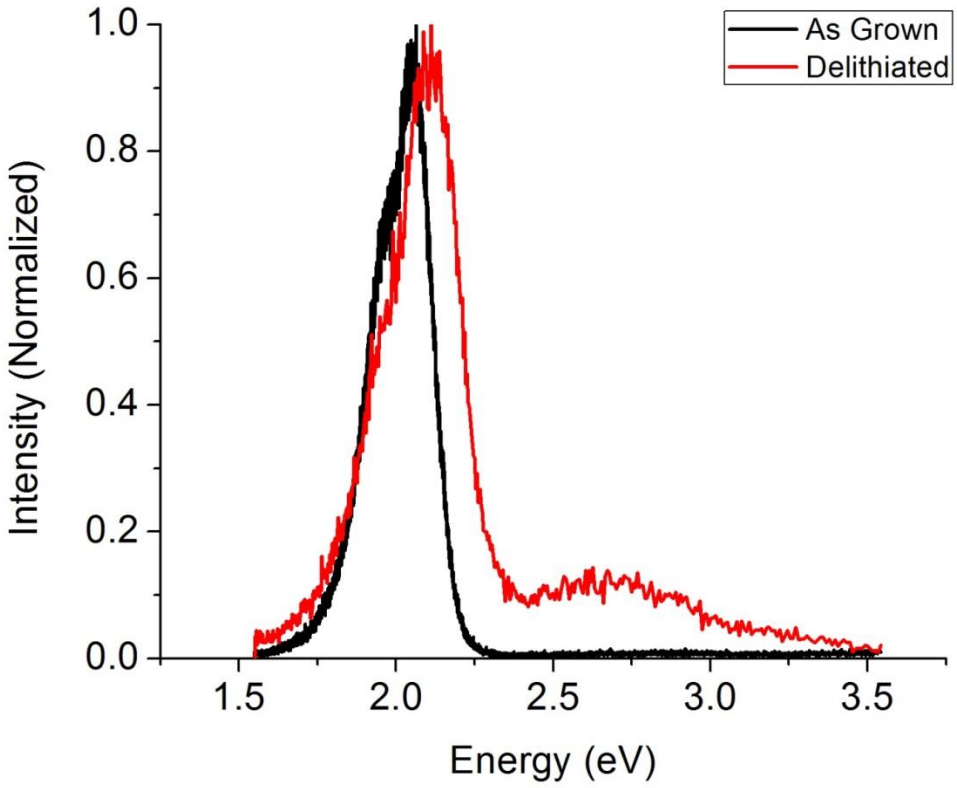

Figure 4-7: A comparison of lithium niobite photoluminescence as grown and with lithium chemically removed. The chemically treated sample exhibits a shift in the primary peak and additional higher energy transitions.

When the lithium niobite sample was deintercalated in 37% HCl for 72 hours it exhibited no observable photoluminescence as shown in Figure 4-8. This is consistent with but not conclusive proof of the predicted transition to an indirect band gap semiconductor with increased non-radiative recombination. Alternatively, this could be due to a dramatic loss of crystallinity or a different band structure modification resulting in higher mobility electrons in the conduction band that are then able to interact with defects through non-radiative recombination. However, no degredation of the material was observed in this work or in the cited deintercalation study for samples exposed to HCl [88].

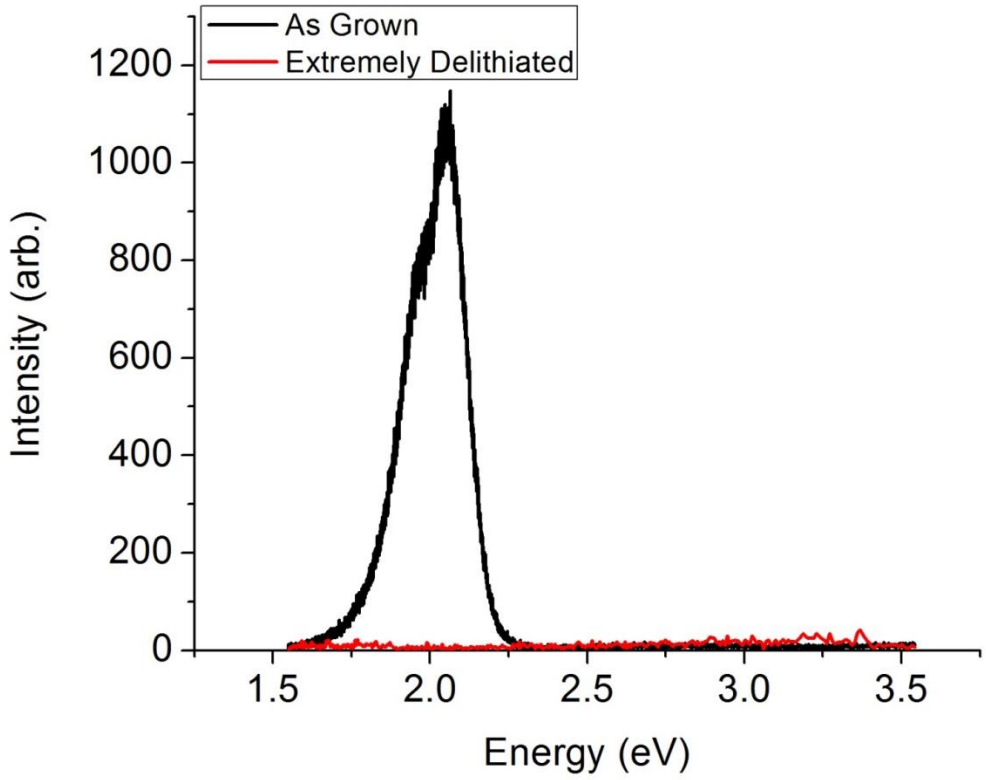

Figure 4-8: A comparison of lithium niobite photoluminescence as grown and with chemically treated with HCl 37% for 72 hours. The chemically treated sample exhibits no observable photoluminescence suggesting that the predicted transition from a direct to indirect band gap semiconductor when sufficient lithium is removed is correct.

4.4 Opto-Ionic Coupling

Initial photoluminescence measurements revealed unexpected spectral shifts between successive measurements mimicking the changes resulting from lithium deintercalation. Shown in Figure 4-9 are the photoluminescence spectra for an as grown sample, the as grown sample after prolonged (30 minute) exposure to the UV laser, and the sample after chemical removal of lithium. Both the optically saturated and chemically deintercalated spectra show a shift in the primary peak toward higher energy and the appearance of higher energy transitions. Given the similarity in the chemically

deintercalated and the optically saturated spectra, these results are consistent with the UV laser coupling to the highly mobile lithium ions and moving the ions out of the laser spot such that later measurements sampled a range of lithium concentrations. While the high energy tail of the chemically deintercalated and optically saturated spectra are nearly identical, the additional intensity observed in the optically saturated spectra, around 2.5 eV, is attributed to sampling a range of lithium concentrations in the optically saturated sample rather than a single concentration in the chemically treated sample.

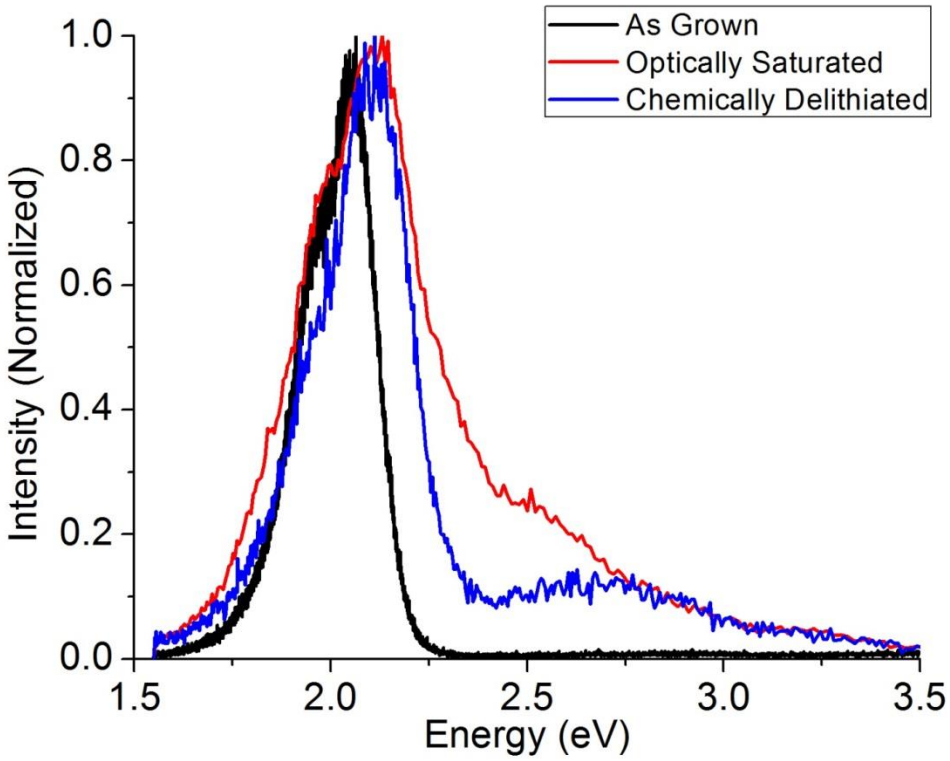

Figure 4-9: A comparison of lithium niobite photoluminescence as grown, optically saturated with the UV laser, and chemically treated. The optically saturated material exhibits several features similar to the chemically treated sample including a shift in the peak energy and additional higher energy transitions.

The enhanced movement of atoms by UV annealing is a well-known phenomenon [146]. Previous NMR work on lithium niobite has shown an activation energy for lithium

movement on the order of 100 meV and an average hopping time of 100 μs [75, 76]. It is therefore not surprising that electron-hole pairs recombining with multiple eV of energy can provide enough energy to move lithium away from the laser spot. As will be shown in the next section, this optical coupling is not thermal, but is instead some form of energy transfer from the electron-hole pairs to the lithium ions.

4.5 Optically Induced Resistance Changes

The electrical properties of lithium niobite were explored to determine how the optical ion coupling might be used as an ionic optical sensor. Shown in Figure 4-10 is the resistance of a 1 mm long by 3 mm wide lithium niobite resistor when exposed to a broad spectrum ELH solar lamp. The resistance of the device increases when exposed to light with a delay of a few seconds. While traditional photoconductivity as the result of optical generation of electron-hole pairs would decrease the device resistance, the observed increase in resistance is the opposite of the photoconductivity effect and thus is not due to simple electron-hole pair generation. Moreover, this change in resistance is also not a thermal effect because the resistivity of lithium niobite has been shown to decrease with increased temperature [90], a fact verified in this work by separate experiments using a thermal stage.

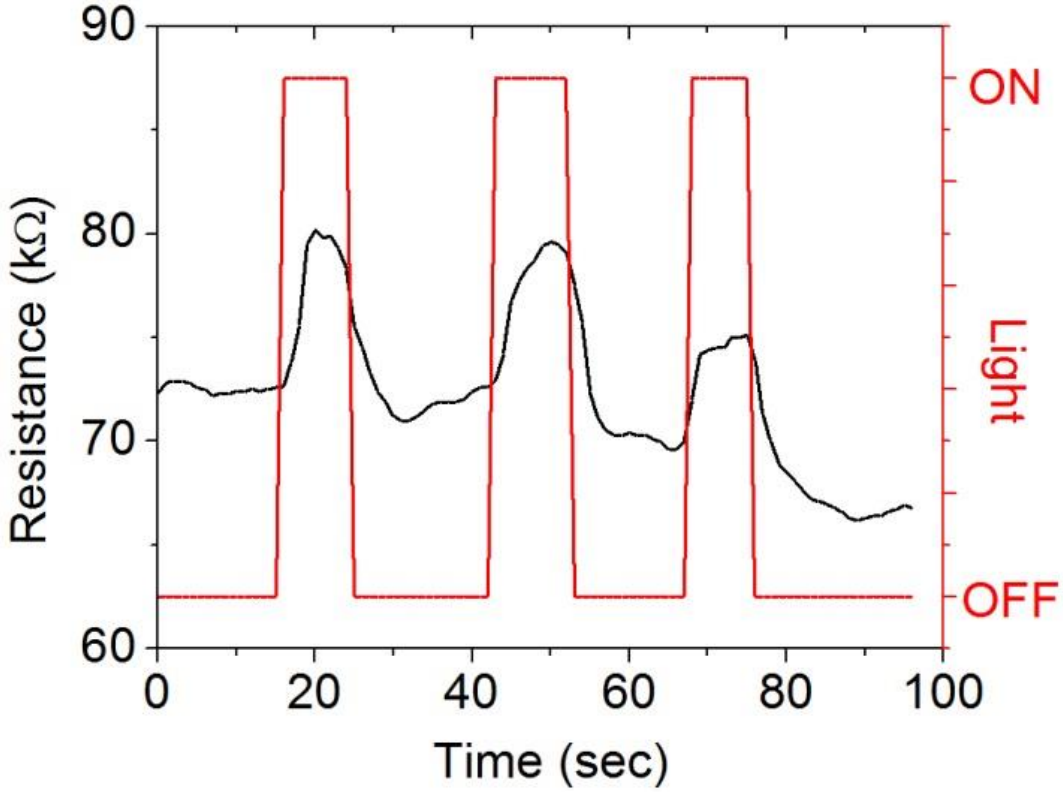

Figure 4-10: The resistance of a lithium niobite resistor when exposed to a broad spectrum solar lamp showing an increased resistance during exposure.

The previously discussed similarities between the optically saturated and chemically deintercalated photoluminescence spectra suggest that light is capable of moving the loosely bound lithium ions in lithium niobite. Previous impedance measurements demonstrate that lithium motion increases the impedance of the material [21] and device simulations predict that lithium accumulation also increases the impedance by reducing the density of acceptors [87]. The observation of increased resistance when exposed to light is consistent with these previous observations in that increased lithium motion in the exposed area will accumulate lithium near the contacts

increasing the impedance. Thus, this new light-matter interaction, photon induced ion motion, could be used as a biologically realistic artificial retina.

4.6 Summary of Photoluminescence in Lithium Niobite

Lithium niobite ($LiNbO_2$) exhibits photoluminescence despite a high vacancy density that would normally be associated with non-radiative recombination. The photoluminescence spectrum is attributed to a band to band transition from a flat conduction band to a partially empty valence band as predicted by theoretical calculations. Photoluminescence measurements made on samples exposed to dilute HCl, which is known to remove lithium from lithium niobite, confirm that lithium vacancies modulate the Fermi level within the valence band. Sufficient removal of lithium completely removes the photoluminescence intensity supporting prior assertions that lithium niobite does transition from a direct to indirect band gap semiconductor as lithium is removed.

In addition, optical coupling between a UV laser or a UV deficient solar lamp and the lithium ions locally depletes the lithium content resulting in photoluminescence spectra similar to the chemically deintercalated material. The band structure modifications and electrical changes induced by this optical coupling facilitate new opportunities in multi-functional sensor applications.

CHAPTER 5

LITHIUM NIOBITE MEMRISTORS

Lithium niobite memristors have been investigated for neuromorphic computing due to their memristive properties and their ionic physics, which is similar to the ionic physics encountered in biological neurons [74]. Two-terminal devices were fabricated by evaporating metal contacts onto sputter deposited lithium niobite films. Two device geometries were investigated as shown in Figure 5-1. The first geometry was an annular ring-dot pattern deposited onto a field of lithium niobite. The second geometry was a linear device in which the lithium niobite was deposited through a shadow mask to form an isolated line and the metal contacts were evaporated onto either end. The ring-dot geometry has previously been investigated for devices on both thin film MBE grown [21] and bulk LPEE growth lithium niobite [95].

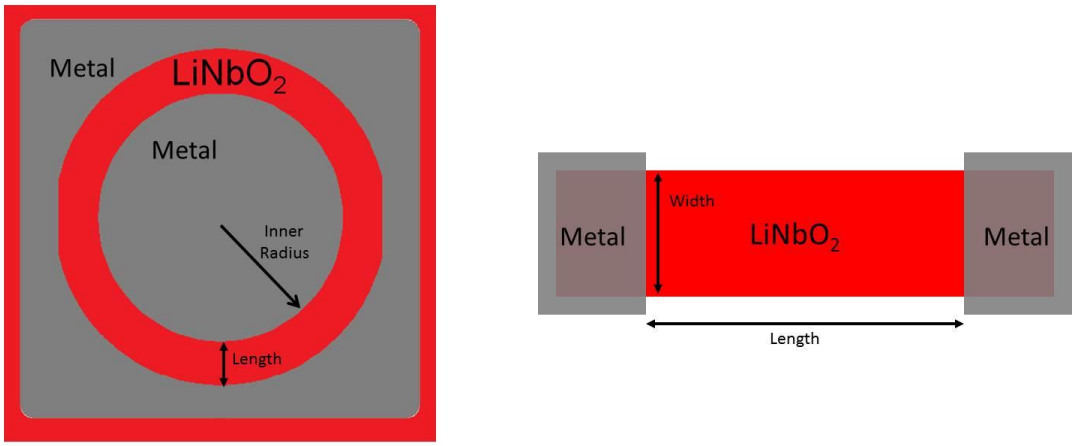

Figure 5-1: Two geometries for lithium niobite memristors. (Left) an annular ring-dot pattern studied in previous work. (Right) a linear structure with isolated lithium niobite preventing any lithium from diffusing away from the device.

The photolithography required to produce the ring-dot pattern proved difficult due to the tendency for sputtered lithium niobite to react with aqueous solutions. As discussed

in Chapter 2 and shown in Figure 2-20, Figure 2-21, and Figure 2-22 the sputter deposited material forms a layer of lithium oxide on top of the lithium niobite. This layer is water soluble and produces gaseous products when dissolved in aqueous solutions including the photoresist developer. Therefore, all films had to be pre-reacted with deionized water before photolithography could be attempted.

Fabricated devices were tested to compare their behavior to previous lithium niobite memristors and to test the effect of contact metal on device performance. Previous work focused on contacts that block lithium motion such as Ti, Ni, and Cu [99]. This arrangement keeps all of the lithium inside the lithium niobite and allows the material to relax back to an equilibrium condition when the external voltage is removed resulting in a volatile memristor. However, other contact metals, such as Al and Au, are known to absorb and alloy with lithium [99]. By storing lithium outside the lithium niobite, non-volatile memristors are explored.

5.1 Volatile Lithium Niobite Memristors

Previous volatile lithium niobite memristors have been characterized by current-voltage curves [95], voltage step transient response [21], and by small signal impedance spectroscopy [74]. Lithium niobite memristors with lithium blocking contacts were fabricated in the ring-dot geometry using 300 nm of titanium, a lithium blocking material, and 100 nm of gold as a probe layer.

As previously discussed in Chapter 2 and reproduced in Figure 5-2, two-terminal memristors made from sputter deposited lithium niobite exhibit the pinched hysteresis I-

V curve of a memristor. In addition, the I-V curve rotates over the first few measurements before converging to a repeatable hysteresis loop. This effect where the first few cycles would be different than the steady state solution was theorized for mixed ion-electron conductors when the ions are free to move.

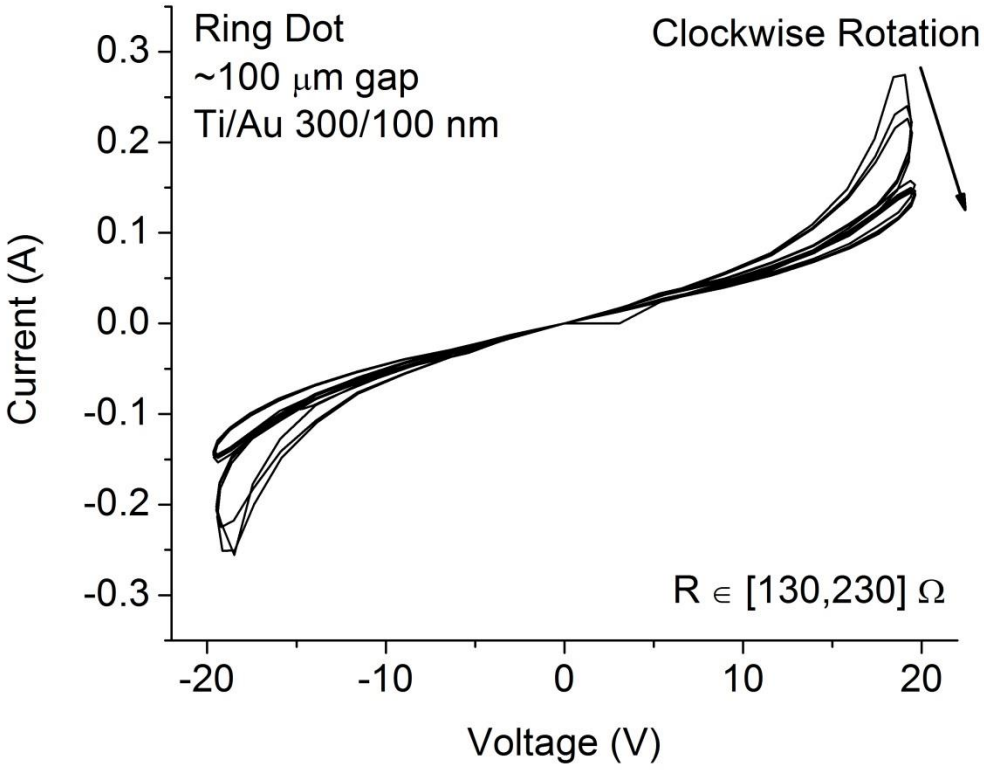

Figure 5-2: The current-voltage curve of a sputter deposited lithium niobite device exhibiting memristive hysteresis and rotation characteristic of a mixed ion-electron conductor.

Lithium niobite memristors were also tested with voltage steps in order to examine their transient response. The resistance was measured for voltage pulses at both ±1V and ±5V while the "minimally biased" device resistance was measured at 0.1V. As shown in Figure 5-3, the device resistance decreases for both positive and negative voltage pulses. Examining the time constant for the resistance to saturate after a voltage

step, the 1/e point is at 1.47 seconds. However, the transient response is not a pure exponential as the $1/e^2$ point is at 10.18 seconds almost seven times the 1/e time rather than twice the 1/e time. These transient features are in agreement with past p-type volatile lithium niobite memristors that showed a decreasing resistance under bias and a non-exponential resistance transient [21].

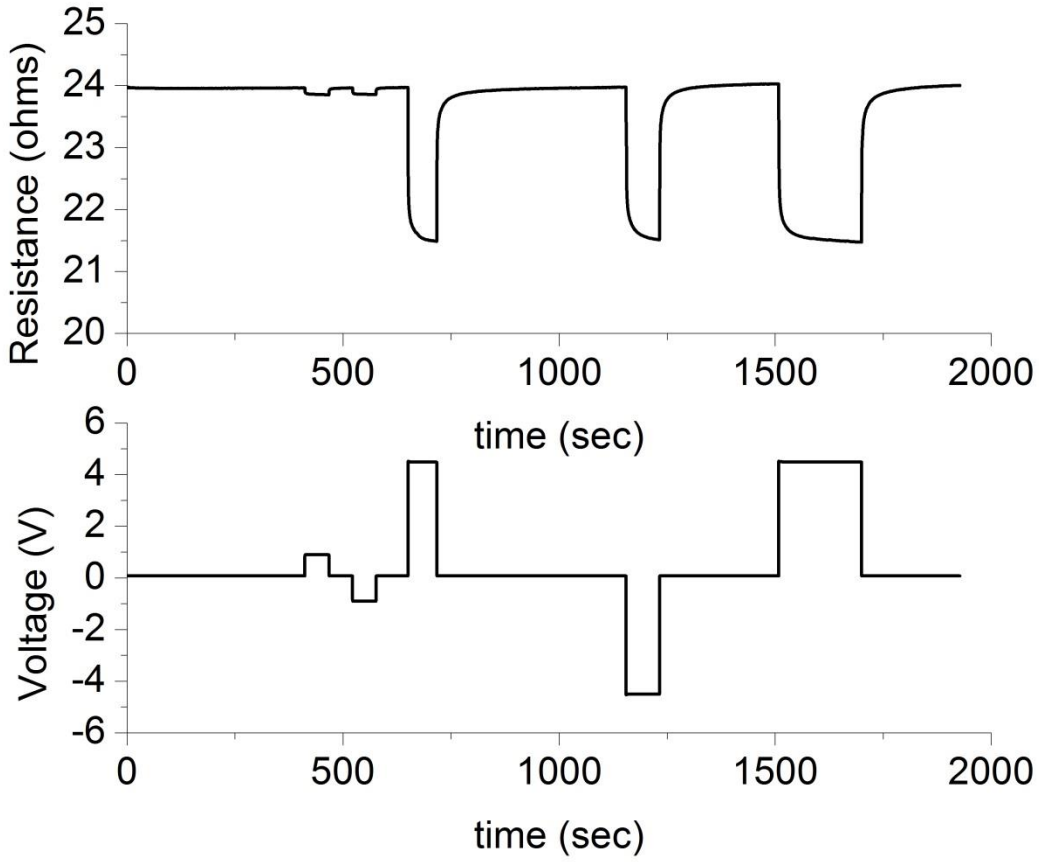

Figure 5-3: Resistance transients of a lithium niobite memristor with lithium blocking contacts causing a volatile device that relaxes back to the same resistance after each voltage pulse. The resistance transient during a voltage pulse has a non-exponential behavior.

Lastly, the volatile lithium niobite memristor's small signal response was measured under both unbiased and DC biased conditions. The small signal response was measured using a 10 mV signal and frequencies from 40 Hz to 10 MHz. As shown in Figure 5-4, the unbiased small signal response changes from a purely resistive load at low

frequencies to a mixed resistive-reactive load at high frequencies with a capacitive reactance. However, when the lithium niobite memristor was DC biased the low frequency impedance gained a positive reactance indicative of inductive behavior. These features are in agreement with past volatile lithium niobite memristors [74].

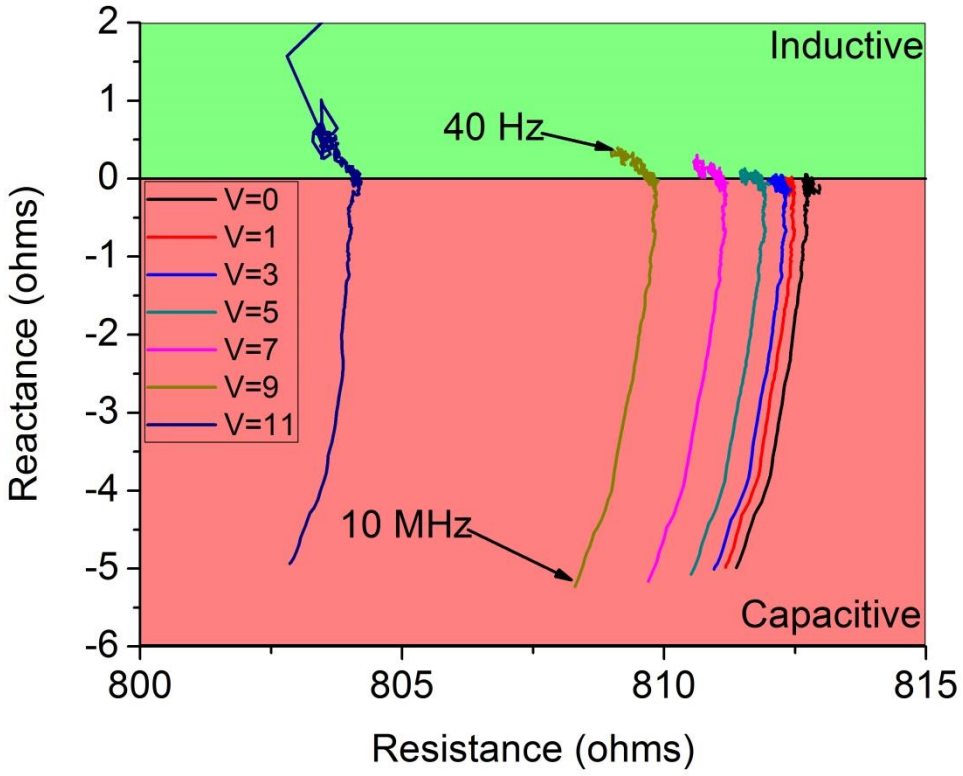

Figure 5-4: Small signal impedance of a sputter deposited lithium niobite memristor. With no DC bias the memristor is purely resistive at low frequencies and gains a capacitive reactance at high frequencies. Under DC bias the memristor gains a low frequency inductive reactance.

Examining the frequency response of the "inductive" behavior, shown in Figure 5-5, the reactance decays with frequency rather than increasing with frequency like a typical inductor (i.e. X = jwL). Therefore, the "inductive" reactance can be better approximated as a negative capacitance. The existence of low frequency positive

reactance has been previously observed in systems with stored energy such as batteries [147], electric double layers [148], and quantum well photodetectors [149]. It is therefore not unreasonable to find negative capacitance in lithium niobite memristors under bias when a lithium ion gradient is induced storing energy in the chemical gradient. In addition, an anomalous inductive behavior has been observed in biological neurons, which possess a bias due to an ion gradient [150]. It is possible that this anomalous inductance is actually an ionic negative capacitance as observed in $LiNbO_2$.

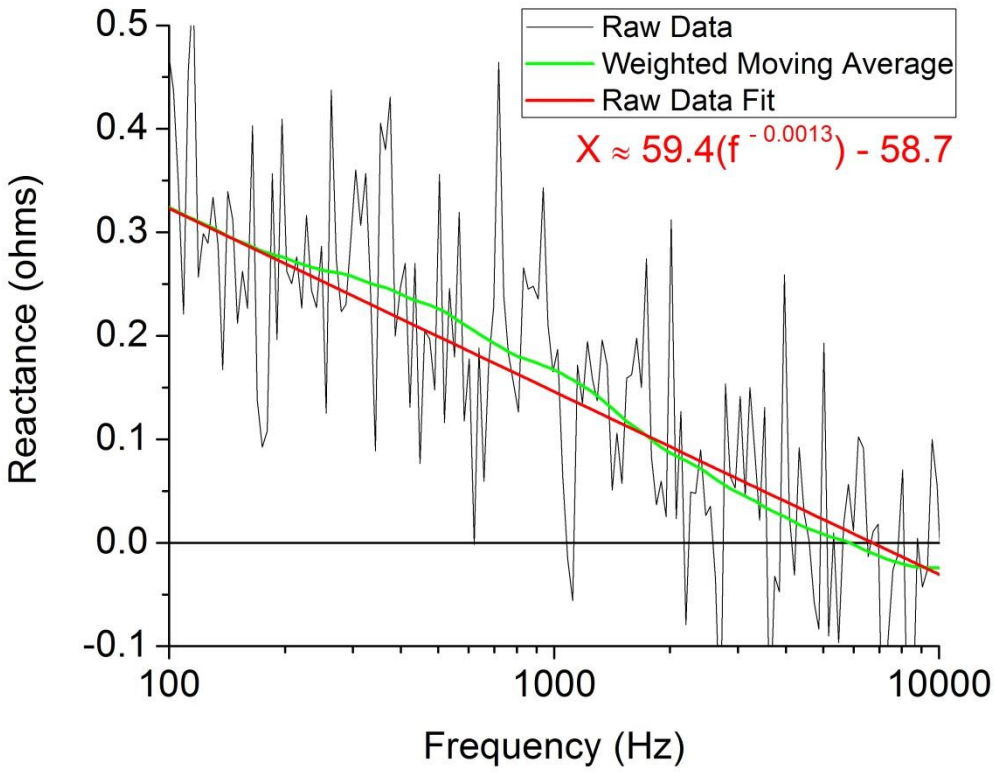

Figure 5-5: The low frequency inductive reactance observed in a lithium niobite memristor under bias. The reactance decreases with frequency rather than increasing as would be expected for an inductor (X = jωL). The positive reactance that decreases with frequency can be described by a negative capacitance.

It has been previously noted that capacitance originating from a diffusive physical phenomena obeys a reduced power law behavior of the form shown in Equation 5.1 [151].

$$C(w) \propto (j\omega)^{n-1}, n < 1 \qquad \text{Equation 5.1}$$

The positive reactance observed in lithium niobite memristors also obeys a reduced power law, as shown by the fit in Figure 5-5, further suggesting that the positive reactance may be caused by the lithium ion gradient under bias and the diffusion of the ions under low frequency conditions. However, for most diffusive phenomenon the fitting exponent is much less than 1 (n << 1), whereas the fitting exponent for lithium niobite is only slightly less than 1 (n = 0.9987).

5.2 Non-Volatile Lithium Niobite Memristors

Two terminal memristors were manufactured on sputter deposited lithium niobite in the line geometry with one lithium blocking contact composed of titanium-gold, similar to the volatile device contacts, and the other contact composed of lithium absorbing aluminum. The line geometry was utilized in order to confine the lithium to the device and eliminate any effects due to lithium diffusing into the device from the surrounding material. The device resistance was measured with an oscillating ±0.1V sense signal and the memristors were programmed using positive and negative pulses. As shown in Figure 5-6, when voltage pulses of alternating polarity were applied, the device resistance alternated between two resistance ranges. However, when successive pulses of the same polarity were applied, the device resistance incrementally decreased indicating that the resistance change is an analog process rather than a discrete state change.

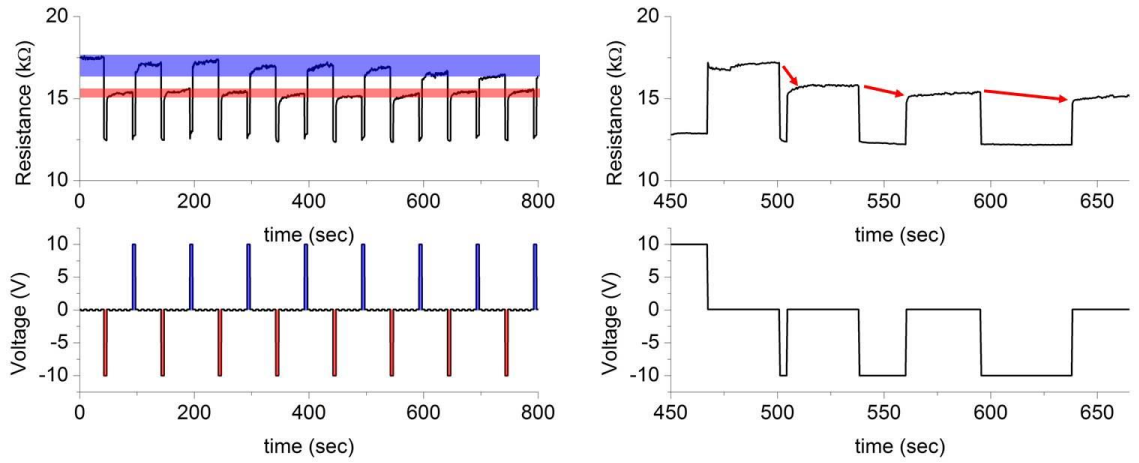

Figure 5-6: Resistance transients of a lithium niobite memristor with one lithium absorbing aluminum contact. The ability to absorb lithium out of the lithium niobite creates non-volatile resistance changes that are both analog and reversible.

In order to verify that the lithium absorbing aluminum contact is responsible for the programmable resistance, an identical device was made with two lithium blocking titanium contacts. As shown in Figure 5-7, the device with two lithium blocking contacts did not possess multiple resistance states and tended to relax back toward the same resistance value during the sense signal.

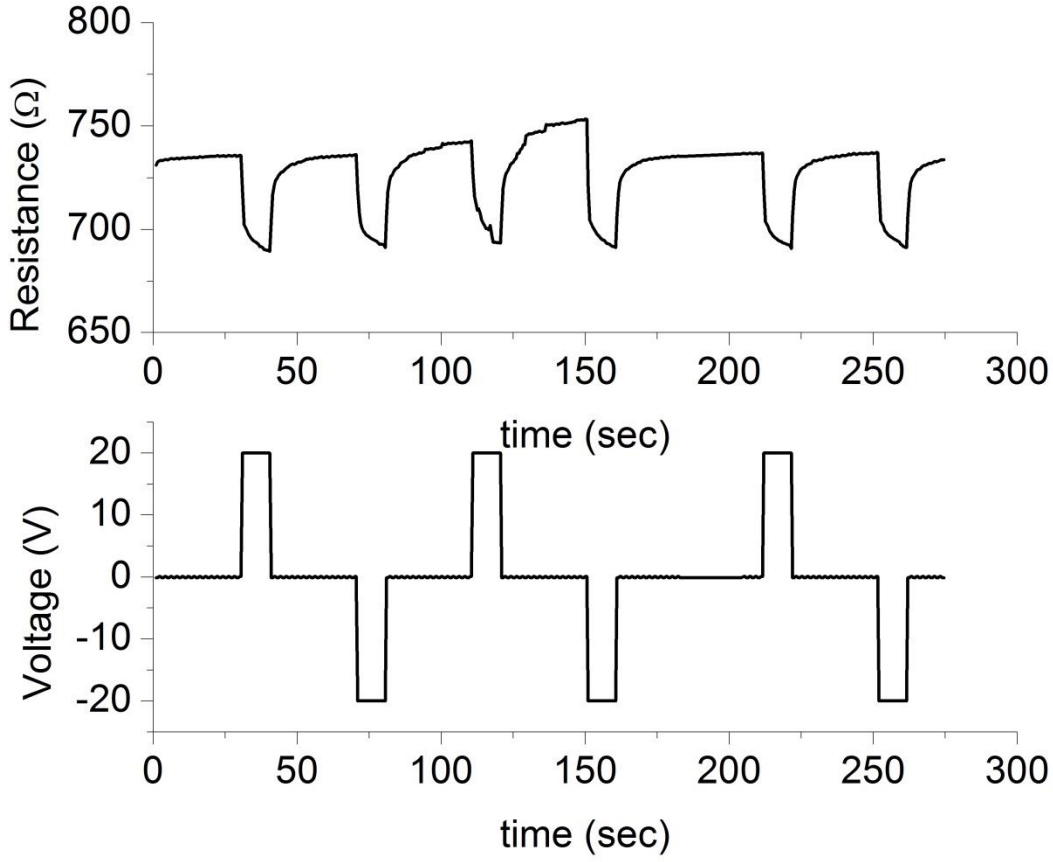

Figure 5-7: Resistance transients of a lithium niobite memristor identical to the device measured in Figure 5-6 except that the lithium absorbing aluminum contact was replaced with a lithium blocking contact. The single contact change both eliminates the non-volatile resistance changes and lowers the resistance by a factor of 20.

Examining the non-volatile device data in Figure 5-6, positive polarity pulses cause the resistance to increase while negative polarity pulse cause the resistance to decrease. However, positive polarity pulses should drive lithium into the aluminum electrode, decreasing the amount of lithium in the lithium niobite, and decreasing the device resistance. Therefore, while the lithium absorbing aluminum contacts do induce non-volatile behavior, the resistance change is not likely due to changes in the lithium content of the lithium niobite layer.

Further, the non-volatile device measured in Figure 5-6 and the volatile device measured in Figure 5-7 were identical except for their contacts. By exchanging a titanium contact for an aluminum contact the total device resistance was increased by a factor of 20. It order to examine the effects of lithium absorbing aluminum contacts while minimizing any changes to the lithium content of the lithium niobite layer, device were fabricated on > 100 um thick bulk grown lithium niobite. A volatile device was fabricated using lithium blocking copper contacts. As shown in Figure 5-8, this device exhibits memristive hysteresis with the device resistance between 8 – 18 Ω. A non-volatile device was fabricated with one lithium blocking titanium contact and one lithium absorbing aluminum contact. As shown in Figure 5-8, the non-volatile device is significantly more resistive than the volatile device. In addition, the non-volatile device still exhibits a programmable resistance where positive voltage pulses increase the device resistance and negative voltage pulses decrease the device resistance. For this device on bulk lithium niobite, any lithium absorbed into the contacts (≈300 nm thick) should have a minimal effect on the lithium content of the bulk lithium niobite (≈100 um thick).

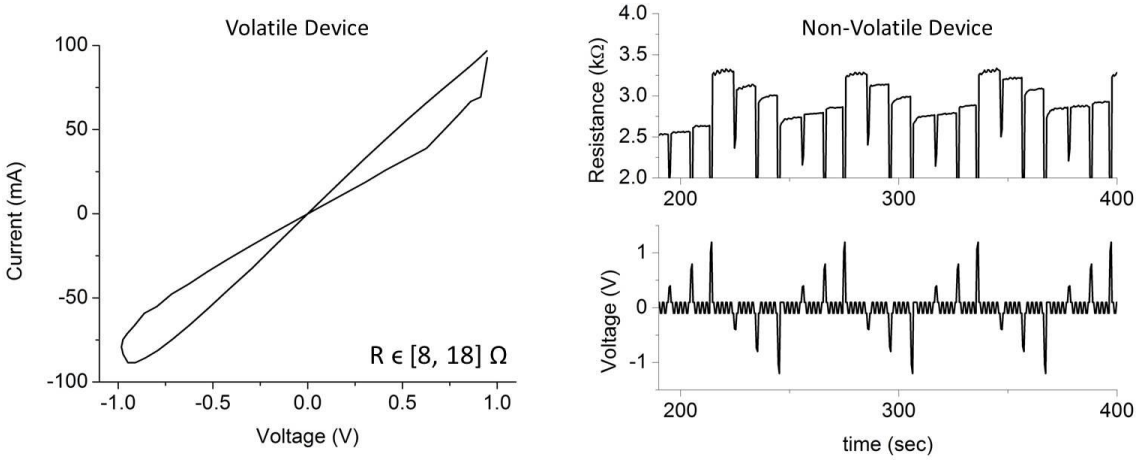

Figure 5-8: (Left) Current-voltage curve from a volatile memristor fabricated on bulk lithium niobite with a resistance range of 8 – 18 ohms. (Right) Resistance transients from a non-volatile memristor fabricated on bulk lithium niobite with a resistance range of 2.5 – 3.3 kohms.

By plotting the non-volatile device's resistance change as a function of pulse voltage, shown in Figure 5-9, it is apparent that the resistance change is non-linear with pulse voltage where the resistance change is larger at high voltages than would be expected from a linear extrapolation. This non-linear programming creates opportunities for non-volatile lithium niobite memristors to replicate the learning functionality of biological synapses in a neuromorphic circuit.

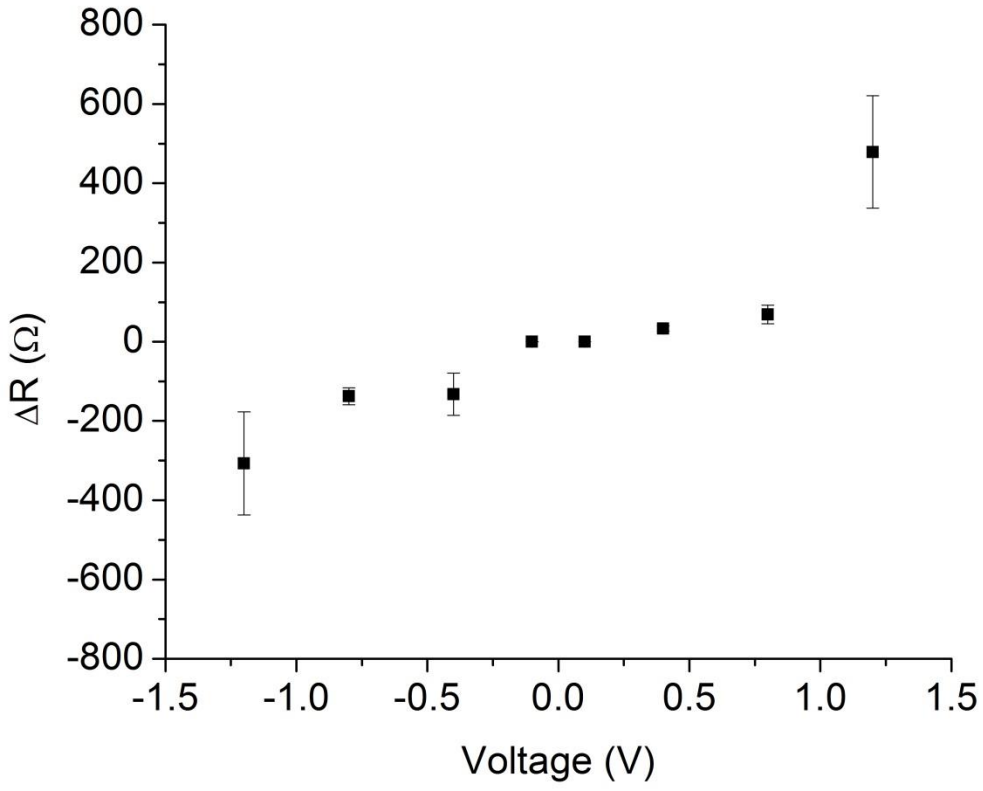

Figure 5-9: The change in resistance of a non-volatile lithium niobite memristor as a function of applied voltage pulse.

One form of learning within biological neurons is a process called spike timing dependent plasticity (STDP). In STDP, the strength of a synaptic connection is changed

based on the relative timing of the pre-synaptic action potential and the post-synaptic action potential as shown in Figure 5-10. If the pre-synaptic action potential arrives at the synapse immediately prior to the post-synaptic action potential, then activity at that synapse is a good predictor of the post-syanptic neuron's activity and the synaptic connection is strengthened. If the pre-synaptic action potential arrives at the synapse immediately after the post-synaptic action potential, then activity at that synapse is a poor predictor of the post-syanptic neuron's activity and the synaptic connection is weakened.

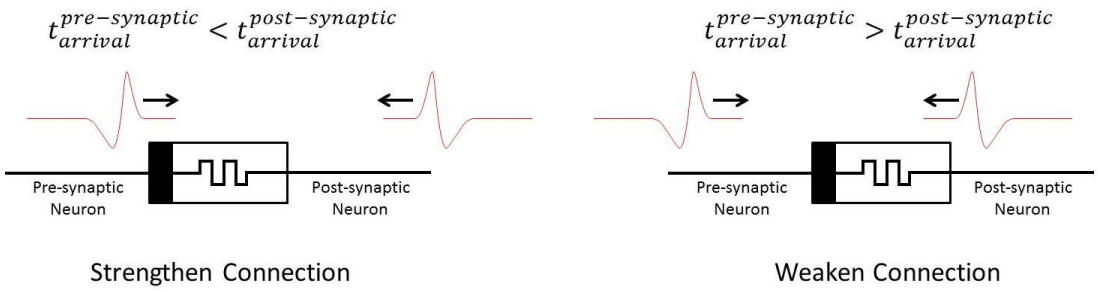

Figure 5-10: Description of spike-timing dependent plasticity (STDP) in which the relative timing of action potentials arriving at a synapse determines the change in synaptic conduction.

In memristive neuromorphic circuitry, STDP has been implemented by noting that action potentials contain both positive and negative voltages as shown in Figure 5-11. Therefore, if two action potentials arrive at a memristor from opposite sides, the voltage across the memristor will be a function of their relative arrival times.

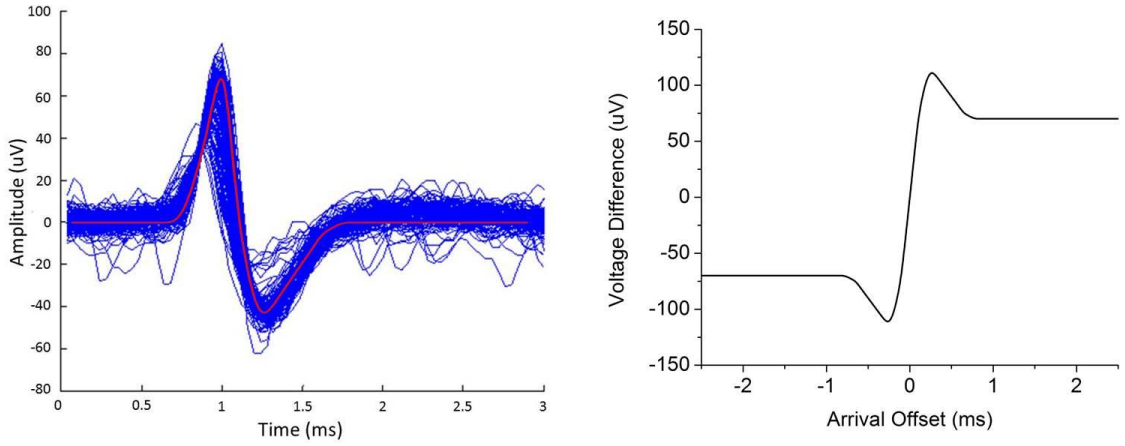

Figure 5-11: (Left) Typical action potentials recorded from biological neurons. (Right) The magnitude of the resultant voltage pulse when two action potentials arrive at a biological synapse at times offset from one another.

The non-linear resistance changes observed in the non-volatile lithium niobite memristor, shown in Figure 5-9, can be roughly fit to a cubic function as shown in Figure 5-12a. By combining the expected voltage difference across the memristor as a function of action potential arrival times and the resistance change as a function of pulse voltage, the resistance change as a function of action potential arrival time can be calculated. The calculated response of a non-volatile lithium niobite synapse, shown in Figure 5-12b, exhibits STDP where a small positive arrival time offset significantly increases the resistance while a small negative arrival time offset significantly decreases the resistance. If the arrival time offset is large in either direction, then only small changes are made to the memristor resistance.

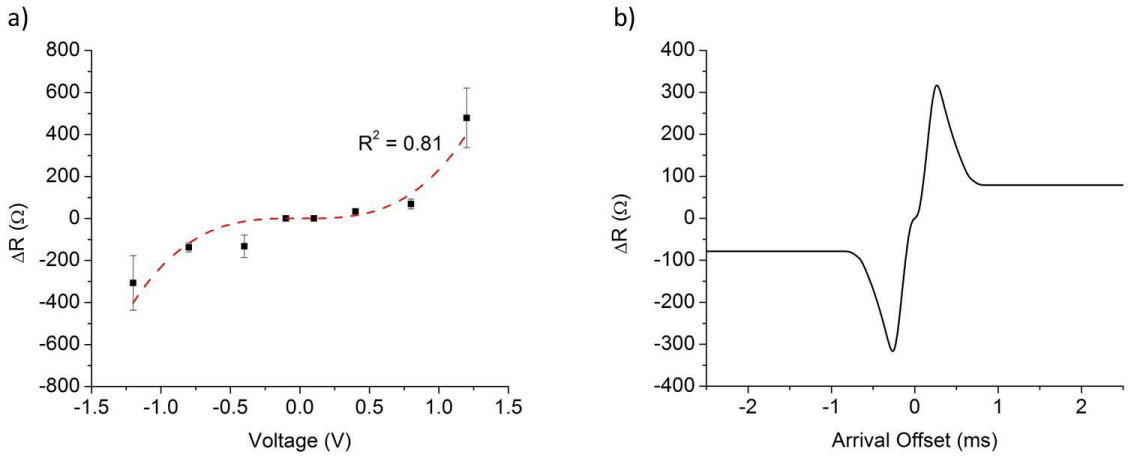

Figure 5-12: (Left) Cubic fit to the resistance change data shown in Figure 5-9. (Right) The calculated resistance change as a function of action potential offset timing displaying the characteristic behavior of STDP.

In summary, both volatile and non-volatile memristors have been fabricated on sputter deposited thin film $LiNbO_2$ as well as on bulk grown $LiNbO_2$. These devices exhibit memristive hysteresis useful for replicating the biological functionality of synapses, dendrites, and axons in neuromorphic circuit applications. Lithium niobite memristors also exhibit the low frequency inductive behavior observed in biological neurons [150]. The programming of non-volatile lithium niobite memristors exhibits non-linear behavior mimicking the STDP learning behavior in biological synapses.

CHAPTER 6

THIN FILM LITHIUM NIOBITE BATTERIES

In addition to two terminal lithium niobite memristors, useful for replicating biological functionality in the synapses, dendrites, and axon, lithium niobite based batteries are potentially applicable to neuromorphic computing in order to replicate the ionic integration that occurs in the soma in which ion transport across an insulating layer creates a chemical potential. Likewise, ion transport across a battery's insulating electrolyte creates a chemical potential that can drive a neuromorphic circuit. For application as a neuromorphic soma, a thin film battery must be able to cycle repeatedly and have low resistive losses.

6.1 Background and Theory

The first application explored for lithium niobite was as a battery cathode using powdered material [90, 94]. Lithium niobite shares the layered structure of other battery cathode materials that enables the intercalation and deintercalation of lithium ions. Early lithium niobite batteries used powdered material for the lithium niobite cathode, a liquid electrolyte, and lithium metal anodes. This early work reported open circuit voltages between 2.4 – 2.8 V vs a reference Li anode [90, 94].

One potential advantage of lithium niobite compared to the more common battery cathode material $LiCoO_2$ is a significantly lower resistance. $LiCoO_2$ is an insulating oxide with a room temperature resistivity of approximately 10^{11} Ω-cm [100]. In contrast, lithium niobite is a metallic oxide with a room temperature resistivity of approximately 10^{-5} Ω-cm [88]. This 16 order of magnitude difference in resistivity creates electrical

losses in $LiCoO_2$ as electrons need to travel through the cathode to neutralize the intercalated lithium ions. Bulk $LiCoO_2$ batteries overcome this limitation by mixing the $LiCoO_2$ powder with conductive carbon, a procedure not easily accomplished in thin film batteries. The inclusion of carbon in the battery lowers the active volume density of the cathode reducing both the theoretical and practically achieved capacity.

While lithium niobite is more conductive than $LiCoO_2$, it has a lower open-circuit voltage (V_{LiNbO2} = 2.4 – 2.8 V, V_{LiCoO2} = 3 – 4.2 V) and a lower theoretical fully dense charge capacity (C_{LiNbO2} = 200 mAh/g, C_{LiCoO2} = 272 mAh/g) [152] than $LiCoO_2$. Due to the need for graphite additives to achieve conduction and the inability to use the entire volume in a thin film, the practically achievable bulk $LiCoO_2$/graphite and thin film $LiCoO_2$ capacities are approximately 160 mAh/g [153] and 80 mAh/g [154] respectively. The theoretical charge capacity C_{LiNbO2} can be calculated by Equation 6.1.

$$C = \frac{q*\#_{Li}}{3.6*V*\rho} \qquad \text{Equation 6.1}$$

$$C_{LiNbO2} = \frac{2Li}{u.c.}\ \frac{u.c.}{77.5\ A^3}\ \frac{10^{24}A^3}{cm^3}\ \frac{cm^3}{5.739\ g}\ \frac{1.602x10^{-19}\ C}{Li}\ \frac{mAh}{3.6\ C} = 200\,\frac{mAh}{g}$$

where q is the charge of an electron, $\#_{Li}$ is the number of lithium atoms per unit cell, V is the volume of the unit cell, and ρ is the material's density. While a lower voltage and charge capacity does reduce the energy density of the battery, impeding its use as a primary power source, a high energy density is not required for neuromorphic applications where the battery will be cycled through only a small fraction of its potential capacity. As shown in Figure 6-1, the region over which ionic integration occurs is much smaller than the voltage plateau where the battery accumulates charge.

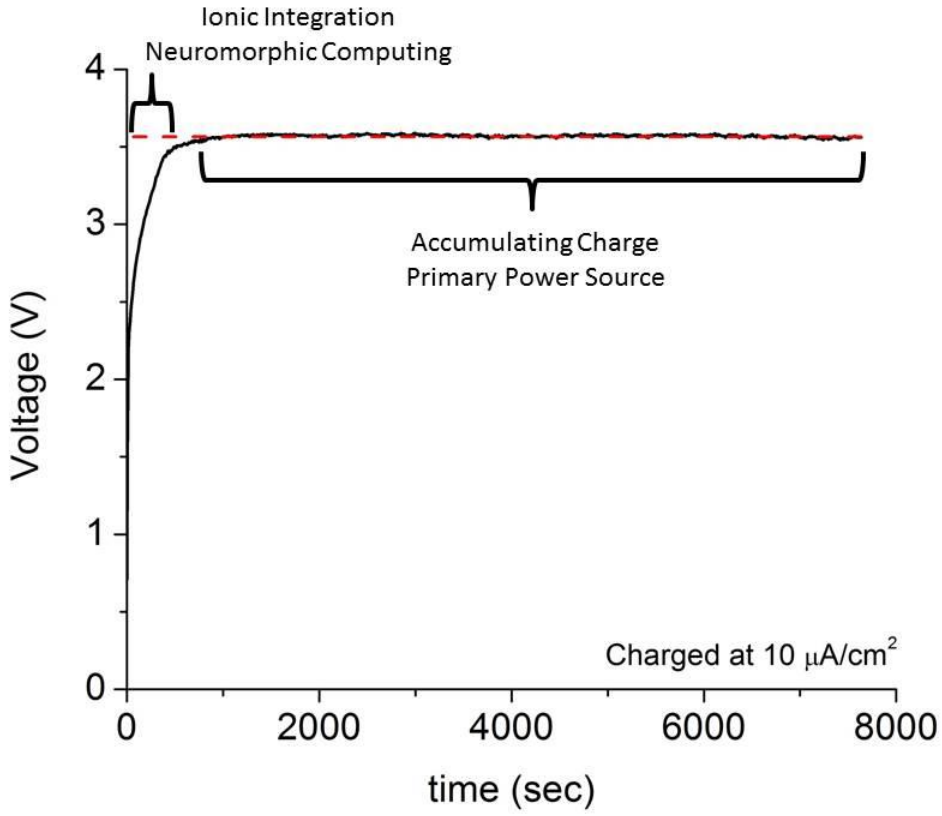

Figure 6-1: Open-circuit voltage of a thin film lithium niobite battery from this work during charging. The voltage increases during the first portion of the charge cycle before stabilizing. Ionic integration useful for neuromorhic computing only occurs during a small percentage of the total charge cycle.

6.2 Battery Fabrication

No thin film lithium niobite battery has ever been reported. Therefore, fabrication was guided by prior efforts on thin film $LiCoO_2$ batteries [154-156]. These thin film batteries each consisted of four layers: 1) a metallic current collector, 2) a sputter deposited $LiCoO_2$ cathode, 3) a sputter deposited LiPON electrolyte, and 4) a metallic anode. Several different metallic anodes have been attempted. Evaporated lithium metal has been used as an anode [155], but metallic lithium is very reactive and generally avoided due to safety concerns [157]. Aluminum has been used as an anode material due

to its ability to intercalate lithium [156]. Aluminum has a theoretical capacity between 993 mAh/g for LiAl and 2234 mAh/g for Al_4Li_9 [129] which is 2 – 6 times the capacity of graphitic carbon used in bulk lithium ion batteries [131]. Finally, nickel has been used as a lithium blocking anode where lithium metal is electroplated under the nickel after the battery has been formed [154].

Lithium niobite batteries were fabricated using these same procedures as shown in Figure 6-2. A titanium/nickel current collecting layer was evaporated onto a sapphire substrate. The lithium niobite cathode was then sputter deposited through a shadow mask to define the battery area. The LiPON electrolyte was sputter deposited onto the lithium niobite cathode. A larger area shadow mask was used to define the LiPON area in order to ensure no edge effects would short the thin film batteries. Lastly, a metallic anode was evaporated onto the LiPON through a shadow mask with the same dimensions as the original lithium niobite deposition. Both lithium absorbing aluminum and lithium blocking nickel anodes were investigated.

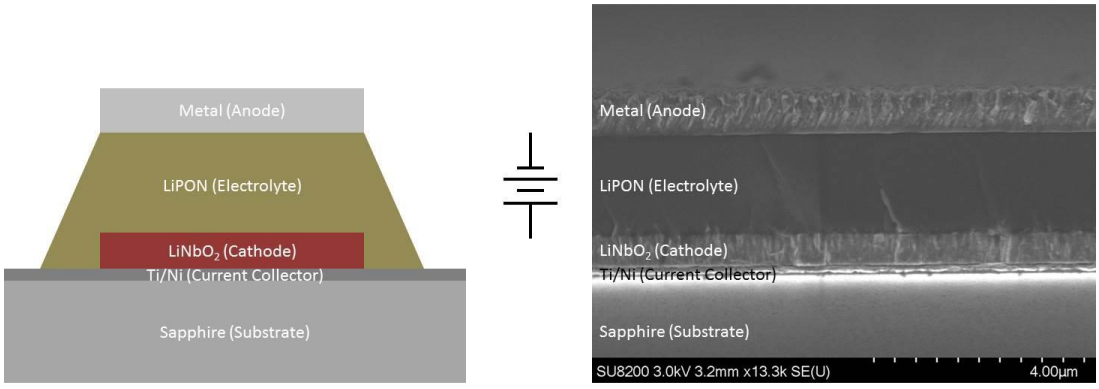

Figure 6-2: (Left) Schematic Structure of the fabricated thin film lithium niobite batteries. (Right) Cross-sectional SEM showing the five layers of the thin film battery.

6.3 Experimental Results

6.3.1 Electrical Performance

Thin film lithium niobite batteries with lithium blocking nickel anodes were capable of cycling repeatedly. As shown in Figure 6-3, the cell could be charged to a voltage of 3 V and discharged. The discharge plateau was measured between 1.5 – 2.5 V, substantially lower than the open circuit voltages for bulk lithium niobite batteries using metallic lithium anodes, V_{OC} = 2.4 – 2.8 V. Since the chemical potential of nickel (-0.25 vs. standard hydrogen electrode (SHE)) is less negative than the chemical potential of lithium (-3.05 vs. SHE), the lower cell voltages may be due to a combined nickel/lithium anode.

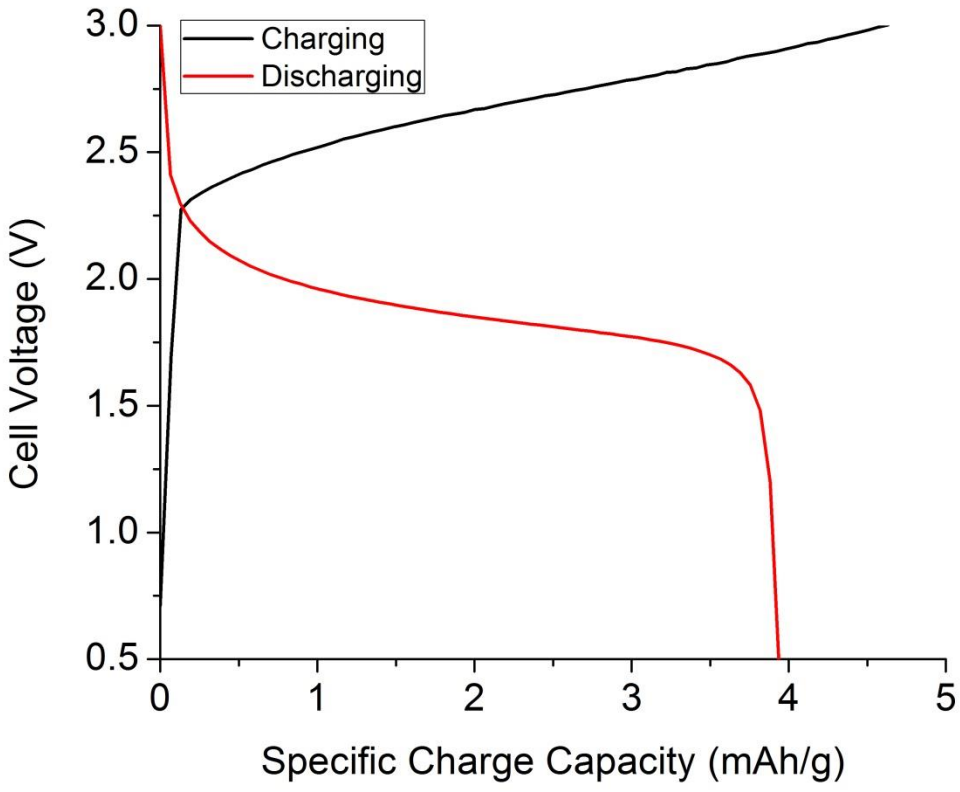

Figure 6-3: Measured open-circuit voltages of a nickel anode battery during a charge and discharge cycle. The charge cycle does not contain a voltage plateau as the battery is being operated within the ionic integration regime of Figure 6-1. During discharge the battery has an operation voltage between 1.5-2.5 V.

The nickel anode battery was cycled 100 times in order to determine its long term stability. As shown in Figure 6-4, the discharge capacity decreased over the first few cycles before stabilizing at 1.3 mAh/g, approximately 35% of the first cycle capacity. This is similar to thin film batteries made with $LiCoO_2$ that show a stable capacity between 20 – 30% of their first cycle capacity [154]. The observed capacity fade in thin film batteries is likely due to irreversible reactions during the first few cycles that condition the battery anode.

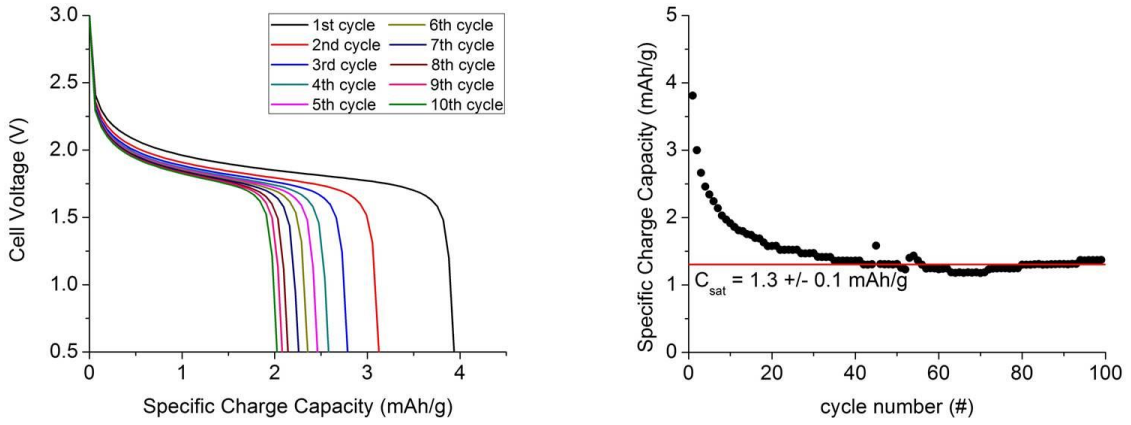

Figure 6-4: (Left) Open-circuit voltages during the first ten discharge cycles showing a decreasing capacity but a stable operating voltage. (Right) The battery's specific capacity over the first 100 cycles stabilizes at 1.3 mAh/g.

Attempts to make a thin film battery using lithium absorbing aluminum anodes were unsuccessful. As shown in Figure 6-5, the battery initially charged starting at a cell voltage of approximately 1.5 V and increasing toward 3 V. However, for cell voltages above 2 V, the cell resistance increased with stored charge requiring a higher over-potential to maintain the 10 $\mu A/cm^2$ charging current density. After storing approximately 60 mAh/g, ~30% of the theoretical capacity, the cell failed and no longer

supported a voltage. The increase in cell resistance could have been caused by two effects. First, as observed in Chapter 5 intercalating lithium into an aluminum contact significantly increased the device resistance of a two terminal memristor and could have increased the resistance of the aluminum anode battery. Alternatively, as shown in Figure 6-5, the aluminum anode delaminated effectively reducing the battery area. This delamination is likely due to stress from the volumetric expansion of aluminum which doubles in volume when intercalated with lithium [129].

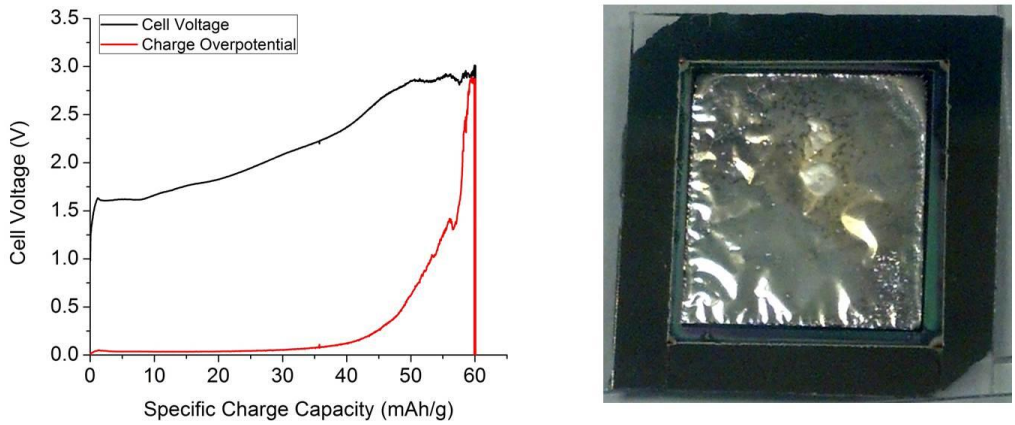

Figure 6-5: (Left) Open-cell voltage of a thin film lithium niobite battery with a lithium absorbing aluminum anode. During charging the cell overpotential necessary to drive a constant current (i.e. the cell resistance) increases dramatically. (Right) The aluminum anode battery after charging showing the anode has delaminated from the underlying battery structure.

One objective of using lithium niobite as the battery cathode is to reduce the cell resistance and enable fast charge-discharge batteries. In general, charge transport within a battery is determined by the ionic and electronic conductivities of the anode, cathode, electrolyte, and interfaces each of which can be further divided into conduction mechanisms such as drift, diffusion, trap assisted conductivity, percolation conductivity, etc. [158]. In a simplified model, as shown in Figure 6-6, there are five charge transport processes that contribute to the resistance of a battery.

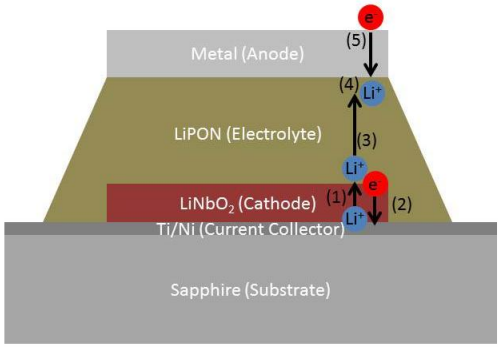

#	Transport Process	Conductivity (S/cm)
1	Lithium in $LiNbO_2$	3×10^{-6}
2	Electrons in $LiNbO_2$	4×10^{5}
3	Lithium in LiPON	1×10^{-6}
4	Lithium into Anode	N/A
5	Electrons in Anode	1×10^{5}

Figure 6-6: (Left) Schematic diagram of the charge transport processes in a thin film battery. (Right) Measured conductivities (see paragraphs below) for each of the five charge transport processes.

Charge transport within a battery can be simplified to 1) ion conduction in the cathode, 2) electron conduction in the cathode, 3) ion conduction through the electrolyte, 4) ion conduction in the anode, and 5) electron conduction in the anode. In order to determine the rate limiting ion conductivity, each of the above layer conductivities was measured. In thin film batteries based on $LiCoO_2$, the low electron conductivity of $LiCoO_2$ is the limiting conduction mechanism. However, examining the conductivities for each of the charge transport mechanisms in a lithium niobite battery, shown in Figure 6-6, the limiting conductivity is ion conduction through the LiPON electrolyte. It should be noted that with a lithium blocking nickel electrode lithium does not move through the anode and instead electroplates a layer of lithium under the anode.

6.3.2 Ion Conductivity Measurements

The ion conductivities shown in Figure 6-6 are calculated from frequency dependent measurements termed electrochemical impedance spectroscopy (EIS) using Equation 6.2 [159].

$$2\pi f_i = \frac{\sigma_i}{\epsilon} \qquad \text{Equation 6.2}$$

Where f_i is the ion relaxation frequency determined from the minimum in the reactance of an EIS spectrum, σ_i is the ion conductivity, and ϵ is the low frequency dielectric constant. Example EIS spectra are shown in Figure 6-7 for both the sputtered lithium niobite cathode and the LiPON electrolyte. The ion relaxation frequency in lithium niobite is approximately 50 times higher than the ion relaxation frequency in LiPON, although LiPON also has a high dielectric constant (ϵ_r = 16.6) [160] leading to a smaller difference in the calculated ion conductivities. While the dielectric constant of lithium niobite is unknown, a value of ϵ_r = 1 was assumed do to the high electron conductivity of lithium niobite and its metallic nature.

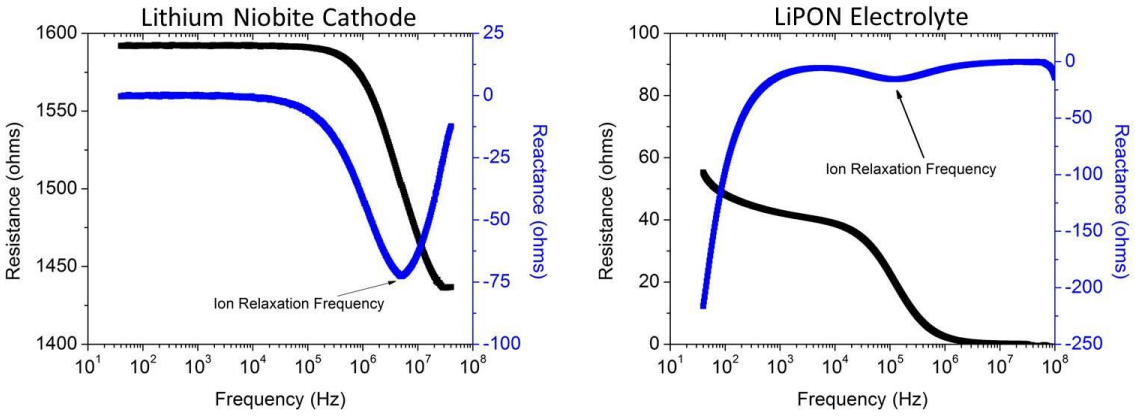

Figure 6-7: Electrochemical Impedance Spectroscopy spectra for both the lithium niobite cathode and the LiPON electrolyte showing a significantly higher ion relaxation frequency in the lithium niobite.

In order to further improve the conductivity of thin film lithium niobite batteries, the ion conductivities of the electrolyte and the lithium niobite cathode should be improved. The ion relaxation frequency in lithium niobite grown by molecular beam epitaxy (MBE) is greater than 10^8 Hz corresponding to an ion conductivity greater than 6

x 10^{-5} S/cm. The higher ion conductivity in MBE grown material is likely due to its higher crystal quality.

Thin films of LiPON with slightly higher ion conductivities (3.3 x 10^{-6} S/cm) have been demonstrated [161]. It was theorized that the ion conductivity in LiPON was enabled by a cross-linked N-3P structure. The LiPON film with the highest reported conductivity had approximately 20% of the nitrogen in this cross-linked N-3P structure as measured by XPS [161]. As shown in Figure 6-8, XPS of the LiPON films used in this work shows three distinct binding energies for nitrogen along with their reported structures. As with the highest reported conductivity LiPON films, in these films the N-3P structure, shown in green, composes 20.8 ± 1.9 % of the nitrogen signal.

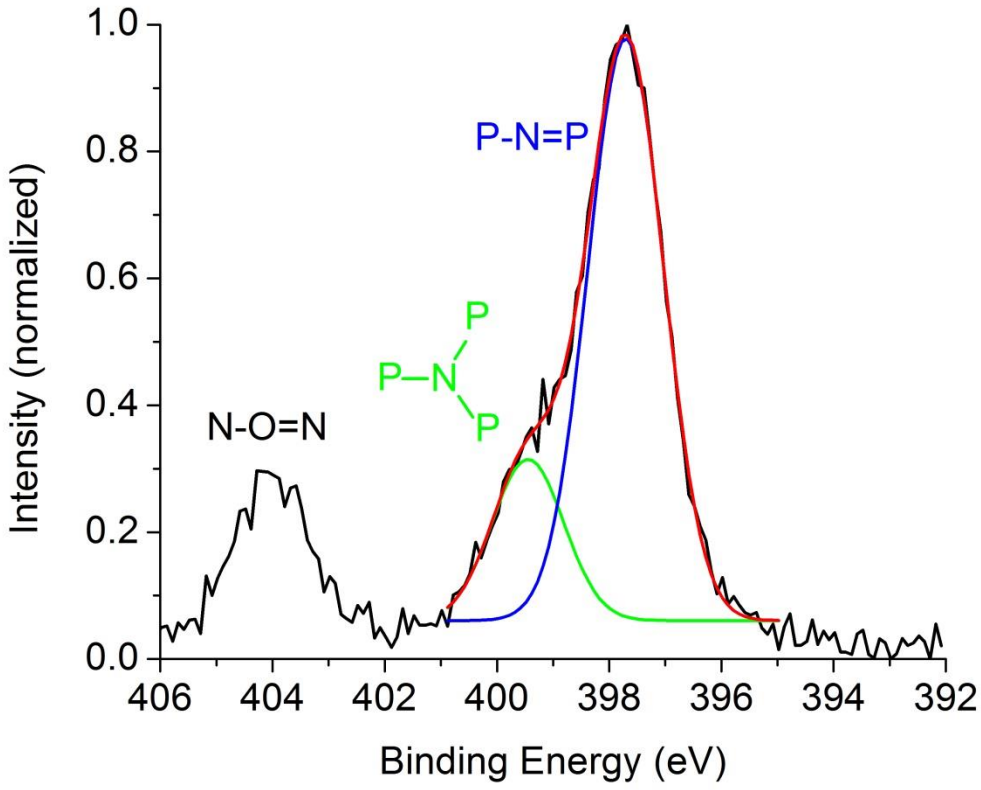

Figure 6-8: Measured N1s XPS spectrum for the sputter deposited LiPON electrolyte. Approximately 20% of the nitrogen signal is associated with the N-3P structure that enables lithium ion conduction.

An alternative method to limit the impact of the low ion conductivity in LiPON is to reduce the thickness of the electrolyte layer thus reducing its resistance. However, one of the common failure modes in lithium ion batteries is the formation of metallic lithium dendrites across the electrolyte that short out the battery. Thin films (approximately 1 µm thick) of LiPON have been shown to passivate such dendrite formation [162]. However, thin film lithium niobite batteries fabricated with LiPON thicknesses less than 1 µm resulted in rapid performance deterioration and the formation of a short circuit. Cross sectional SEM, shown in Figure 6-9, confirms the existence of a dendritic structure bridging the battery anode and cathode.

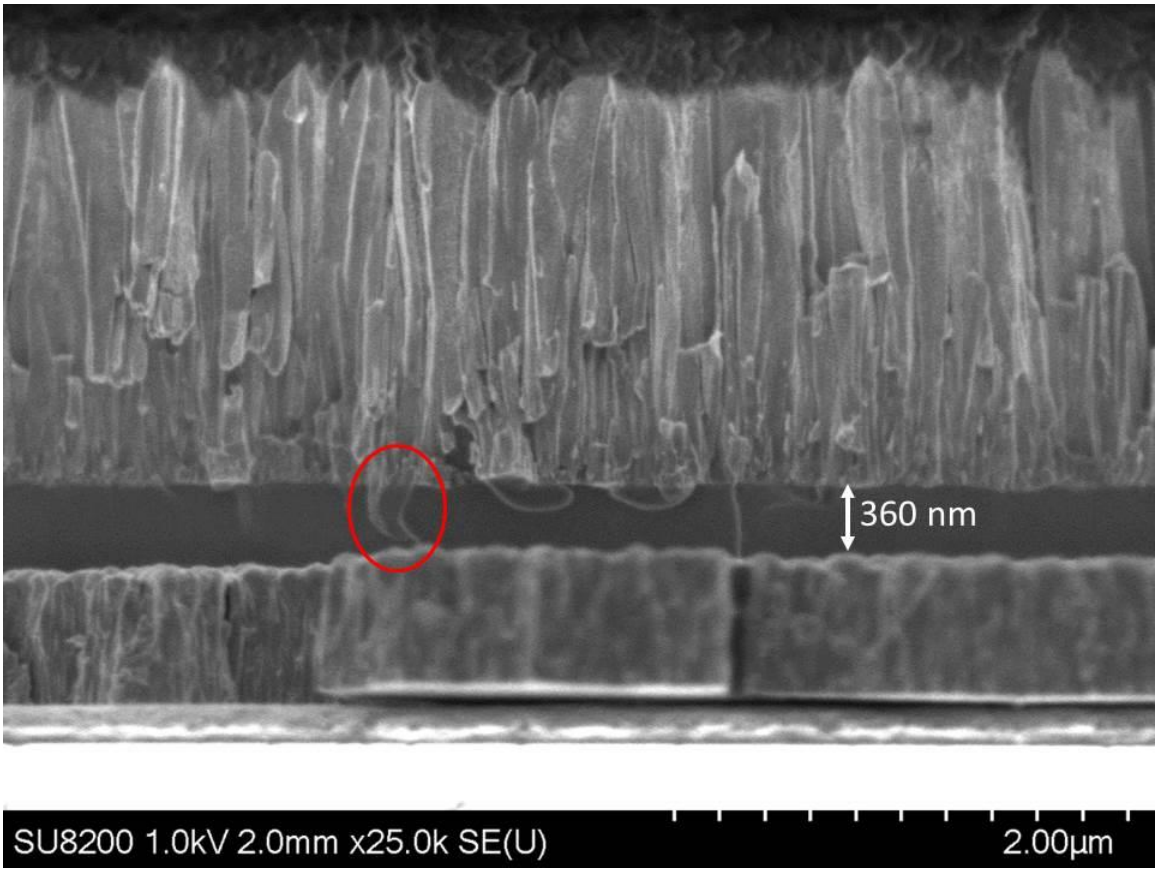

Figure 6-9: Cross sectional SEM of a thin film lithium niobite battery with a thin LiPON electrolyte layer showing the formation of a lithium dendrite bridging the anode and cathode.

Therefore, in order to improve the conductivity of the lithium niobite battery either the LiPON electrolyte must be improved past previously reported record conductivities or a different solid electrolyte must be used. Multiple solid electrolytes with high ion conductivity have been reported. $Li_{0.34}La_{0.51}TiO_{2.94}$ has a reported ion conductivity of almost 10^{-4} S/cm, but reacts with lithium metal becoming electrically conductive ruining its ability to act as a battery electrolyte [163]. Likewise, $Li_7La_3Zr_2O_{12}$ has a reported ion conductivity of approximately 10^{-4} S/cm, but only in crystalline form requiring high temperature processing [164]. When processed at low temperatures, Li-La-Zr-O is amorphous with an ion conductivity of approximately 10^{-7} S/cm.

In summary, solid-state batteries using lithium niobite as the cathode were demonstrated. Batteries fabricated with a lithium absorbing aluminum anode failed due to volumetric expansion of the aluminum. However, batteries fabricated with a lithium blocking nickel anode were successfully cycled. Cycling the batteries to 3V over 100 cycles caused a decrease in specific energy capacity that stabilized at 1.3 mAh/g. The batteries were operated over a small range of potential capacity in which ionic integration occurs useful for replicating the ionic integration of a biological neuron. By using electrically conductive lithium niobite as the cathode material the limiting conductivity mechanism became ion conduction through the solid electrolyte. Further improvements to the battery conductivity will require improving the solid electrolyte layer.

CHAPTER 7

ANOMOLOUS RECTIFICATION AND HYSTERESIS IN NIOBIUM PENTOXIDE CAPACITORS

7.1 Literature Survey

In 1962, a neuristor circuit was theorized for propagating signals without attenuation as is observed between biological neurons [165]. In 2013, a NbO_2 memristor was demonstrated that replicates the voltage triggered switching behavior observed in biological ion channels enabling a physical neuristor circuit to be built [23]. These NbO_2 memristors replicate the rectification observed in voltage-gated biological ion channels [166] as well as the hysteresis necessary for the proposed neuristor circuit to operate [23]. However, the NbO_2 memristors are manufactured by electroforming an insulating layer of Nb_2O_5 into the semiconductor NbO_2, a process that introduces challenges for scaling to dense circuits. Additionally, previous work has not reported a capacitance in NbO_2 memristors requiring an additional parallel capacitance for the neuristor circuit to operate [23]. Herein, an Nb_2O_{5-x} based metal-insulator-metal (MIM) device is investigated that does not require electroforming, possesses a dispersive capacitance advantageous for neuromorphic circuits, and exhibits the rectification and hysteresis necessary to replicate ion channel functionality for the neuristor circuit.

Niobium Pentoxide (Nb_2O_5) has been studied as an insulating layer in MIM diodes since at least the 1960's [167]. These early studies on Nb – Anodized Nb_2O_5 – Au devices found rectification [167] and a Poole-Frenkel conduction mechanism [168]. The

defect state enabling Poole-Frenkel conduction was found to lie between 0.22 – 1.2 eV [167, 168] below the conduction band edge likely due to oxygen vacancies [168]. Additionally, it was found that upon dielectric breakdown these devices exhibited bistable switching in small conducting regions similar to the NbO_2 devices used in the 2013 neuristor demonstration [169]. There is debate in the literature regarding the operating mechanism of the electroformed NbO_2 devices with both a Mott Metal-Insulator transition [23] and a Joule heat driven Poole-Frenkel mechanism [170] suggested.

7.2 Niobium Pentoxide Characterization

MIM diodes were produced on sapphire substrates in three steps. First, a ground plane consisting of a 50 nm titanium adhesion layer and 300 nm of metal (Cu, Au, Ni, or Pt) was deposited by electron beam evaporation across the entire chip. Next, a layer of niobium oxide was deposited through a shadow mask by room temperature reactive sputtering. Finally, 300 nm thick top metal contacts were deposited through a second shadow mask using electron beam evaporation.

The niobium oxide insulating layer was sputter deposited at room temperature using a reactive deposition process. A metallic niobium target was sputtered in a mixed Ar/O_2 environment using gas flows of 35 sccm and 15 sccm respectively. The chamber pressure was maintained at 10 mTorr. The niobium target was energized with 4.8 W_{DC}/cm^2 producing a deposition rate of 5 angstroms per minute. It was previously shown that even low temperature annealing impacts the structural and electrical properties of

Nb_2O_5 [171]. Thus, the low power deposition allowed precise control of the oxide thickness and minimized unintentional heating of the devices.

The niobium oxide explored herein was sputter deposited at room-temperature and was characterized by x-ray diffraction (XRD), x-ray reflectivity (XRR), optical transmission spectroscopy, and x-ray photoelectron spectroscopy (XPS) as shown in Figure 7-1. Symmetric XRD measurements revealed no peaks except for the sapphire substrate indicating the deposited niobium oxide is amorphous. The density of the deposited niobium oxide was determined by XRR to be 4.1 +/- 0.1 g/cm^3, significantly lower than the ideal density of 4.55 g/cm^3 for Nb_2O_5 consistent with approximately 8 - 12% oxygen deficiency [172]. Applying the Tauc method to the optical absorption spectra revealed an optical band gap of 3.15 ± 0.004 eV, slightly lower than the reported range of band gaps from 3.2 – 4 eV [173]. This matches previous reports of a lower band gap for low density Nb_2O_5 [171]. Lastly, the oxygen to niobium ratio, as measured by XPS, was 2.30 ± 0.02, approximately 7 - 9% lower than the ideal ratio of 2.5. This indicates that the niobium oxide layer is oxygen deficient and that there may be a high density of oxygen vacancies. The niobium XPS spectrum indicates a single Nb^{5+} oxidation state with no detectible NbO_2 present.

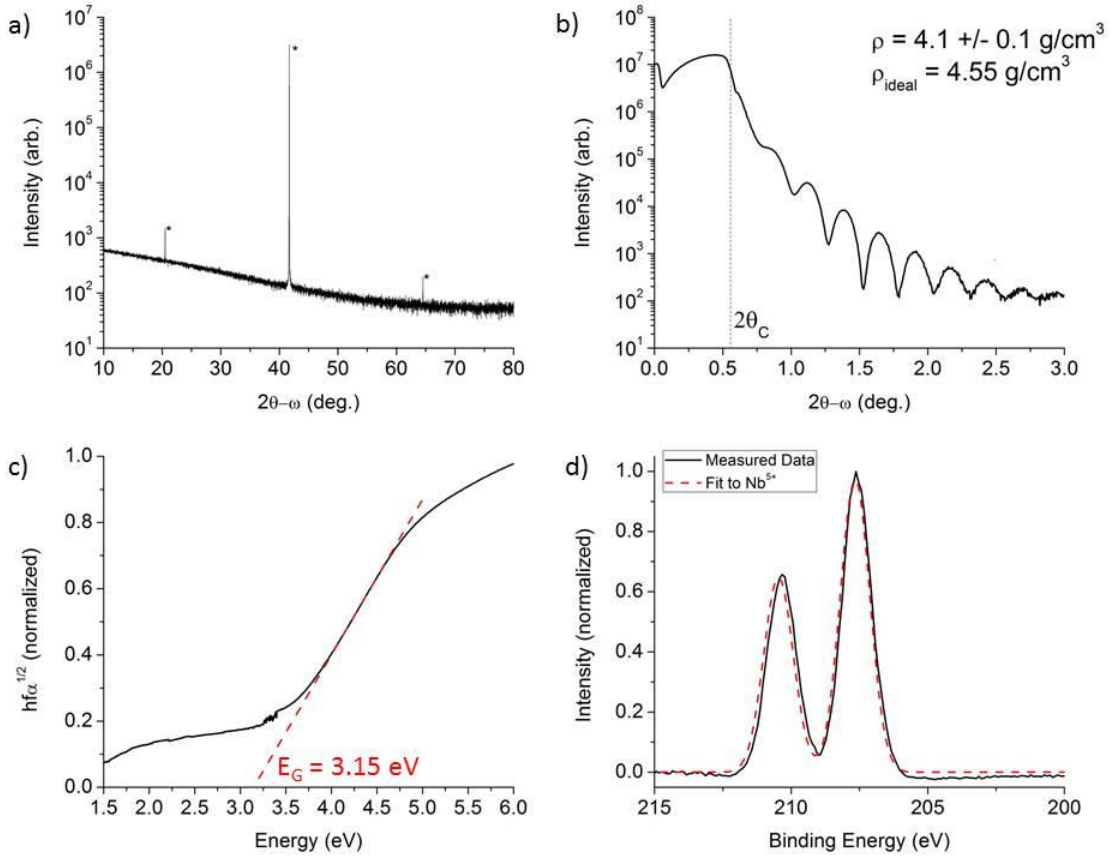

Figure 7-1: a) Symmetric XRD exhibits no peaks other than the sapphire substrate (*) indicating that the deposited layer is amorphous. b) XRR shows oscillations out to 3 degress (2θ-ω) allowing precise determination of the film thickness. The critical frequency allows the film density to be determined as 4.1 g/cm^3 significantly lower than the ideal density for Nb_2O_5. c) Tauc plot of optical absorption data indicating a bandgap of 3.15 eV. d) Nb 3d XPS spectrum showing a single oxidation state doublet that matches the 5+ oxidation state.

Fabricated MIM diodes were electrically tested to determine their steady state current-voltage relation, frequency dependent impedance, and capacitance both with and without bias. Steady state measurements were performed using a Keithley 6517A Electrometer. Frequency dependent measurements were performed using an Agilent 4294A Precision Impedance Analyzer over a frequency range from 40 Hz – 10 MHz.

7.3 Anomalous Rectification and Hysteresis

The current-voltage characteristics for a Metal-Nb_2O_{5-x}-Metal diode exhibit rectification and hysteresis, as shown in Figure 7-2a. This measurement was performed using 50 mV steps and holding for 15 seconds at each voltage step. At each voltage step the current transient was measured and is shown in Figure 7-2b. For voltages below turn-on, the current decreases as a function of time in a nearly exponential fashion. For voltages above turn-on, the current increases with time. As shown in Figure 7-2c, the current transients above turn-on have not saturated to a steady state current after 150 seconds indicating that a slow phenomenon is responsible for the current transient. The hysteresis present in the current-voltage curves may therefore be due to the slow timeframe for reaching a steady state current allowing a broad range of frequencies for neuromorphic device operation (i.e. f > 1/150 Hz). The combination of rectification and memristive hysteresis led to the term memdiode consistent with previous devices that exhibit these features [174].

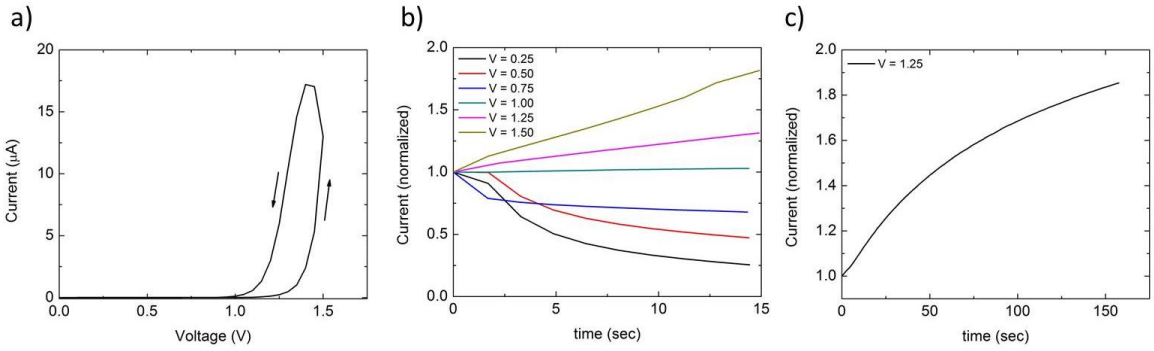

Figure 7-2: a) Current-Voltage curve for a metal-Nb_2O_{5-x}-metal device showing rectification and hysteresis. b) Current transients at several voltage steps in (a) normalized to the first data point showing a decreasing current below the turn-on voltage of 1 volt and increasing current above the turn-on voltage. c) An extended current transient above the turn-on voltage showing that the time scale to reach steady state is hundreds of seconds.

In addition to rectification and hysteresis, it is desirable for the memristors in the neuristor circuit to exhibit capacitance. This eliminates the need for an external parallel

capacitor, enabling higher density circuits. Measurements of various sized Nb_2O_{5-x} MIM diode's capacitance indicate the relative dielectric constant ε_r is 37.1 ± 1.0 at 1 MHz. As shown in Figure 7-3a, the memdiode capacitance is dependent on frequency and the capacitance at biological frequencies (< 100 Hz) is significantly higher (ε_r > 180) than the capacitance at 1 MHz. This allows the memdiode to be scaled to nanometer sizes without large external capacitors in the neuristor circuit.

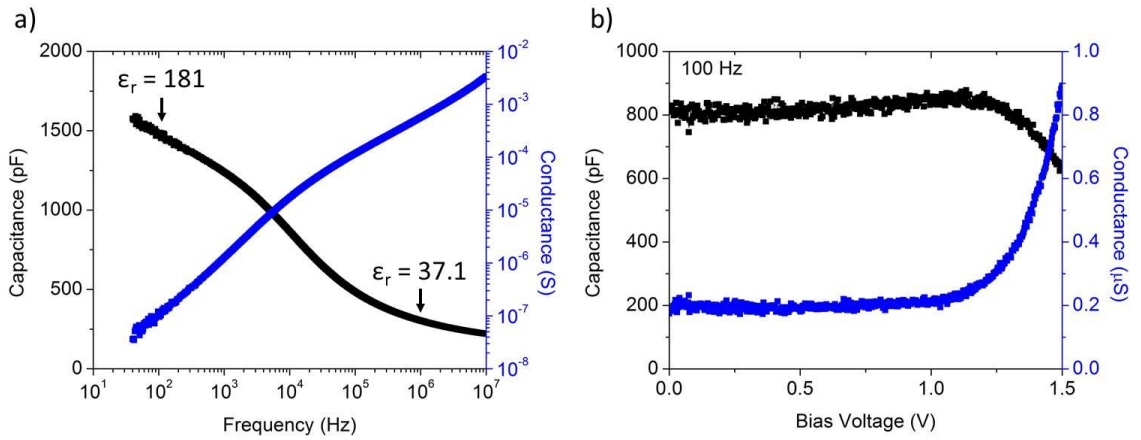

Figure 7-3: a) The capacitance and conductance as a function of frequency. The capacitance is highly dependent on frequency with a relative dielectric constant greater than 180 at neurological frequencies (< 100 Hz). b) The capacitance and conductance as a function of DC bias voltage measured at 100 Hz. The capacitance is relatively unchanging below the turn-on voltage, increasing by only 6%. The slight increase in capacitance is likely due to image-force lowering decreasing the effective insulator thickness. Above the turn-on voltage the capacitance decreases and the conductance exhibits rectification.

As shown in Figure 7-3b, the bias dependent capacitance and conductance of the memdiodes shows that, unlike a traditional p-n junction diode, the capacitance increases slightly for voltages below the turn on voltage and decreases above the turn on voltage. The device conductance exhibits rectification similar to the quasi-steady state measurements shown in Figure 7-2a. The memdiode therefore maintains the ability to store charge under bias, particularly above turn-on, which is necessary for the neuristor circuit to operate.

Devices of similar thickness were fabricated with Cu, Au, Ni, and Pt contacts in order to investigate the effects of the metal work function on device performance. As shown in Figure 7-4a, each device exhibited a transition between a high resistance region and a low resistance region when plotted on a semi-log plot. This transition voltage scales linearly with the ideal metal work function [175], as shown in Figure 7-4b, indicating that the transition is associated with the metal-Nb_2O_{5-x} Schottky barrier height. In addition, the electron affinity of amorphous Nb_2O_5 is determined to be 4.50 +/- 0.07 eV by extrapolating the ideal work function to zero transition voltage.

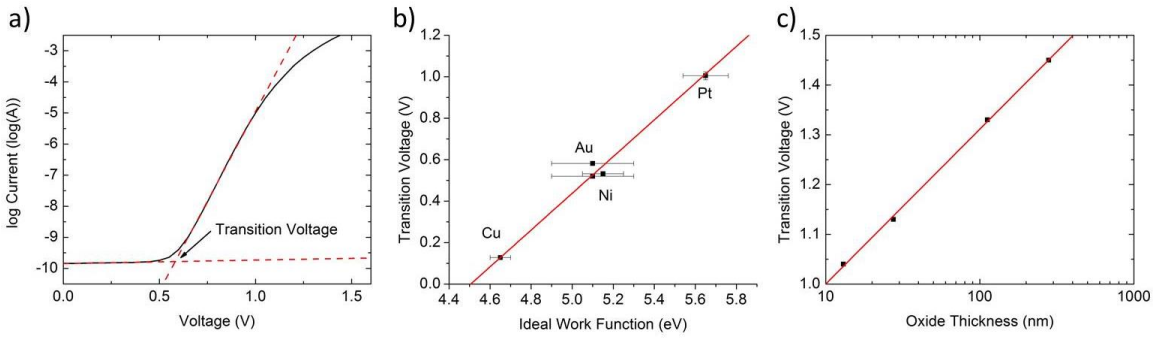

Figure 7-4: a) Semi-log plot of the current-voltage sweep defining a transition voltage between the off and on states. b) The transition voltage is linearly proportional to the ideal metal work function indicating that the transition is tied to the Schottky barrier height. c) The transition voltage is logarithmically related to the oxide thickness in contrast to traditional MIM diodes.

Devices were also fabricated with a range of Nb_2O_{5-x} thicknesses ranging between 10 – 300 nm. As shown in Figure 7-4c, the transition voltage scales as the logarithm of thickness with thicker devices requiring a larger voltage to transition to the conducting state. This contrasts with a traditional MIM diode based on Fowler-Nordheim tunneling for which the turn-on voltage scales nearly linearly with thickness making thick devices impractical.

7.4 Theoretical Explanation

Rectification in MIM diodes is typically associated with a transition in current mechanism from thermionic emission in the off state to Fowler-Nordheim tunneling in the on state [145]. However, this interpretation should lead to a turn-on voltage nearly linear dependent on the thickness and weakly dependent on the metal-insulator Schottky barrier height. However, the devices discussed herein exhibit rectification at lower voltages more consistent with the expected Schottky barrier heights for the metal-Nb_2O_5 junction and possess turn on voltages logarithmically dependent on thickness. This can be explained by considering charge transport via the defect states of the Nb_2O_{5-x} layer and by considering two separate regions within the Nb_2O_{5-x} layer. As shown in Figure 7-5, when the defect states in Region 1 are empty a fixed positive charge and an enhanced electric field result compared to Region 2 where the defects are occupied and thus neutral. This spatially varied charge occupation results in two distinct conduction states.

Under low voltage conditions, shown in Figure 7-5a, the supply of electrons into Region 1 is governed by thermionic emission over a Schottky barrier which limits overall current flow. These injected electrons are swept into Region 2 where they propagate via the Poole-Frenkel mechanism. With each successive voltage increment, the electric field within Region 2 momentarily drives a Poole-Frenkel current larger than the thermionic current depleting electrons from the edge of Region 1. This depletion of electrons leaves behind additional positively charged defects, widening Region 1which supports a larger proportion of the applied voltage. This conversely reduces the electric field within Region 2 and thus reduces the Poole-Frenkel current to balance the available thermionic current in the steady-state.

After sufficient voltage is applied to reach the device turn on, shown in Figure 7-5b, tunneling across the charged Region 1 can occur from the metal electrode directly into Region 2. For niobium oxide with a sufficient number of defects, the electric field in Region 1 is dominated by the amount of ionized charge in Region 1 causing the turn-on voltage to be controlled by the Schottky barrier height rather than the device thickness as is experimentally observed in Figure 7-4. As the voltage is increased beyond the turn-on voltage, an increase in the electric field in Region 2 results in an increase in the Poole-Frenkel current. Thus, the Poole-Frenkel current dominates the current flow and dictates the injected tunneling current through control of the width of Region 1 by the emptying (or filling) of defects at the interface between the two regions.

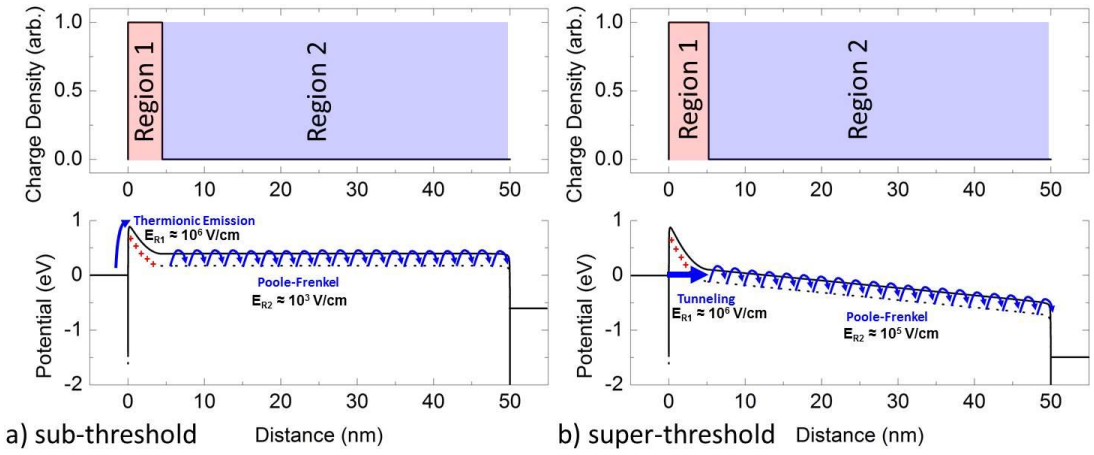

Figure 7-5: The charge density and electron potential of the proposed device model both a) below and b) above the turn-on voltage. Removal of electrons from traps in Region 1 leaves fixed positive charge that supports a large electric field (10^6 V/cm). The steady state width of Region 1 is determined by balancing the injection of electrons by thermionic emission below the turn-on voltage or tunneling current above the turn-on voltage with the removal of electrons by Poole-Frenkel current through Region 2. a) Below the turn-on voltage a small electric field (10^3 V/cm) is required in Region 2 to remove the electrons injected by thermionic emission. b) Above the turn-on voltage a larger electric field (10^5 V/cm) is required in Region 2 to remove electrons injected by tunneling.

This proposed model for these metal-Nb_2O_{5-x}-metal memdiodes predicts that for voltages below turn-on the conduction will be controlled by the Schottky barrier height

and the associated thermionic current. Above the turn-on voltage, current will be limited by the Poole-Frenkel current described by Equation 7.1.

$$J_{PF} = q\mu N_o E \exp\left(-\frac{q}{k_B T}\left(\phi_D - \sqrt{\frac{qE}{\pi\varepsilon}}\right)\right) \qquad \text{Equation 7.1}$$

where μ is the electron mobility, N_o is the concentration of defects, E is the electric field, ϕ_D is the defect trap energy, and ε is the high frequency dielectric constant [145].

Based on Equation 7.1, plotting the logarithm of current divided by the electric field, ln(I/E), vs the square root of the electric field will reveal any Poole-Frenkel controlled voltage regimes as a linear region. As shown in Figure 7-6, for voltages above a threshold value there is a linear regime confirming the Poole-Frenkel current mechanism controls conduction at high voltages.

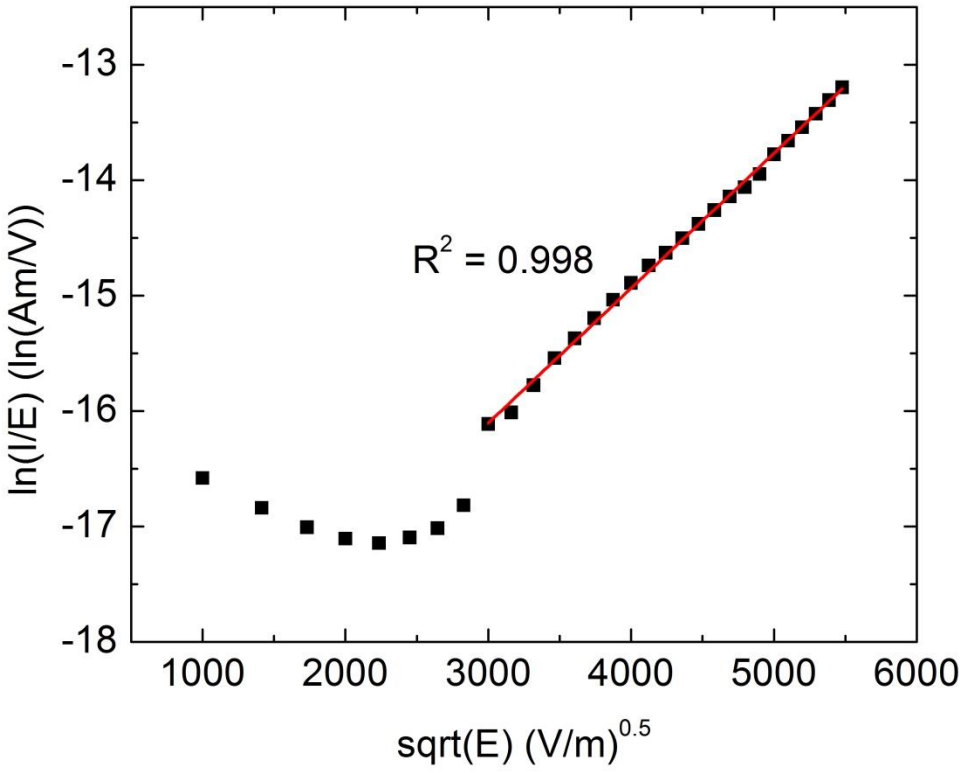

Figure 7-6: A Poole-Frenkel plot exhibiting a linear region above the turn-on voltage indicating that the Poole-Frenkel mechanism controls the current flow within this voltage range. The coefficient of determination (R^2) is 0.998 indicating good agreement between the experimental measurements and the linear fit.

To determine the trap energy, temperature dependent conductivity measurements were performed at DC biases above the turn-on voltage where the device was shown to be controlled by the Poole-Frenkel current. As shown in Figure 7-7a, measured at 1.25 V, the temperature dependent current exhibits rectification. The rectification is caused by the supply of electrons transitioning from a tunneling current mechanism at low temperature to thermionic emission current at high temperatures. By fitting $\ln(I/T^2)$ for the thermionic current at high temperatures and ln(I) for the Poole-Frenkel current, which controls the tunneling current as previously shown, at low temperatures, the Schottky barrier height

and the Poole-Frenkel trap depth can be determined. The Schottky barrier height was determined for the thickest device in Figure 7-4c, 280 nm, to be 0.96 ± 0.08 eV comparable to the theoretical barrier height for Pt/Nb_2O_5 of 1.0 eV, but slightly lower than the measured turn-on voltage for this device of 1.12 V. The higher experimental turn-on voltage is likely due to an additional small voltage drop over Region 2 in thicker devices as shown in Figure 7-4c. A less likely explanation for the temperature rectification observed in Figure 7-7a is activation of a deep defect state that contributes to the Poole-Frenkel current. Fitting the high temperature activation energy of the Poole-Frenkel Arrhenius plot yields a defect energy of 1.0 eV slightly lower than the 1.1 eV energy for the second ionization of an oxygen vacancy in Nb_2O_5 [168]. However, emission from such a deep defect is extremely slow, resulting in a negligible contribution to current. Thus, it is assumed that the observed temperature rectification is due to a transition from a shallow defect Poole-Frenkel current at low temperatures to thermionic emission over the Schottky barrier at high temperatures.

As shown in Equation 7.1, the Poole-Frenkel trap energy is modified by an electric field term that must be fit by measuring the temperature dependent current at multiple electric fields. As shown in Figure 7-7b, fitting the measured Poole-Frenkel activation energies yields a defect depth of 0.22 ± 0.01 eV, in perfect agreement with the previously reported 0.22 eV activation energy for an oxygen vacancy in amorphous Nb_2O_5 [168].

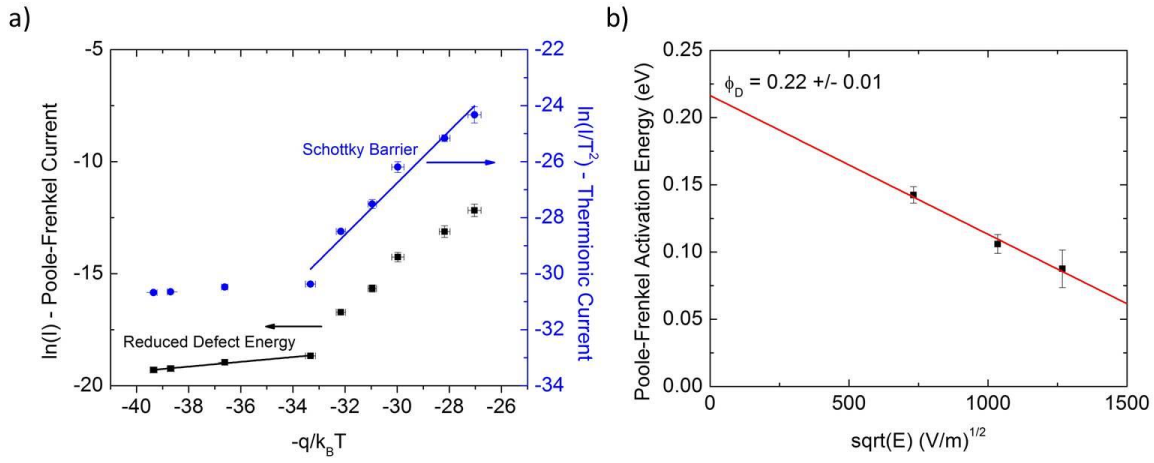

Figure 7-7: a) Temperature dependent measurements of the device current showing rectification with temperature. The current was measured at 1.25 V, which is above the turn-on voltage. At low temperatures the Poole-Frenkel current controls the current flow with a low activation energy while at high temperatures thermionic emission over a higher energy barrier controls current flow. b) Plotting the Poole-Frenkel activation energy at a variety of applied voltages reveals a defect trap depth of 0.22 ± 0.01 eV matching the previously reported trap depth for oxygen vacancies in Nb_2O_5.

The hysteresis necessary for neuristor circuit operation is caused by not reaching a steady state current when operating at frequencies of interest to neurological processes. It was experimentally observed that the time scale to reach steady state is on the order of 10's to 100's of seconds indicating any reasonable neuromorphic frequency, f > 0.1 Hz, will exhibit hysteresis. The fixed charge in Region 1 determines the Region 1 width and thus the current through the device. Therefore the rate of filling and emptying of traps at the boundary between Region 1 and Region 2 sets the time scale to reach a steady state current. Such slow trap dynamics could be caused by either slow emission of electrons from the trap states or a current limited filling and emptying of traps. The capture (c_e) and emission (e_e) rates for the trap states can be calculated according to Equations 7.2 – 3 [145].

$$c_e = \nu_{th}\sigma_n n N_t \qquad \text{Equation 7.2}$$

$$e_e = \nu_{th}\sigma_n N_C N_t \, exp\left[-\frac{E_C - E_t}{k_B T}\right] \qquad \text{Equation 7.3}$$

where ν_{th} is the thermal velocity, σ_n is the electron capture cross section, *n* is the density of available electrons, N_t is the density of traps, N_C is the effective density of states in the conduction band, and $(E_C - E_t)$ is the depth of the trap below the conduction band edge. While the exact values for some of these variables are unknown for amorphous Nb_2O_5, typical ranges for these variables are: $\nu_{th} \approx 10^7$ cm/s, $\sigma_n \in [10^{-14}, 10^{-16}]$ cm^2, $N_C \in [10^{16}, 10^{20}]$ cm^{-3}. Based on these values, the timescale for an emission limited process (N_t/e_e) is nanoseconds to milliseconds, significantly faster than the experimentally observed current transients. However, for the experimentally observed range of currents, the timescale for a current supply limited capture process (N_t/c_e) is milliseconds to kiloseconds, matching the experimental timescale for the current transients. Therefore, the memdiode hysteresis is likely caused by a current limited electron capture process which enables a wide range of frequencies for which the memdiode will exhibit the hysteresis necessary for neuromorphic circuitry.

CHAPTER 8

LIQUID PHASE ELECTRO-EPITAXY OF BULK LITHIUM NIOBITE

The devices explored in Chapter 5 (memristors), Chapter 6 (batteries), and Chapter 7 (memdiodes) each replicate the functionality of a sub-structure of a biological neuron. However, biological neurons exist within a conductive ionic fluid, the cerebrospinal fluid (CSF), which may be reproduced by bulk lithium niobite.

8.1 Neuromorphic "Sea of Ions"

While most neuromorphic architectures focus on replicating the generation, scaling, and propagation of voltage spikes called action potentials, biological neurons produce action potentials by exchanging ions with the surrounding CSF. This sea of ions that surrounds biological neurons is often treated as a ground plane in neuromorphic designs, but biologically can support ionic currents. Synchronized activity in a group of neurons creates ion waves that can be detected outside the skull via Electroencephalography (EEG).

Mounting evidence indicates that non-synaptic ionic signals within the CSF also transmit information between neurons [176]. One example is in single celled bacteria that do not possess axons or dendrites. Within a cluster of bacteria, electrical signals of K^+ ions are exchanged through the surrounding fluid to control the growth of the bacterial cluster [177]. The presence of non-synaptic electrical communication in single celled organisms suggests that non-synaptic communication is phylogenetically old originating in a "protoneuron". As higher vertebrates developed, these protoneurons differentiated

into many types of neurons, some of which still communicate via non-synaptic electrical signals. As one review article summarized, "If a neuronal form is functioning for about 600 million years we should consider it as an important structure in the basic functions of the central nervous system" [176]. In order to replicate the ionic environment of the CSF, growth of bulk lithium niobite was explored.

8.2 Historical Liquid Phase Electro-Epitaxy of Lithium Niobite

The first reported growth of lithium niobite by liquid phase electro-epitaxy (LPEE) was in 1994 and produced hexagonal crystals approximately 2 mm across [92]. This and later work [88] were accomplished by electrolysis of a molten salt solution consisting of $NaBO_2$, LiF, $LiBO_2$, and Nb_2O_5. Small crystallites of lithium niobite were formed by applying a constant voltage across the molten salt solution.

Lithium metaborate ($LiBO_2$) and Sodium metaborate ($NaBO_2$) are glass forming compounds capable of dissolving Nb_2O_5 [96]. The fusion of Nb_2O_5 in a borate solution creates a niobium bearing mixture that is liquid above 850^oC whereas Nb_2O_5 does not melt until 1512^oC. Aside from molten borate solutions, niobium compounds are difficult to dissolve and other methods for producing a niobium containing solution often involve terrifying procedures [178].

A simpler LPEE chemistry was developed in 2014 by reducing the melt constituents to only $LiBO_2$ and Nb_2O_5 [95]. It was shown that the previous chemistry resulted in 9.2% Na and 4.4% F in the resulting crystals. By eliminating the sources of sodium and fluorine, these contaminants were also eliminated. While the simpler

chemistry eliminated contaminants, it does require higher temperatures (900^{o}C) [95] than the melt containing $NaBO_2$ (800^{o}C) [92]. Heteroepitaxial deposition onto SiC has also been explored, but resulted in nucleation of small crystallites rather than a coherent film [95]. All previous work on LPEE of lithium niobite has explored a single borate flux to Nb_2O_5 ratio and a single deposition voltage for each substrate.

8.3 Heteroepitaxial Growth on SiC

Heteroepitaxial deposition was performed on n-type SiC substrates with a range of melt compositions and deposition voltages. The melt compositions varied from a molar ratio ($Li_2B_2O_4$:Nb_2O_5) of 267:1 to 8.9:1 where previous attempts at LPEE of lithium niobite were from melts with a molar ratio of 15:1. For each melt the current as a function of deposition voltage was measured as shown in Figure 8-1. As the quantity of dissolved Nb_2O_5 increases (decreasing molar ratio), the hysteresis in the I-V sweep decreases. In addition, for low concentrations of Nb_2O_5 a plateau is visible between 1 – 1.25 V.

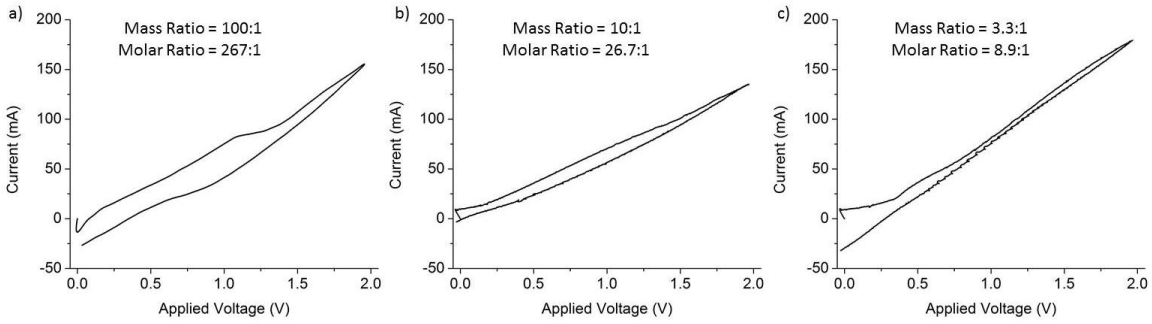

Figure 8-1: Current voltage curves for molten solutions with varying ratios of $Li_2B_2O_4$:Nb_2O_5. For solutions with a high molar ratio hysteresis is present and a current plateau occurs. The hysteresis is diminished and the current plateau is absent for low molar ratio solutions.

In traditional aqueous electrodeposition, each of the three regions in Figure 8-1a are associated with a specific growth process as shown in Figure 8-2. At low voltages the lowest energy reaction occurs and can be described by the Butler-Volmer equation shown in Equation 8.1 [179].

$$J = J_o \left[\exp\left(-\frac{zF\alpha_c\eta_a}{RT}\right) - \exp\left(\frac{zF\alpha_a\eta_a}{RT}\right)\right] \qquad \text{Equation 8.1}$$

Where J_o is the exchange current density, z is the ionic charge, F is Faraday's constant, α is the charge transfer coefficient for an anodic (α_a) or cathodic (α_c) reaction, η_a is the activation overpotential, R is the gas constant, and T is temperature [179].

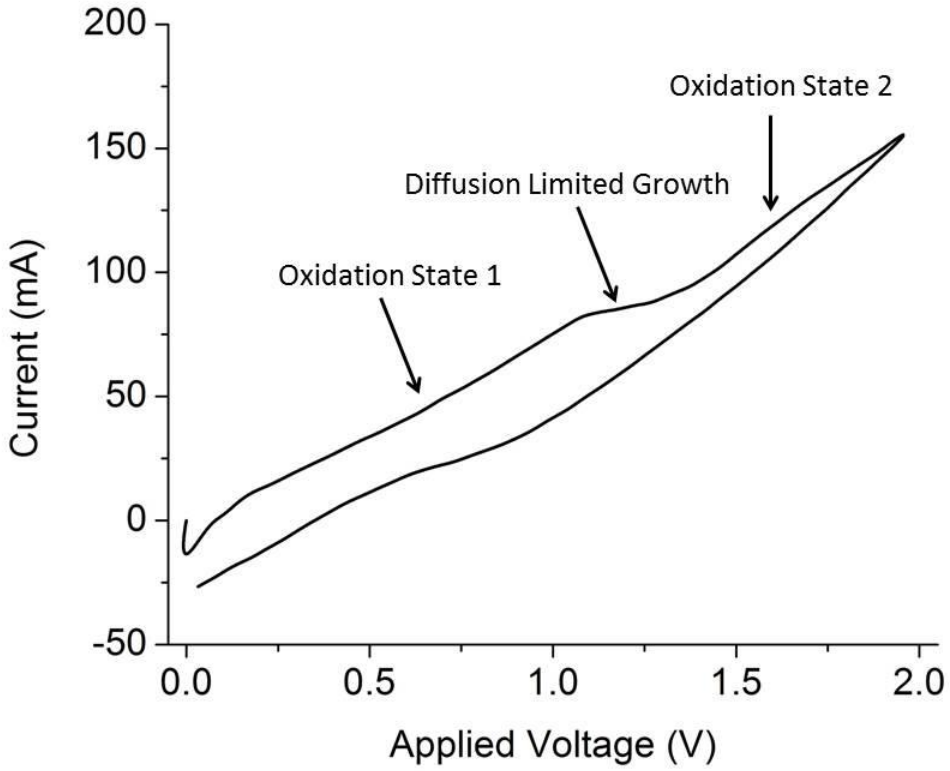

Figure 8-2: Traditional interpretation of the three regions present in the current-voltage curve of a high molar ratio solution.

Equation 8.1 assumes an abundant supply of ions at the electrode surface. For voltages within the current plateau, the reaction becomes mass transport limited where diffusion of ions to the electrode surface limits the reaction rate and thus the current. For this condition the current density is described by Equation 8.2 [179].

$$J = J_1\left(1 - \exp\left(\frac{zF\eta_c}{RT}\right)\right) \qquad \text{Equation 8.2}$$

where J_1 is the limiting current density and η_c is the concentration overpotential.

The high voltage region can be described by the activation of a second reaction and a return to reaction limited deposition. The lack of a current plateau in melts with higher concentrations of Nb_2O_5 is consistent with the traditional interpretation where the extra Nb_2O_5 prevents a mass transport limited regime. Likewise, the loss of hysteresis for melts with higher concentrations of Nb_2O_5 suggests that the reaction product deposited onto the electrode cannot be re-dissolved into the high concentration melt eliminating the second term of Equation 8.1.

Depositions onto SiC substrates were performed within each of the three voltage regimes. As shown in Figure 8-3a, deposition at low voltage (0.5 V) from a melt with low Nb_2O_5 concentration (267:1 molar ratio) produced a coalesced thick film of lithium niobite with no other phases visible in the XRD. The XRD omega rocking curve for this film, shown in Figure 8-3b, had a full width at half maximum of 220 arcsec indicating a film well aligned to the underlying SiC substrate with little tilt in the grains.

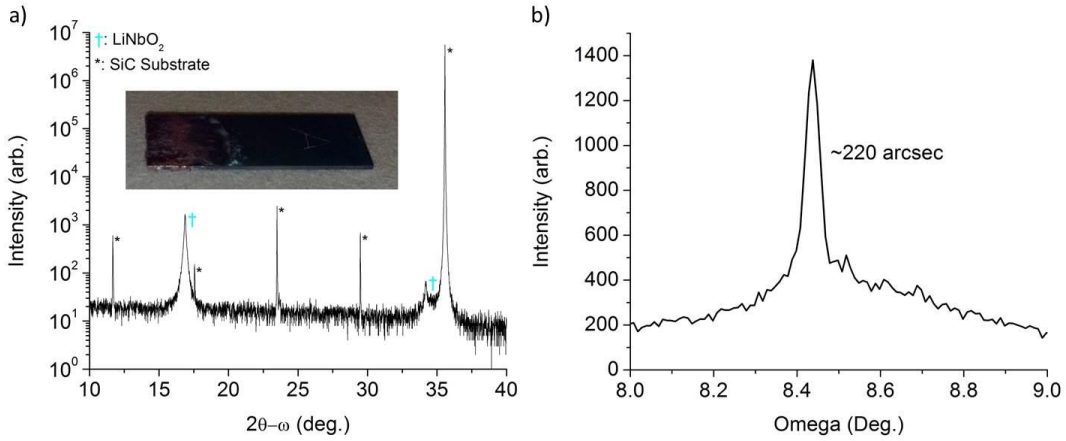

Figure 8-3: a) Symmetric XRD of a thick film deposited onto SiC from a high molar ratio solution at low voltage. The deposited material is c-oriented lithium niobite. b) The omega rocking curve of the deposited lithium niobite has a FWHM of 220 arcsec indicating well aligned grains.

As shown in Figure 8-4a, deposition at a voltage (1.2 V) within the current plateau of Figure 8-2a also produced single phase lithium niobite, but with much lower XRD intensity than the low voltage deposition. Further, the XRD rocking curve was significantly wider with a full width at half maximum of 900 arcsec. This wide rocking curve indicates the material is not as well aligned to the SiC substrate.

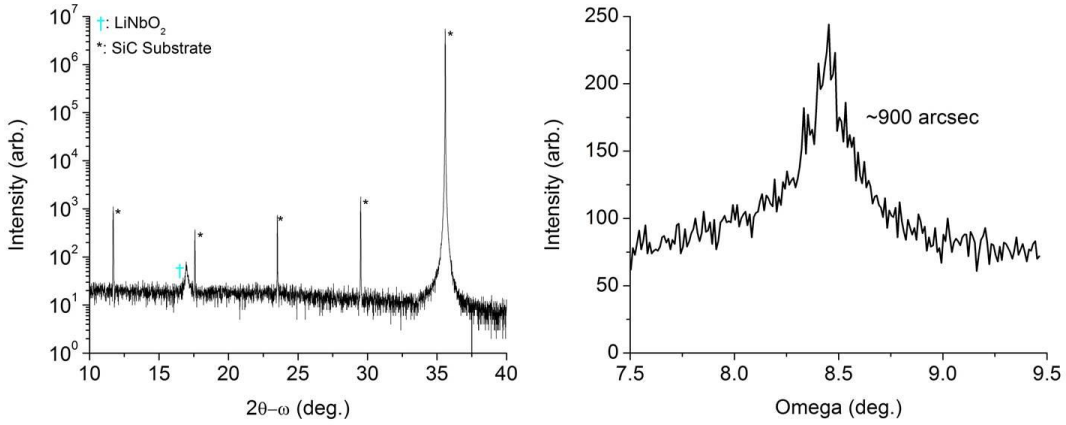

Figure 8-4: a) Symmetric XRD of a film deposited onto SiC from a high molar ratio solution at a voltage within the current plateau. A single XRD peak is visible from c-oriented lithium niobite, but with significantly less intensity than the film deposited at low voltage. b) The omega rocking curve of the deposited lithium niobite has a FWHM of 900 arcsec indicating less aligned grains than the film deposited at low voltage.

Examining the surface of the deposited film using AFM, shown in Figure 8-5, the film consists of a porous field with a high density of hexagonal pits. These pits are approximately 3 µm deep. The appearance of porous material is consistent with a diffusion limited growth mode where dissolved ions immediately nucleate upon contacting the electrode with little surface mobility. The high rate of nucleation leads to porous material with low crystalline quality and low adhesion to the substrate [179].

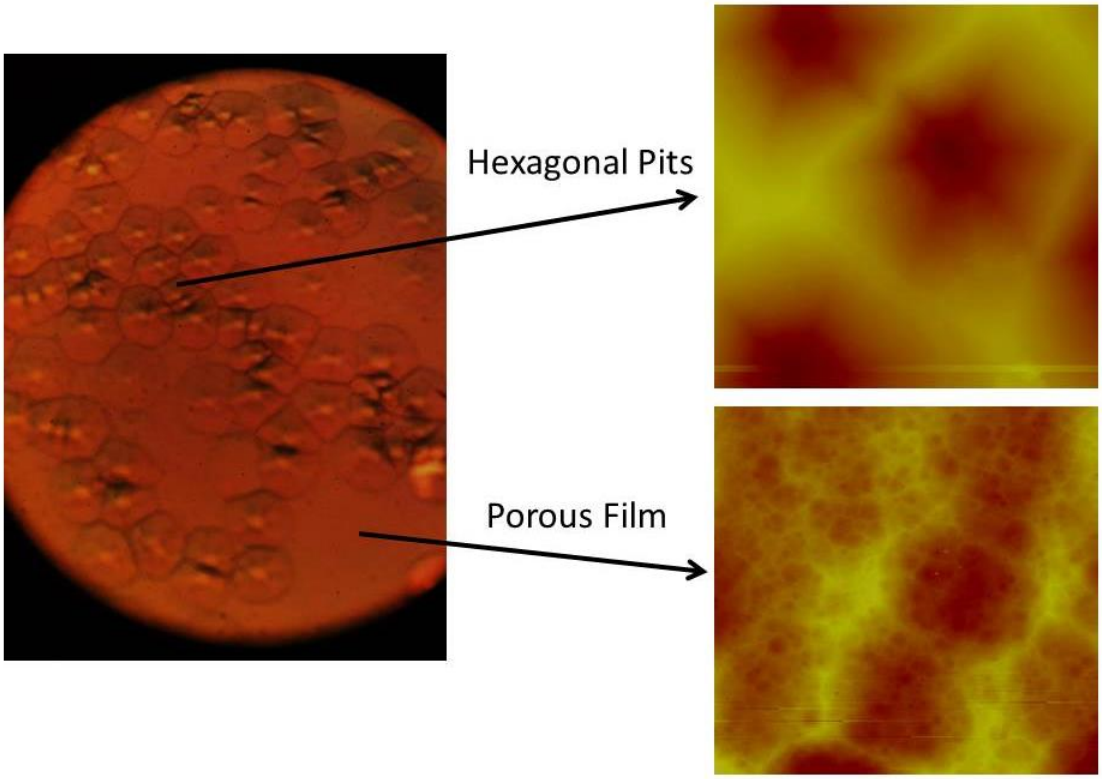

Figure 8-5: AFM of the film deposited at a voltage within the current plateau showing a porous film with hexagonal pits. The porous nature of the film is consistent with diffusion limited growth and poor adatom surface mobility.

As shown in Figure 8-6, deposition at a high voltage (1.8 V) produced a thick uneven layer of material with practically no crystalline order. It is unknown what material is formed in the higher voltage oxidation state, but the uneven material formed suggests a field driven growth mode that amplifies any substrate roughness.

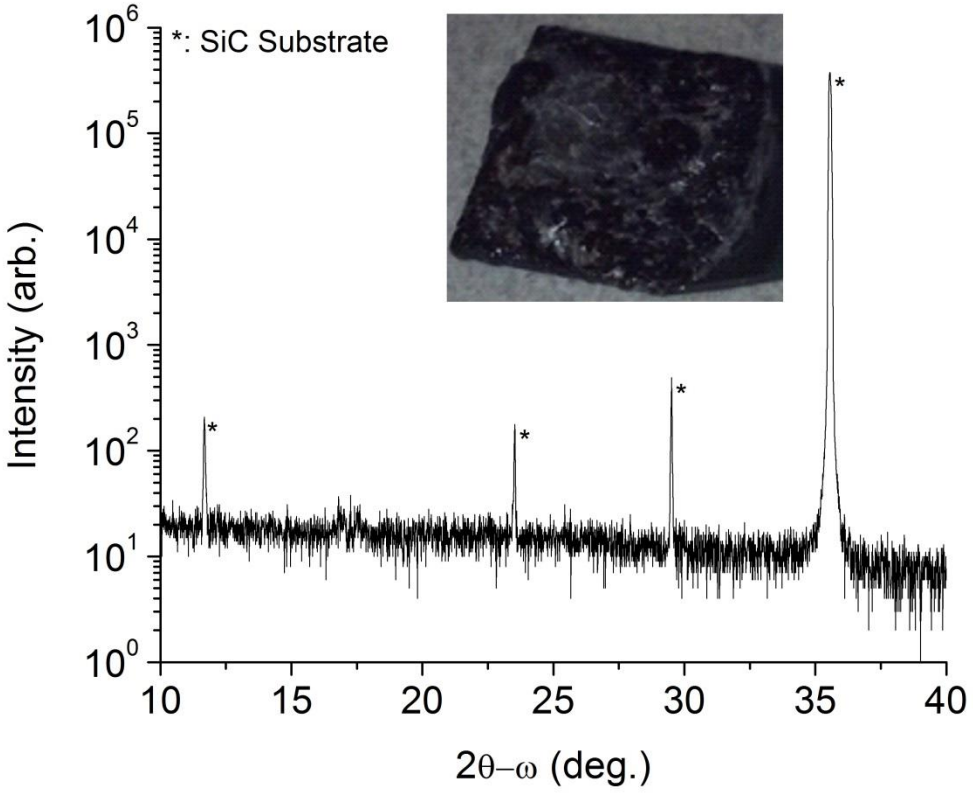

Figure 8-6: Symmetric XRD of material deposited at high voltage from a solution with high molar ratio.

The current-voltage curves for melts with higher molar ratios of 26.7:1 and 8.9:1 show little to no hysteresis and no current plateau. These melt compositions are similar to the previously reported composition with a molar ratio of 15:1, which produced small crystallites of lithium niobite on SiC that did not coalesce into a film.

As shown in Figure 8-7, depositions from a melt with a molar ratio of 26.7:1 produced mixtures of lithium niobite and lithium niobate. Depositions at lower voltages (1.2 V) produced a coalesced film with hexagonal pits and low intensity XRD peaks of both lithium niobite and lithium niobate as shown in Figure 8-7a. Depositions at higher voltages (1.8 V) produced the same underlying film, but with large hexagonal platelets

growing on the surface. XRD of the higher voltage deposition, shown in Figure 8-7b, reveals significantly higher intensity lithium niobite peaks suggesting the higher voltage drives the formation of lithium niobite platelets as was previously observed [95].

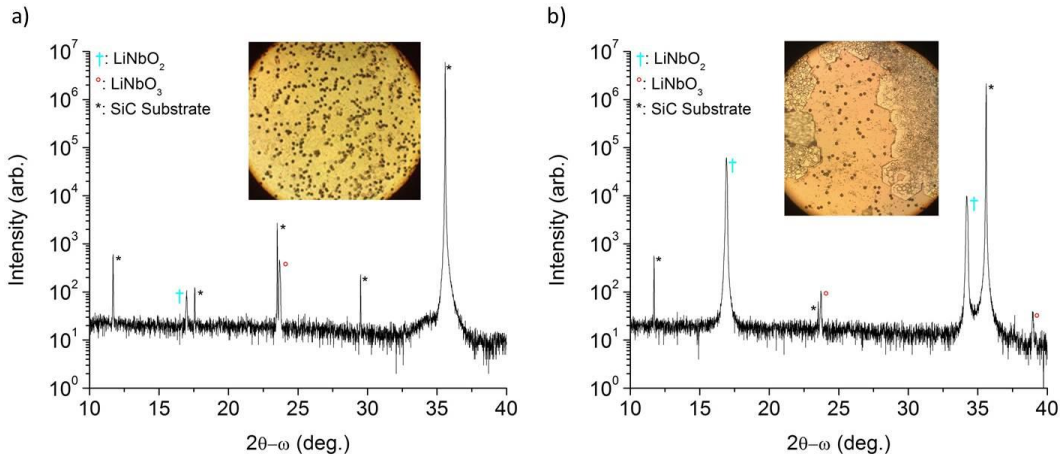

Figure 8-7: Symmetric XRD and optical images from films deposited from a solution with a molar ratio of 26.7:1 at a) 1.2V and b) 1.8V. The low voltage deposition produced a mixture of lithium niobiate ($LiNbO_3$) and lithium niobite ($LiNbO_2$). The high voltage deposition produced platelets of predominately lithium niobite as was previously observed.

Depositions from a melt with a molar ratio of 8.9:1 were crystagraphically similar to depositions from the melt with a molar ratio of 26.7:1. At low voltages (0.5 V) a mixture of lithium niobite and lithium niobate was formed as shown in Figure 8-8a. At high voltages (1.8 V) only lithium niobite was visible in the XRD as shown in Figure 8-8b. However, neither deposition produced large XRD peaks.

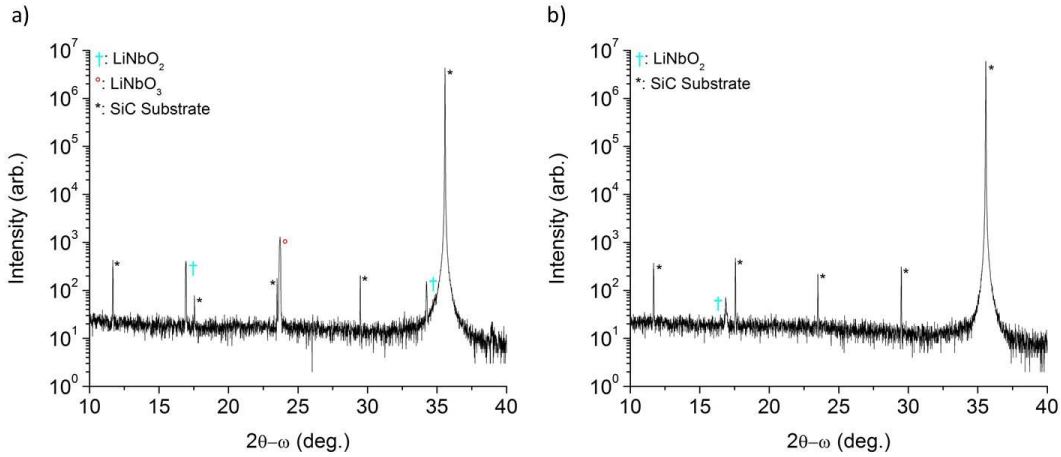

Figure 8-8: Symmetric XRD from films deposited from a solution with a molar ratio of 8.9:1 at a) 0.5V and b) 1.8V. The low voltage deposition produced a mixture of lithium niobiate ($LiNbO_3$) and lithium niobite ($LiNbO_2$). The high voltage deposition produced predominately lithium niobite. Neither deposition produced material with large XRD peaks.

The reason for the small XRD peaks shown in Figure 8-8 is that little material adhered to the SiC substrates. As shown in Figure 8-9, a melt with a molar ratio of 8.9:1 contains enough source material to produce volume nucleation within the melt itself. These free standing crystals are removed when the borate solution is dissolved away from the substrate.

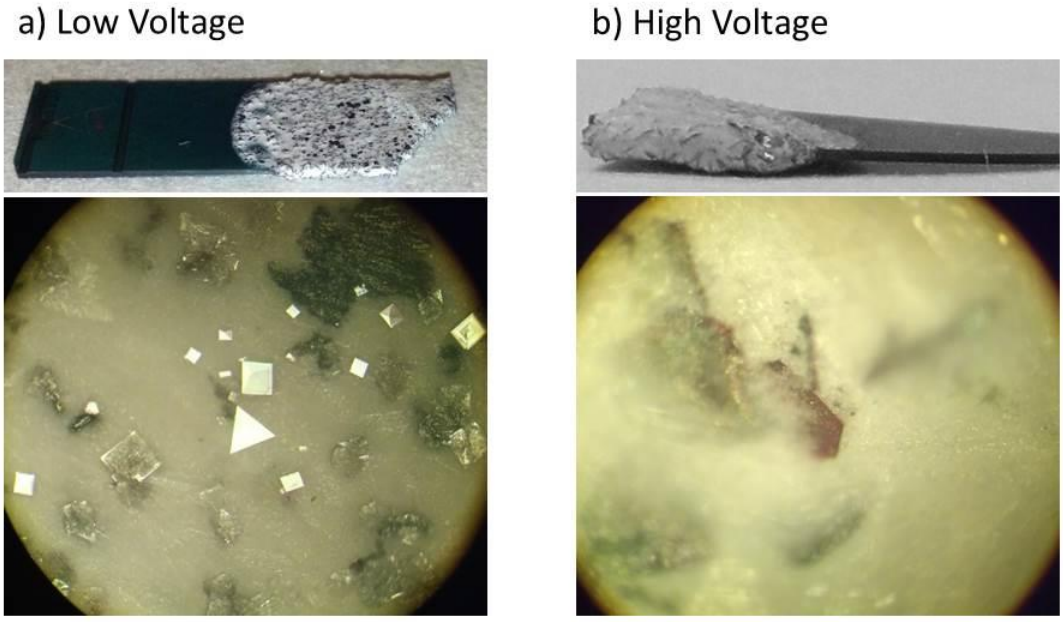

Figure 8-9: optical images of the material deposited from a solution with molar ratio 8.9:1. At both a) low voltage (0.5V) and b) high voltage (1.8V) volume nucleation within the molten solution produces crystals away from the substrate surface.

Examining the depositions performed at a variety of applied voltages and melt ratios, two conclusions can be made. First, increasing the amount of Nb_2O_5 dissolved into the melt changes the mass transport properties of the deposition so that at low concentrations it is possible to have a mass transport limited deposition and at high concentrations the deposition is always reaction rate limited. In addition, increasing the Nb_2O_5 concentration increases the average oxidation state of the melt allowing the formation of higher oxidation state materials such as lithium niobate.

The second conclusion is that increasing the applied voltage reduces the oxidation state of the deposited material. This conclusion should be expected because the applied electric field drives cations toward the SiC electrode and anions away from the SiC electrode. However, the oxidation state of the resulting deposition is not purely derived from the applied voltage as the Nb_2O_5 concentration also affects the deposited material.

8.4 Homoepitaxial Growth of Bulk Lithium Niobite

The ideal form of bulk lithium niobite to replicate the biological sea of ions in an ion based neuromorphic architecture would be free standing lithium niobite wafers. Previously reported LPEE of lithium niobite created free standing crystals with dimensions of a few millimeters. These depositions often yielded crystals with larger apparent dimensions that were composed of multiple small crystals attached together as shown in Figure 8-10. It is unclear if the larger collections of crystals were attached by nucleating new crystallites onto the face of the growing crystal or by bonding crystals together with non-soluble reaction products. When breaking apart the attached crystals a white powder is often visible between the individual crystals.

Figure 8-10: Example of a bulk lithium niobite crystal composed of layers of smaller crystals. It is unclear if this layering is due to nucleating new crystals onto the surface of the growing crystal or due to the precipitation of insoluble material between the individual crystals.

Reduction of the borate melt to form an insoluble compound is one option for the source of the observed white powder. It is known that lithium metaborate ($LiBO_2$) participates in the electrochemical reaction to form lithium niobite because it is the only source of lithium present in the melt. Removing lithium from lithium metaborate yields lithium tetraborate ($Li_2B_4O_7$). Lithium tetraborate has a melting point of 917 ^oC higher than the 900 ^oC operating temperature previously used. Therefore, all attempts to grow bulk lithium niobite herein were performed at an operating temperature of 950 ^oC to avoid lithium tetraborate precipitants.

Attempts to grow bulk lithium niobite by homoepitaxial LPEE were performed at the previous standard operating conditions (1.1 V from a molten solution with molar ratio 15:1) [95]. Multiple iterations of 1 hour depositions were performed. After each deposition, the largest single crystal was chosen to seed the next deposition and a new solution was prepared. After three iterations the seed had grown from less than 0.01 g to 0.71 g, but still consisted of multiple layers of material as shown in Figure 8-11.

Figure 8-11: Bulk lithium niobite crystal grown by homoepitaxial LPEE

CHAPTER 9

DEVICE MODEL FOR VOLATILE MEMRISTORS WITH LOW ACTIVATION ENERGY FOR ION MOTION

Memristive systems are described by the set of Equations 9.1 – 9.2, where $\vec{u}$, $\vec{y}$, and $\vec{x}$ are respectively the system input, the system output, and an internal state variable and functions f and g are arbitrary [26]. These three variables are generally vector quantities allowing for multiple inputs, multiple outputs, and multiple internal mechanisms. This formalism provides a framework to describe multi-functional memristive devices that can be controlled electrically, thermally, chemically, optically, or magnetically.

$$\frac{d\vec{x}}{dt} = f(\vec{x}, \vec{u}, t) \qquad \text{Equation 9.1}$$

$$\vec{y} = g(\vec{x}, \vec{u}, t) * \vec{u} \qquad \text{Equation 9.2}$$

While the mathematical, state variable description for a memristor provides no insight into the physical mechanisms behind a real device, mixed ion-electron conductors (MIEC) such as lithium niobite [73] have demonstrated a rich set of behaviors including energy storage, rectification, negative differential resistance, and memristive hysteresis [180, 181]. In general, the kinetics of atomic motion are governed by ionic hopping conductivity [181] thermally activated according to an Arrhenius relation, as shown in Equation 3.5. Shown in Table 1 are a variety of MIEC memristors and their associated activation energies for ion motion.

9.1 Activated Mobile Ion Hopping Conduction

Ion conduction between discretely bound sites can be described by hopping conductivity where the hopping frequency (Γ) is given by Equation 9.3 [182, 183].

$$\Gamma = \left[\omega_o(1-c)e^{-\left(\frac{2d}{\alpha}\right)}\right] e^{-\left(\frac{E_A}{kT}\right)} \qquad \text{Equation 9.3}$$

Where ω_o is the hopping attempt frequency (related to the phonon frequency), c is the probability of finding an occupied site at the hopping destination and is dependent on the vacancies present, d is the hopping distance, E_A is the energy barrier between hopping sites, k is the Boltzmann constant, T is temperature in Kelvin, and α is a localization parameter related to the extent of the ion's wavefunction. While we retain the full equation as described by Mott [182, 183], this general form of Equation 9.3 is often simplified by replacing the bracketed term with one value by combining the distance dependence into the attempt frequency and ignoring the probability of finding an unoccupied site, which is acceptable for dilute concentrations.

When exposed to an electric field E, the energy barrier E_A is lowered by qEd in the direction of the electric field and raised by the same amount opposing the electric field, as shown in Equation 9.4, where q is the charge of an electron.

$$\Gamma = \omega_o(1-c)e^{-\left(\frac{2d}{\alpha}\right)} e^{-\left(\frac{E_A - qEd}{kT}\right)} \qquad \text{Equation 9.4}$$

The resulting current density, J_{ij}, from site i to neighboring site j with corresponding ion concentration N_i and N_j can be described by Equation 9.5.

$$J_{ij} = ZqdN_i\Gamma_{ij} - ZqdN_j\Gamma_{ji} \qquad \text{Equation 9.5}$$

where Z is the charge of the ion. Substituting the hopping frequency into the above equation and separating common terms yields Equation 9.6.

$$J_{ij} = ZqdN_o\omega_o e^{-\left(\frac{2d}{\alpha}\right)}\left[c_i\left(1-c_j\right)e^{-\left(\frac{E_A-qEd}{kT}\right)} - c_j(1-c_i)e^{-\left(\frac{E_A+qEd}{kT}\right)}\right]$$

Equation 9.6

where the concentrations N_i and N_j are separated into the stoichiometric concentration N_o and the probability of finding an ion at that site c_i such that $N_i = N_o c_i$ and likewise for site j. Equation 9.6 can be reduced to Equation 9.7 by separating the common activation energy term.

$$J_{ij} = Zqd\omega_o N_o e^{-\left(\frac{2d}{\alpha}\right)}e^{-\left(\frac{E_A}{kT}\right)}\left[c_i e^{\left(\frac{qEd}{kT}\right)} - c_j e^{-\left(\frac{qEd}{kT}\right)} - 2c_i c_j \sinh\left(\frac{qEd}{kT}\right)\right]$$

Equation 9.7

Equation 9.7 can be linearized for small electric fields where the concentration gradient is small and the exponential terms are nearly linear. The linearized form of the electric field modified activation energy is given by Equation 9.8.

$$e^{-\left(\frac{E_A-qdE}{kT}\right)} \approx e^{-\left(\frac{E_A}{kT}\right)}\left(1+\frac{qdE}{kT}\right)$$ Equation 9.8

Substituting this linearization into the hopping current density, Equation 9.7, yields the linearized ion current density, Equation 9.9, which can be further simplified into Equation 9.10.

$$J_{ij} = ZqdN_o\omega_o e^{-\left(\frac{2d}{\alpha}\right)}\left[c_i\left(1-c_j\right)e^{-\left(\frac{E_A}{kT}\right)}\left(1+\frac{qdE}{kT}\right) - c_j(1-c_i)e^{-\left(\frac{E_A}{kT}\right)}\left(1-\frac{qdE}{kT}\right)\right]$$

Equation 9.9

$$J_{ij} = ZqdN_o\omega_o e^{-\left(\frac{2d}{\alpha}\right)}e^{-\left(\frac{E_A}{kT}\right)}\left[\left(c_i+c_j-2c_ic_j\right)\left(\frac{qdE}{kT}\right)+\left(c_i-c_j\right)\right]$$ Equation 9.10

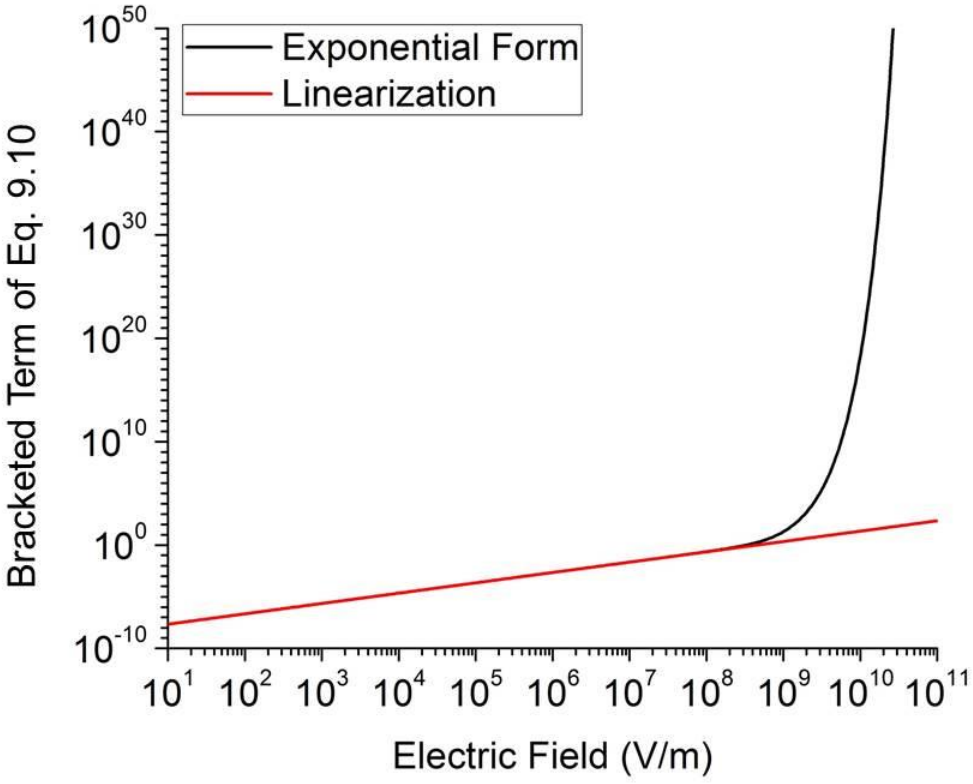

Figure 9-1: The bracketed terms in the full exponential form of hopping conductivity, Equation 9.7, and the linearized form, Equation 9.10. The linear approximation matches the exponential form at low electric fields but diverges at high electric fields. This data was calculated using d = $3x10^{-10}$ m and T = 800K.

As shown in Figure 9-1, the linear approximation is not valid for fields as high as 10^{10} V/m, as are experienced during the breakdown of filamentary memristors, but is approximately true for fields as high as 10^{8} V/m, which covers most of the practical breakdown fields in real materials. Therefore, for large devices such as $LiNbO_2$ memristors [74] with length scales on the order of 100 μm and low electric fields, the ion current can be linearized.

By factoring the bracketed term, the linearized ion hopping current equation appears as a classical drift – diffusion equation, shown in Equation 9.11, where the

mobility and diffusion coefficient become concentration dependent, as shown in Equations 9.12 – 9.14.

$$J_{ij} = Zqd^2 N_o \omega_o e^{\left(\frac{-2d}{\alpha}\right)} e^{-\left(\frac{E_A}{kT}\right)} \left(c_i + c_j - 2c_i c_j\right) \frac{q}{kT} \left[E - \frac{kT}{q}\left(\frac{1}{c_i + c_j - 2c_i c_j}\right)\frac{\left(c_j - c_i\right)}{d}\right]$$

$$= ZqN\left(\mu_{hopping} E - D\frac{\left(c_j - c_i\right)}{d}\right) \qquad \text{Equation 9.11}$$

Where,

$$\mu_{hopping} = 2\omega_o d^2 e^{\frac{-2d}{\alpha}} e^{-\frac{E_A}{kT}} \left[\frac{kT}{q}\right]^{-1} \left(1 - \frac{2c_i c_j}{c_i + c_j}\right) \qquad \text{Equation 9.12}$$

$$N = N_o \frac{c_i + c_j}{2} \qquad \text{Equation 9.13}$$

$$D = \frac{1}{2}\frac{kT}{q}\left(\frac{c_i + c_j}{\left(c_i + c_j - 2c_i c_j\right)^2}\right)\mu_{hopping} \qquad \text{Equation 9.14}$$

9.2 Generalized Memristor Model

To develop a mathematical model for mixed ion-electron memristors, we begin with the general system of equations for a memristive device, Equations 9.1 – 9.2, informed by the ion hopping kinetics previously developed, Equations 9.11 – 9.14. We define the input to the system as the applied voltage V and the output of the system as the current through the device I. The specific physical state variable parameters replacing the generalized state variables, $\vec{x}$, are the scalars φ, representing the distribution of ions, and the temperature T. Rewriting Equations 9.1 – 9.2 with the above variables yields Equations 9.15 – 9.17.

$$I = G(\vec{x}, V, t) * V = G(\varphi, T, V, t) * V \qquad \text{Equation 9.15}$$

$$\frac{d\vec{x}}{dt} = f(\vec{x}, V, t) = f(\varphi, T, V, t) \qquad \text{Equation 9.16}$$

$$\vec{x} = \begin{bmatrix} x_1 \\ x_2 \end{bmatrix} = \begin{bmatrix} \varphi \\ T \end{bmatrix}$$ Equation 9.17

where G is function describing the device conductance and t is time. Looking first at the state variable dynamics, Equation 9.16, the temperature of the device can be easily approximated by the differential Equation 9.18 that balances Joule heating and conductive heat transfer.

$$\frac{dx_2}{dt} = \frac{dT}{dt} = \frac{1}{m*C} * \left[G * V^2 - \frac{k*A*(T-T_E)}{\Delta L} \right]$$ Equation 9.18

Equation 9.18 is the result of thermal energy input to the device by Joule heating and conductive heat transfer removing heat from the device along a thermal length. The device's temperature change is governed by the total heat capacity. The variables involved are: m is the mass of the device, C is the material's specific heat capacity, V is the applied voltage, k is the thermal conductivity, A is the surface area of the device, T_E is the temperature of the environment, and ΔL is the length for thermal transfer. The first term in the brace describes Joule heating while the second term is the conductive heat loss. No explicit device geometry is defined for this generalization, but various geometries can be approximated by changing the mass, surface area, and thermal transfer length.

While the temperature dynamics can be derived from basic physical relationships, the specific dynamics of the ion distribution state variable φ will depend generally on the internal physics of the modelled device. However, it will be shown that the rich behavior of memristive devices can be described by the ion distribution state variable dynamics shown in Equation 9.19.

$$\frac{dx_1}{dt} = \frac{d\varphi}{dt} = A * V - D * \varphi$$ Equation 9.19

A is a parameter dependent on device geometry (i.e. scaling of voltage to electric field), but in more complex implementation can encompass many other physical effects that relate the external applied voltage to the change in ion distribution. A is thus a generalized parameter describing the strength of the applied voltage V on the ion distribution state variable. Likewise, D describes the strength of ion distribution recovery accounting for physical effects such as diffusion. The ion distribution state variable dynamics, Equation 9.19, build on earlier models that include the first voltage driven term but neglect any recovery mechanisms [46]. It should be noted that the ion distribution state variable, φ, cannot be explicitly defined outside the context of a specific device geometry and as such the units of φ, A, and D are not yet definable.

In general, the coefficients A and D can be functions of many variables. However, because they describe the ease of ion motion, both coefficients must follow an Arrhenius relationship and thus, from Equations 9.11 – 9.12, account for the ion motion activation energy shown in Equation 9.20.

$$A, D \propto e^{-\frac{E_A}{kT}} \qquad \text{Equation 9.20}$$

Examining Equation 9.20, it is clear that in the steady state when there is no net ion movement (i.e. $\frac{d\varphi}{dt} = 0$), the voltage driven term and distribution recovery term must balance. This limits the extent of the ion distribution state variable placing a maximum value on φ, shown in Equation 9.21, for a given maximum voltage V_{max}.

$$\varphi_{max} = \frac{AV_{max}}{D} \qquad \text{Equation 9.21}$$

Finally, while the ion motion is controlled by the activation energy and available thermal energy, the conductivity of the device is controlled by the available electrons (or holes) and their distribution. The exact form of the device conductivity as a function of

ion distribution G(φ) will depend on the specific memristor. Equations 9.15, 9.18, and 9.19 combined forms a set of equations that fully describe memristor behavior, specifically, the conductance, thermal response, and the associated thermally activated hopping motion of ions. The task for modelling memristors of differing underlying physics is then to define A, D, and a functional relationship between G and φ.

9.3 Lithium Niobite Memristor Model

For the lithium niobite volatile memristor the internal state variable is based on a continuous ion distribution. Finite element models of the $LiNbO_2$ memristor [87] show transient complex ion distributions and the resulting conductance. However, in all cases, at slow excitation or in steady state, the complex ion distributions collapse into a steady state linear ion distribution and an associated conductance. In these materials operated in electric fields from 10^1 to 10^5 V/m, the linearized mobility model is certainly valid. Given this linear ion distribution and its associated conductance state, one can easily connect the ion distribution (a slope in steady state) to the conductance, G, and again connect that conductance to the flux-linkage, φ, through the use of the current-voltage curve.

Examining experimental data, shown in Figure 9-2, from a large scale volatile $LiNbO_2$ memristor, the characteristic pinched hysteresis of a memristor is observed. This data was measured at 42 mHz on a lateral ring-dot structure with asymmetric contact areas and a device length of 55 μm.

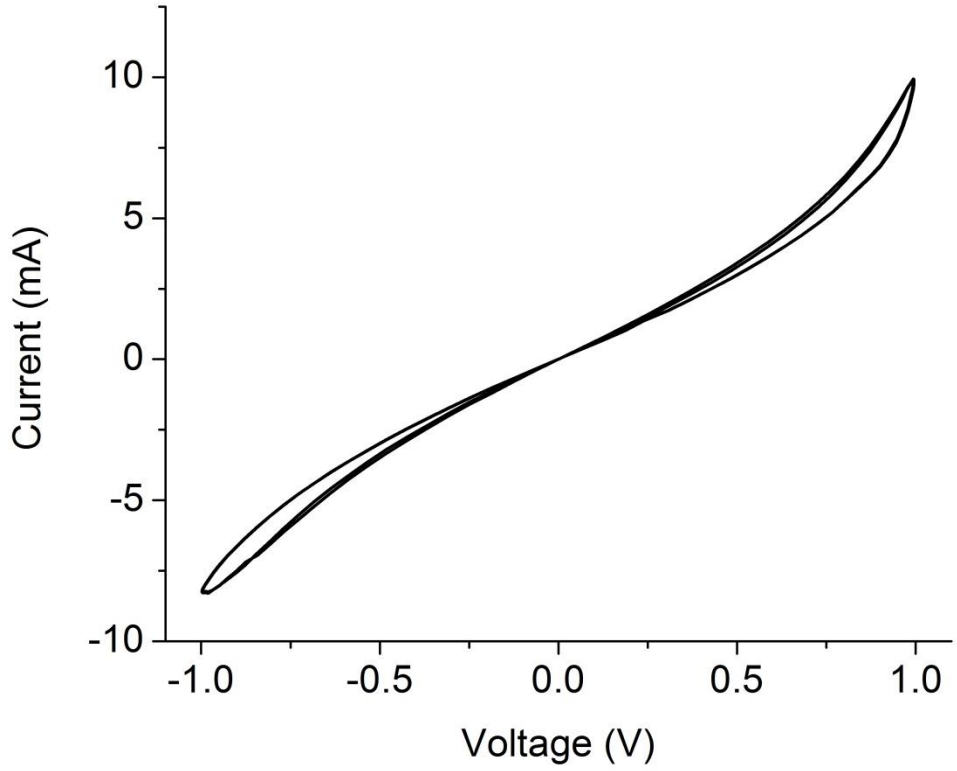

Figure 9-2: The experimental current – voltage relation for a volatile $LiNbO_2$ memristor measured at 42 mHz.

Since the conductance of the device is known from the slope of the current-voltage curve for each time point and the flux-linkage can be determined as the time integral of the voltage, one can plot the experimental data in Figure 9-2 as a conductance versus flux-linkage as shown in Figure 9-3. The flux linkage represents the combined effects of an applied voltage and the time the voltage has been applied making small voltages applied for long times as effective as large voltages for short times. In Figure 9-3, two conductance values at zero φ and asymmetric shape around zero φ are apparent. This asymmetry in the experimental data is likely due to asymmetric contacts on the ring-

dot structure and is not accounted for in the following model. Such effects have been accounted for in previous finite element models [87].

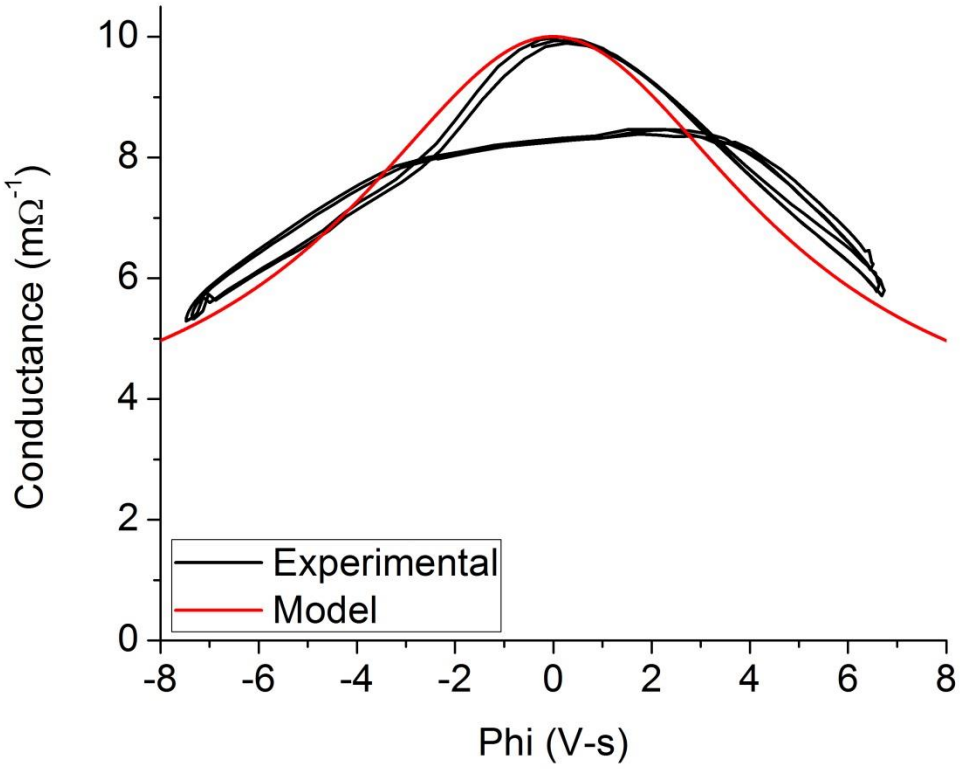

Figure 9-3: The experimental Conductance – Phi relation from a $LiNbO_2$ memristor and the fit used to model the device. The two values at Phi = 0 are due to the asymmetric contact geometry of the experimental device. By modelling only one contact geometry a symmetric device is modelled.

Fitting the experimental data for one of the contact polarities, which forces a symmetric response, the following conductance, shown in Equation 9.22, was empirically fit to the experimental volatile memristor conductance.

$$G(\varphi) = G_L - \frac{G_L - G_H}{1+(c\varphi)^2} \qquad \text{Equation 9.22}$$

Where G_H = 0.01 Ω^{-1} is the high conductance state, G_L = 0.005 Ω^{-1} is the low conductance state, and c = 0.2 is a width parameter used to fit the experimental data.

For steady state simulations, it has been shown that the ion concentration profile, N(x), in these volatile memristors is linear [87]. However, a linear ion distribution is incompatible with the current continuity equation when simplifications are made that are necessary for a simple model compatible with large scale circuit applications. Such simplifications include a uniform electric field and a negligible space charge due to ion-electron separation (i.e. quasi-neutrality). The linear ion distribution incompatibility arises because the derivative of the current density (dJ/dx) does not include a diffusion term necessary to balance the drift term and bring the ion motion (dN_{Li}/dt) to zero as shown in Equation 9.23.

$$\frac{dN}{dt} = -\frac{1}{q}\frac{dJ}{dx} = -\frac{1}{q}q\mu_{Li}\frac{dN}{dx}E \neq 0 \qquad \text{Equation 9.23}$$

This non-physical result is likely due to the two assumptions above. At long time scales the electrons and ions separate violating quasi-neutrality and setting up an electric field opposing the applied field. However, for shorter time scales, a transient ion distribution occurs [87] that is modelled herein as a cubic ion distribution profile as shown in Equation 9.24.

$$N(x) = N_o + \gamma(t)\left(x - \frac{L}{2}\right) + \lambda(t)\left(x - \frac{L}{2}\right)^3 \qquad \text{Equation 9.24}$$

The cubic distribution does not violate the current continuity equation and can thus be modelled simply as shown in Equation 9.25.

$$\frac{dN}{dt} = -\frac{1}{q}\frac{dJ}{dx} = \mu_{Li}\frac{dN}{dx}E - qD_{Li}\frac{d^2N}{dx^2} \qquad \text{Equation 9.25}$$

Taking the first and second derivatives of Equation 9.24 and inserting them into Equation 9.25 yields Equation 9.26.

$$\frac{dN}{dt} = \mu_{Li}\left(\gamma(t) + 3\lambda(t)\left(x - \frac{L}{2}\right)^2\right)E - qD_{Li}\left(6\lambda(t)\left(x - \frac{L}{2}\right)\right) \qquad \text{Equation 9.26}$$

Because γ(t) and λ(t) are of the same order of magnitude for the modelled devices and the length scale is on the order of 10^{-2} cm, the second drift term is much smaller than the first drift term and may be dropped. This simplification yields Equation 9.27.

$$\frac{dN}{dt} = \mu_{Li}\gamma(t)E - 6qD_{Li}\left(x - \frac{L}{2}\right)\lambda(t) \qquad \text{Equation 9.27}$$

At long time scales the ion distribution becomes linear and the cubic term in the ion distribution, λ(t), presumably goes to zero. However, for faster time scales the linear term γ(t) is nearly constant and the cubic term becomes the dominant time dependent term. An estimate for the frequency at which this transition occurs can be determined from previous finite element models that examine the step response of $LiNbO_2$ memristors [21]. Previous models have shown that for a device with order 1 um length, a cubic profile is present 0.1 sec after the voltage step, but a linear profile is present after 1 sec [87]. Scaling these times for the 100 um device modelled herein, it is expected that the cubic approximation can be made for time scales shorter than 10 seconds or faster than 0.1 Hz. This is consistent with experimental results testing the step response of $LiNbO_2$ memristors [21]. Thus for the time scales of interest to neuromorphic computing (0.1 – 100 Hz) the linear term can be treated as effectively constant, $\gamma(t) \approx \gamma$, and the cubic term is the dominant time dependent term in the ion motion. Taking the time derivative of the ion concentration under this assumption yields Equation 9.28.

$$\frac{dN}{dt} = \frac{d\lambda(t)}{dt}\left(x - \frac{L}{2}\right)^3 \qquad \text{Equation 9.28}$$

Evaluating the change in ion concentration at the contact (x = L) and setting Equation 9.27 and Equation 9.28 equal, we then obtain the ion dynamics Equation 9.29.

$$\frac{d\lambda(t)}{dt} = \mu_{Li}\gamma\left(\frac{L}{2}\right)^{-3}E - 6D_{Li}\left(\frac{L}{2}\right)^{-2}\lambda \qquad \text{Equation 9.29}$$

This dynamical equation follows the same form as Equation 9.19 allowing the assignment of the ion distribution state variable, φ, to be the cubic ion distribution term, λ. Thus the ion dynamics can be written as Equations 9.30 – 9.32.

$$\frac{d\varphi}{dt} = \left[\frac{8\mu_{Li}\gamma}{L^4}\right]V - \left[\frac{24D_{Li}}{L^2}\right]\varphi = AV - D\varphi \qquad \text{Equation 9.30}$$

$$A = \frac{8\mu_{Li}\gamma}{L^4} \qquad \text{Equation 9.31}$$

$$D = \frac{24D_{Li}}{L^2} \qquad \text{Equation 9.32}$$

The simulated result, shown in Figure 9-4, matches the experimental results except at negative voltages where the change from an asymmetric to a symmetric device becomes apparent.

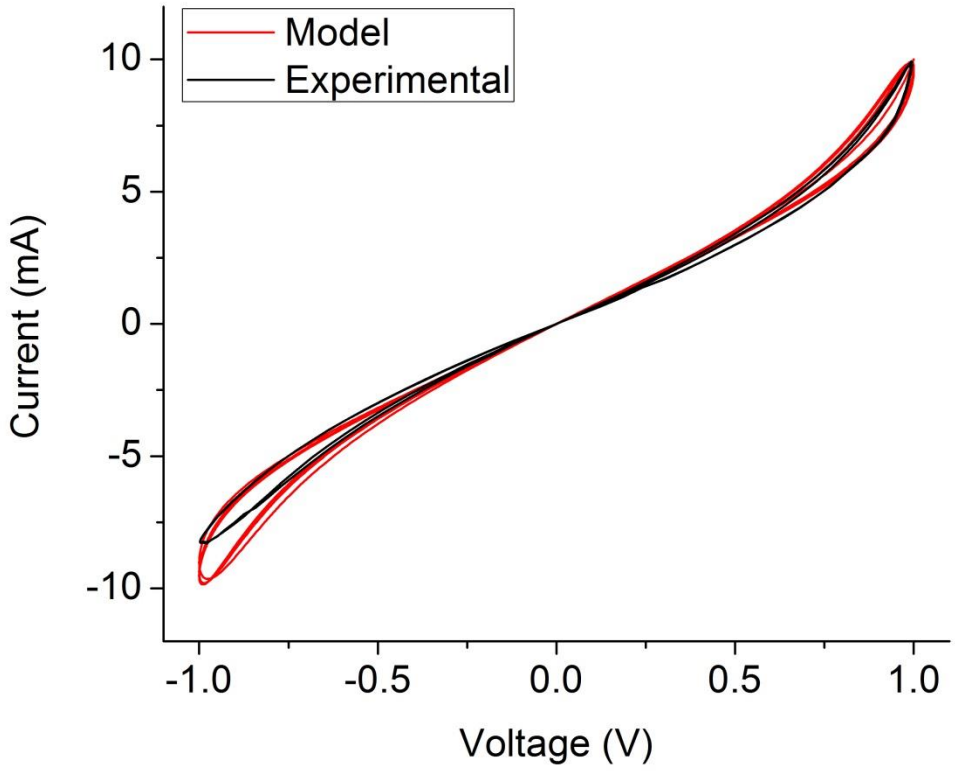

Figure 9-4: Simulated and experimental current – voltage relation of a volatile memristor based on $LiNbO_2$. Deviation between the modelled and experimental results at negative voltages is due to the asymmetric geometry of the experimental device, which was not considered for the model.

In addition, the activation of ion motion by thermal energy is not necessary for the low activation energy lithium motion as the temperature of the simulated device varies by less than 1^oC as shown in Figure 9-5.

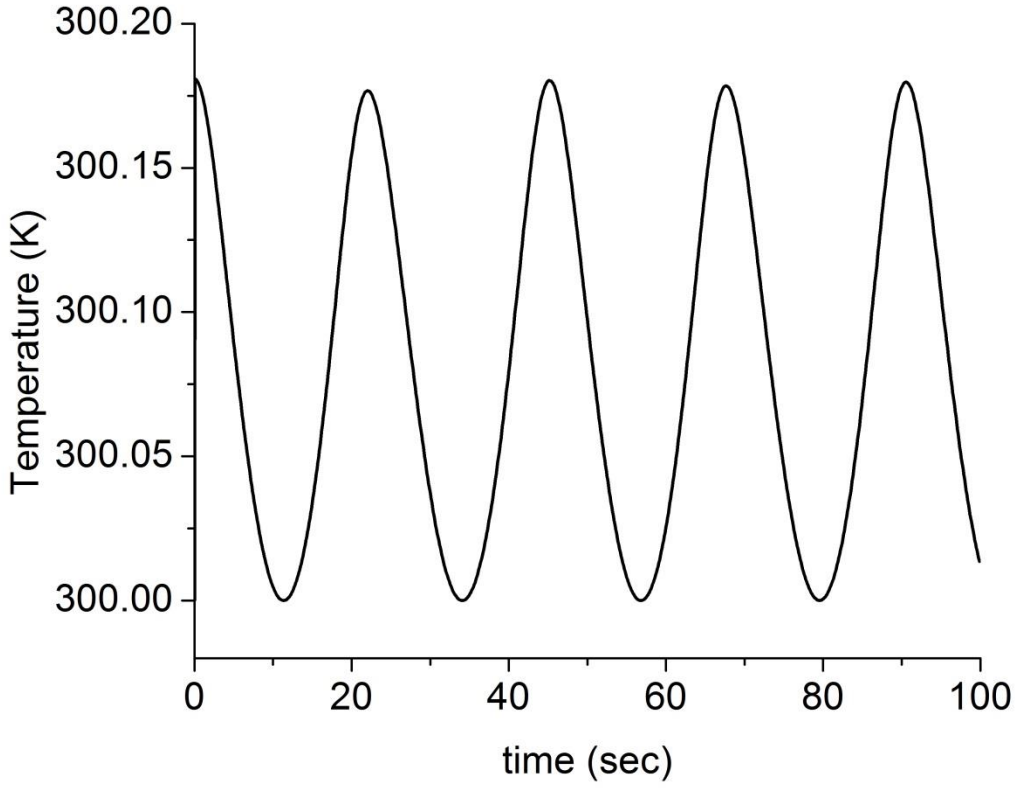

Figure 9-5: The temperature of a simulated volatile memristor showing effectively room temperature operation.

It was theorized that for memristive mobile ion-electron conductors (MIECs), a decrease in frequency would lead to a current-voltage relation with peaks as the mobile dopants redistribute [180]. This effect is reproduced, as shown in Figure 9-6a, using the same simulation parameters as in the volatile memristor example, by decreasing the frequency one order of magnitude. It should be noted that this current-voltage relation is distinctly different than that for the filamentary memristor, which also exhibits a peak with dynamic negative differential resistance. The difference arises near the origin where a filamentary memristor's current-voltage relation crosses at the origin, but a volatile memristor's current-voltage relation is pinched at the origin. The peaks in the volatile

memristor current-voltage curve result from diffusion assisted ion recovery returning the ion gradient to zero before the voltage reaches the maximum value. When the ion gradient (φ) is zero, the conductance is maximized as shown in Figure 9-3.

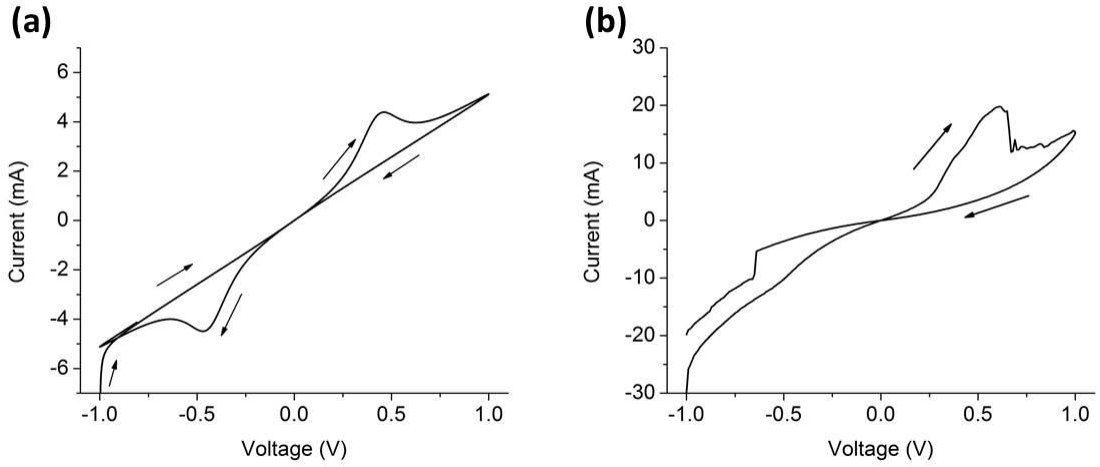

Figure 9-6: a) Simulated current – voltage relation for a volatile memristor at low frequency exhibiting dynamic negative differential resistance as ionic diffusion returns the ion gradient to zero before the voltage reaches a maximum. b) Experimental data showing dynamic negative differential resistance and an initial high conductance transient.

This dynamic negative differential resistance has been experimentally observed in lithium niobite volatile memristors. As shown in Figure 9-6b for a single current-voltage sweep, a peak in current occurs before the voltage reaches its maximum value. In addition to the dynamic negative differential resistance, both the simulation, Figure 9-6a, and the experimental data, Figure 9-6b, show an initial increase in resistance as the voltage sweep begins at -1 volt. This initial transient effect is caused by the maximum (in magnitude) voltage (-1 V) occurring at the same time as the maximum conductance state resulting from $V \cdot t=0$ in Figure 9-3. This condition does not occur again after the initial condition because the diffusion assisted ion recovery creates a phase offset between the maximum voltage and flat ion distribution.

9.4 Simplified Model for SPICE Circuit Simulations

Equations 9.30 – 9.32 describing the behavior of a lithium niobite memristor can be implemented directly as a SPICE circuit element as shown in Figure 9-7.

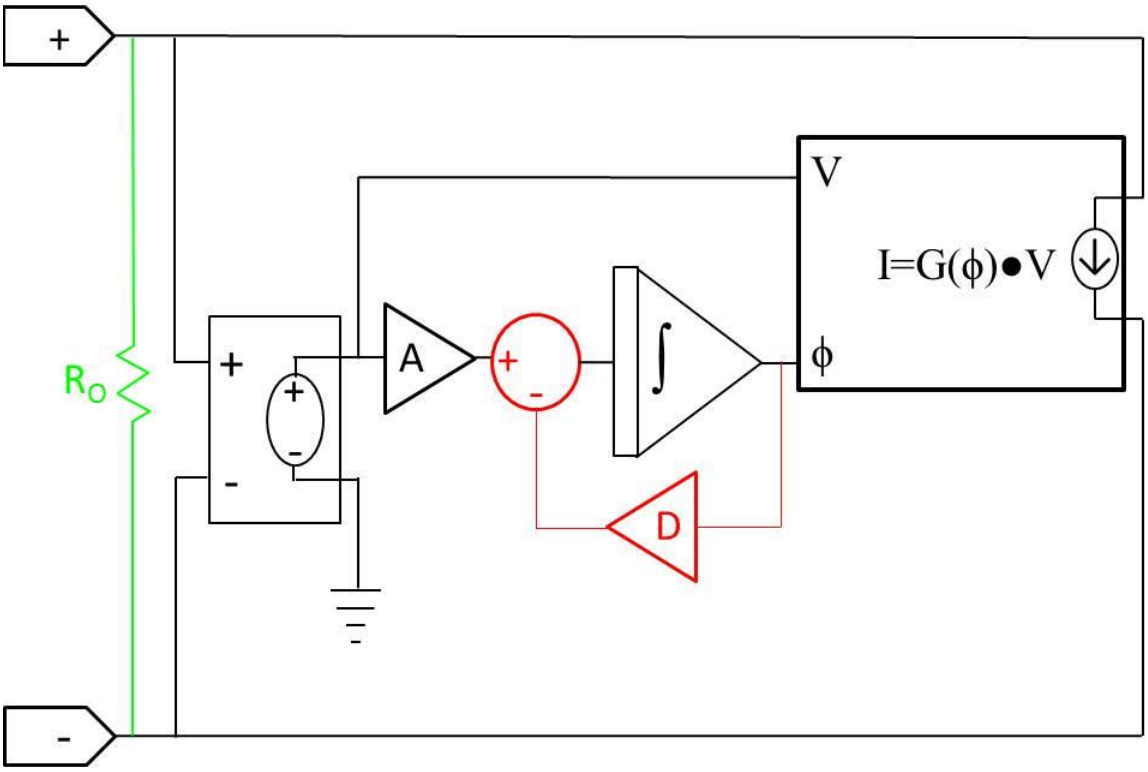

Figure 9-7: SPICE schematic for the memristor model. Portions in black directly implement the characteristic equation of a memristor while the red portion implements feedback necessary for volatile behavior. The input resistor shown in green provides continuity during the first simulation step and should be chosen to have a large value so that it does not affect the model's operation.

The portions of this SPICE implementation shown in black are identical to early memristor SPICE elements that directly implemented the memristor equations without any physical associations [184]. The red feedback loop implements the ion state variable recovery dynamics through the diffusion of lithium ions. Finally, the green resistor R_O should be chosen such that it is significantly more resistive than the device conductance

G in order to minimize its impact on the element. R_O ensures model continuity during the first simulation step.

CHAPTER 10

VOLATILE ADAPTABILITY IN NEUROMORPHIC CIRCUITRY

The device model for a volatile memristor discussed in Chapter 9 is computationally simple while still incorporating physical parameters such as device geometry and dopant levels that can be used to modify device operation parameters such as the device speed and the magnitude of the memristance change. While these volatile memristors could implement simple neural functions such as short term memory as a single device, they do not necessarily implement more complex neuromorphic functions on their own. However, when included in neuromorphic circuits, volatile memristors can add biologically realistic volatile functionality without significantly increasing the complexity of these circuits. Two example circuits are discussed herein including a simple Schmitt Trigger circuit and the Neuristor circuit.

Biologically realistic spike-frequency adaptation is implemented in a Schmitt Trigger based neuron circuit by replacing one of the resistors with a volatile memristor. Likewise, replacing a resistor with a volatile memristor in the Neuristor circuit results in bursting/chattering behavior that is not present in the circuit prior to the change.

10.1 Schmitt Trigger with Spike Frequency Adaptation

Previously a non-volatile memristor with external programming circuitry was included in an op-amp Schmitt Trigger to create a variable threshold Schmitt Trigger [185]. The circuit presented in Figure 10-1 differs from this previous work in two ways that are important for neuromorphic circuit applications. First, the memristor implementation is a volatile analog memristor rather than a non-volatile filamentary

memristor. Second, the circuit presented is self-programming and requires no external programming controller. This leads to a higher computational density. These distinctions make it useful for neuromorphic spike-frequency adaptation.

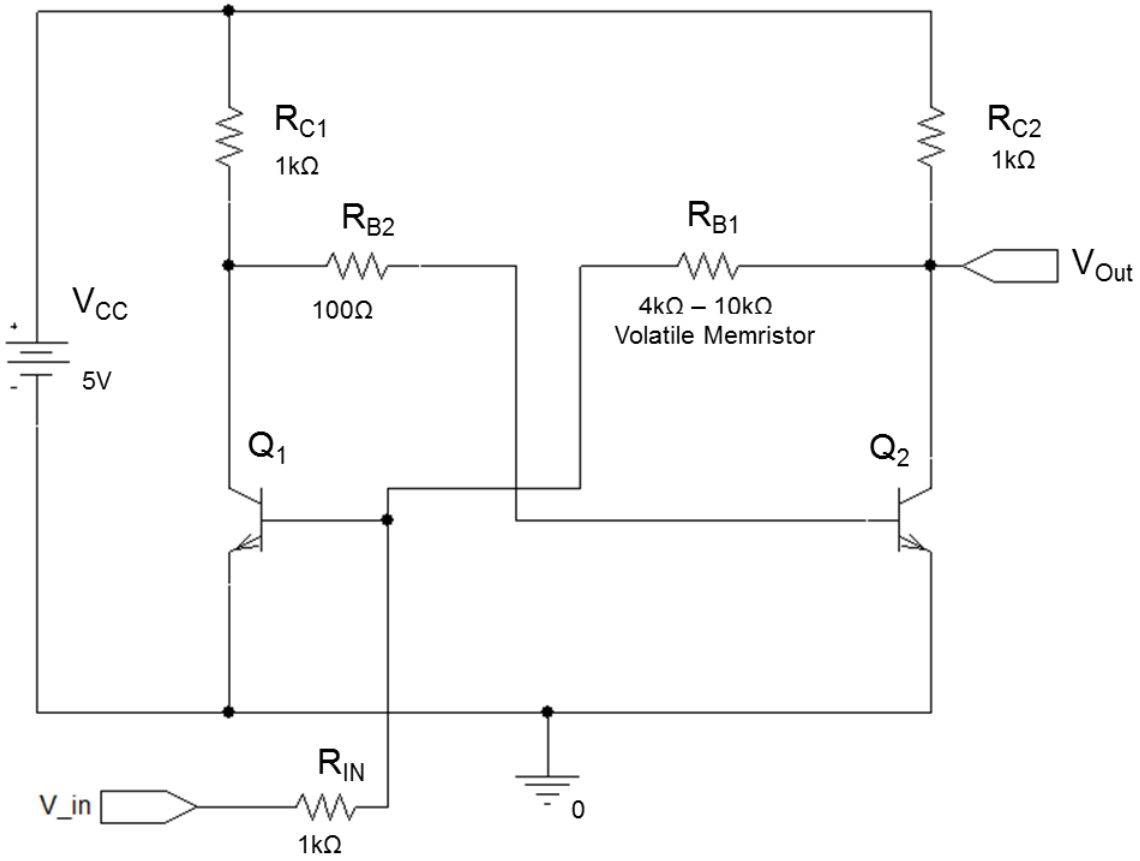

Figure 10-1: A collector-base coupled BJT Schmitt Trigger circuit diagram with a volatile memristor substituted for resistor R_{B1}.

The circuit shown in Figure 10-1 is a classical collector-base coupled BJT Schmitt Trigger. Advantages of this design for a neuromorphic threshold detector are a near zero low-output voltage and a high-output voltage set by the voltage divider R_{C2}, R_{B1}. These two attributes provide a near ground output and an adaptable high state output for the analog spike generation circuit this Schmitt Trigger controls.

The BJT Schmitt Trigger circuit works as follows: while V_{in} is below the rising threshold, transistor Q1 is off and Q2 is on. The output voltage is tied to ground through transistor Q2. The base-emitter voltage of Q1 is set by the voltage divider R_{in}, R_{B1} and the rising threshold occurs when this voltage divider forward biases the base-emitter junction of Q1.

After transitioning to the high-output state, transistor Q1 is on and Q2 is off. The output voltage is set by the voltage divider R_{C2}, R_{B1}. As V_{in} decreases, the falling threshold occurs when the base of Q1 is deprived of current. This requires the current through R_{B1} to equal the current through R_{in}. Assuming ideal BJTs, these thresholds and outputs are given by Equations 10.1 – 10.4.

$$V_{T\uparrow} \approx \frac{(R_{in}+R_{B1})V_{BE}}{R_{B1}} \qquad \text{Equation 10.1}$$

$$V_{T\downarrow} \approx V_{BE} - \frac{R_{in}(V_{cc}-V_{BE})}{R_{B1}+R_{C2}} \qquad \text{Equation 10.2}$$

$$V_{Out-Low} \approx 0 \qquad \text{Equation 10.3}$$

$$V_{Out-High} \approx \frac{R_{B1}(V_{cc}-V_{BE})}{R_{B1}+R_{C2}} \qquad \text{Equation 10.4}$$

Where $V_{T\uparrow}$ is the rising threshold voltage, $V_{T\downarrow}$ is the falling threshold voltage, V_{CC} is the power supply voltage, V_{BE} is the BJT base-emitter forward bias voltage and the low and high subscript on V_{Out} indicates the output voltage in the low and high state respectively.

From Equations 10.1 – 10.4 it is clear that resistor R_{B1} is crucial in setting the rising threshold, the falling threshold, and the high output voltages. Figure 10-2 shows the Schmitt Trigger circuit transfer function for two values of R_{B1} easily achievable with the lithium niobite memristors described in Chapter 5 and Chapter 9.

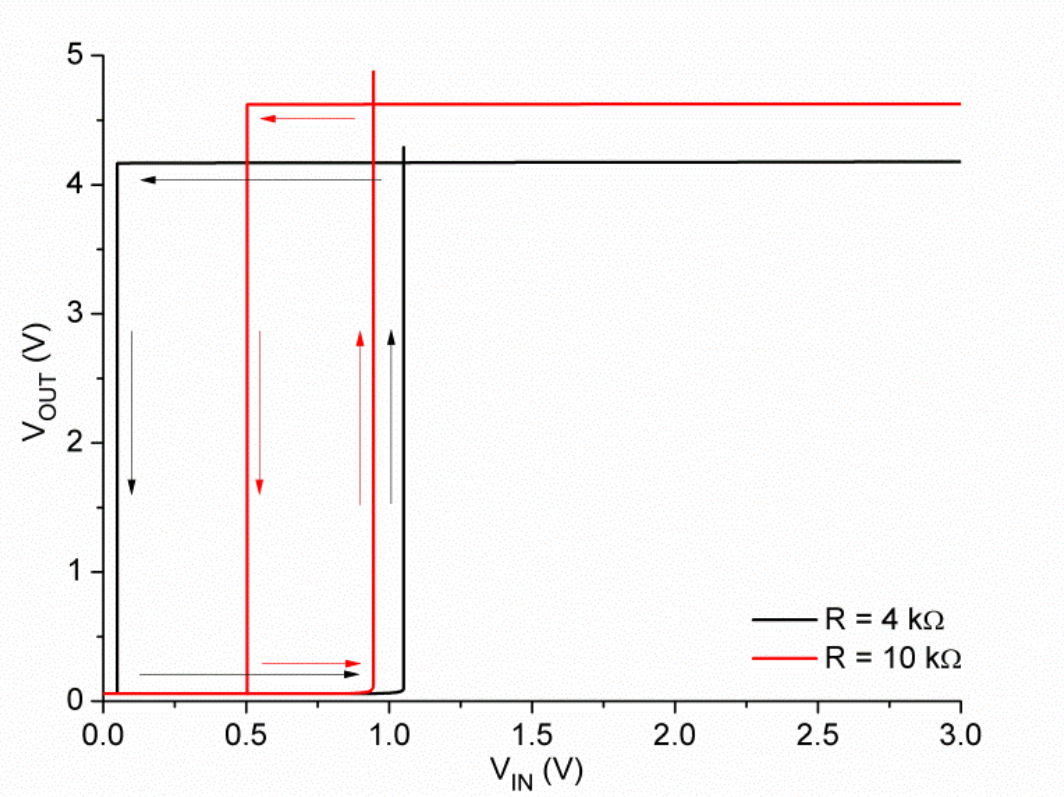

Figure 10-2: Changes in the Schmitt Trigger transfer function for different values of the memristor resistance including changes in the rising threshold voltage, falling threshold voltage, and high output voltage.

Changing the value of R_{B1} by only 150% changes the rising threshold by -10%, the falling threshold by 1000%, and the high output voltage by 10%. The low output voltage remains unchanged in the millivolt range. As the resistance of R_{B1} changes in Figure 10-2 from 10kΩ to 4kΩ, three distinct changes occur that are important for neural processing:

First, the rising threshold voltage increases. The rising threshold indicates how much input signal must be accumulated before the neuron outputs a spike. By increasing the rising threshold voltage, spikes become harder to initiate.

Second, the high output voltage decreases. A decrease in the high output voltage could be used by the spike generation circuit to implement spike-amplitude adaptation. It

is known that some biological neurons exhibit decreasing spike amplitude during bursting behavior while others show no change or more complex behaviors [166].

Third, the falling threshold decreases. This is important because the pulse width is related to the difference between the rising threshold and the falling threshold. After the Schmitt Trigger goes to the high state and initiates an output pulse, feedback must reset the input integrator. Since the Schmitt trigger can only be reset by the integrator being discharged below the falling threshold, the time that the Schmitt Trigger remains in the high state increases as the falling threshold is reduced. This increased spike time is consistent with biological spike-frequency adaptation and may also be useful for spike-shape adaptation in the spike generation circuit. For example, the "afterhyperpolarization" phase of a biological neuron spike becomes more pronounced after a high level input [166]. The increased pulse width produced by the Schmitt Trigger for high level inputs could be used in the spike generation circuit to accomplish this spike-shape adaptation.

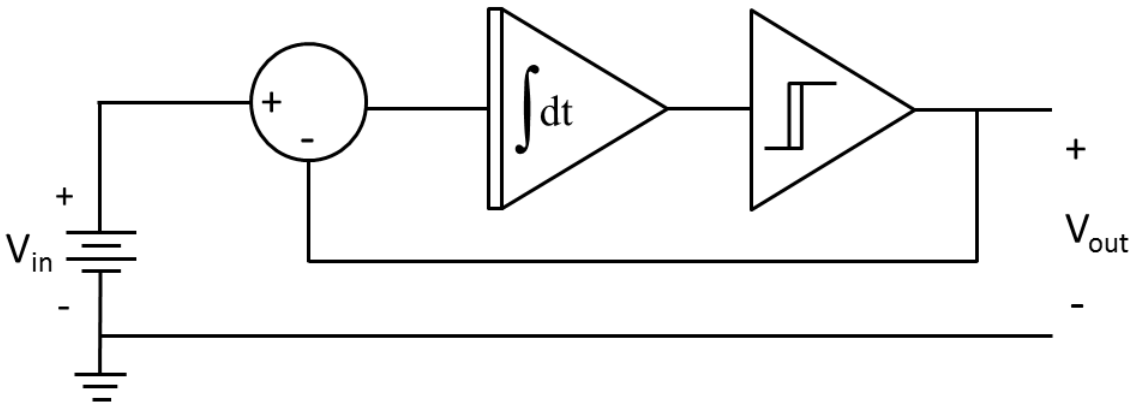

Figure 10-3: Diagram of a simplified neuron used to demonstrate the effects of the volatile memristor Schmitt Trigger on the overall neuron performance. The output of the Schmitt Trigger is fed back to the integrator to reset the integrator after the neuron outputs a spike.

The volatile memristor Schmitt Trigger was simulated in the simplified neuromorphic circuit shown in Figure 10-3. The negative feedback from the Schmitt Trigger to the integrator was used as the integrator reset mechanism.

It has been shown experimentally that for small constant inputs biological neurons produce repetitive spikes with frequencies that scale with the input value. Additionally, larger value inputs produce temporally-expanded spike widths that are sometimes accompanied by decreased spike amplitude [166]. As will be shown, this circuit mimics these biological behaviors that are thought to be crucial for biological and neuromorphic computation.

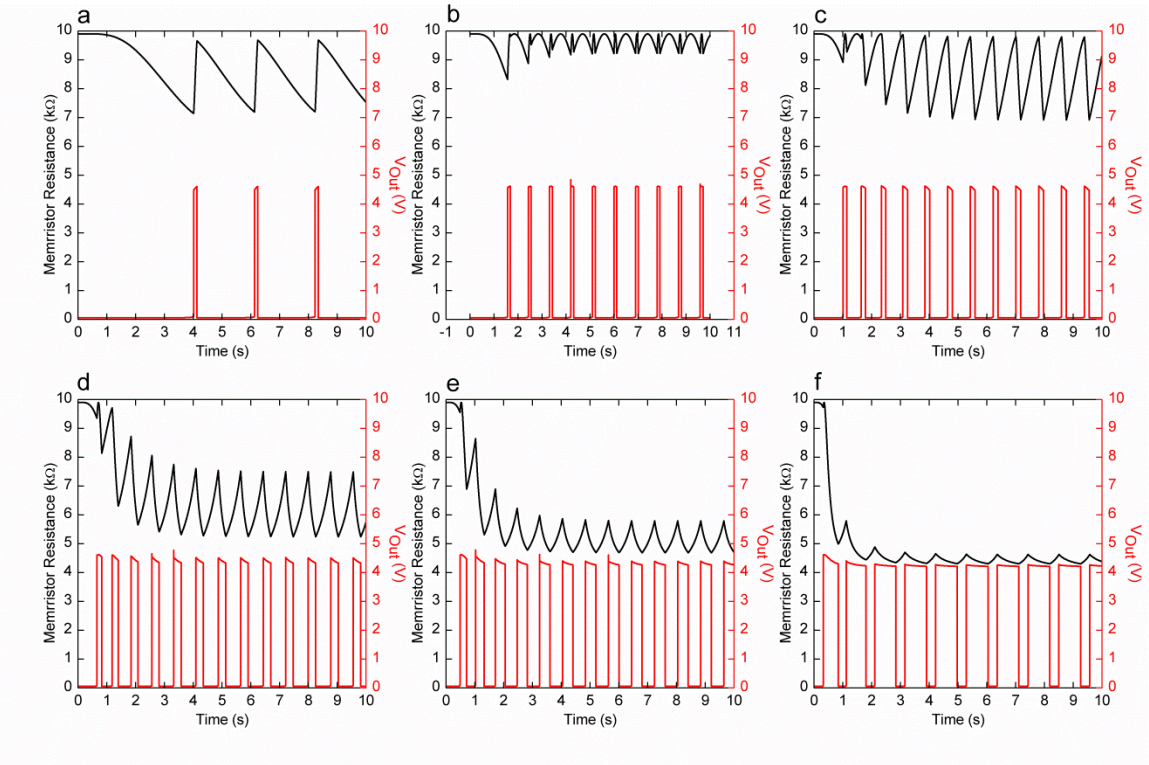

Figure 10-4: The output voltage and memristor resistance for six different DC input voltages to the circuit in Figure 16. The six input voltages are: a) 0.3 V, b) 0.67 V, c) 1 V, d) 1.5 V, e) 2 V, and f) 3V.

The output voltage for the volatile memristor Schmitt Trigger neuromorphic circuit is shown in red in Figure 10-4 for six different DC inputs. For Figure 10-4a-c

corresponding to smaller inputs 0.3 – 1 volts, the circuit produces repetitive pulses that increase in frequency with increasing input. In Figure 10-4d-f corresponding to larger inputs 1.5 – 3 volts, the output shows signs of adaptation including pulse broadening and a smooth decrease in pulse amplitude. Compared to biological pulse broadening, this simulation produced magnified results. Biological neurons broaden spikes by 20% - 100% [166] while this simulation demonstrates pulse broadening of 540%. This increased pulse broadening compared to biological spike broadening could be limited by choosing a smaller memristance change.

Examining the resistance of the volatile memristor for each of these six cases, shown in black in Figure 10-4, reveals why this adaptation occurs. For the small input voltages of Figure 10-4a-c, the memristor programming is balanced by the pulses and inter-pulse intervals so that the resistance remains near 10kΩ corresponding to the $\varphi = 0$ value in Figure 9-3. This allows each successive pulse to start from the same value on the $W(\varphi)$ curve. Thus, the circuit has no memory of previous pulses. For the larger inputs in Figure 10-4d-f, there is insufficient inter-pulse time for the memristor to fully recover back to 10kΩ and the memristor self-programs. This memory functionality of the memristor causes temporary changes in the Schmitt Trigger transfer function and thus the pulse widths and magnitudes. These changes mimic biological spike frequency adaptation.

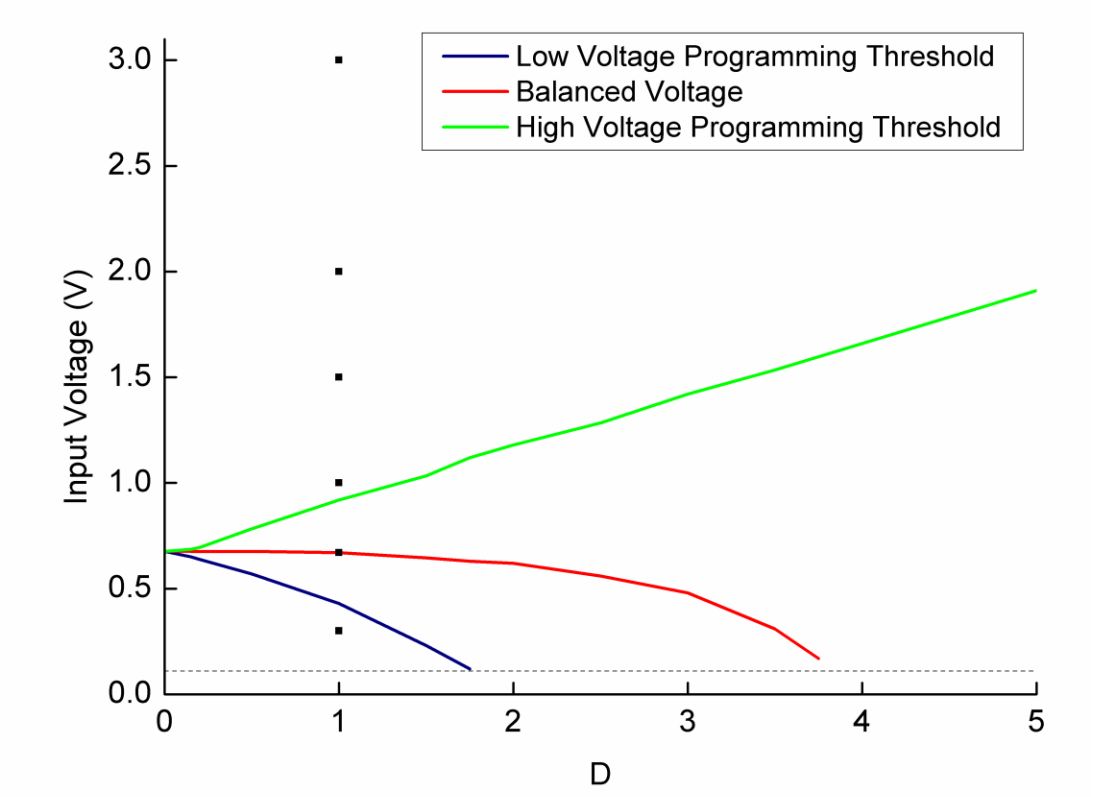

Figure 10-5: Three operational regimes for the Adaptive Schmitt Trigger. Input voltages below the low voltage programming threshold or above the high voltage programming threshold program the memristor producing spike frequency adaptation. Input voltages between these limits produce repetitive pulses that do not change with time.

The range of input voltages that result in adaptive and non-adaptive behavior is shown in Figure 10-5 where the feedback coefficient D, described by Equation 9.32, determines the range of input values for which the memristor causes adaptation. By noting that the polarity of the voltage across the memristor switches sign for pulses versus inter-pulse time periods we see that adaptation occurs when the voltage across the memristor during each pulse is not sufficiently balanced by the restoring voltage across the memristor during the inter-pulse time. Input voltages larger than the high voltage programming threshold (green line in Figure 10-5) program the memristor during each output pulse because there is insufficient inter-pulse time for recovery. This condition

results in spike-frequency adaptation. Likewise, inputs below the low voltage programming threshold (blue line in Figure 10-5) program the memristor during the inter-pulse time. This low input programming condition is easily avoidable by choosing a sufficiently large value for D, described in Equation 9.32, making relaxation faster. The balanced voltage curve (red line in Figure 10-5) indicates the input voltage required to maintain a mean value of $\varphi=0$. This occurs when the pulse frequency balances programming from the pulse and the inter-pulse interval. Also shown by a dashed line in Figure 10-5 is the circuit activation threshold. Because the Schmitt Trigger output is subtracted from the integrator input as a reset mechanism, shown in Figure 10-3, inputs below the Schmitt Trigger's low state output cannot initiate a pulse. This low input "leak" effectively implements a leaky integrate and fire neuron model.

The six simulation conditions shown in Figure 10-4 are indicated on Figure 10-5 as dots. Figure 10-4a, V_{in} = 0.3V, is slightly below the low voltage programming threshold and Figure 10-4c, V_{in} = 1V, is slightly above the high voltage programming threshold. Since neither of these cases show significant adaptation, this reveals that the programming thresholds are soft thresholds defining the limits of memristor programming. This soft threshold is more consistent with biology than a hard threshold device in that biological spike-frequency adaptation is governed by ionic concentrations changing populations of conductances [166].

In order to mimic spike-frequency adaptation, there are two reasons this circuit must use a volatile memristor. First, after the circuit has been stimulated by an input above the high voltage programming threshold such that the memristor becomes programmed, it is necessary for the circuit to recover back to the un-programmed state.

While it may be possible to accomplish this with a non-volatile memristor and some extra circuitry, a volatile memristor can be implemented in a single device without additional wiring and will improve the overall circuit density. Second, the ability of the circuit to produce repeatable pulses for a range of small value inputs and then adapt for larger inputs cannot be achieved with a non-volatile memristor.

As shown in Figure 10-5, as D approaches zero and the memristor becomes non-volatile the range of stable input voltages where the memristor does not program collapses to a single value. This collapse occurs because without the restoring feedback, non-volatile memristors cannot balance the programming voltages from the pulses and inter-pulse intervals.

10.2 Adaptive Neuristor Circuit

The Neuristor circuit was first proposed in 1962 as a method for signal propagation over long distances without attenuation similar to signal propagation in a biological axon [165]. The original circuit consists of relaxation oscillators biased below the threshold for oscillation resistively coupled together as shown in Figure 10-6. A small input pulse destabilizes the first oscillator which in turn destabilizes the next oscillator and so forth propagating the initial pulse down the cable regenerating it at each node. In 2013, a modified topology was proposed that reduced the number of circuit components by combining many of the control resistors and coupling resistors [23].

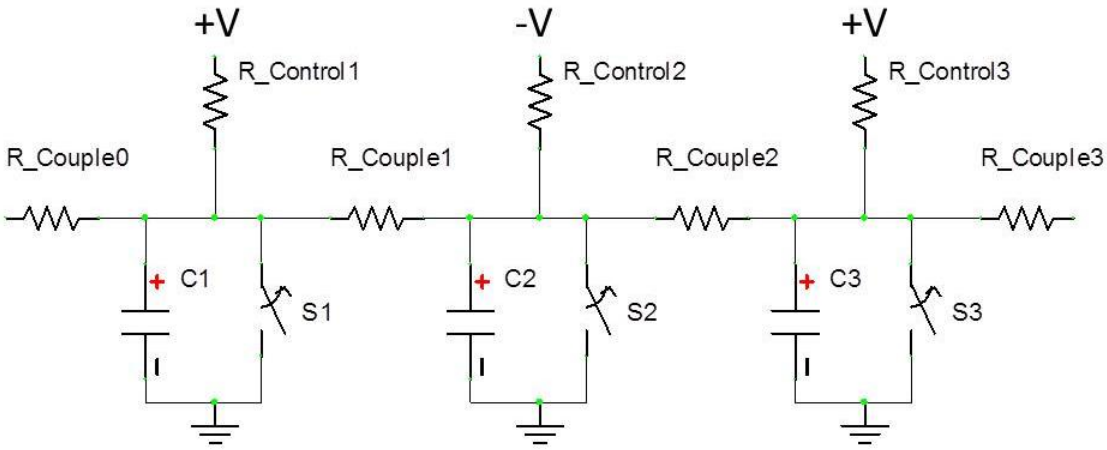

Figure 10-6: Circuit schematic for the original Neuristor with coupled relaxation oscillators that are triggered in a cascade propagating an original input pulse so that it regenerates at each node.

In order to enable the relaxation oscillators in the Neuristor circuit, a switching element must be included. Multiple physical devices have been proposed for this element including thyristors [165] and memristors [23]. In addition, the memdiode discussed in Chapter 7 exhibits the rectification and hysteresis necessary for this circuit element. For the following circuit simulations, a switch with hysteresis is implemented with the current-voltage characteristics shown in Figure 10-7.

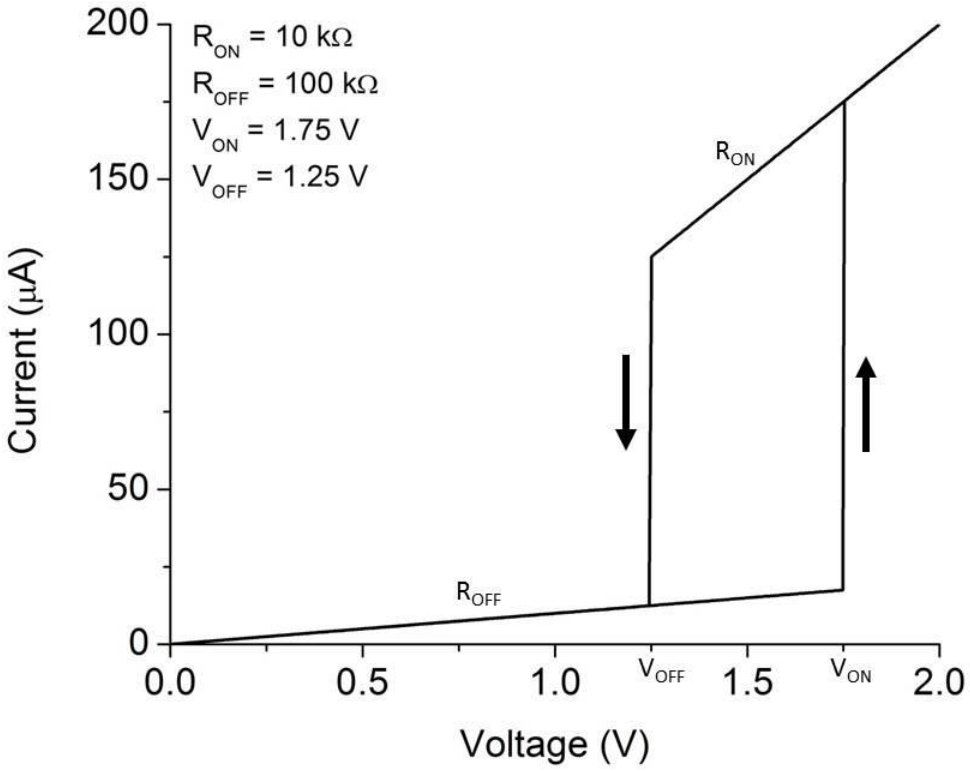

Figure 10-7: Current-voltage curve for the switch used in the following simulations.

The key parameters that define the switching element are the voltage at which it switches from the high resistance state to the low resistance state (V_{ON}), the voltage at which it switches from the low resistance state to the high resistance state (V_{OFF}) and the resistances in the high resistance state (R_{OFF}) and low resistance state (R_{ON}). It should be noted that this switching element model does not capture slow time dependent current transients, such as those observed in the memdiodes discussed in Chapter 7, which may add additional functionality.

10.2.1 Relaxation Oscillators

A single relaxation oscillator, shown in Figure 10-8, only oscillates if the applied voltage and control resistance are within certain limits. Under steady state conditions, the

voltage across the switch is determined by the voltage divider $R_{Control}$ – Switch. The voltage across the control resistor (V_R) can then be described by $V_{Applied} - V_{Switch}$ as shown by the red dashed lines in Figure 10-8. The relaxation oscillator only oscillates if the current-voltage curve for the control resistor crosses the negative resistance line of the switch as shown in Figure 10-8.

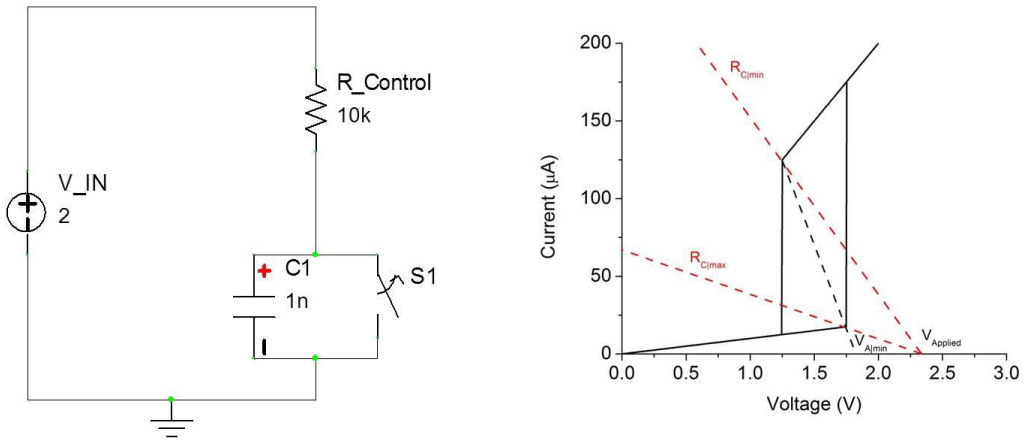

Figure 10-8: (Left) Circuit schematic for a relaxation oscillator. (Right) Current-voltage curve of the switching element and control resistor. The relaxation oscillator will oscillate so long as the current-voltage curve of the control resistor crosses the negative resistance portion of the switching element's current-voltage curve.

The limits on the applied voltage and control resistance can thus be described by Equations 10.5 – 10.7

$$V_A > V_{ON}\left(1 + (V_{ON} - V_{OFF})\left(\frac{R_{ON}}{V_{OFF}R_{OFF} - V_{ON}R_{ON}}\right)\right) \qquad \text{Equation 10.5}$$

$$R_C > R_{ON}\frac{(V_A - V_{OFF})}{V_{OFF}} \qquad \text{Equation 10.6}$$

$$R_C < R_{OFF}\frac{(V_A - V_{ON})}{V_{ON}} \qquad \text{Equation 10.7}$$

where V_A is the applied input voltage and V_{ON}, V_{OFF}, R_{ON}, and R_{OFF} are the four parameters previously defined for the switching element. The effects of the applied

voltage and the control resistance on the relaxation oscillator are shown in Figure 10-9. Unless otherwise specified, the various component values are as shown in Figure 10-8.

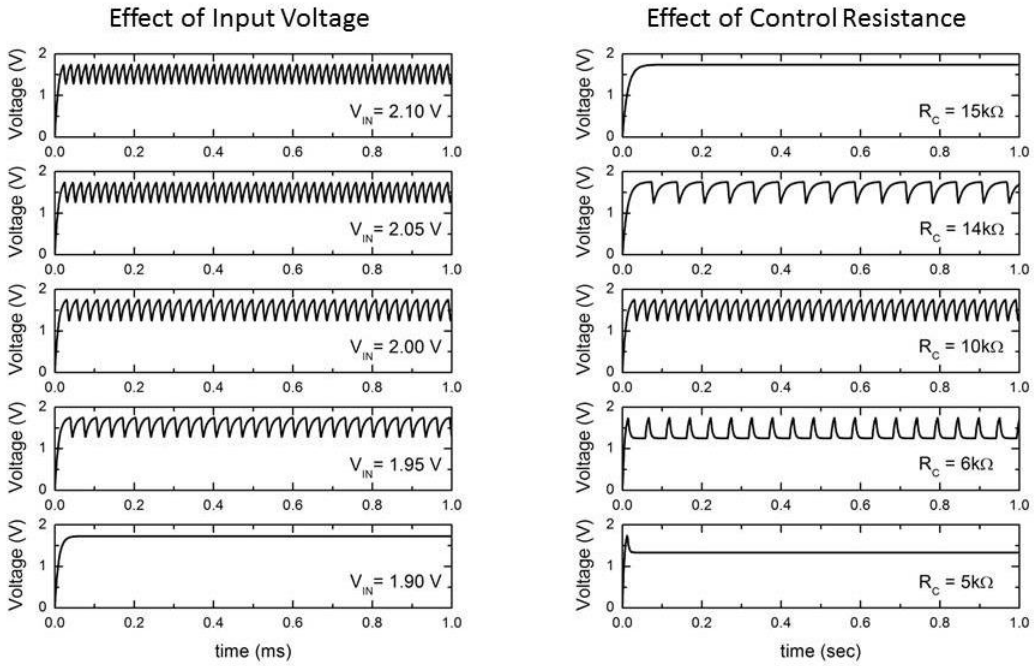

Figure 10-9: Effect of input voltage and control resistance on the behavior of a relaxation oscillator.

For applied voltages below the threshold voltage, the circuit does not oscillate as the switching element is never turned on. However, above the threshold voltage, increasing the voltage applied to the relaxation oscillator increases the oscillation frequency by increasing the current charging the capacitor. The time necessary to discharge the capacitor is slightly increased by increasing the input voltage as the capacitor is simultaneously being charged through the control resistor and discharged through the switching element.

Changing the resistance of the control resistor also affects the relaxation oscillator behavior. For resistances above the allowable resistance range, defined in Equation 10.7, the switching element never switches on. Likewise, for resistances below the allowable

resistance range, defined in Equation 10.6, the switching element never switches off. However, between the resistance limits, there is a maximum in the oscillation frequency as shown in Figure 10-10. High values for the control resistor create long charge times, given in Equation 10.8, decreasing the oscillation frequency. Likewise, low values for the control resistor create long discharge times, given in Equation 10.9, by simultaneously charging the capacitor during the discharge cycle. Therefore, by replacing the control resistance in the Neuristor's relaxation oscillators with a volatile memristor that spans this range of behaviors, it is expected that adaptive behaviors can be added to the Neuristor circuit.

$$t_{charge} = -\frac{R_C R_{OFF} C}{R_C + R_{OFF}} \ln\left(\frac{V_{ON} - V_A\left(\frac{R_{OFF}}{R_C + R_{OFF}}\right)}{V_{OFF} - V_A\left(\frac{R_{OFF}}{R_C + R_{OFF}}\right)}\right) \quad \text{Equation 10.8}$$

$$t_{discharge} = -\frac{R_C R_{ON} C}{R_C + R_{ON}} \ln\left(\frac{V_{OFF} - V_A\left(\frac{R_{ON}}{R_C + R_{ON}}\right)}{V_{ON} - V_A\left(\frac{R_{ON}}{R_C + R_{ON}}\right)}\right) \quad \text{Equation 10.9}$$

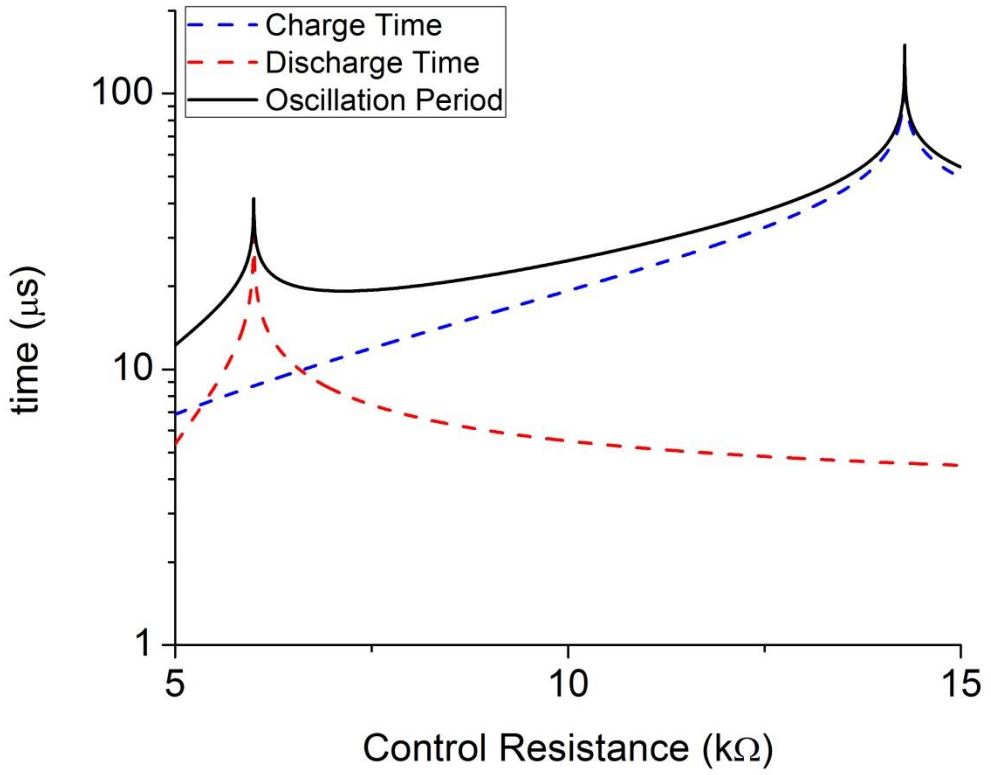

Figure 10-10: Effect of the control resistor on the period of a relaxation oscillator. A minimum in period occurs between the limits on the control resistor.

10.2.2 Neuristor Circuit

The Neuristor circuit only replicates the signal propagation functionality of a biological axon. In order to explore adaptive behavior in the Neuristor, a simple neuron circuit was simulated as shown in Figure 10-11. The input to the Neuristor was attached to a simple RC integration circuit replicating the biological cell body. The RC time constant of this integrator was set to the RC time constant observed in biological neurons [166]. The biological synapses and dendrites were simulated with a DC current source representing the summation of a large number of pulses. While the DC current source is

not strictly an accurate representation of an *in-vitro* biological neuron, it is a standard procedure for testing the response of biological neurons [166].

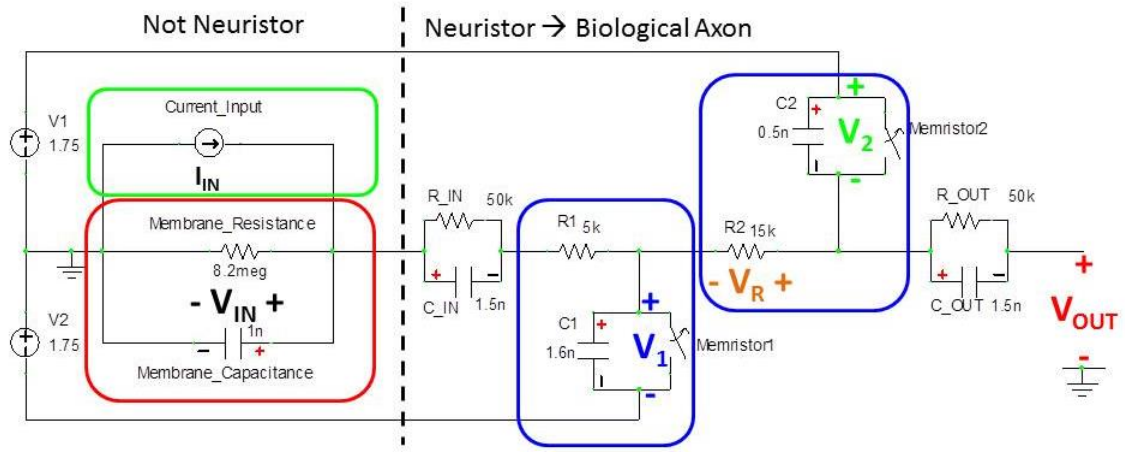

Figure 10-11: Circuit schematic of a simple artificial neuron composed of a DC input current (green) representing the summation of many input spikes, an RC circuit (red) representing the resistance and capacitance of a neurons cell membrane, and the neuristor circuit representing the neuron's axon. The Neuristor is composed of cascaded relaxation oscillators (blue).

The Neuristor circuit as proposed does not exhibit any adaptive behavior such as bursting, chattering, or spike-frequency adaptation. As shown in Figure 10-12 and Figure 10-13a, increasing the input current increases the output spike frequency similar to how increasing the input voltage of a single relaxation oscillator increases the output frequency. Therefore, another component within the Neuristor circuit must supply the dynamics for volatile adaptive behavior. As shown in Figure 10-9, changing the control resistor in a single relaxation oscillator can significantly affect the output frequency. Likewise, changing the resistor R_2 will change the behavior of the second relaxation oscillator containing $Memristor_2$. In addition, changing the resistor R_2 will change the coupling dynamics between the two relaxation oscillators.

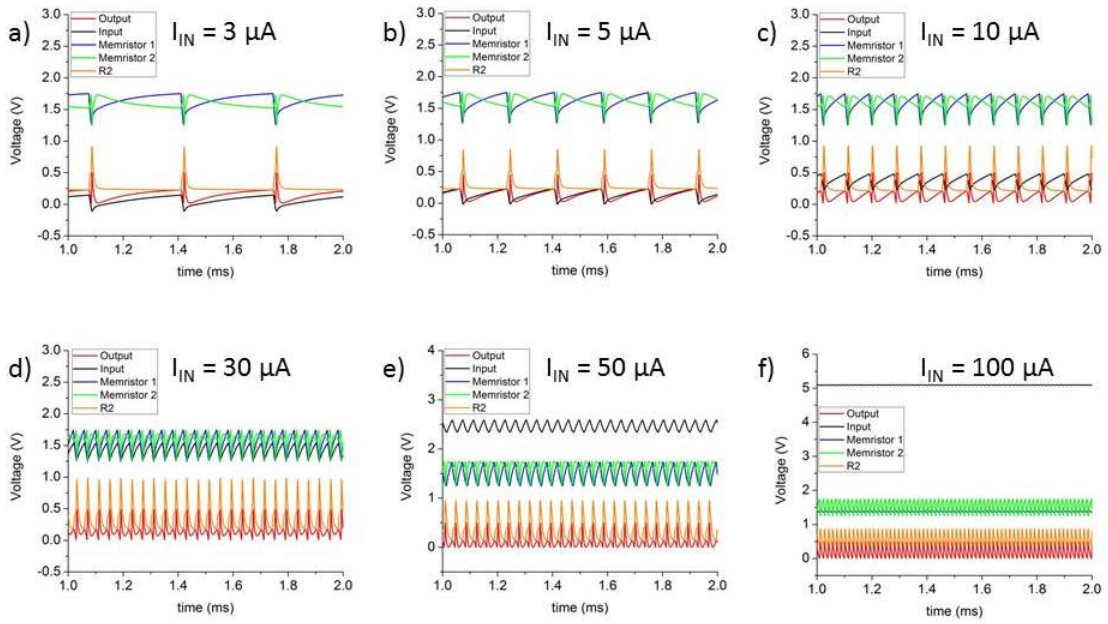

Figure 10-12: Effect of varying input currents to the simple Neuristor based neuron circuit. Increasing the input current increases the spike rate and causes accumulation of charge on the input capacitor, but does not result in chattering or bursting behavior.

The maximum voltage across resistor R_2 during a spike does not change with increasing input current as the current is set by the voltage divider $Memristor_1 - R_2 - Memristor_2$. However, increasing the input current does increase the spike frequency which in turn increases the average voltage across R_2 in a linear manner as shown in Figure 10-13c. As changing the resistance of R_2 is expected to change the Neuristor's behavior, the relation between input current and average voltage across R_2 provides a mechanism to program R_2.

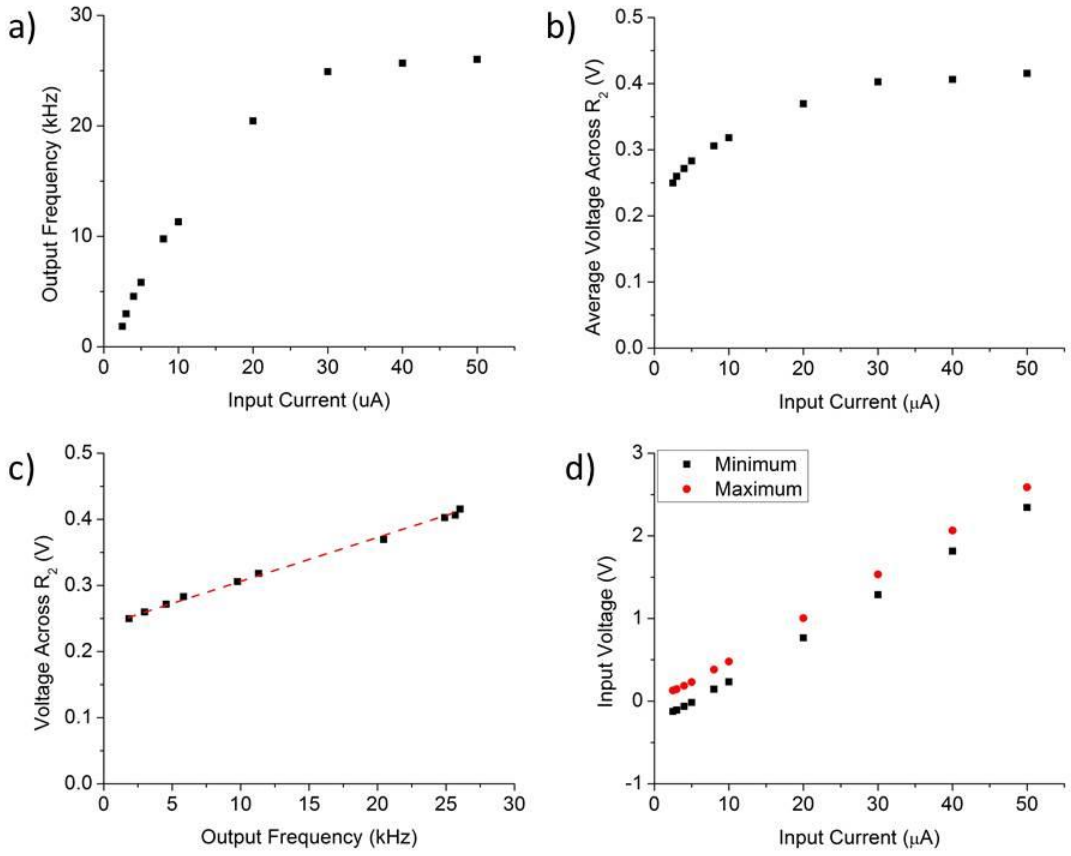

Figure 10-13: a) Effect of input current on the output spike frequency of the Neuristor based neuron circuit. b) Effect of input current on the average voltage across resistor R_2. c) Effect of output spike frequency on the average voltage across R_2 showing a linear trend. d) Effect of input current on the voltage range of the input capacitor showing accumulated charge as the input current increases.

Changing the resistance of R_2, shown in Figure 10-14, produces a variety of different spike behaviors. For larger resistances, trains of single spikes occur where the spike frequency increases with decreasing resistance. However, within this range the average voltage across R_2 decreases because, despite the slight increase in spike frequency, the voltage profile narrows such that the resistor is exposed to higher voltages for less time.

Decreasing the resistance of R_2 below a threshold produces both chattering (12 kΩ) and bursting (10 kΩ) behavior. In each of these modes the RC time constant of the

second relaxation oscillator has decreased such that it can charge and discharge multiple times within the RC time constant of the first relaxation oscillator.

Not shown in Figure 10-14 are two other regimes. For very large resistances, insufficient charge can transfer from the first relaxation oscillator to the second and no output spikes are generated. Instead only sub-threshold oscillations occur. Likewise, for very small resistances, R_2 cannot support sufficient voltage to switch the memristors off and a DC output results.

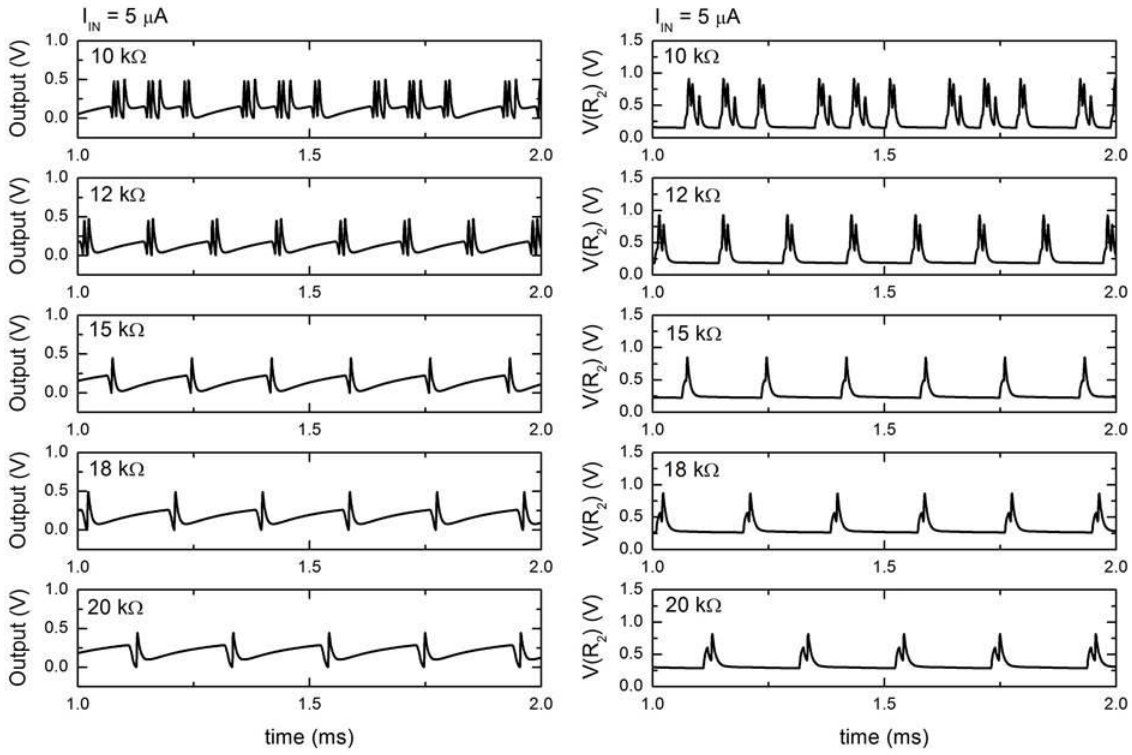

Figure 10-14: Effect of varying the value of resistor R_2 on (Left) the output voltage and (Right) the voltage across R_2. By decreasing the value of R_2, chattering and bursting behavior are observed.

The four modes of operation and the resulting voltages across R_2 are shown in Figure 10-15. A minimum in the voltage across R_2 occurs between the spike train and bursting modes. Within the spike train mode, a decrease in R_2 also decreases the voltage

across R_2 creating a stable negative feedback mechanism within the circuit. However, if R_2 is decreased sufficiently to enter the bursting mode then decreasing R_2 increases the voltage across R_2 creating a potentially unstable positive feedback mechanism.

Therefore, it is expected that if R_2 is replaced with a volatile memristor that decreases in resistance with accumulated voltage, similar to the lithium niobite memristor simulated in Chapter 9, then the Neuristor will be able to transition from sub-threshold swings to spike trains to bursting and finally to a DC output. However, the circuit may be unstable in the bursting regime do to positive feedback within circuit.

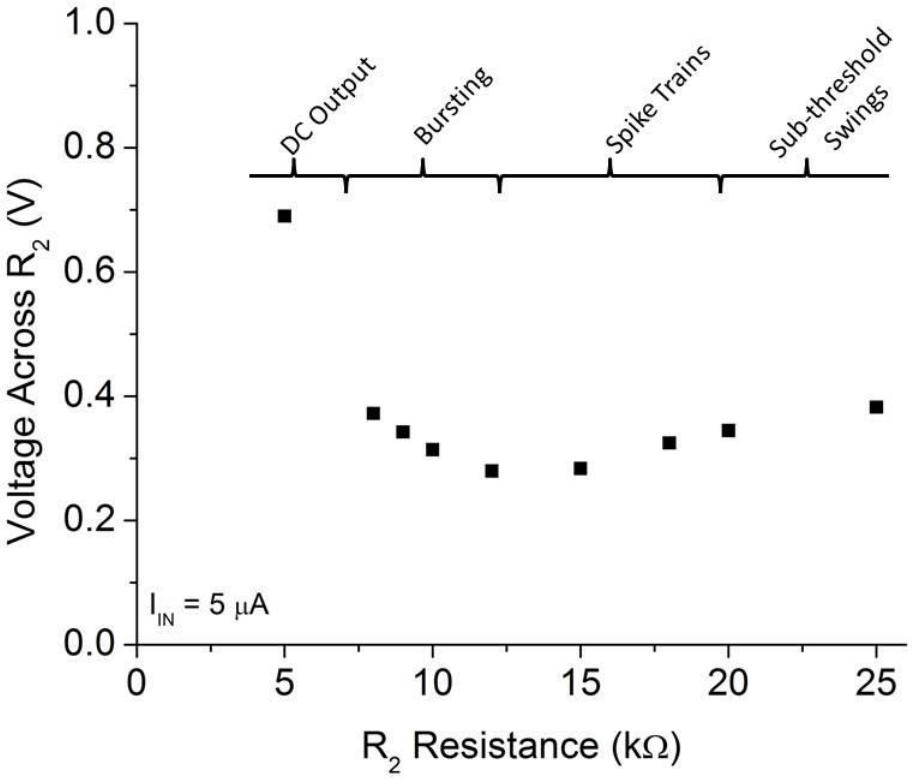

Figure 10-15: Effect of the value of R_2 on the voltage across R_2. For large values of R_2 insufficient charge transfers between the relaxation oscillators and the input pulse is not propagated. Within the range of single spike trains, decreasing R_2 also decreases the voltage across R_2providing a stabilizing negative feedback mechanism. Below a threshold value, bursting behavior begins and the voltage across R_2 increases with decreasing R_2 causing potentially unstable positive feedback. For sufficiently low values of R_2 the relaxation oscillators cannot turn off and a DC output results.

An adaptive Neuristor circuit was modelled by replacing R_2 with a volatile memristor. As shown in Figure 10-16, for a small input current of 5 uA the memristor programs slightly, but the Neuristor remains within the spike train mode of operation.

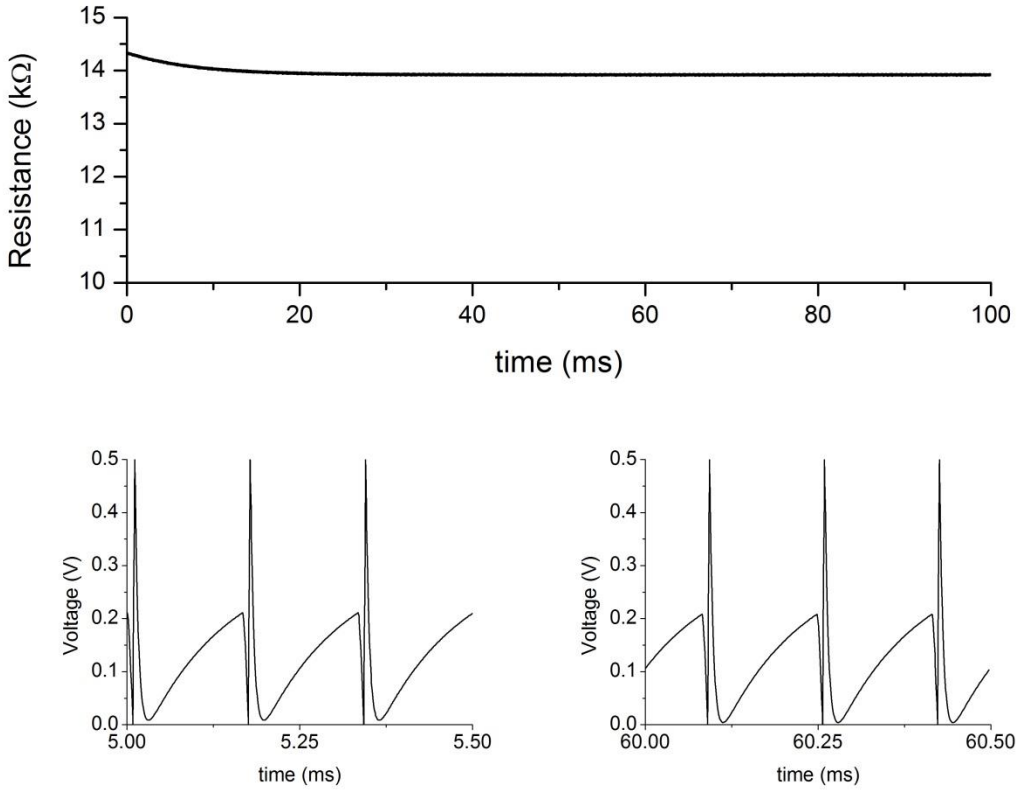

Figure 10-16: Resistance and output voltages for the Neuristor based neuron circuit stimulated with a small 5 uA input. The memristor adapts but is stabilized by the negative feedback inherent in the circuit.

As shown in Figure 10-17, for a moderate input current of 15 uA the memristor begins to program within the spike train mode of operation. However, it passes through the threshold resistance entering the bursting mode. Within the bursting mode range the resistance decreases further due to the circuit's positive feedback, but is stabilized by the negative feedback of the volatile memristor itself.

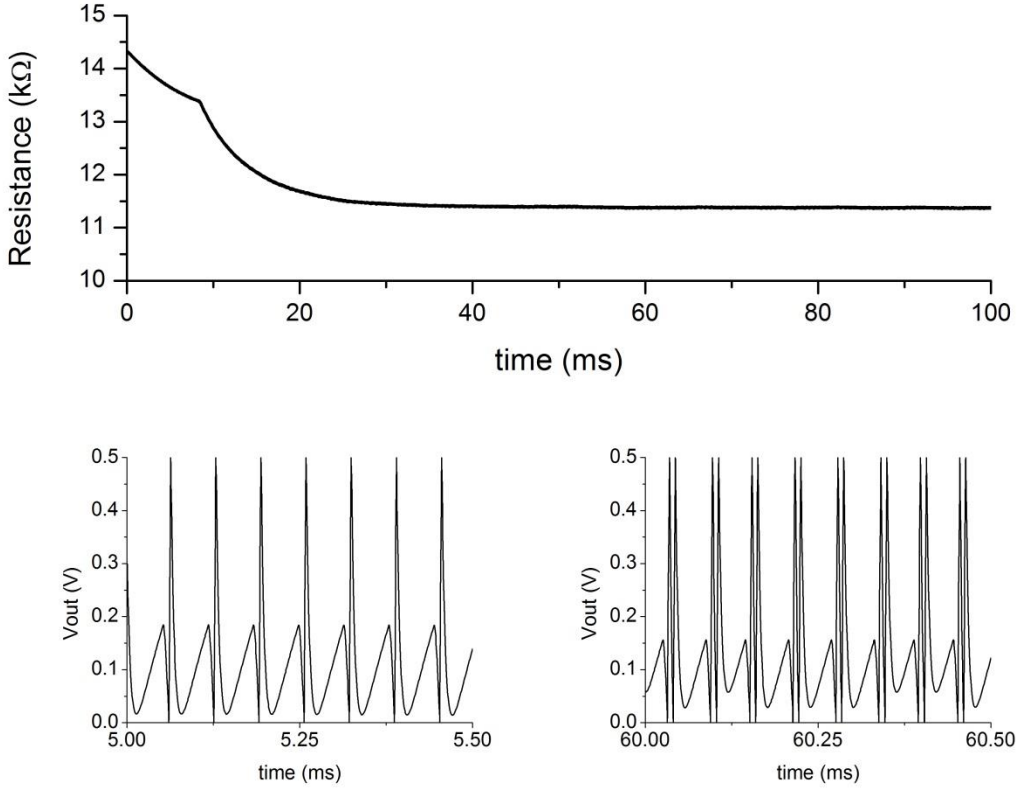

Figure 10-17: Resistance and output voltages for the Neuristor based neuron circuit stimulated with a moderate 15 uA input. The memristor adapts and begins to stabilize, but enters the bursting mode causing further resistance change. The memristor is eventually stabilized by the negative feedback inherent in the memristor itself in which ion diffusion and drift balance.

As shown in Figure 10-18, for a large input current of 40 uA the memristor programs through the spike train mode and the bursting mode eventually reaching the DC output mode. Once again the resistance stabilizes due to the negative feedback of the volatile memristor itself.

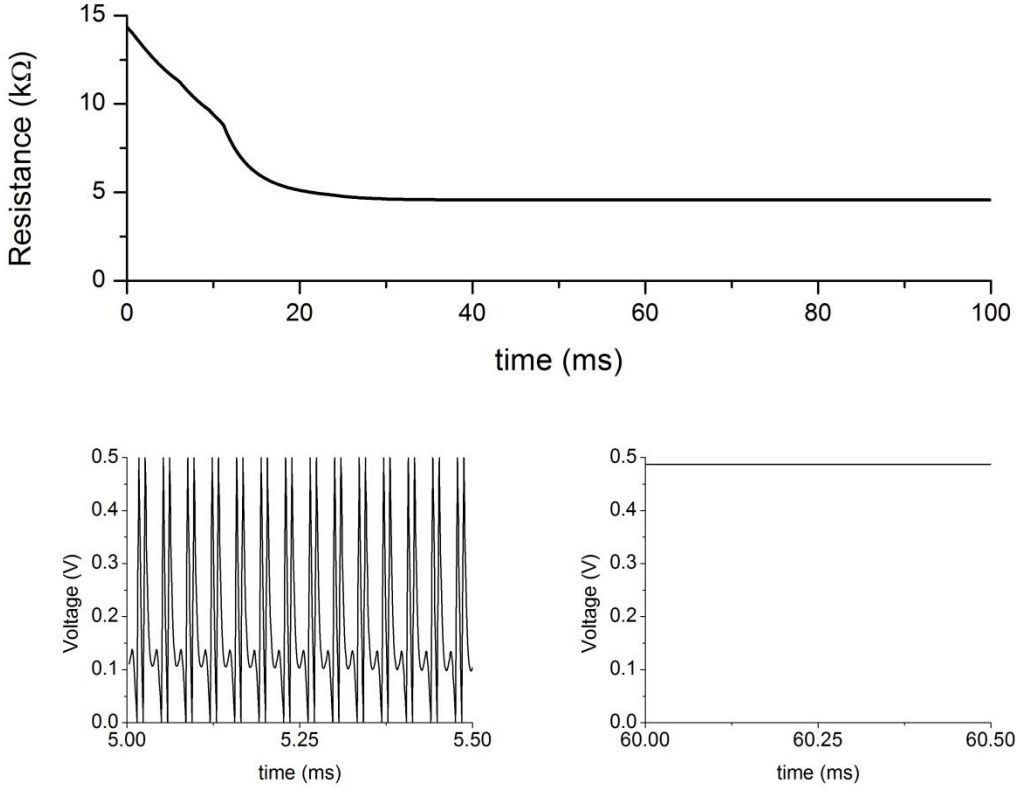

Figure 10-18: Resistance and output voltages for the Neuristor based neuron circuit stimulated with a large 40 uA input. The memristor adapts passing through the spike train and bursting mode regimes and is eventually stabilized by the negative feedback inherent in the memristor itself. However, the memristor stabilizes in the DC output regime stopping all spike propagation.

In summary, adaptive behavior was added to the Neuristor circuit by changing one resistor to a volatile memristor. Multiple spiking behaviors were added enabling the circuit to replicate both individual spikes as well as bursting mode outputs. The transition between these spiking behaviors was controlled by the magnitude of the input current without adding any other inputs to the circuit. Finally, for very large inputs the circuit transitioned into a DC output where all functionality was suppressed.

APPENDIX A

DENTON DISCOVERY 2 OPERATIONS MANUAL

This manual consists of 3 sections: 1) a Recipe Writing Guide, 2) Maintenance Procedures, and 3) Standard Recipes used in this thesis. In general, the Denton Discovery 2 software is self-explanatory and intuitive to use. However, there are a few bugs and unexpected behaviors that will be indicated at various points within this manual.

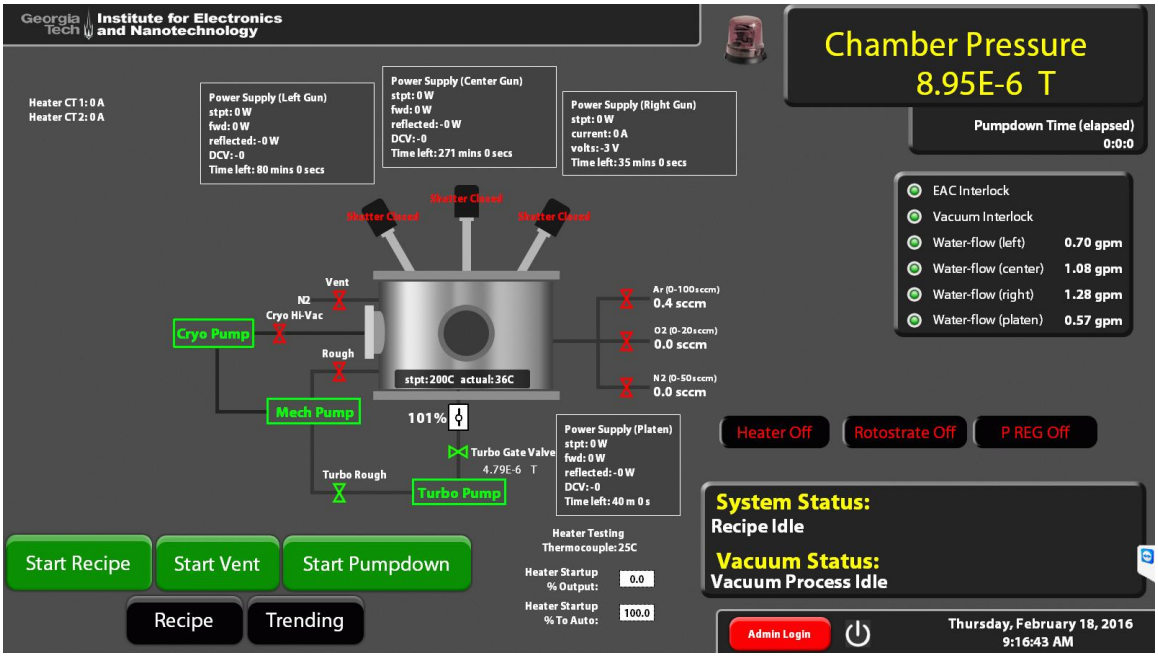

The main overview page, shown above, allows the user to both run sputter deposition recipes and monitor their progress. A typical use of the Denton Discovery 2 follows these steps:

1) Log into the tool using the IEN access system
2) Vent the chamber by pressing the Start Vent button

   Note: The Pressure sensor is not well calibrated for atmospheric pressures and the chamber is vented at a pressure of 640 Torr. If the vent process stops before this pressure it may be necessary to apply manual force to the chamber lid.

3) Load your samples and check that each shutter is in the correct position.

4) Pump down the chamber by pressing Start Pumpdown

5) Write your deposition recipe within the Recipe page

6) Wait for the chamber to pump down to the desired base pressure

   Note: The system's base pressure is usually in the mid 10^{-7} Torr range. Most recipes are run after the pressure has reached the 1-3 x 10^{-6} Torr range, which should take 20-30 minutes.

7) Press the Rotostrate Off button to switch the rotostrate on.

8) Press the Start Recipe button

9) Wait for the recipe to finish

10) Vent the chamber, remove your samples, and pump the chamber back down.

Recipe Writing Guide

Writing a deposition recipe consists of at least 2 setups (Pressure and Power) and optionally 2 additional setups (Temperature and Cooling). Within each of these setups multiple items can be controlled. For example, within the Pressure Setup the Oxygen flow, Argon flow, Nitrogen flow and Pressure set point are controlled. Each of these items runs a parallel recipe independent of all other items. ***It is therefore important when programming a recipe to make sure that each item's recipe totals to the same amount of time.*** The software does not automatically check this and if the times are incorrect the deposition will not work as intended.

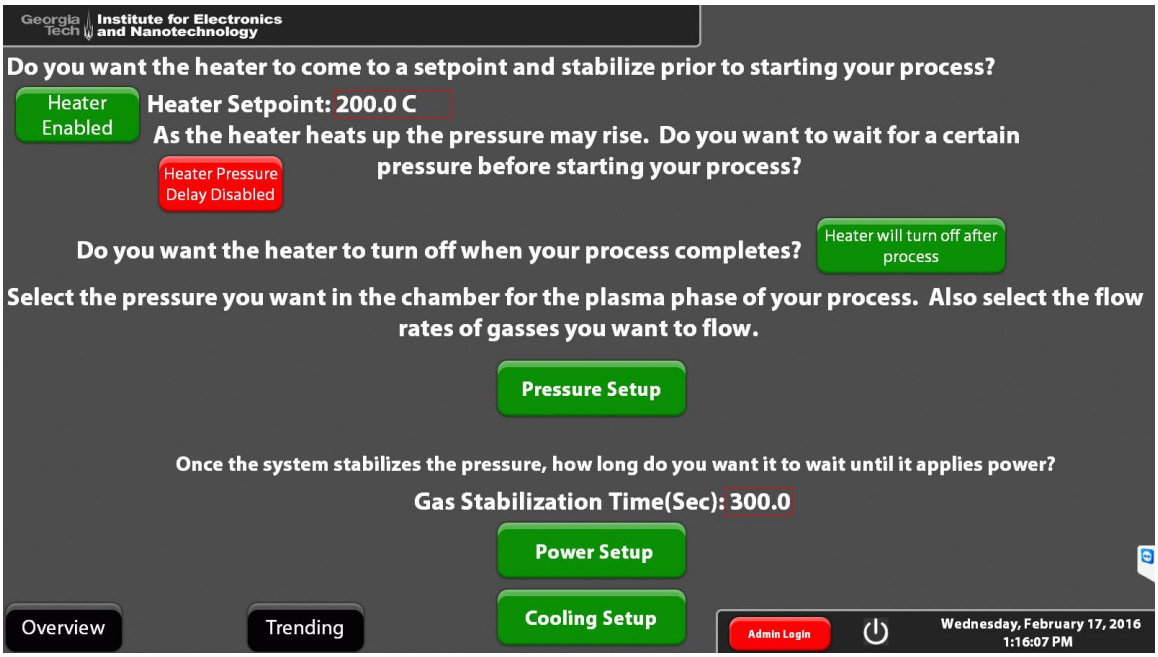

Pressure Setup

The Pressure Setup allows the user to set the mass flows of oxygen, argon, and nitrogen while controlling the chamber pressure. The mass flow controllers allow for 20 SCCM of oxygen, 100 SCCM of argon, and 50 SCCM of nitrogen. Despite some of the labels, each step sets the flow in SCCM, the ramp time in minutes, and the hold time in minutes. ***The second number in each step is a ramp time NOT a ramp rate.***

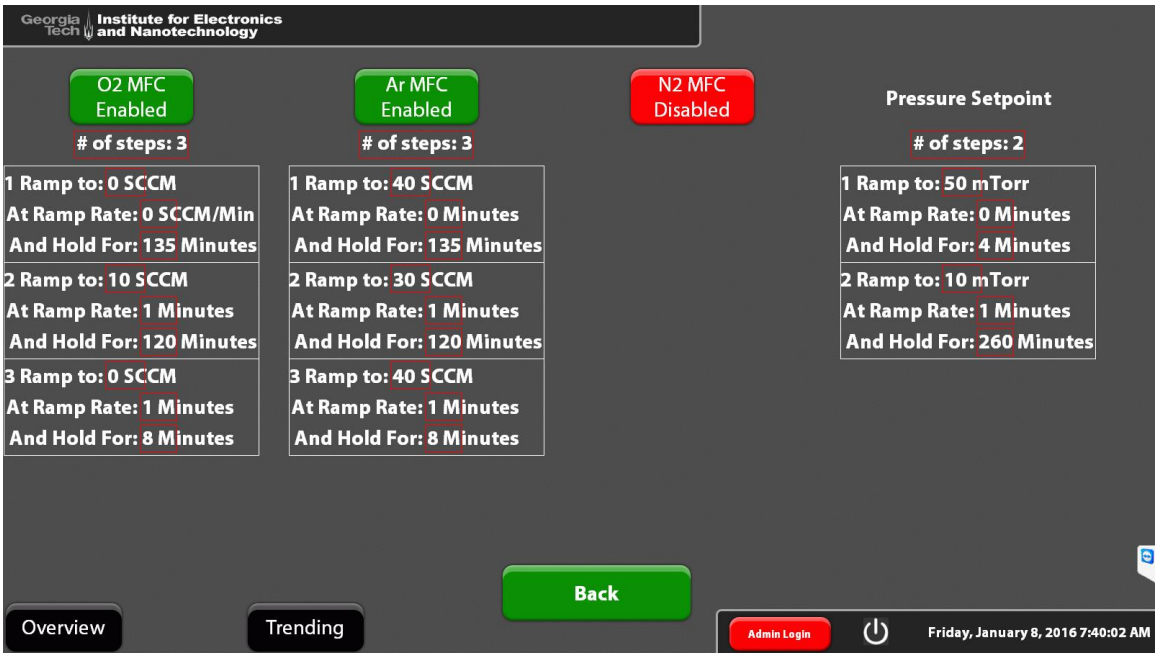

The chamber pressure is controlled by a throttle valve in front of the turbo pump. When choosing a combination of total gas flow and pressure, the chart provided can be used to approximate the throttle valve position. The pressure is most controllable when the throttle valve position is away from the extremes of 0% (closed) or 100% (open). In addition to approximating the throttle valve position, the chart can also be used to approximate the mean free path of an atom coming off the sputtering targets.

Throttle Valve Position

Pressure (mTorr)

Gas Flow (sccm Ar) % open	3	5	8	10	12	15	20
2	16	12	9	8	6	-	-
5	24	20	17	15	13	11	-
8	31	24	20	18	17	15	12
10	49	26	21	20	18	17	14
15	51	34	26	23	21	19	17
20	-	41	29	26	24	22	19
40	-	-	47	38	33	29	24
50	-	-	61	45	38	32	26
λ_0(mm)	26	16	10	7.7	6.5	5.2	3.9
λ_1(mm)	36	22	14	11	9.2	7.3	5.5

Mean Free Path (mm)

The mean free paths are given by Equation A1 and Equation A2. Equation A1 describes the mean free path assuming a gas at equilibrium. Equation A2 describes the mean free path of a particle with significantly higher energy than the surrounding gas. A sputtered atom typically has much higher energy (10's of eV) than the surrounding gas (10's of meV). However, once it has scattered the sputtered atom will transfer energy to the gas and approach equilibrium.

$$\lambda_0 = \frac{k_B T}{\sqrt{2}\pi d^2 P} \qquad \text{Equation A1}$$

$$\lambda_1 = \frac{k_B T}{\pi d^2 P} \qquad \text{Equation A2}$$

λ is the mean free path, k_B is Boltzmann's constant, T is temperature, d is the diameter of the gaseous atoms, and P is pressure. For the mean free paths given in the chart, an atomic diameter of 300 pm was chosen as an approximate atomic diameter.

Argon has a covalent diameter of 212 pm and a Van der Waal diameter of 376 pm. Niobium has an atomic diameter of 292 pm.

When writing the Pressure Setup for a recipe, it is important to "strike" the targets at high pressure before lowering the pressure to the desired deposition pressure. For DC plasmas, the breakdown voltage is given by Paschen's Curve shown in below. While this curve is not directly applicable to a sputtering magnetron, the theory is generally applicable that too low of a pressure or too short of a target shutter distance will prevent the plasma from forming.

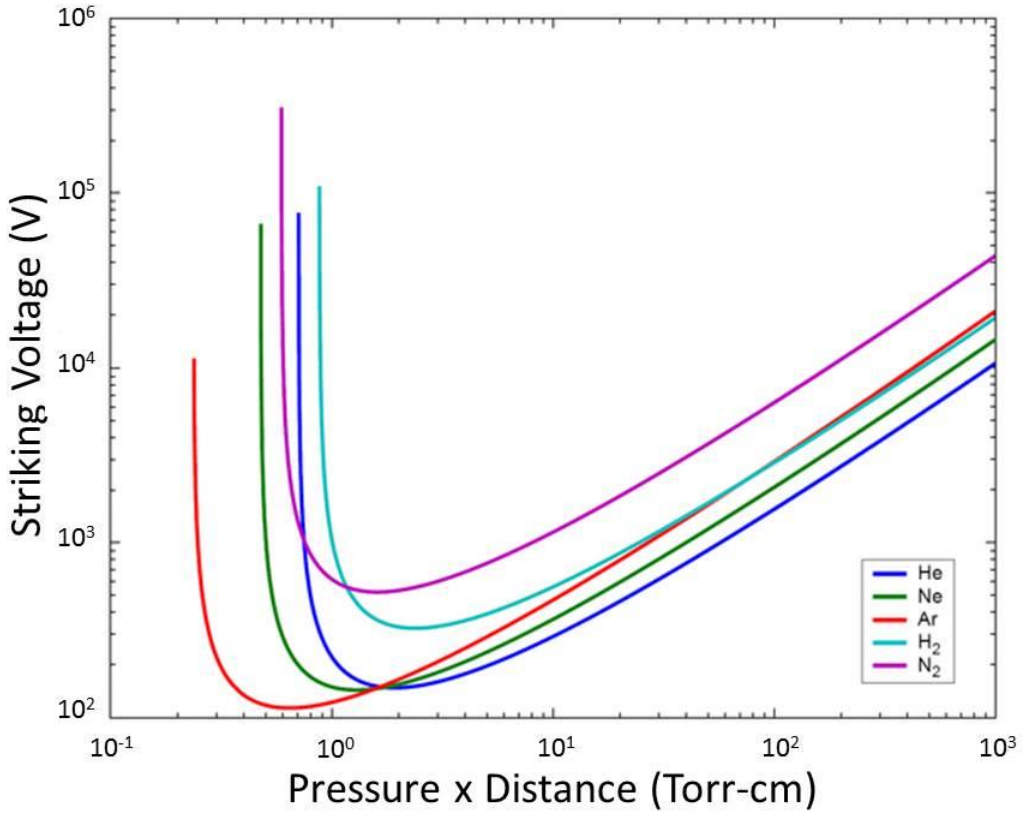

When setting the chamber pressure it should be noted that the throttle valve control seems to accept a margin of error of approximately ±0.5 mTorr. For example,

when lowering the pressure from the 50 mTorr striking pressure to 1 mTorr operation pressure, the system often stabilizes at approximately 1.4 mTorr.

Power Setup

The Power Setup allows the user to set the applied power to the Left Gun, Center Gun, Right Gun, and Platen. The Left Gun, Center Gun, and Platen are attached to RF power supplies while the Right Gun is attached to a DC power supply. Each item's recipe sets the power in Watts, the ramp time in minutes, and the hold time in minutes. ***The second number in each step is a ramp time NOT a ramp rate.***

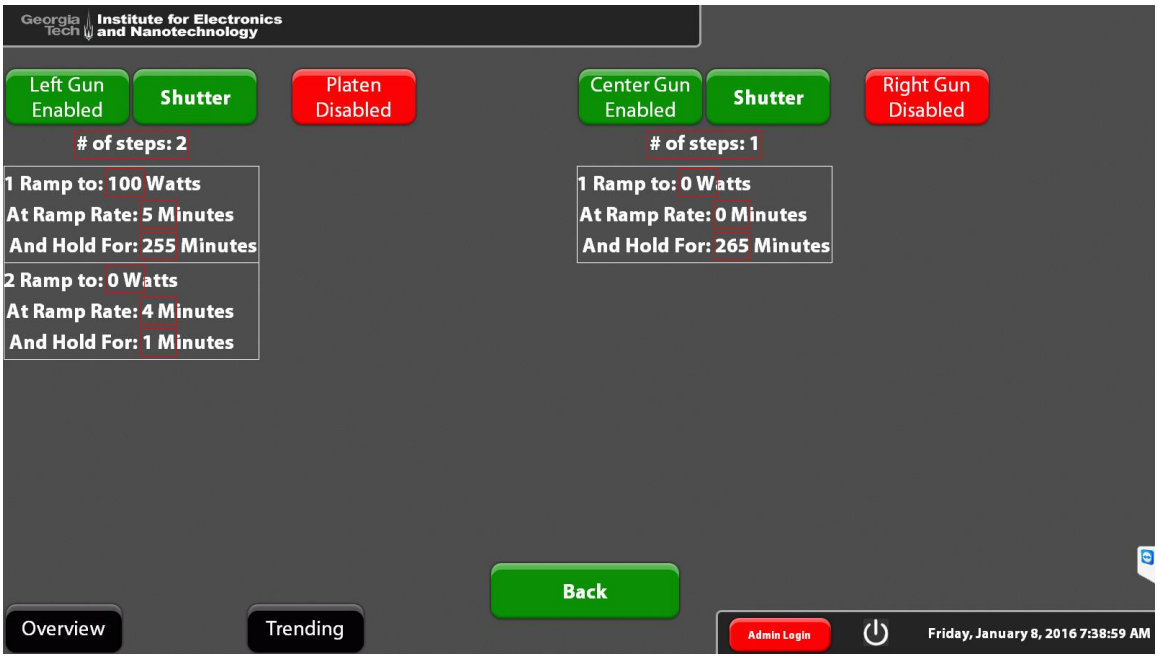

The Power Setup is perhaps the most difficult task when writing a recipe due to several bugs and non-idealities. 1) ***The last hold in each recipe cannot be zero.*** For some reason the software will skip the last step in a recipe if it ends in "hold for 0 minutes". As the last step is usually ramping down the target power, this will crash the target possibly causing it to crack. 2) There is an offset between the Right Gun power set point and the actual applied power. The applied power is consistently 11 W lower than the set point. 3)

The Center Gun tuning network is broken. In order to use the Center Gun, an RF extension cable must be run from the Left Gun. The recipe must then be written to power the Left Gun (which is now physically connected to the Center Gun) but to open the Center Gun Shutter. An example recipe that does this procedure is the Cr/Cr_2O_3 deposition recipe provided.

Temperature Setup

The Temperature Setup is on the Recipe page and the main Overview page. The Recipe page allows the user to turn the heater on or off, set a temperature, set a minimum pressure before the deposition begins, and set whether the heater will turn off after the deposition is complete. The Overview page allows the user to set the heater's ramp parameters.

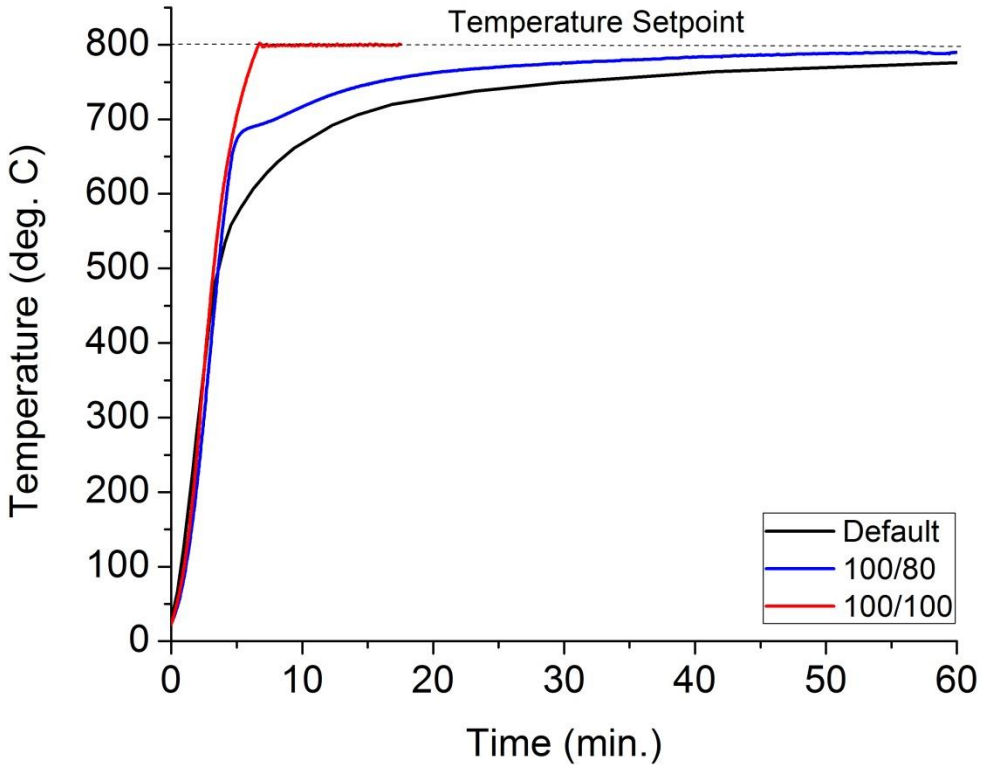

The platen temperature is controlled by pulse width modulation of the heat lamps. The default temperature controller is an adaptive PID controller that is very stable, but is slow to reach high temperatures. Therefore, the parameters on the Overview page allow the user to bypass the default controller and set a constant % pulse width that will be applied if the temperature is below a set % of the temperature set point. When the temperature is above the set % of the temperature set point the default PID controller once again takes over. As shown, this two-step control scheme allows the system to reach high temperatures much faster than with the default PID controller alone.

Despite the temperature shielding that surrounds the high power IR lamps, the entire chamber heats up during a high temperature deposition. This can increase the temperature of the cryo-pump arrays causing them to outgas raising the system pressure. ***For platen temperatures above 600 ^{o}C the cryo-pump gate valve should be closed.***

Cooling Setup

Cooling down from a high temperature deposition can take up to 8 hours if natural radiation and conduction are the only heat transfer mechanisms. Therefore, the user may choose to purge the chamber with gas using the Cooling Setup. The forced cooling is a two-step procedure.

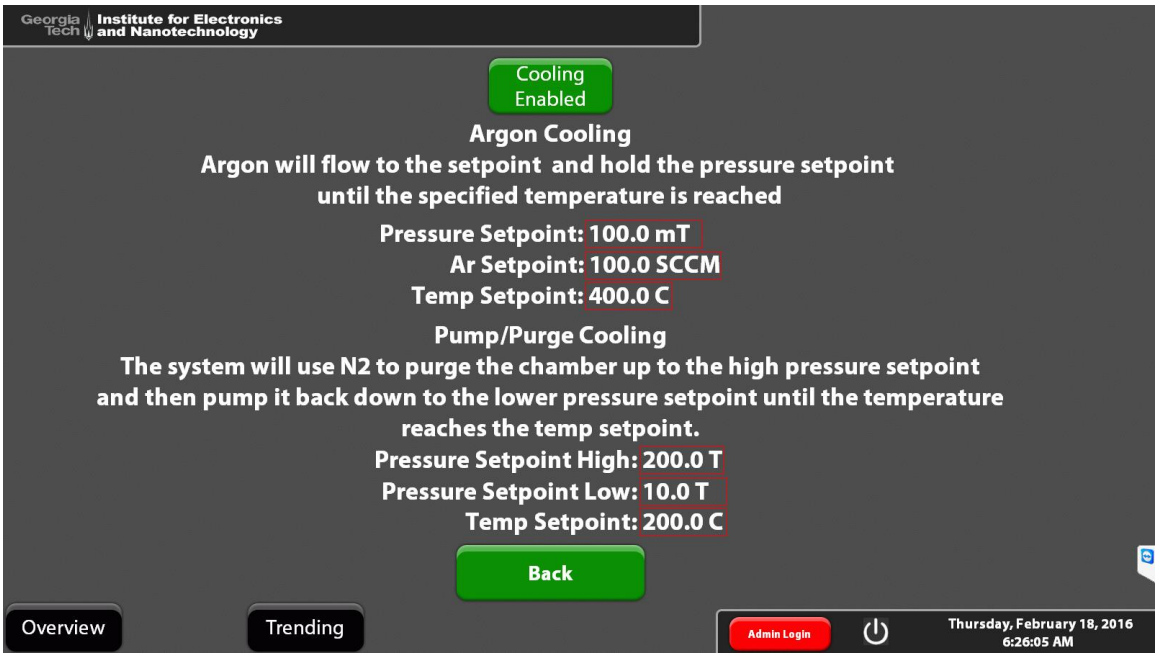

The first step is intended for high temperatures when the deposited film may react with any introduced gasses. The chamber is purged with a constant flow of Argon at a fairly low pressure so that the chamber pressure is still within the operating range of the turbo pump. The second step is intended for lower temperatures where radiation is no longer the dominant heat transfer mechanism. The chamber is purged with nitrogen to a high pressure which absorbs some heat from the chamber. The chamber is then pumped back down using the rough pump removing the heated gas.

It should be noted that it is possible to have forced cooling while leaving the heaters on after the deposition has finished. It is unknown what effect this will have on the system.

Maintenance Procedures

The following section describes several maintenance procedures for the Denton Discovery 2 including both common and uncommon tasks. In the order that they appear the procedures are:

- Chamber Cleaning
- Cathode Disassembly / Target Replacement
- Replacing the Heat Lamps
- Cryo-Pump Regeneration
- Long-term Shutdown

Chamber Cleaning

By far the most common maintenance procedure is chamber cleaning. Sputter deposition builds up thick layers on the cathode shutters, cathode dark shields, and the sample platen. If these parts are not regularly cleaned the built up material tends to flake and fall onto the platen and wafers. In extreme cases build up on the dark shields can cause a target short potentially damaging the target.

The following instructions apply only to the Left and Right directly cooled targets. To remove the shutters use a 3/32" hex key to loosen the shutter clamps and slide the shutters off of the shutter rods. To remove the dark shields use the same 3/32" hex key to loosen the three screws around top of each dark shield and slide the dark shields forward off of the targets. To remove the platen remove the center bolt using a 3/16" hex key and lift the platen out of the chamber. The Center target's shutter can be removed by loosening the set screw and sliding the shutter off of the shutter rod. The dark shield and target clamp can be removed by unscrewing them from the target body. Any films that have built up on these parts can be removed with a bead blaster. Use of a sand blaster is not recommended as it will damage the metal surfaces, increase roughness, and impede chamber pump down.

Cathode Disassembly / Changing Targets

To replace the directly cooled targets on the Right and Left cathodes, the entire cathode must be disassembled. ***Turn off all power supplies and disconnect the power cables before opening a sputtering cathode.***

1. Turn off the water supply to the cathode and drain the water lines into a bucket.
2. Vent the chamber
3. Remove the top cover held in place by three set screws
4. Disconnect the internal water connections (1/4" swage)
5. Use a large adjustable wrench to loosen the large nut. This nut clamps the water cooling block against an o-ring inside the chamber. As you loosen the nut the cooling block will move toward the platen.
6. Use a 3/32" hex key to loosen the 12 screws along the back edge of the water cooling block.
7. Use a thin pry bar (combination of razors and small screw drivers) to slowly remove the cooling block and target from the cathode.

Replacing the Heat Lamps

Before performing maintenance on the heating system, disconnect power to the heat lamps by pulling the fuses in the back of the system.

In order to replace the heat lamps, first remove the platen (3/16" hex key) and chamber shield (1/4" wrench) to expose the heat shield box. Next, remove the shim stock that has been inserted around the edges of the heat shield box. Next, lift the top sections of the box off revealing the IR heat lamps and lamp reflectors.

The IR lamps are held in place by terminal blocks and once accessed can be easily replaced.

Cryo-Pump Regeneration

The cryo-pump has an onboard controller that is used to regenerate the pump. However, the cryo-pump and turbo pump share the same rough pump. ***Therefore, before regenerating the cryo-pump the gate valve between the turbo pump and chamber should be closed and the turbo pump should be spun down to avoid a full speed crash of the turbo pump.*** This procedure requires administrator level control to manually actuate the gate valves.

1) Close the gate valve between the cryo-pump and chamber.
2) Close the gate valve between the turbo pump and chamber.
3) Spin down the turbo pump.
4) Use the on-board controller to regenerate the cryo-pump.
5) Wait until the cryo-pump has begun cooling down again.
6) Open the gate valve between the turbo pump and chamber. This will rough out the chamber through the turbo pump.
7) Open the gate valve between the cryo-pump and chamber.
8) Spin the turbo pump back up.

Note: allowing the cryo pump to cool down while being actively pumped by the turbo is an unusual procedure compared to most cryo-pump regeneration procedures. However, it will not harm the system and allows the operator to return the system to automatic controls earlier than waiting for the cryo-pump to cool down.

Long-term Shutdown

If the cleanroom is going to be abandoned for an extended period of time, such as during winter break, the Discovery 2 should be placed in a safe state in case of power

outage, water outage, or other unforeseen event. This procedure requires administrator level control to manually actuate the gate valves.

1) Close the gate valve between the turbo pump and chamber.
2) Spin down the turbo pump.
3) Turn off all of the source power supplies.

Standard Recipes

The following recipes are included:

1) The Cr/Cr2O3 backside metallization used for oxide MBE samples
2) Nb_2O_5 used for the memdiodes
3) $LiNbO_2$ used for memristors and batteries
4) LiPON used for the thin film battery electrolyte

Standard Recipe for Cr / Cr2O3 (Backside Metal for MBE Samples)

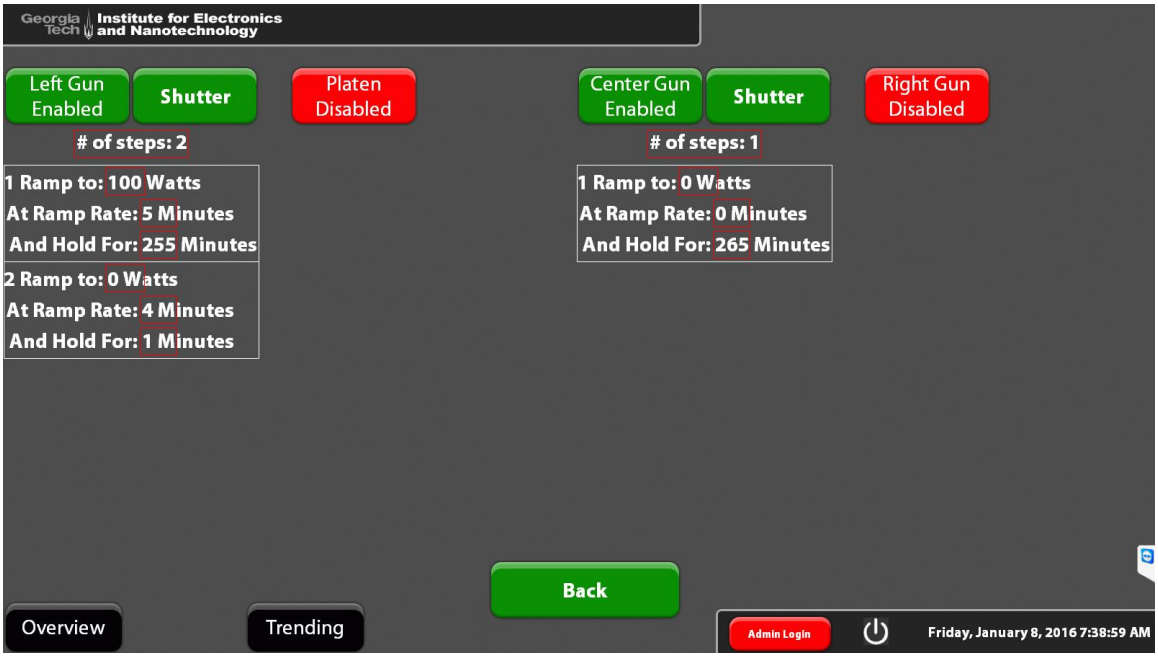

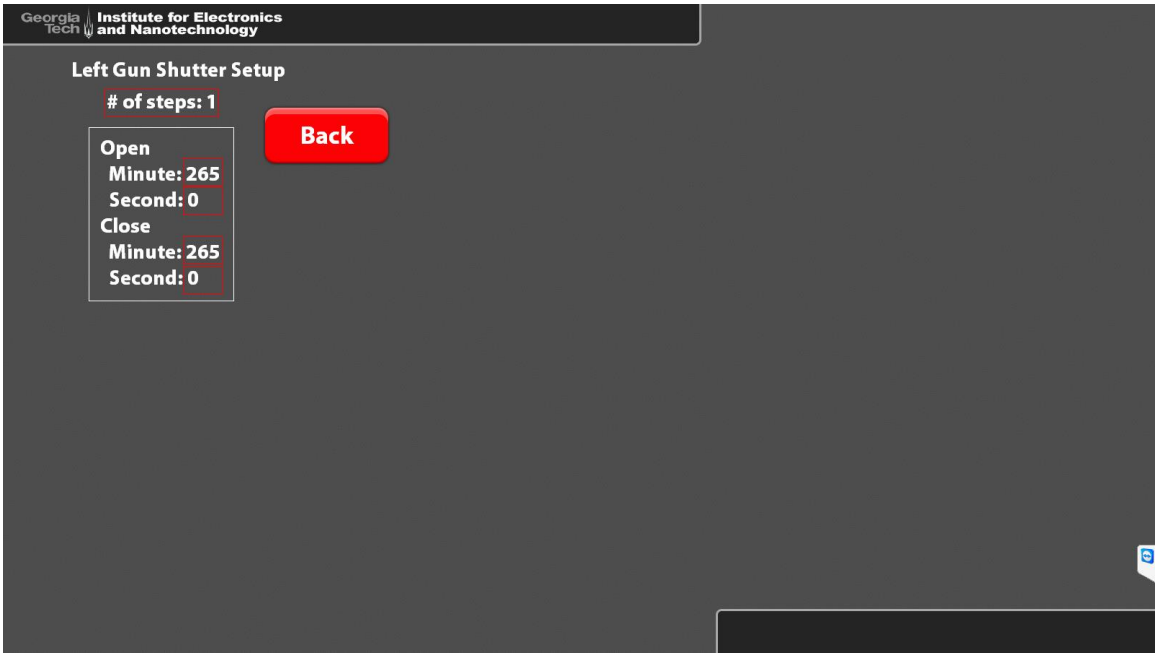

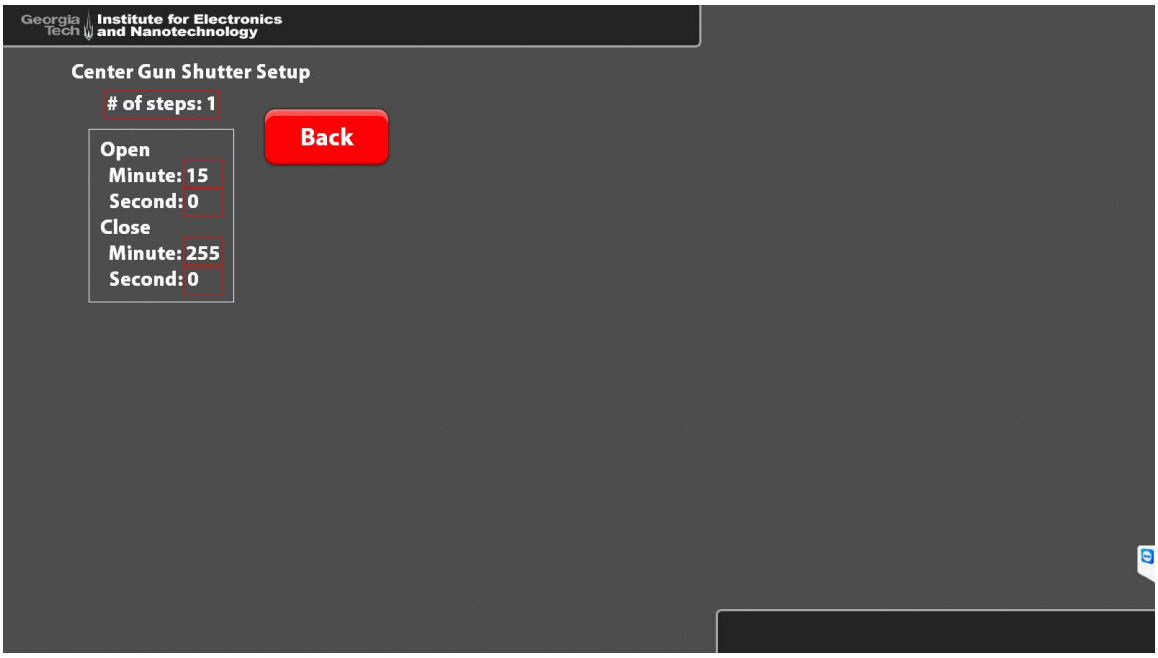

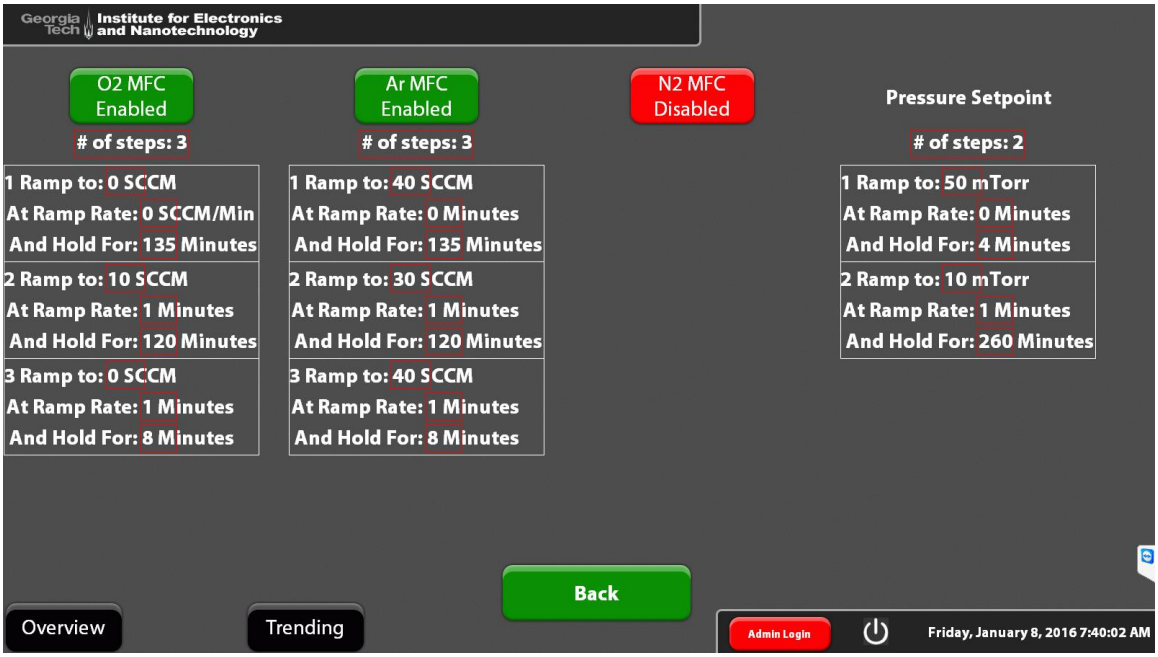

NOTES:

1. This recipe requires the Center gun and thus requires switching the power cables from the Left Gun to the Center Gun.

2. We use the IEN's chrome target for this process. The last pressure step burns the oxide off of the target to create a clean surface. Be considerate and do not remove this step.

Standard Recipe for Nb2O5

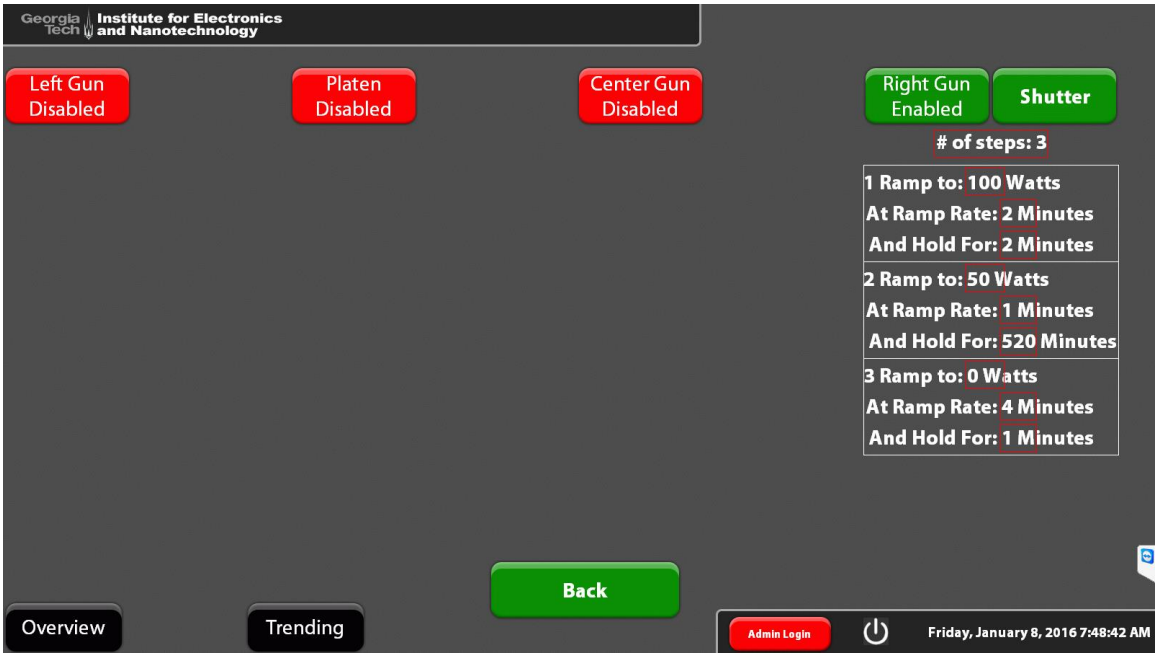

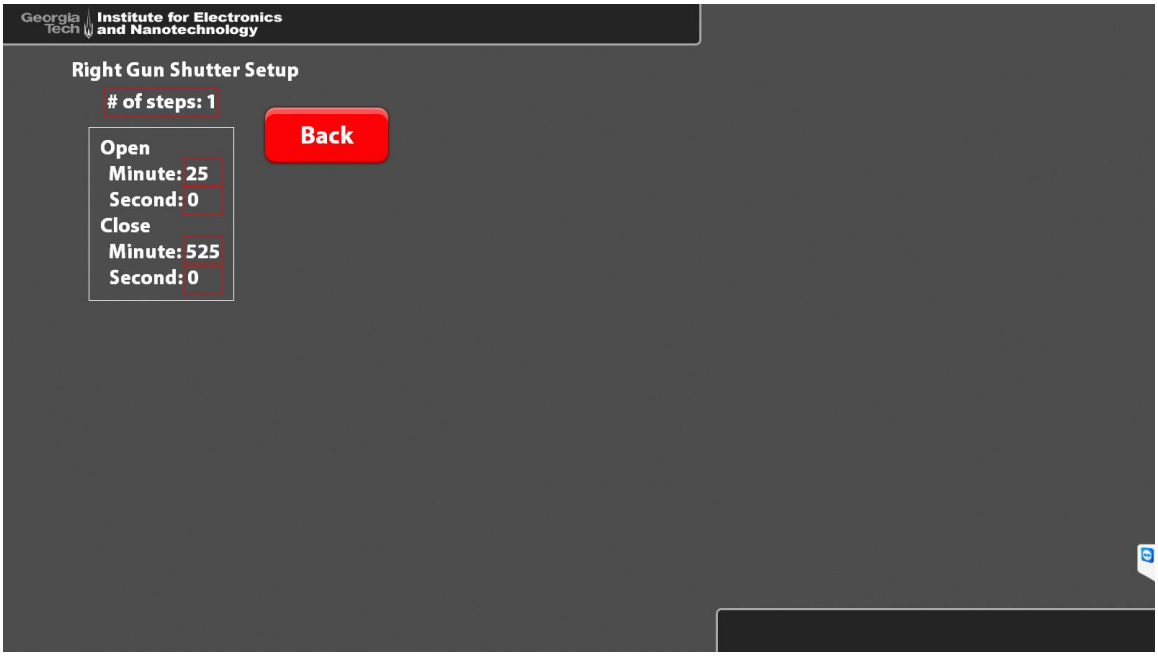

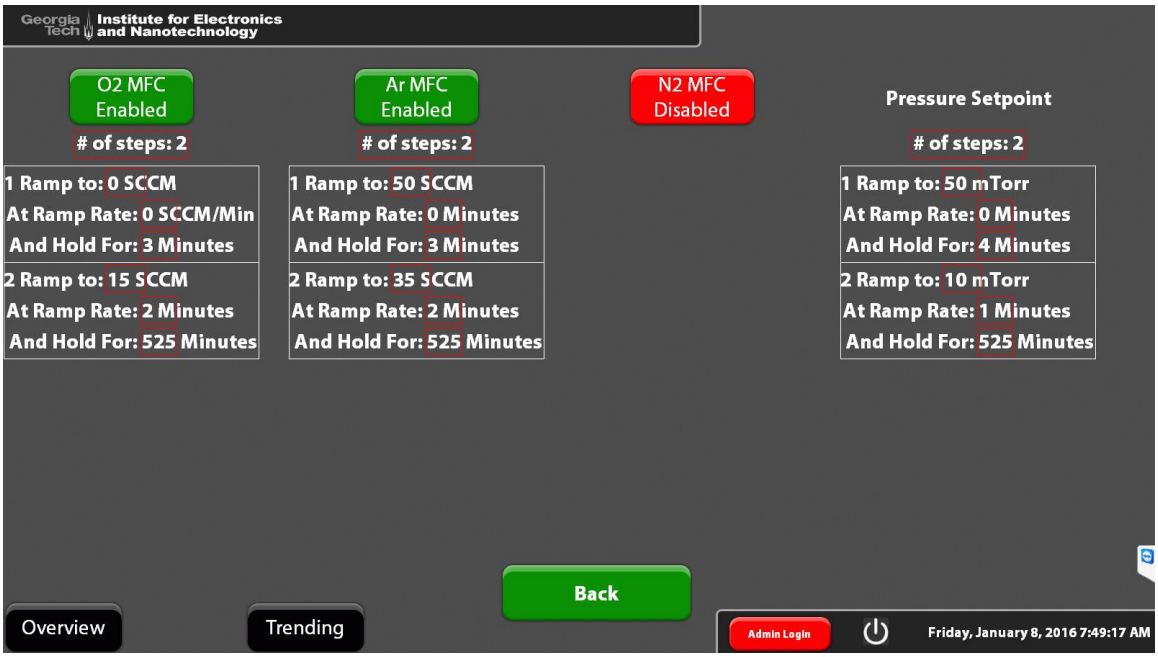
Georgia Tech Institute for Electronics and Nanotechnology
O2 MFC Enabled
Ar MFC Enabled
N2 MFC Disabled
Pressure Setpoint
# of steps: 2
# of steps: 2
# of steps: 2
1 Ramp to: 0 SCCM
At Ramp Rate: 0 SCCM/Min
And Hold For: 3 Minutes
2 Ramp to: 15 SCCM
At Ramp Rate: 2 Minutes
And Hold For: 525 Minutes
1 Ramp to: 50 SCCM
At Ramp Rate: 0 Minutes
And Hold For: 3 Minutes
2 Ramp to: 35 SCCM
At Ramp Rate: 2 Minutes
And Hold For: 525 Minutes
1 Ramp to: 50 mTorr
At Ramp Rate: 0 Minutes
And Hold For: 4 Minutes
2 Ramp to: 10 mTorr
At Ramp Rate: 1 Minutes
And Hold For: 525 Minutes
Back
Overview
Trending
Admin Login
Friday, January 8, 2016 7:49:17 AM

Standard Recipe for $LiNbO_2$

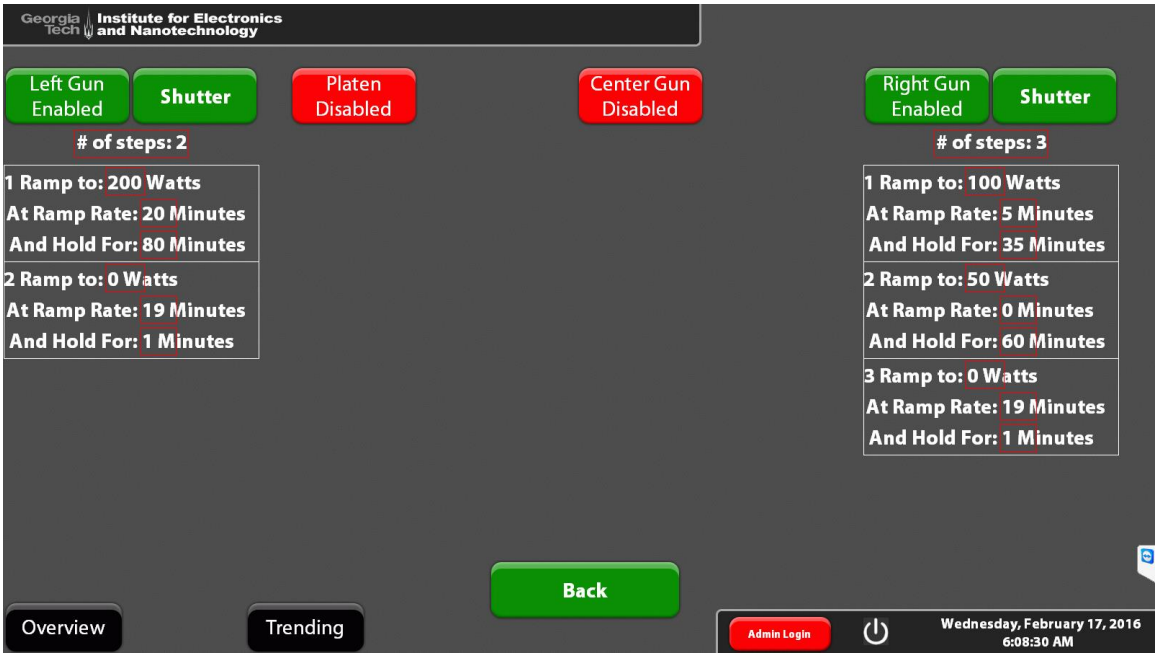

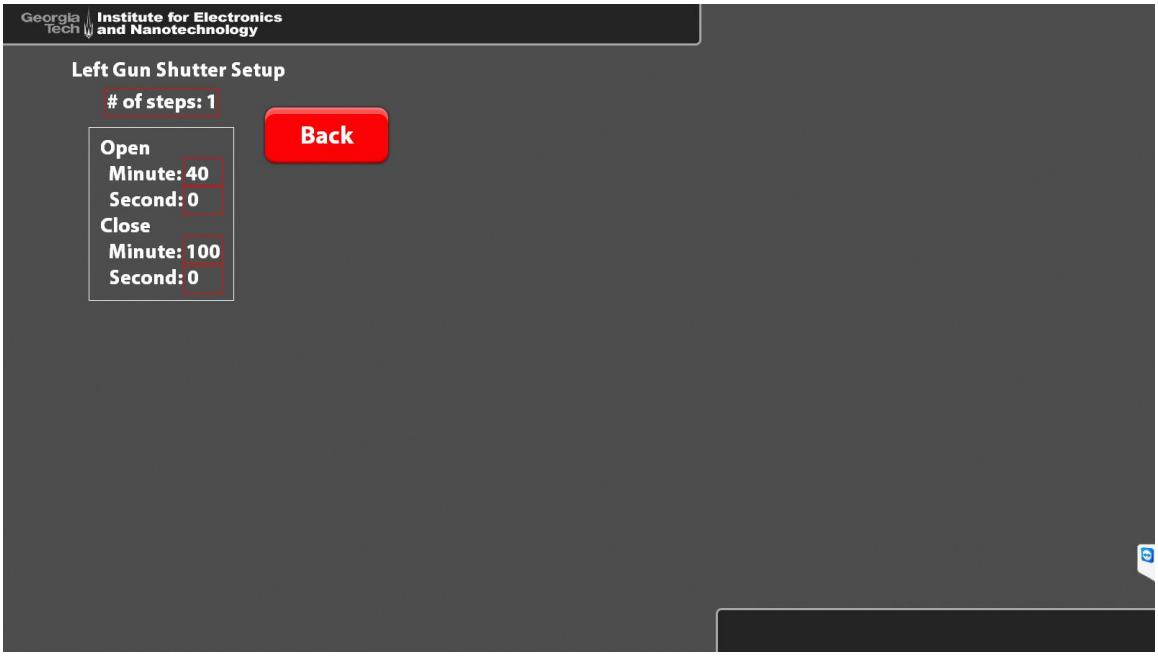

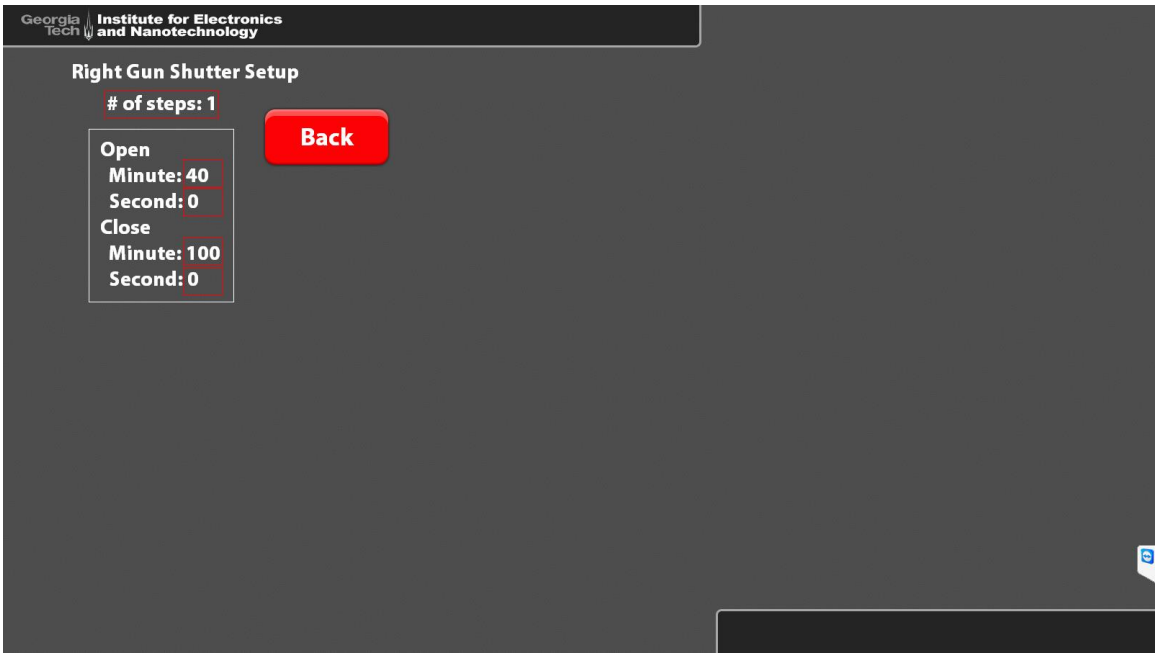

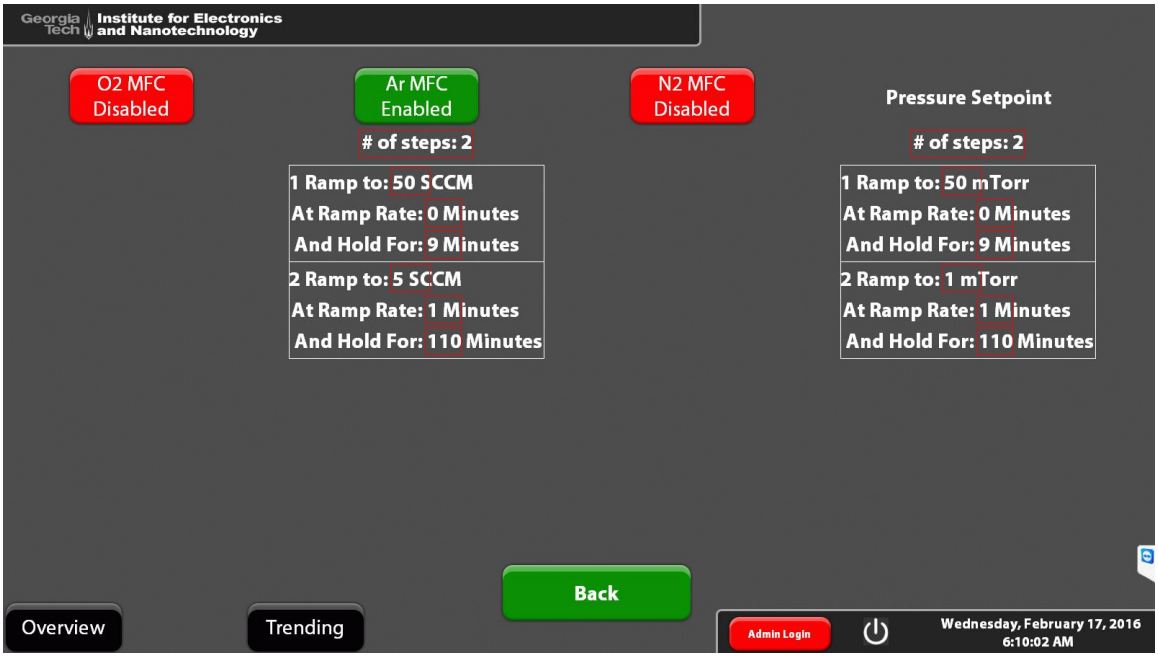

Notes:

1. The sudden drop from 100W to 50W as the shutter opens is to reduce transients in the right gun. It is unclear if this has any impact on the film.

Standard Recipe for LiPON

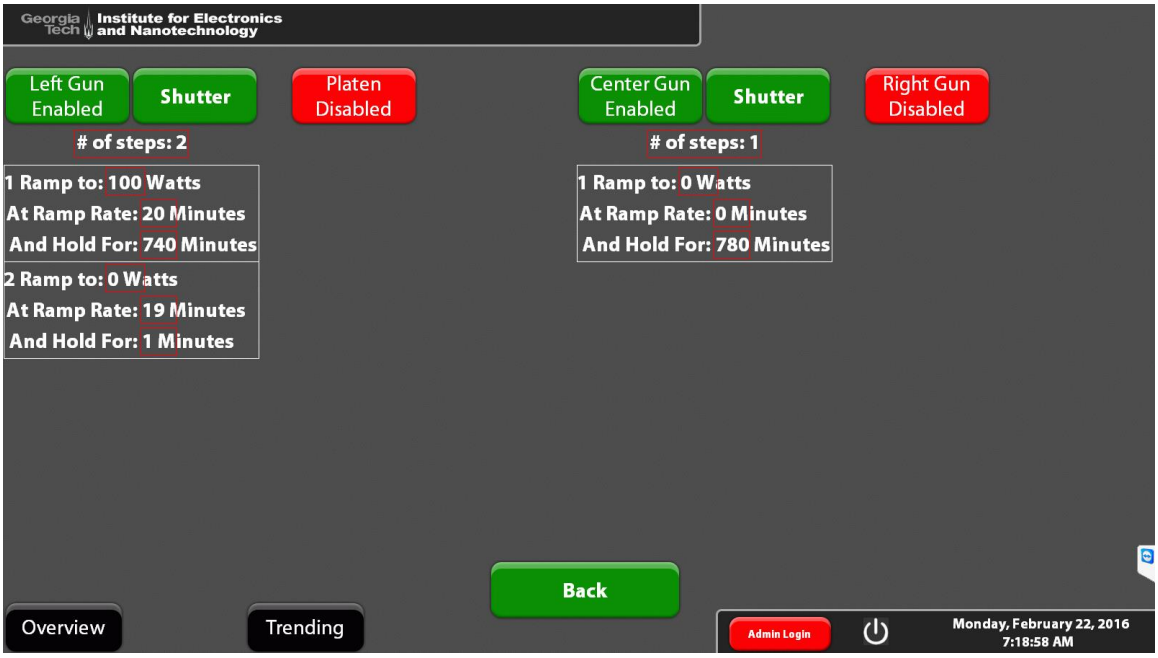

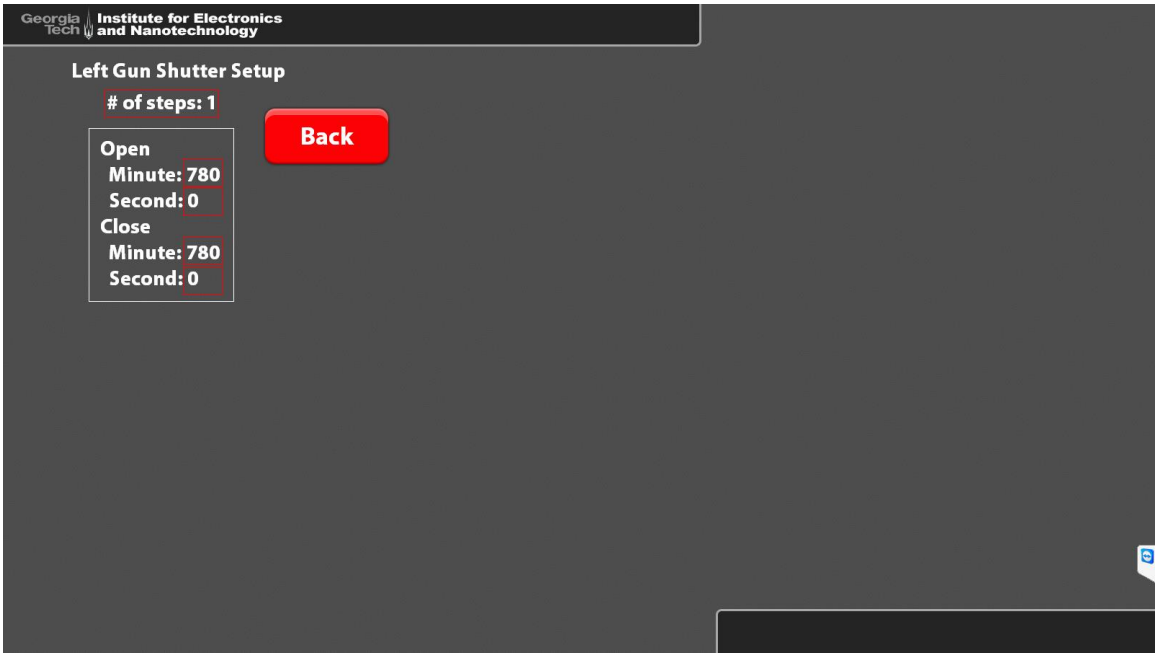

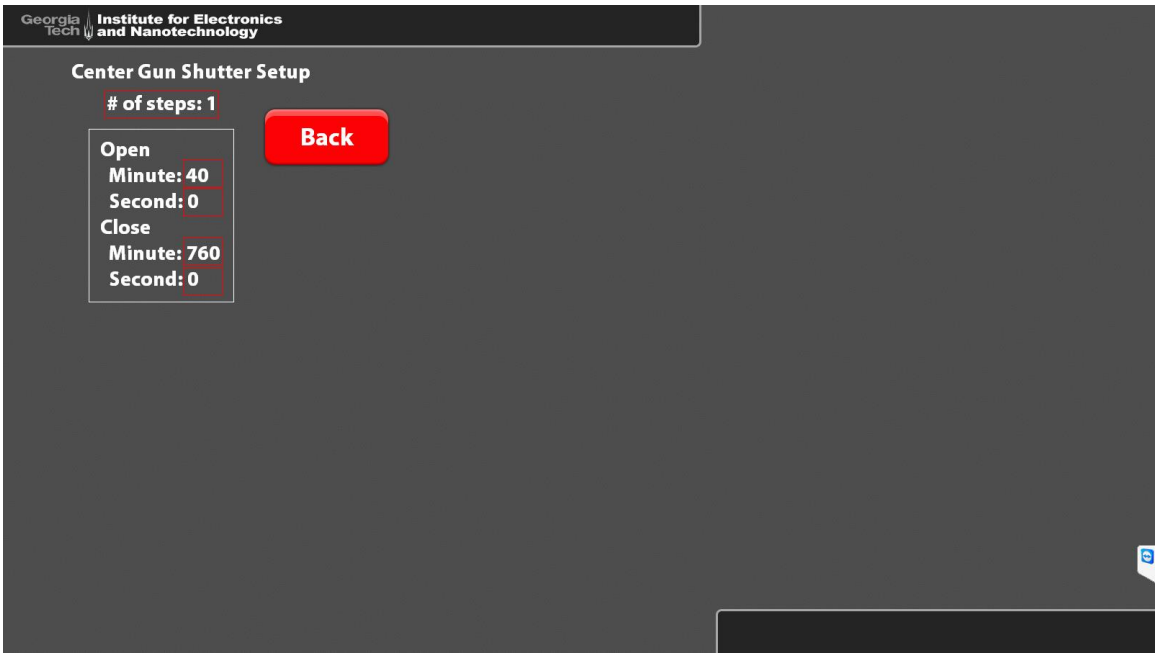
Georgia Tech Institute for Electronics and Nanotechnology
Center Gun Shutter Setup
# of steps: 1
Back
Open
Minute: 40
Second: 0
Close
Minute: 760
Second: 0

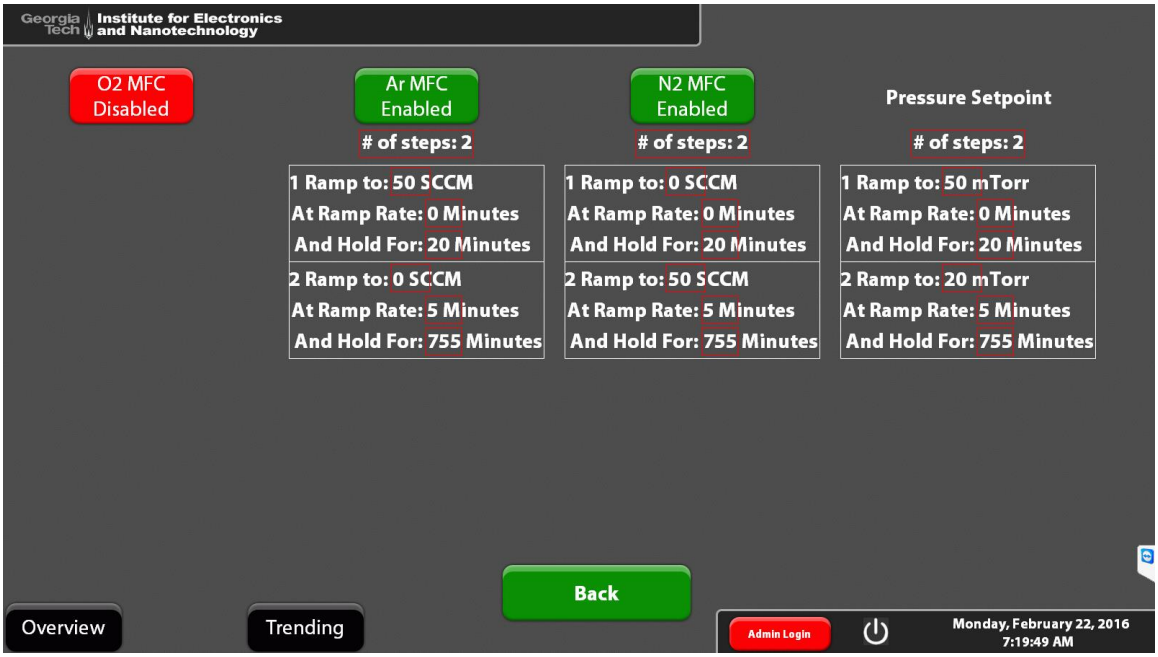
Georgia Tech Institute for Electronics and Nanotechnology
O2 MFC Disabled
Ar MFC Enabled
# of steps: 2
1 Ramp to: 50 SCCM
At Ramp Rate: 0 Minutes
And Hold For: 20 Minutes
2 Ramp to: 0 SCCM
At Ramp Rate: 5 Minutes
And Hold For: 755 Minutes
N2 MFC Enabled
# of steps: 2
1 Ramp to: 0 SCCM
At Ramp Rate: 0 Minutes
And Hold For: 20 Minutes
2 Ramp to: 50 SCCM
At Ramp Rate: 5 Minutes
And Hold For: 755 Minutes
Pressure Setpoint
# of steps: 2
1 Ramp to: 50 mTorr
At Ramp Rate: 0 Minutes
And Hold For: 20 Minutes
2 Ramp to: 20 mTorr
At Ramp Rate: 5 Minutes
And Hold For: 755 Minutes
Back
Overview
Trending
Admin Login
Monday, February 22, 2016
7:19:49 AM

Special Thanks

The following people deserve special thanks for their contributions to designing, building, and upgrading the Denton Discovery 2 sputtering system.

Gary Spinner

Jason Herrington

John Pham

Vinh Nguyen

Thomas Johnson-Averett

Dean Sutter

Scott Fowler

APPENDIX B

NEUROPHYSIOLOGY FOR ELECTRICAL ENGINEERS

The neuron model discussed in this thesis is simplistic compared to a biological neuron. The necessity of this simplification is due to the need to create structural primitives from which more advanced work can progress. This appendix will provide a brief overview of some neural complexities that were either mentioned briefly in the main thesis or skipped over entirely.

Effect of Cell Morphology

In Chapter 1 it was briefly stated that the structure of the dendritic tree affects spike propagation and synaptic learning. Dendrites are fundamentally transmission lines described by distributed elements of internal resistance, membrane resistance, and membrane capacitance [186]. The physical size and shape of the dendrites determines the values for these circuit elements and thus determines the effective propagation distance and filtering properties of the dendritic tree [22]. In some neuron morphologies it is possible to have a synapse far enough away from the cell body to never impact the integrated charge because any input action potentials are suppressed and filtered before they arrive at the cell body [186].

However, in addition to passive cable propagation, dendrites often express voltage-gated ion channels similar to the axon, although typically with a lower density than is observed in an axon [187]. The low density of voltage-gated ion channels allow for some active action potential regeneration, but not sufficient regeneration to cancel the effects of passive cable filtering. This low level regeneration allows single action

potentials to propagate efficiently, but suppresses high frequency bursts or trains of action potentials [22].

In addition to affecting action potential propagation, the dendritic structure also affects memory and learning. As discussed in Chapter 5, one of the primary learning mechanisms in neural systems is spike-timing dependent plasticity (STDP) in which the relative timing of pre-synaptic and post-synaptic action potentials determines the change in synaptic conduction. This model of neural learning has been experimentally demonstrated [188], but requires the ability to back-propagate action potentials through the dendritic tree to reach the synapses. Neurons with few branches in their dendritic trees can back-propagate action potentials fairly reliably, but other neurons such as Purkinje cells have extensively branched dendritic trees that unreliably back-propagate action potentials [187].

Another effect of cell morphology is the temporal and spatial summation of the dendritic tree. The complex geometrical structure a dendritic tree creates complex filtering and attenuation functions by combining thousands of synaptic inputs at different locations through the branches of the dendritic tree. It has been shown that synaptic inputs that are in close physical proximity and fire closely in time exhibit sub-linear summation rather than the linear summation from physically or temporally distant synapses [186].

Finally, the cell morphology described in Chapter 1, synapses → dendrites → soma → axon hillock → axon, includes all of the major cellular sub-structures. However, not all neurons include every sub-structure. For example, the starburst neuron located in the retina does not have an axon or axon hillock and the soma is thought to play

essentially no role in processing information. Instead, the star burst neuron has several sets of isolated semi-independent dendritic trees that receive inputs along their periphery and send outputs from their central portions. This cell morphology is thought to play a role in our ability to sense the direction of motion [16].

Advanced Hodgkin-Hukley Model

The Hodgkin-Hukley model of an axon shown in Figure 1-3 has been modified since its original conception to include more complex cellular structures and behaviors. Perhaps the most significant modification is the addition of a parallel current source representing the Na^{+}-K^{+} ATPase pumps that exchange sodium and potassium ions across the cell membrane maintaining the equilibrium concentrations. These pumps were not discovered until 1957, 5 years after the original Hodgkin-Huxley model was proposed [189]. One estimate of neural energy consumption predicts that ATPase pumps maintaining the neuron's resting potential use more than half of the neuron's power consumption [190] making them an important structure for creating an artificial neuron.

In addition to the discovery of ATPase pumps, multiple new ion channels and ion channel characteristics have been discovered since the original Hodgkin-Huxley model was published in 1952. Examples include Ca^{2+} ion channels and Cl^{-} ion channels thought to have wide ranging regulatory functionalities including regulation of the neuron's electrical excitability [191]. While the ionic basis for such regulatory behavior was not explicitly stated in Chapter 10, it is modelled in both the adaptive Schmitt Trigger displaying spike-frequency adaptation and the adaptive Neuristor displaying transitions to bursting behavior.

In addition to ion channels not captured in the original Hodgkin-Huxley model, approximately 40 genes encode potassium channels suggesting a wide variety of possible ion channels with varying dynamics [192]. The impact of these varying ion channel dynamics is still not well understood.

Stochastic Nature of Neural Computation

The Hodgkin-Huxley model is fundamentally a deterministic system. However, biological neurons are subject to stochastic processes such as thermodynamic fluctuations, ion channel noise, and synaptic noise [193]. Multiple modifications to the Hodgkin-Huxley model have been proposed to account for thermodynamic [194] and other stochastic process [193]. The stochastic nature of memristors has also been modelled for reproducing stochastic behavior in neuromorphic circuitry [195].

The Self-Organizing Brain

One aspect of neurobiology that is often overlooked in the discussion of neuromorphic computing architectures is the fact that the brain is a self-organizing system rather than a genetically specified design. Estimates of the human genome place the number of genes between 20,000 – 25,000, not nearly enough to deterministically specify the 10^{12} neurons each with 10^{3} – 10^{4} synaptic connections. Therefore, environmental factors also likely contribute to the brain's development.

The self-organizing nature of the brain directly contrasts with modern CMOS processors that are fully specified before fabrication. While it is unknown how these differing design philosophies affect the system's design and optimization, it is an aspect of neurobiology that has only recently been considered for neuromorphic circuitry with the advent of memristor enabled reconfigurable circuitry [196].

APPENDIX C

CLASSES OF MEMRISTORS

The memristor was first proposed as the fourth fundamental two-terminal passive circuit element by Leon Chua in 1971 [47]. The primary argument for the inclusion of the memristor was a matter of symmetry. There are four fundamental quantities when considering the passive circuit elements: charge (q), current (I), voltage (V), and flux-linkage (ϕ). These four quantities can be related to each other in six ways, shown in Equations 2.1a-f. The relations between charge to current and voltage to flux-linkage are fundamental definitions. Three of the remaining four relations describe the well-known passive devices: a resistor (voltage to current), a capacitor (charge to voltage), and an inductor (flux-linkage to current). Chua's 1971 paper theorized a fourth device that would relate flux-linkage and charge. A theoretical development of this relationship revealed that the device would act like a variable resistor with memory of its input. Thus the name memristor was given [47].

Fundamental Definition	$dq = I * dt$	Equation 2.1a
Fundamental Definition	$d\phi = V * dt$	Equation 2.1b
Resistor	$dV = R * dI$	Equation 2.1c
Capacitor	$dq = C * dV$	Equation 2.1d
Inductor	$d\phi = L * dI$	Equation 2.1e
Memristor	$d\phi = M * dq$	Equation 2.1f

In 1976, Chua expanded the memristor definition to include a class of devices termed memristive systems [26]. These devices are described by a set of dynamic relations, shown in Equations 2.2a-b, that include the original memristor definition but allow for more complex behavior such as multiple inputs, $\vec{u}$, multiple outputs, $\vec{y}$, and

multiple internal mechanisms described by the state variables, $\vec{x}$, allowing for threshold voltages and volatile behavior.

$$\vec{y} = g(\vec{x}, \vec{u}, t) * \vec{u} \quad \text{Equation 2.2a}$$

$$\frac{d\vec{x}}{dt} = f(\vec{x}, \vec{u}, t) \quad \text{Equation 2.2b}$$

These additional behaviors are important for physical devices because no physical implementation of a memristor has been shown to follow the more restrictive 1971 definition. While memristors were first theorized in 1971 and first experimentally reported in 2008, a review of historical devices reveals memristive behavior in a wide range of devices including tungsten filament lamps, vapor discharge tubes, and thermistors [60]. The following sub-sections summarize a few of the major classes of memristors that have received attention since the 2008 publication reintroduced memristors to the research community. Other memristor summaries have been tabulated elsewhere including comparisons of switching speed, retention time, and endurance [70].

Filamentary Memristors

The filamentary memristor was first published by HP labs in 2008 [46], although filamentary resistive switching devices were published and well characterized before this [62]. Fundamentally these devices operate by the creation and destruction of a conducting filament through an otherwise insulating material. When the filament connects the electrodes together a low resistance state exists and when the filament is broken a high resistance state exists. The formation of the filament requires the motion of mobile ions such as oxygen anions in TiO_2 [46], NiO [48], WO_x [49], TaO_x [50], or NbO_x [51], or metal cations in Ag_2S or GeSe [62]. While these devices are typically binary, careful

control of timing and compliance currents can program analog resistance states by controlling the distance between the filament edge and one electrode [72].

Filamentary memristors can be further divided into unipolar and bipolar devices. Unipolar devices are capable of switching when a voltage of either polarity is applied. Filament formation occurs at a fairly low voltage while filament destruction occurs at a higher voltage. These devices are often compared to a nano-scale fuse [62]. In contrast, bipolar filamentary memristors require voltages of opposite polarities to switch between the high and low resistance states by electrically drifting the mobile ions in each direction.

Filamentary memristors are typically not manufactured with the filaments preformed and filaments must by initialized by an electroforming process. This process requires higher voltage and current than normal operation and has been shown to cause electrode damage in switchable oxides as mobile oxygen bursts through the electrode [66, 67]. In addition to the filament formation, filamentary memristor operation creates extreme thermal and electrical conditions. It is estimated that a switching memristor produces power densities on the order of 10^{12} W/cm^3 [62] reaching temperatures of 800 K [69] and electric fields above 10^6 V/cm [68].

Mobile Ion Wavefront Memristors

While filamentary memristors can be considered one geometry of mixed ion-electron conducting (MIEC) memristors, another geometry is the mobile ion wave front memristor. This geometry is similar to the bipolar switching filamentary memristor, but no filament is formed. Instead, mobile dopants move throughout a host lattice creating regions of highly doped and semi-insulating material.

One example of this geometry is the cosputtered Ag/Si memristor in which the conduction front is created by introducing the dopant silver part of the way into a silicon deposition. This eliminates the need for electroforming as the device is fully formed during fabrication [63]. Mobile ion wave front devices have demonstrated nearly analog switching, but have not been demonstrated with as wide a dynamic range (R_{ON} / R_{OFF}) as filamentary memristors. The $LiNbO_2$ memristors examined in this thesis fall into this category.

Oxidation/Reduction Memristors

While memristors were originally defined as two terminal devices [47], the memristive system definition allows for multiport systems [26]. Such memristive systems have been demonstrated in mobile ion systems in which the mobile ions are allowed to leave the memristive material through a gated electrolyte. This three terminal transistor structure results in the oxidation or reduction of the active material changing the conductance between the source and drain terminals. Experimental examples of this structure include the oxidation/reduction of organic materials [58] and the lithiation of inorganic battery cathodes [57]. These three terminal devices are important for neuromorphic applications because many biological models include batteries with variable resistance [25] and the biological synapse is fundamentally a three terminal device – involving the presynaptic neuron, the post-synaptic neuron, and the intracellular fluid – although it is often replaced by two terminal memristors in neuromorphic circuits.

Spintronic Memristors

While mobile ion-electron conducting memristors modify the electron conductivity either with doping or phase transitions, memristive effects have also been

observed in materials where resistance modulation and memory are provided by a degree of freedom other than mobile ions. One such system is the broad class of spintronic devices where electron transport is sensitive to the electron-spin polarization, which can be changed by an externally applied voltage [54]. By controlling the ferromagnetic polarization of a free polarization layer compared to a reference polarization layer across a tunneling junction, the current flow through the tunnel junction can be controlled [55]. Many of these devices can also be switched by an external magnetic field [56] making them multi-input devices best described by the memristive system formalism.

Ferroelectric Switches

Similar to the spintronic memristors are ferroelectric memristors where device resistance is controlled by the ferroelectric polarization near a tunnel barrier. For nanoscale devices with small domains, a nearly continuous range of resistances can be achieved [65].

Mott Metal-Insulator Switches

In addition to ion motion, magnetic polarization, and electric polarization, thermal energy can provide a degree of freedom capable of producing memristive behavior. In materials with a Mott metal-insulator transition, joule heating has been demonstrated to produce memristive effects. When sufficient voltage is applied to heat the device above the metal-insulator transition temperature, the device switches to a conducting state. The conducting state (higher current) dissipates more power, requiring a lower voltage to switch back to the insulating state [23]. Later work demonstrated that the internal temperature was not high enough to cause the metal-insulator transition and that the

memristive hysteresis was caused by smaller temperature changes modifying a Poole-Frenkel current [170].

REFERENCES

1. G. Moore, in *Electronics* (1965), pp. 114-117.
2. First Commercial MOS IC Introduced, http://www.computerhistory.org/semiconductor/timeline/1964-Commecial.html
3. More-than-Moore, 2010, www.itrs.net
4. International Technology Roadmap for Semiconductors, 2013, www.itrs.net
5. S. E. Thompson and S. Parthasarathy, Materials Today **9** (6), 20-25 (2006).
6. J. Wang and M. Lundstrom, presented at the Electron Devices Meeting, 2002. IEDM'02. International, 2002 (unpublished).
7. V. V. Zhirnov, R. K. Cavin, J. A. Hutchby and G. I. Bourianoff, Proceedings of the IEEE **91** (11), 1934-1939 (2003).
8. C. Moore, presented at the The Salishan Conference on High Speed Computing, 2011 (unpublished).
9. P. Chaparro, J. González, G. Magklis, Q. Cai and A. Gonzalez, Parallel and Distributed Systems, IEEE Transactions on **18** (8), 1055-1065 (2007).
10. J. D. Owens, M. Houston, D. Luebke, S. Green, J. E. Stone and J. C. Phillips, Proceedings of the IEEE **96** (5), 879-899 (2008).
11. A. Steane, Reports on Progress in Physics **61** (2), 117 (1998).
12. A. Sawchuk and T. C. Strand, Proceedings of the IEEE **72** (7), 758-779 (1984).
13. C. Mead, Proceedings of the IEEE **78** (10), 1629-1636 (1990).
14. Brain Facts and Figures, http://faculty.washington.edu/chudler/facts.html
15. Intel Releases Broadwell-U, 2015, http://www.anandtech.com/show/8814/intel-releases-broadwell-u-new-skus-up-to-48-eus-and-iris-6100/2
16. G. L. Fain, *Molecular and Cellular Physiology of Neurons*. (Harvard University Press, Cambridge, Mass, 1999).
17. W. Gerstner, A. K. Kreiter, H. Markram and A. V. Herz, Proceedings of the National Academy of Sciences **94** (24), 12740-12741 (1997).
18. P. Häfliger, Neural Networks, IEEE Transactions on **18** (2), 551-572 (2007).
19. B. Linares-Barranco, T. Serrano-Gotarredona, L. A. Camuñas-Mesa, J. A. Perez-Carrasco, C. Zamarreño-Ramos and T. Masquelier, Frontiers in Neuroscience **5** (2011).
20. Y. Shu, A. Hasenstaub, M. Badoual, T. Bal and D. A. McCormick, The Journal of neuroscience **23** (32), 10388-10401 (2003).
21. J. D. Greenlee, W. Calley, W. Henderson and W. A. Doolittle, Physica status solidi (c) **9** (2), 155-160 (2012).
22. D. Johnston, J. C. Magee, C. M. Colbert and B. R. Christie, Annual review of neuroscience **19** (1), 165-186 (1996).
23. M. D. Pickett, G. Medeiros-Ribeiro and R. S. Williams, Nat Mater **12** (2), 114-117 (2013).
24. S. A. Buffington and M. N. Rasband, European Journal of Neuroscience **34** (10), 1609-1619 (2011).
25. A. L. Hodgkin and A. F. Huxley, The Journal of physiology **117** (4), 500-544 (1952).
26. L. O. Chua and K. Sung Mo, Proceedings of the IEEE **64** (2), 209-223 (1976).

27. A. Katsiamis and E. Drakakis, Biomimetic Based Applications (2011).
28. C. A. Mead and M. A. Mahowald, Neural Networks **1** (1), 91-97 (1988).
29. J. G. Harris, C. Koch, E. Staats and J. Luo, International Journal of Computer Vision **4** (3), 211-223 (1990).
30. R. F. Lyon, presented at the Acoustics, Speech, and Signal Processing, IEEE International Conference on ICASSP'82., 1982 (unpublished).
31. R. F. Lyon and C. Mead, Acoustics, Speech and Signal Processing, IEEE Transactions on **36** (7), 1119-1134 (1988).
32. B. B. Lee, D. M. Dacey, V. C. Smith and J. Pokorny, Proceedings of the National Academy of Sciences of the United States of America **96** (25), 14611-14616 (1999).
33. E. Hornstein, J. Verweij, P. Li and J. Schnapf, The Journal of neuroscience: the official journal of the Society for Neuroscience **25** (48), 11201 (2005).
34. M. Mahowald and R. Douglas, Nature **354** (6354), 515-518 (1991).
35. G. Indiveri, presented at the ISCAS (4), 2003 (unpublished).
36. F. Folowosele, A. Harrison, A. Cassidy, A. G. Andreou, R. Etienne-Cummings, S. Mihalas, E. Niebur and T. J. Hamilton, presented at the Circuits and Systems, 2009. ISCAS 2009. IEEE International Symposium on, 2009 (unpublished).
37. J. H. Wijekoon and P. Dudek, Neural Networks **21** (2), 524-534 (2008).
38. G. Indiveri, B. Linares-Barranco, T. J. Hamilton, A. van Schaik, R. Etienne-Cummings, T. Delbruck, S.-C. Liu, P. Dudek, P. Häfliger, S. Renaud, J. Schemmel, G. Cauwenberghs, J. Arthur, K. Hynna, F. Folowosele, S. SAÏGHI, T. Serrano-Gotarredona, J. Wijekoon, Y. Wang and K. Boahen, Frontiers in Neuroscience **5** (2011).
39. J. Hasler and B. Marr, Frontiers in Neuroscience **7** (2013).
40. T. J. Koickal, A. Hamilton, S. L. Tan, J. Covington, J. W. Gardner and T. C. Pearce, Circuits and Systems I: Regular Papers, IEEE Transactions on **54** (1), 60-73 (2007).
41. Y. Wang and S.-C. Liu, Neural computation **22** (8), 2086-2112 (2010).
42. P. Häfliger and H. K. Riis, presented at the Circuits and Systems, 2003. ISCAS'03. Proceedings of the 2003 International Symposium on, 2003 (unpublished).
43. B. Linares-Barranco and T. Serrano-Gotarredona, presented at the Nanotechnology, 2009. IEEE-NANO 2009. 9th IEEE Conference on, 2009 (unpublished).
44. M. Noack, C. Mayr, J. Partzsch, M. Schultz and R. Schüffny, presented at the Mixed Design of Integrated Circuits and Systems (MIXDES), 2012 Proceedings of the 19th International Conference, 2012 (unpublished).
45. A. Mortara and E. Vittoz, Neural Networks, IEEE Transactions on **5** (3), 459-466 (1994).
46. D. B. Strukov, G. S. Snider, D. R. Stewart and R. S. Williams, Nature **453** (7191), 80-83 (2008).
47. L. O. Chua, Circuit Theory, IEEE Transactions on **18** (5), 507-519 (1971).
48. M. J. Lee, S. I. Kim, C. B. Lee, H. Yin, S. E. Ahn, B. S. Kang, K. H. Kim, J. C. Park, C. J. Kim and I. Song, Advanced Functional Materials **19** (10), 1587-1593 (2009).

49. X. Liu, S. M. Sadaf, S. Kim, K. P. Biju, X. Cao, M. Son, S. H. Choudhury, G.-Y. Jung and H. Hwang, ECS Solid State Letters **1** (5), Q35-Q38 (2012).
50. J. J. Yang, M. Zhang, J. P. Strachan, F. Miao, M. D. Pickett, R. D. Kelley, G. Medeiros-Ribeiro and R. S. Williams, Applied Physics Letters **97** (23), 232102 (2010).
51. H. Sim, D. Choi, D. Lee, S. Seo, M.-J. Lee, I.-K. Yoo and H. Hwang, Electron Device Letters, IEEE **26** (5), 292-294 (2005).
52. Y. Nian, J. Strozier, N. Wu, X. Chen and A. Ignatiev, Physical review letters **98** (14), 146403 (2007).
53. J. C. Shank, M. B. Tellekamp and W. A. Doolittle, Journal of Applied Physics **117** (3), 035704 (2015).
54. Y. V. Pershin and M. Di Ventra, Physical Review B **78** (11), 113309 (2008).
55. X. Wang, Y. Chen, H. Xi, H. Li and D. Dimitrov, Electron Device Letters, IEEE **30** (3), 294-297 (2009).
56. H. Mahmoudi, T. Windbacher, V. Sverdlov and S. Selberherr, Solid-State Electronics **84**, 191-197 (2013).
57. J. D. Greenlee, C. F. Petersburg, W. G. Daly, F. M. Alamgir and W. A. Doolittle, Applied Physics Letters **102**, 213502 (2013).
58. V. Erokhin, T. Berzina and M. P. Fontana, Journal of Applied Physics **97** (6), 064501 (2005).
59. M. E. Fouda, A. S. Elwakil and A. G. Radwan, Microelectronics journal **46** (9), 834-838 (2015).
60. T. Prodromakis, C. Toumazou and L. Chua, Nature materials **11** (6), 478 (2012).
61. T. Hickmott, Journal of Applied Physics **33** (9), 2669-2682 (1962).
62. R. Waser and M. Aono, Nature materials **6** (11), 833-840 (2007).
63. S. H. Jo, T. Chang, I. Ebong, B. B. Bhadviya, P. Mazumder and W. Lu, Nano Letters **10** (4), 1297-1301 (2010).
64. W. E. Henderson, W. Laws Calley, A. G. Carver, H. Chen and W. Alan Doolittle, Journal of Crystal Growth **324** (1), 134-141 (2011).
65. A. Chanthbouala, V. Garcia, R. O. Cherifi, K. Bouzehouane, S. Fusil, X. Moya, S. Xavier, H. Yamada, C. Deranlot and N. D. Mathur, Nature materials **11** (10), 860-864 (2012).
66. R. Münstermann, J. J. Yang, J. P. Strachan, G. Medeiros-Ribeiro, R. Dittmann and R. Waser, physica status solidi (RRL)-Rapid Research Letters **4** (1-2), 16-18 (2010).
67. D.-H. Kwon, K. M. Kim, J. H. Jang, J. M. Jeon, M. H. Lee, G. H. Kim, X.-S. Li, G.-S. Park, B. Lee and S. Han, Nature nanotechnology **5** (2), 148-153 (2010).
68. M. Noman, A. A. Sharma, Y. M. Lu, R. Kamaladasa, M. Skowronski, P. A. Salvador and J. A. Bain, Applied Physics Letters **104** (11), 113510 (2014).
69. J. P. Strachan, D. B. Strukov, J. Borghetti, J. J. Yang, G. Medeiros-Ribeiro and R. S. Williams, Nanotechnology **22** (25), 254015 (2011).
70. S. D. Ha and S. Ramanathan, Journal of Applied Physics **110** (7), 071101 (2011).
71. A. Thomas, Journal of Physics D: Applied Physics **46** (9), 093001 (2013).
72. T.-W. Lee and J. H. Nickel, Electron Device Letters, IEEE **33** (10), 1456-1458 (2012).

73. J. D. Greenlee, C. F. Petersburg, W. Laws Calley, C. Jaye, D. A. Fischer, F. M. Alamgir and W. Alan Doolittle, Applied Physics Letters **100** (18), 182106-182106-182104 (2012).
74. J. D. Greenlee, W. Calley, M. W. Moseley and W. A. Doolittle, IEEE Transactions on Electron Devices **60** (1), 427-432 (2013).
75. M. J. Geselbracht, A. M. Stacy, A. R. Garcia, B. G. Silbernagel and G. H. Kwei, The Journal of Physical Chemistry **97** (27), 7102-7107 (1993).
76. A. McDowell, D. Snyderman, M. S. Conradi, B. Silbernagel and A. Stacy, Physical Review B **50** (21), 15764 (1994).
77. E. L. Wooten, K. M. Kissa, A. Yi-Yan, E. J. Murphy, D. Lafaw, P. F. Hallemeier, D. Maack, D. V. Attanasio, D. J. Fritz and G. J. McBrien, Selected Topics in Quantum Electronics, IEEE Journal of **6** (1), 69-82 (2000).
78. K. K. Wong, *Properties of Lithium Niobate*. (INSPEC, 2002).
79. G. Meyer and R. Hoppe, Angewandte Chemie International Edition in English **13** (11), 744-745 (1974).
80. J. Akimoto, Y. Gotoh and Y. Oosawa, Journal of Solid State Chemistry **141** (1), 298-302 (1998).
81. A. Miura, K. Tadanaga, E. Magome, C. Moriyoshi, Y. Kuroiwa, T. Takahiro and N. Kumada, Journal of Solid State Chemistry **229**, 272-277 (2015).
82. E. R. Ylvisaker and W. E. Pickett, Physical Review B **74** (7), 075104 (2006).
83. R. Huisman, R. de Jonge, C. Haas and F. Jellinek, Journal of Solid State Chemistry **3** (1), 56-66 (1971).
84. D. Novikov, V. Gubanov, V. Zubkov and A. Freeman, Physical Review B **49** (22), 15830 (1994).
85. M. J. Geselbracht, T. J. Richardson and A. M. Stacy, Nature **345**, 324 - 326 (1990).
86. V. Cherkashenko, M. Korotin, V. Anisimov, V. Shumilov, V. Galakhov, D. Kellerman, V. Zubkov and E. Kurmaev, Zeitschrift für Physik B Condensed Matter **93** (4), 417-424 (1994).
87. J. D. Greenlee, J. C. Shank, M. B. Tellekamp and W. A. Doolittle, Journal of Applied Physics **114** (3), 034504 (2013).
88. E. Moshopoulou, P. Bordet and J. Capponi, Physical Review B **59** (14), 9590 (1999).
89. J. K. Burdett and T. Hughbanks, Inorganic Chemistry **24** (12), 1741-1750 (1985).
90. N. Kumada, S. Muramatu, F. Muto, N. Kinomura, S. Kikkawa and M. Koizumi, Journal of Solid State Chemistry **73** (1), 33-39 (1988).
91. H. F. Roth, G. Meyer, Z. Hu and G. Kaindl, Zeitschrift für anorganische und allgemeine Chemie **619** (8), 1369-1373 (1993).
92. P. Bordet, E. Moshopoulou, S. Liesert and J. Capponi, Physica C: Superconductivity **235**, 745-746 (1994).
93. D. Kellerman, V. Gorshkov and A. Tyutyunnik, (1992).
94. S. Chang, H. Park, A. Maazaz and C. Delmas, COMPTES RENDUS DE L ACADEMIE DES SCIENCES SERIE II **308** (5), 475-478 (1989).
95. J. D. Greenlee, J. C. Shank, M. B. Tellekamp, B. Gunning, C. A. Fabien and A. Doolittle, Crystal Growth & Design **14** (5), 2218-2222 (2014).
96. M. Loubser, University of Pretoria, 2009.

97. D. Chirkov and D. Vasiliovych, UNIVERSITÀ DEGLI STUDI DI PADOVA, 2010.
98. J. A. Thornton, Journal of Vacuum Science & Technology **11** (4), 666-670 (1974).
99. A. Dey, Journal of The Electrochemical Society **118** (10), 1547-1549 (1971).
100. Q. Lin, Q. a. Li, K. E. Gray and J. F. Mitchell, Crystal Growth & Design **12** (3), 1232-1238 (2012).
101. J. Hertz, Q. Huang, T. McQueen, T. Klimczuk, J. Bos, L. Viciu and R. Cava, Physical Review B **77** (7), 075119 (2008).
102. W. D. Sproul, D. J. Christie and D. C. Carter, Thin Solid Films **491** (1), 1-17 (2005).
103. S. Berg and T. Nyberg, Thin Solid Films **476** (2), 215-230 (2005).
104. R. Bland, G. Kominiak and D. Mattox, Journal of Vacuum Science & Technology **11** (4), 671-674 (1974).
105. Z. Sitar, F. Gitmans, W. Liu and P. Günter, presented at the MRS Proceedings, 1995 (unpublished).
106. W. A. Doolittle, A. Carver, W. Henderson and W. L. Calley, ECS Transactions **2** (5), 103-114 (2006).
107. Z. Lu, R. Hiskes, S. DiCarolis, R. Route, R. Feigelson, F. Leplingard and J. Fouquet, Journal of Materials Research **9** (09), 2258-2263 (1994).
108. S. Takada, M. Ohnishi, H. Hayakawa and N. Mikoshiba, Applied Physics Letters **24** (10), 490-492 (1974).
109. S. Schwyn, H. Lehmann and R. Widmer, Journal of Applied Physics **72** (3), 1154-1159 (1992).
110. T. A. Rost, H. Lin, T. A. Rabson, R. C. Baumann and D. L. Callahan, Journal of Applied Physics **72** (9), 4336-4343 (1992).
111. C.-L. Liao and K.-Z. Fung, Journal of Power Sources **128** (2), 263-269 (2004).
112. Y. Yoon, S. Lee, S. Cho and S. Nam, Journal of The Electrochemical Society **158** (12), A1313-A1319 (2011).
113. J. Whitacre, W. West and B. Ratnakumar, Journal of Power Sources **103** (1), 134-139 (2001).
114. J. Malherbe, S. Hofmann and J. Sanz, Applied surface science **27** (3), 355-365 (1986).
115. L. Birks and H. Friedman, Journal of Applied Physics **17** (8), 687-692 (1946).
116. P. Scherrer, Nachr. Ges. Wiss. Göttingen **2**, 96-100 (1918).
117. F. Frost, B. Ziberi, T. Höche and B. Rauschenbach, Nuclear Instruments and Methods in Physics Research Section B: Beam Interactions with Materials and Atoms **216**, 9-19 (2004).
118. G. Carter and V. Vishnyakov, Physical Review B **54** (24), 17647 (1996).
119. P. Karulkar, Journal of Vacuum Science & Technology **18** (2), 169-174 (1981).
120. N. Kumada, S. Watauchi, I. Tanaka and N. Kinomura, Materials research bulletin **35** (11), 1743-1746 (2000).
121. J. Tauc and A. Menth, Journal of Non-Crystalline Solids **8**, 569-585 (1972).
122. C. Wagner, L. Davis, M. Zeller, J. Taylor, R. Raymond and L. Gale, Surface and interface analysis **3** (5), 211-225 (1981).

123. C. F. Miller, G. W. Simmons and R. P. Wei, Scripta Materialia **42** (3), 227-232 (2000).
124. Y.-J. Hsiao, T.-H. Fang, S.-J. Lin, J.-M. Shieh and L.-W. Ji, Journal of Luminescence **130** (10), 1863-1865 (2010).
125. G. Blasse, physica status solidi (a) **20** (2), K99-K102 (1973).
126. M. Murai, K. Takizawa, K. Soejima and H. Sotouchi, Journal of The Electrochemical Society **143** (11), 3456-3462 (1996).
127. M. B. Tellekamp, J. D. Greenlee, J. C. Shank and W. A. Doolittle, Journal of Crystal Growth **425** (0), 225-229 (2015).
128. S. Zhou, J. Xu, S. Li, W. Yang, G. Peng, J. Zou, Y. Wang, S. Liu, G. Zhao and H. Li, Journal of Crystal Growth **267** (3), 564-568 (2004).
129. Y. Hamon, T. Brousse, F. Jousse, P. Topart, P. Buvat and D. Schleich, Journal of Power Sources **97**, 185-187 (2001).
130. J. J. Wu and W. R. Bennett, presented at the Energytech, 2012 IEEE, 2012 (unpublished).
131. M. L. Terranova, S. Orlanducci, E. Tamburri, V. Guglielmotti and M. Rossi, Journal of Power Sources **246**, 167-177 (2014).
132. N. G. Rudawski, B. L. Darby, B. R. Yates, K. Jones, R. Elliman and A. Volinsky, Applied Physics Letters **100** (8), 083111 (2012).
133. J. R. Szczech and S. Jin, Energy & Environmental Science **4** (1), 56-72 (2011).
134. R. Whatmore, Reports on Progress in Physics **49** (12), 1335 (1986).
135. I. Kaminow and J. Carruthers, Applied Physics Letters **22** (7), 326-328 (1973).
136. E. Zhang, D. Fleetwood, N. Pate, R. Reed, A. Witulski and R. Schrimpf, IEEE Trans. Nucl. Sci. **60** (6), 4470-4475 (2013).
137. J. D. Greenlee, J. C. Shank, M. B. Tellekamp, E. X. Zhang, J. Bi, D. M. Fleetwood, M. L. Alles, R. D. Schrimpf and W. A. Doolittle, IEEE Trans. Nucl. Sci. **60** (6), 4555-4562 (2013).
138. S. Zhang, K. Xu and T. Jow, Electrochimica acta **51** (8), 1636-1640 (2006).
139. E. D. N. Soppera, M. Bossant, *JANIS Book of proton-induced cross-sections*. (OECD NEA Data Bank, 2012).
140. J. Srour, C. J. Marshall and P. W. Marshall, IEEE Trans. Nucl. Sci. **50** (3), 653-670 (2003).
141. C. Poivey, NASA GSFC, USA [Online]. Available: http://nepp.nasa.gov/DocUploads/A6B8B953-E2DD-4D92-AB8A873A04F0B10A/NSREC02_SC_Poivey.pdf (2002).
142. P. Pizani, E. Leite, F. Pontes, E. Paris, J. Rangel, E. Lee, E. Longo, P. Delega and J. Varela, Applied Physics Letters **77** (6), 824-826 (2000).
143. E. Iliopoulos, D. Doppalapudi, H. Ng and T. Moustakas, Applied Physics Letters **73** (3), 375-377 (1998).
144. C. Liang, K. Terabe, T. Tsuruoka, M. Osada, T. Hasegawa and M. Aono, Advanced Functional Materials **17** (9), 1466-1472 (2007).
145. S. M. Sze and K. K. Ng, *Physics of Semiconductor Devices*. (John Wiley & Sons, Hoboken, NJ, 2007).
146. S. Shishiyanu, R. Singh, T. Shishiyanu, S. Asher and R. Reedy, Electron Devices, IEEE Transactions on **58** (3), 776-781 (2011).

147. M. Keddam, Z. Stoynov and H. Takenouti, Journal of applied electrochemistry **7** (6), 539-544 (1977).
148. G. Torrie, The Journal of chemical physics **96** (5), 3772-3774 (1992).
149. M. Ershov, H. Liu, L. Li, M. Buchanan, Z. Wasilewski and A. K. Jonscher, Electron Devices, IEEE Transactions on **45** (10), 2196-2206 (1998).
150. K. S. Cole, The Journal of general physiology **25** (1), 29-51 (1941).
151. A. K. Jonscher, Journal of the Chemical Society, Faraday Transactions 2: Molecular and Chemical Physics **82** (1), 75-81 (1986).
152. H. Xia, S. Y. Meng, L. Lu and G. Ceder, (2007).
153. M. Jo, S. Jeong and J. Cho, Electrochemistry Communications **12** (7), 992-995 (2010).
154. W. West, J. Whitacre, V. White and B. Ratnakumar, Journal of Micromechanics and Microengineering **12** (1), 58 (2001).
155. J. Whitacre, W. West, E. Brandon and B. Ratnakumar, Journal of The Electrochemical Society **148** (10), A1078-A1084 (2001).
156. J. Song, X. Yang, S.-S. Zeng, M.-Z. Cai, L.-T. Zhang, Q.-F. Dong, M.-S. Zheng, S.-T. Wu and Q.-H. Wu, Journal of Micromechanics and Microengineering **19** (4), 045004 (2009).
157. J.-M. Tarascon and M. Armand, Nature **414** (6861), 359-367 (2001).
158. M. Park, X. Zhang, M. Chung, G. B. Less and A. M. Sastry, Journal of Power Sources **195** (24), 7904-7929 (2010).
159. A. Yariv, S. S. Orlov and G. A. Rakuljic, JOSA B **13** (11), 2513-2523 (1996).
160. Z.-W. Fu, W.-Y. Liu, C.-L. Li, Q.-Z. Qin, Y. Yao and F. Lu, Applied Physics Letters **83** (24), 5008-5010 (2003).
161. J. Bates, N. Dudney, G. Gruzalski, R. Zuhr, A. Choudhury, C. Luck and J. Robertson, Journal of Power Sources **43** (1-3), 103-110 (1993).
162. W. West, J. Whitacre and J. Lim, Journal of Power Sources **126** (1), 134-138 (2004).
163. Y. Inaguma, C. Liquan, M. Itoh, T. Nakamura, T. Uchida, H. Ikuta and M. Wakihara, Solid State Communications **86** (10), 689-693 (1993).
164. D. Kalita, S. Lee, K. Lee, D. Ko and Y. Yoon, Solid state ionics **229**, 14-19 (2012).
165. H. D. Crane, Proceedings of the IRE **50** (10), 2048-2060 (1962).
166. B. W. Connors, M. J. Gutnick and D. A. Prince, Journal of Neurophysiology **48** (6), 1302-1320 (1982).
167. T. Hickmott, Journal of Applied Physics **37** (12), 4380-4388 (1966).
168. R. Schwartz, Y. Chiou and H. Thompson, Thin Solid Films **6** (2), 81-89 (1970).
169. T. Hickmott, J. Vac. Sci. Technol **6** (5), 828-833 (1969).
170. S. Slesazeck, H. Mähne, H. Wylezich, A. Wachowiak, J. Radhakrishnan, A. Ascoli, R. Tetzlaff and T. Mikolajick, RSC Advances **5** (124), 102318-102322 (2015).
171. S. Venkataraj, R. Drese, C. Liesch, O. Kappertz, R. Jayavel and M. Wuttig, Journal of Applied Physics **91** (8), 4863-4871 (2002).
172. B. Gatehouse and A. Wadsley, Acta Crystallographica **17** (12), 1545-1554 (1964).
173. M. A. Aegerter, Solar energy materials and solar cells **68** (3), 401-422 (2001).

174. D. S. Hong, Y. S. Chen, J. R. Sun and B. G. Shen, Advanced Electronic Materials (2016).
175. S. Halas and T. Durakiewicz, Journal of Physics: Condensed Matter **10** (48), 10815 (1998).
176. B. Vigh, C. Frank, C. Vincze, S. Czirok, A. Szabó, A. Lukáts and A. Szél, Histology and histopathology **19** (2), 607-628 (2004).
177. S. D. Beagle and S. W. Lockless, Nature **527** (7576), 44-45 (2015).
178. M. Nete, W. Purcell, E. Snyders and J. T. Nel, South African Journal of Chemistry **63**, 130-134 (2015).
179. R. K. Pandey, S. N. Sahu and S. Chandra, *Handbook of Semiconductor Electrodeposition*. (Marcel Dekker inc., 1996).
180. A. Leshem, E. Gonen and I. Riess, Nanotechnology **22** (25), 254024 (2011).
181. I. Riess and J. Maier, Physical review letters **100** (20), 205901 (2008).
182. N. Mott, Journal of Non-Crystalline Solids **1** (1), 1-17 (1968).
183. A. Nenashev, F. Jansson, S. Baranovskii, R. Österbacka, A. Dvurechenskii and F. Gebhard, Physical Review B **78** (16), 165207 (2008).
184. V. Biolkova, Z. Kolka, Z. Biolek and D. Biolek, presented at the Proceedings of the European conference of systems, and European conference of circuits technology and devices, and European conference of communications, and European conference on Computer science, 2010 (unpublished).
185. Y. V. Pershin and M. Di Ventra, Circuits and Systems I: Regular Papers, IEEE Transactions on **57** (8), 1857-1864 (2010).
186. A. T. Gulledge, B. M. Kampa and G. J. Stuart, Journal of neurobiology **64** (1), 75-90 (2005).
187. P. J. Sjöström, E. A. Rancz, A. Roth and M. Häusser, Physiological Reviews **88** (2), 769-840 (2008).
188. W. Levy and O. Steward, Neuroscience **8** (4), 791-797 (1983).
189. J. C. Skou, Biochimica et biophysica acta **23**, 394-401 (1957).
190. C. Howarth, P. Gleeson and D. Attwell, Journal of Cerebral Blood Flow & Metabolism **32** (7), 1222-1232 (2012).
191. T. J. Jentsch, V. Stein, F. Weinreich and A. A. Zdebik, Physiological Reviews **82** (2), 503-568 (2002).
192. C. J. Schwiening, The Journal of physiology **590** (11), 2571-2575 (2012).
193. K. Pakdaman, M. Thieullen and G. Wainrib, (3), 761-794 (2010).
194. M. Forrest, Computation **2** (2), 47 (2014).
195. M. S. Feali and A. Ahmadi, Neural Processing Letters, 1-14 (2016).
196. G. S. Snider, Nanotechnology **18** (36), 365202 (2007).